Nanoparticles as MRI Contrast Agents and Biomarkers – Applications in Prostate Cancer and Mild Traumatic Brain Injury

by

Armita Dash
B.S.–M.S., Indian Institute of Science Education and Research – Kolkata, 2013

A Dissertation Submitted in Partial Fulfillment
of the Requirements for the Degree of

DOCTOR OF PHILOSOPHY

in the Department of Chemistry

© Armita Dash, 2017
University of Victoria

All rights reserved. This dissertation may not be reproduced in whole or in part, by photocopy or other means, without the permission of the author.

Supervisory Committee

Nanoparticles as MRI Contrast Agents and Biomarkers – Applications in Prostate Cancer and Mild Traumatic Brain Injury

by

Armita Dash
B.S.–M.S., Indian Institute of Science Education and Research – Kolkata, 2013

Supervisory Committee

Dr. ir. Franciscus C. J. M. van Veggel (Department of Chemistry)
Supervisor

Dr. Jeremy E. Wulff (Department of Chemistry)
Departmental Member

Dr. Patrick Nahirney (Division of Medical Sciences)
Outside Member

Abstract

Supervisory Committee
Dr. ir. Franciscus C. J. M. van Veggel (Department of Chemistry)
Supervisor
Dr. Jeremy E. Wulff (Department of Chemistry)
Departmental Member
Dr. Patrick Nahirney (Division of Medical Sciences)
Outside Member

Magnetic Resonance Imaging (MRI) is the most prominent non-invasive technique used in clinical diagnosis and biomedical research. Its development as an imaging technique has been aided by contrast agents (CAs) which enhance contrast to noise ratio in the images. This dissertation deals with paramagnetic lanthanide- and superparamagnetic iron-based nanoparticles (NPs) which are potential CAs at clinical field of 3 T and a high field of 9.4 T. Chapter 1 provides a brief overview of colloidal nanoparticles, with an emphasis on their surface chemistry and magnetic properties for bio-applications. Chapter 2 employs europium as an optical probe to illustrate the contribution of inner, second and outer sphere relaxation towards longitudinal and transverse relaxivities of paramagnetic NP-based CAs. Chapter 3 investigates the positive and the negative contrast enhancement abilities and magnetization of paramagnetic NPs comprising a core of sodium dysprosium fluoride with a sodium gadolinium fluoride shell. Their surface chemistry is tuned to target prostate cancer specifically. The application of these NPs is further extended in Chapter 4 to track an intraneuronal protein called tau following mild traumatic brain injury. Chapter 5 deals with facile synthesis and long-term stability of superparamagnetic iron NPs for their potential application as CAs. Chapter 6 illustrates the concept of MRI correlation using ‘T_1-only’ and ‘T_2-only’ NPs. Chapter 7 investigates on the dynamics involved in the phospholipids coating the surface of NPs. Chapter 8 concludes on the work detailed in the previous chapters and outlines the future outlook.

Table of Contents

List of Tables

List of Figures

List of Abbreviations

2S	second sphere
BE	binding energy
CA(s)	contrast agent(s)
DAPI	4',6-diamidino-2-phenylindole
DLS	dynamic light scattering
DSPE-mPEG	1,2-distearoyl-*sn*-glycero-3-phosphoethanolamine-*N*-[methoxy(polyethylene glycol)-2000] (ammonium salt)
DSPE-PEG-COOH	1,2-distearoyl-*sn*-glycero-3-phosphoethanolamine-*N*-[carboxy(polyethylene glycol)-2000] (sodium salt)
EDC	1-ethyl-3-(3-dimethylaminopropyl)carbodiimide)
EDX	energy-dispersive X-ray spectroscopy
EELS	electron energy-loss spectroscopy
ICP-MS	inductively coupled plasma mass spectrometry
IS	inner sphere
LNCaP	lymph node carcinoma of the prostate
MRI	magnetic resonance imaging
NHS	*N*-hydroxysulfosuccinimide sodium salt
NP(s)	nanoparticle(s)
OS	outer sphere
PC3	prostate cancer cell line
PDF	powder diffraction file
PSMA	prostate-specific membrane antigen
PVP	polyvinylpyrrolidone
SQUID	superconducting quantum interference device
TBI	traumatic brain injury
STEHM	scanning transmission electron holography microscope
TEM	transmission electron microscopy
XRD	(powder) X-ray diffraction

Acknowledgments

First and foremost, I would like to express my sincere gratitude to my supervisor Prof. Frank van Veggel, one of the smartest, distinguished elites I know (he is too modest to accept this). I am very grateful for all his contribution of time, ideas, motivation, and funding, to make my PhD experience productive and inspiring. His immense knowledge during scientific discussions, meticulous scrutiny and remarkable patience have led me overcome obstacles during my PhD pursuit. I am honored and fortunate to have worked under his guidance without which this dissertation would not have been possible.

I thank my fellow labmates for the stimulating confab and fun times that I have shared with in the lab. A special mention to Dr. Anurag Gautam for guiding me in colloidal synthetic chemistry during my first year.

I thank my committee members for their inputs in my research: Prof. Jeremy E. Wulff for his valuable critiques and Prof. Patrick Nahirney for allowing me to work on his transmission electron microscope.

I am highly grateful to the collaborators, specifically, Dr. Boguslaw Tomanek at the University of Alberta and Dr. Barbara Blasiak at the University of Calgary for their untiring help with MRI measurements and animal studies. I am thankful to Dr. Simon Trudel and Dr. Abhinandan Banerjee for performing SQUID measurements at the University of Calgary. I am also thankful to Dr. Garnette Sutherland, Dr. Sanju Llama and Dr. Michael Colicos of the University of Calgary and Dr. Mehdi Arbabi-Ghahroudi of the National Research Council of Canada, Ottawa, for their valuable time and contribution in the studies concerning mild traumatic brain injury.

I thank Prof. Robert D. Burke for his help with the confocal imaging of the prostate cancer cells. I am thankful to Dr. Jody Spence for carrying out ICP-MS analyses at UVic. I am also grateful to other support staff for their assistance during these years.

Finally, I am eternally appreciative to my loving parents for their incessant encouragement in scientific pursuit and inspiration to explore new, complemented with commendable moral and emotional support, that made me embark towards PhD and traverse through it. Last but not the least, this journey has been enlivened with the two young spirits, my beloved husband and my prudent brother.

Chapter 1. Introduction

1.1 Nanoparticles and Nanomedicine

Nanoparticles (NPs) belong to the class of particulate materials in which at least one of the dimensions lies in the range of 1–100 nm.[1] The basic rationale is that these nanometer-sized particles have functional and structural properties that are not available in either discrete molecules or bulk counterparts.[1-2] These size-dependent features include mechanical, thermal, electrical, magnetic, and optical properties which can often be tailored suitably by tuning the size, shape, composition and surface characteristics of NPs for their wide applications in science, engineering, and medicine.[3-4] These applications of nanometer-sized structures specifically concerning molecular imaging, medical diagnostics, targeted therapy, and image-guided surgery collectively form the interdisciplinary field of nanomedicine.[5-8]

The unprecedented potential of NPs in nanomedicine as imaging probes for early detection and diagnosis or as therapeutic agents for treatment of diseases has received enormous attention to target biological sites such as a specific organ, tissue, or even underlying cell.[6] As such, very many type of NPs have been developed including lipid-based, polymeric, inorganic, metallic and carbon-based nanostructures.[4] Amongst all these, inorganic NPs offer the advantage of being robust, and, thus, very stable and resistant to enzymatic degradation when administered in a biological milieu. They are synthesized in sizes of < 20 nm to allow their excretion via renal or fecal route.[9] Unlike small molecule-based imaging agents or drugs, NPs can be designed by integrating both diagnostic and therapeutic features providing a multifunctional platform for simultaneous diagnosis and therapy.[10] For instance, an NP can carry, on one hand, a targeting molecule to a diseased site, and on the other, a drug to treat this disease, while the inorganic core of the NP can provide the means for detection. Also, NPs are capable of carrying several hundreds of ligands that can result in an enhanced local concentration of the drug once they reach the target. In the same way, multivalent presentation of ligands on the surface of the NPs allows for the use of molecules with low affinity towards their target, widening the range of options to achieve specific labelling. Due to their large surface area and interior cargo volume, a low dose of NP administration is effective for target-specific imaging and therapy.[11]

1.2 Physical Chemistry of Nanoparticles for *in vivo* applications

To enhance target-specificity and blood circulation time by limiting their uptake by immune system or more specifically, reticuloendothelial system (RES), a global system of macrophages in liver, spleen and bone marrow, NPs are generally designed based on passive and active targeting strategies. Passive targeting is achieved via the enhanced permeation and retention (EPR) effect in fenestrate vessels that enable high accumulation of NPs in cancerous tissues owing to their high endothelial leakage and poor lymphatic drainage. On the other hand, active targeting is achieved by tagging NPs with a molecular “address,” e.g., conjugating NPs with target-cell-specific antibodies or peptides, which allows them to home in specifically at target sites, often by permeating across a biological barrier that restricts the free access of NPs to underlying organs/cells/subcellular organelles.[12] The relative contribution of EPR effect and active targeting (receptor-mediated) for NPs' accumulation in tumors has not been defined yet.

NPs intended for medical use are required to be designed mimicking the pharmacokinetics of natural lipid vesicles, proteins and other biomolecules, thereby, protecting themselves from defense mechanisms of the body. NPs, when administered into a biological system, face a series of biological barriers which could limit their target-specific availability and prevent proper diagnostic and therapeutic outcomes. One of the major obstacles is sequestration by the mononuclear phagocyte system (MPS) which is initiated by opsonization of NPs – formation of protein corona around NPs – resulting in marked reduction of specificity in active targeting.[13] This process is dependent on NP size, surface charge, hydrophobicity and surface chemistry. Systemically administered NPs should have hydrodynamic diameters from 10 nm to 100 nm. NPs smaller than 5 nm are rapidly filtered by the kidney, and larger than 100 nm get sequestered specifically by sinusoids in spleen and fenestra of liver, which are 150–200 nm in diameter.[14] NP uptake by MPS increases when the surface charge (either positive or negative) increases, while the NPs with lowest absolute value of zeta potential (±5 mV) show prolonged circulation.[14]

Appropriate surface chemistry of inorganic NPs imparts colloidal stability in physiological environment, biocompatibility, biodegradability, bioavailability, *in vivo* pharmacokinetics, specific targeting, and clearance.[15-16] Functionalizing NPs with poly(ethylene glycol) or PEGylation of NPs, which imparts hydrophilicity, sharply increases their circulation time, from minutes to hours.[17] For an efficacious functioning of inorganic NPs inside a living system as a diagnostic or therapeutic agent, the NPs require (i) a biocompatible surface coating to impart hydrophilicity and dispersibility in water and physiological buffer, (ii) reactive functional groups on their surface for subsequent bioconjugation to various biomolecules (such as peptides, proteins, antibodies, etc.) for targeting to a specific site in the body, and (iii) an apt “stealth” surface to cross the biological barriers to reach the target site.[13-14]

To date, dozens of nanostructure-based formulations as diagnostic or therapeutic materials have been approved for clinical use by the Food and Drug Administration (FDA), of which, the majority are composed of a simple formulation with no specificity (e.g., Doxil, Abraxane, or Feridex) and, thus, considered first generation nanomedicine.[18-19] On the other hand, various NPs with high target specificity are actively being studied, of which some are multifunctional NPs with more than one clinical purpose – biomedical imaging and therapeutics.[10,20]

1.3 Magnetic Resonance Imaging (MRI)

Biomedical imaging modalities generally include optical imaging, magnetic resonance imaging (MRI), computed tomography (CT), ultrasound (US) and positron emission tomography (PET) or single photon emission computed tomography (SPECT).[11] Each imaging technique has its own unique advantages alongside with intrinsic limitations, such as inherently low sensitivity (MRI), poor tissue penetration (optical imaging), low spatial resolution (optical imaging, PET, SPECT, US), or radiation risk (PET, SPECT, CT) which make it difficult to obtain accurate and reliable information at the diseased site.[21] Nevertheless, MRI has emerged as one of the most widely used, non-invasive diagnostic techniques that acquires three-dimensional tomographic information of whole tissue samples and animals, including humans, with high spatial (25–100 μm) resolution and soft tissue contrast.[22] It has been the preferred tool for assessing cardiovascular function, imaging nervous system and gastrointestinal tract, and detecting lesions and tumors because MR images are acquired without the use of ionizing radiation or radiotracers.

MRI is based upon the principles of nuclear magnetic resonance (NMR), discovered independently by Bloch and Purcell in 1946, for which they were awarded with the Nobel Prize in 1952.[23-24] In 1973, Lauterbur used the principles of NMR with gradients of strong and weak magnetic fields to identify the position of a particular nucleus, as the strength of the field is proportional to the radiofrequency and, thus, developed MRI for which he was awarded with the Nobel Prize in 2003 alongside with Peter Mansfield.[25-26] In MRI, when the nuclei of hydrogen (^1H from water in most cases) are exposed to a strong magnetic field (B_0 applied along *z*-axis, say), their spins (net magnetic moment) align either parallel or antiparallel to B_0 by precessing under the Larmor frequency. A radio frequency (RF) pulse is applied perpendicular to B_0 with a frequency equal to the Larmor frequency of protons that causes the net magnetic moment to tilt away from B_0. Once the RF signal is removed, the nuclei realign themselves to their initial low-energy state such that their net magnetic moment is again parallel to B_0. This return to equilibrium is referred to as relaxation which is analyzed in terms of two independent processes – longitudinal 'T_1' relaxation (recovery of *z*-component of the nuclear spin magnetization towards its thermal equilibrium along B_0) and transverse 'T_2' relaxation (decay of transverse *xy*-component of magnetization due to dephasing of spins).[22]

1.3.1 MRI Contrast Agents

Although MRI can reveal anatomic details in organs, it has an inherently low sensitivity that leads to difficulty in differentiating normal and diseased cells due to small native relaxation time differences. Currently, about 35% of clinical MR scans need contrast agents (CAs) to improve their sensitivity and diagnostic accuracy.[27] These CAs are paramagnetic, superparamagnetic or ferromagnetic materials that shorten the relaxation times of water protons in applied magnetic field, thereby, enhancing image contrast.[28] The efficiency of a contrast agent to reduce the T_1 or T_2 of water protons is referred to as longitudinal (r_1) or transverse (r_2) relaxivity and defined empirically by[29]

$$\boldsymbol{\frac{1}{T_i} = \frac{1}{T_i^0} + r_i[CA]; i = 1, 2}$$

where [CA] is the concentration of CA, T_i is the observed relaxation time in presence of CA, T_i^0 denote the relaxation times of the water protons in absence of the CA. The CAs are classified as T_1 and T_2 contrast agents based on whether the substance increases the transverse relaxation rate ($1/T_2$) by roughly the same amount that it increases the longitudinal relaxation rate ($1/T_1$) or whether $1/T_2$ is altered to a much greater extent. The T_1 or positive CAs lower T_1 giving rise to increases in signal intensity (brightening of image). The T_2 or negative CAs largely increase the $1/T_2$ of tissue selectively causing a reduction in signal intensity (darkening of image). T_1 CAs are often more desirable than T_2 agents for accurate high-resolution imaging because the dark signal could mislead the clinical diagnosis in T_2-weighted MRI owing to the signal often confused with the signals from bleeding, calcification or metal deposits and susceptibility artifacts.[30]

Most MRI CAs exploit the ^1H relaxation of water molecules which make up about 60% of human body. In absence of a CA, it is usually the motion of the neighboring ^1H protons which creates a fluctuating magnetic field that stimulates a return to equilibrium of the H_2O protons. If a molecule (CA) containing unpaired electrons is introduced into the H_2O molecule environment, they trigger the return of the H_2O protons to equilibrium much more effectively, because the magnetic moment of the electron is 658 times stronger than that of the proton.[29] This action on the relaxation properties of the water hydrogen nuclei generates contrast which is different from X-ray contrast media and nuclear imaging agents where the effect observed is proportional to the concentration of iodine or the radionuclide. This makes the relaxivity of a CA a very important feature since the concentration of water molecules is much higher than that of the administered CA. Table 1.1 enlists ions of transition metals and lanthanides which have unpaired electrons giving rise to magnetic moment.[31-32] For the metal ion to be effective as a CA, the electron spin-relaxation time must match the Larmor frequency of the protons which is met in case of Fe^{3+}, Mn^{2+}, Gd^{3+}, Dy^{3+} and Ho^{3+}. The main problem with paramagnetic heavy metal ions in their native form is their toxicity. Therefore, clinical CAs employ complexes of lanthanide ion (Gd^{3+}) which have comparatively lower cellular toxicity and are cleared by renal filtration. The commercially available T_1 CAs are Gd(III)-chelates (commercial names are Magnevist, Dotarem, Omniscan, etc.) which possess a longitudinal relaxivity (r_1) of 3–5 $mM^{-1}\ s^{-1}$ at magnetic field strengths ranging from 0.47 T to 4.7 T.[33-34] The commercialized T_2 MRI CAs are dextran or siloxane coated superparamagnetic iron oxide NPs (SPIONs; commercial names are Resovist, Feridex, Gastromark, etc.) which possess a very large transverse relaxivity (r_2) of 100–200 mM^{-1} s^{-1} at magnetic field strengths of 0.47 T – 4.7 T.[33,35-36]

Table 1.1. Magnetic properties of transition metal ions and lanthanide ions.

Metal ion	**Ground state configuration**	**Number of unpaired electrons**	**Theoretical magnetic moment[31] (μ_B)**
Fe^{3+}	$^6S_{5/2}$	5 ($3d^5$)	5.92
Mn^{2+}	$^6S_{5/2}$	5 ($3d^5$)	5.92
Eu^{3+}	$^7F_0$	6 ($4f^6$)	0
Gd^{3+}	$^8S_{7/2}$	7 ($4f^7$)	7.94
Tb^{3+}	$^7F_6$	6 ($4f^8$)	9.72
Dy^{3+}	$^6H_{15/2}$	5 ($4f^9$)	10.65
Ho^{3+}	$^5I_8$	4 ($4f^{10}$)	10.6
Er^{3+}	$^4I_{15/2}$	3 ($4f^{11}$)	9.58
Tm^{3+}	$^3H_6$	2 ($4f^{12}$)	7.56

1.3.1.1 Lanthanide (Ln^{3+})-based CAs

As seen in Table 1.1, theoretically, most of the lanthanide (Ln^{3+})-based NPs are potential MRI CAs in a sense that all Ln^{3+} have unpaired electrons and are paramagnetic, except La^{3+} and Lu^{3+}. Their magnetic properties are determined entirely by the ground state (except Sm^{3+} and Eu^{3+}) because the excited states are very well separated from the ground state (owing to spin–orbit coupling), as shown in Figure 1.1, and are, thus, thermally inaccessible.[32] Moreover, the magnetic moment of the Ln^{3+} is essentially independent of environment because the 4*f*-electrons are compactly localized close to the nucleus owing to the shielding of the 4*f* orbitals by filled $5s^25p^6$ subshells.[37] Ln^{3+} have a very small ligand field splitting in the order of 100 cm^{-1} compared to that of 3*d* transition metal ions (20,000 cm^{-1}).[38] This leads to minimal ligand effect on the magnetic properties of Ln^{3+}.

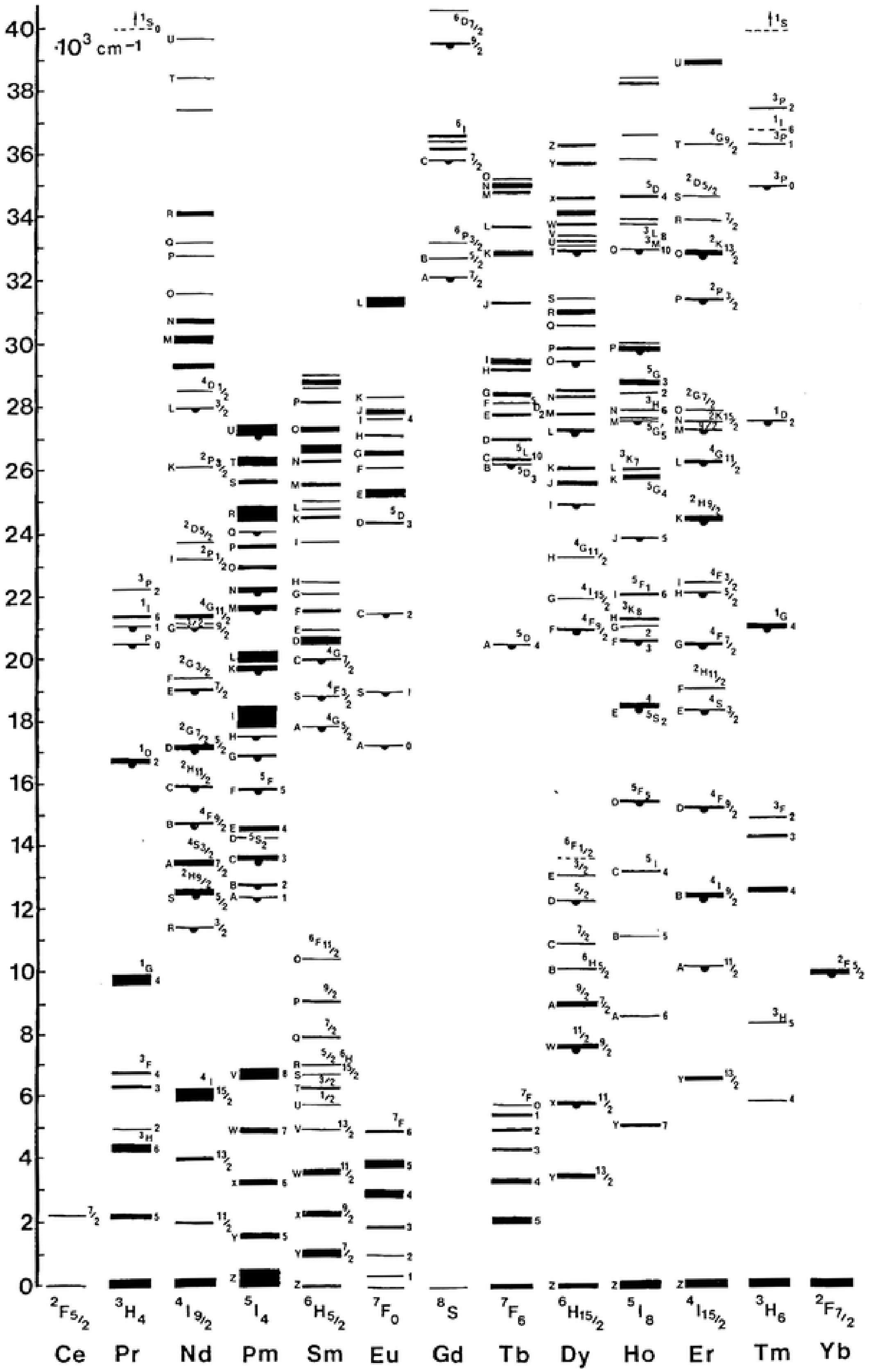

Figure 1.1. Energy levels of the Ln^{3+} ions (from ref. 32).

Among the Ln^{3+}-based CAs, the most popular T_1 CAs used in MRI are composed of gadolinium(III) ions (Gd^{3+}). The choice of Gd^{3+} is explained by its seven unpaired electrons which makes it the most paramagnetically stable metal ion with a large magnetic moment (7.94 Bohr magneton, μ_B). In addition, owing to the symmetric S-state, Gd^{3+} has a relatively long electron spin relaxation time of 10^{-9} s compared to other paramagnetic ions (e.g., Dy^{3+}, Ho^{3+}, Yb^{3+}: 10^{-13} s) which is relevant to its efficiency as a T_1 CA. Gd^{3+}-containing NPs are being developed over clinical Gd^{3+}-chelates to achieve T_1-weighted imaging at magnetic fields of $\geq$ 7 T with higher contrast to noise ratio compared to that of 3 T clinical MRI, increase blood circulation times and overcome the issue of Gd^{3+} leaching. Free Gd^{3+} has its radial size approximately equal to that of Ca^{2+} and can disrupt Ca^{2+}-mediated signaling pathways via transmetallation.[34] This could be prevented by employing Gd^{3+}-based NPs with appropriate surface chemistry.

On the other hand, paramagnetic dysprosium(III) ion (Dy^{3+})-based NPs are shown to be potential T_2 CAs.[39] Dy^{3+} possesses a highly anisotropic electronic ground state having 4*f*-orbital filled with 9 electrons resulting in larger spin-orbit interactions and shorter electron relaxation times (10^{-13} s) compared to that of Gd^{3+}.[40] Their intrinsic high magnetic moment (10.65 μ_B) results in high magnetic susceptibility per unit volume of NPs, thereby, enhancing the r_2 relaxivity at high magnetic fields.[39]

Relaxivity of a paramagnetic metal complex or a paramagnetic ion-based NP is factored into three contributions arising from water present in (i) inner sphere (IS) in which water molecules are directly bonded to the paramagnetic ion, (ii) second sphere (2S) which is less well defined and contains water molecules hydrogen bonded to the metal complex or the ligands coating a NP, and (iii) outer sphere (OS) in which water diffuses freely.[29,41]

The contributions from inner, second and/or outer spheres of relaxation depends primarily on the surface chemistry of NPs which determines the accessibility of water molecules to establish dipolar interactions with the paramagnetic ions of the NPs.

1.3.1.2 Iron oxide-based CAs

Owing to the high sensitivity of Fe metal towards oxidation when exposed to oxygen or water, magnetic iron oxides have been developed – magnetite (Fe_3O_4) and maghemite (γ-Fe_2O_3) – which have characteristic long-range ordering of magnetic moment.[42] These ferromagnetic materials have internal magnetic field which generates magnetostatic energy. The magnetic moments are parallel to minimize the magnetostatic energy in the bulk magnetic materials containing multiple domains. Magnetic NPs show their maximum coercivity (which is the intensity of the applied magnetic field required to reduce the magnetization of NPs to zero after reaching saturation magnetization) at the transition from multi-domains to single domains, and the coercivity then decreases with decreasing size. When the NPs are small enough, superparamagnetism occurs, in which the thermal energy is sufficient to randomize the magnetization. In the absence of an external magnetic field, the coupled individual spin moments in superparamagnetic NPs are not pinned to the crystalline axis and, hence, fluctuate collectively, leading to an effectively zero magnetic moment. Nonetheless, they respond quickly to an external magnetic field and exhibit saturation magnetization equivalent to that of ferro- and ferrimagnetic materials. Superparamagnetic particles behave like small movable magnets, creating a strong magnetic field inhomogeneity in the environment and considerably reducing the T_2

relaxation time of H_2O protons in their vicinity. Current preclinical and clinical MRI utilize formulations of superparamagnetic iron oxide (Fe_3O_4) NPs (SPIONs) as T_2 CAs owing to their non-toxicity in biological environment.[42] However, the r_2 relaxivity of the commercial formulations, which is ascribed to the saturation magnetization of Fe, still remains low leading to false positive diagnosis in hypointense areas such as blood pooling, calcification and metal deposition.[30] Higher r_2 relaxivity could be obtained from larger spherical iron oxide NPs which would have stronger saturation magnetization (M_s). But this could lead to ferri/ferromagnetic properties at room temperature, often resulting in interparticle agglomeration even in the absence of an external magnetic field.[43] Control over size and morphology, and metal doping have been done to produce iron oxide NPs with a large M_s value, leading to a significant increase of r_2 relaxivity.[42,44-45]

1.4 Europium(III) as an Optical Probe

The intricate optical properties of trivalent lanthanides (Ln^{3+}) are reflected perfectly in the article by J. H. van Vleck entitled "The Puzzle of Rare-Earth Spectra in Solids' in 1937.[46] The electronic $[Xe]4f^n$ configurations (n = 0–14) feature them with rich spectroscopic terms which make the lanthanides (except for n = 0, 14) very attractive for optical applications including bioimaging, sensing, therapy, lighting and displays, and photovoltaic devices.[32,47-48] Although the intra-configurational 4*f*-4*f* transitions are principally forbidden for all 4*f* orbital containing elements, for instance, Ln^{3+}, the incorporation of eigenstates (5*d*) leads to partially allowed intra-configurational transitions, which enable large Stokes (> 200 nm)/anti-Stokes shifts in luminescence processes, long luminescent lifetimes, sharp-band emissions (full width at half maximum ~10 nm) and excellent photostability.[47]

Trivalent europium (Eu^{3+}) is well known for its strong red luminescence. Eu^{3+} is particularly interesting over other Ln^{3+} ion because of its even number of 4*f* electrons resulting in non-degenerate ($J = 0$) levels of the transitions in both the excitation and the emission spectra.[47] Since both the ground state ($^7F_0$) and excited state ($^5D_0$) are non-degenerate and, thus, neither of these levels can be split by a ligand field, the absorption band corresponding to a transition between these two levels must consist of a single, unsplit line for a given Eu^{3+} environment. The number of lines observed for the $^5D_0 \rightarrow {}^7F_J$ ($J = 0$–6) transitions in the emission spectrum or the $^5D_J \leftarrow {}^7F_0$ transitions in the excitation spectrum allows determining the site symmetry of the Eu^{3+} ion. The excited state lifetimes of Eu^{3+} are environmentally sensitive and they lie conveniently in the region 100–3,000 μs.[49] Further, the lifetimes of the excited states which decay exponentially are highly sensitive to the positioning of Eu^{3+} ions, for instance, in bulk or surface of a NP,[50] dispersed in deionized water or deuterated water or an organic solvent. Coordination to H_2O results in quenching of radiative lifetimes of Eu^{3+} ascribed to the radiation-less energy transfer from excited states of Eu^{3+} to matching vibrational overtones of O-H of water (Figure 1.2). On the other hand, when Eu^{3+} ions are in proximity with D_2O molecules, a higher overtone of O-D oscillator makes this non-radiative energy transfer exceedingly inefficient. This makes Eu^{3+} as a spectroscopic probe for determining site symmetry[51] and assessing coordination to ligands/molecules such as H_2O[52] which is detailed in Chapter 2.

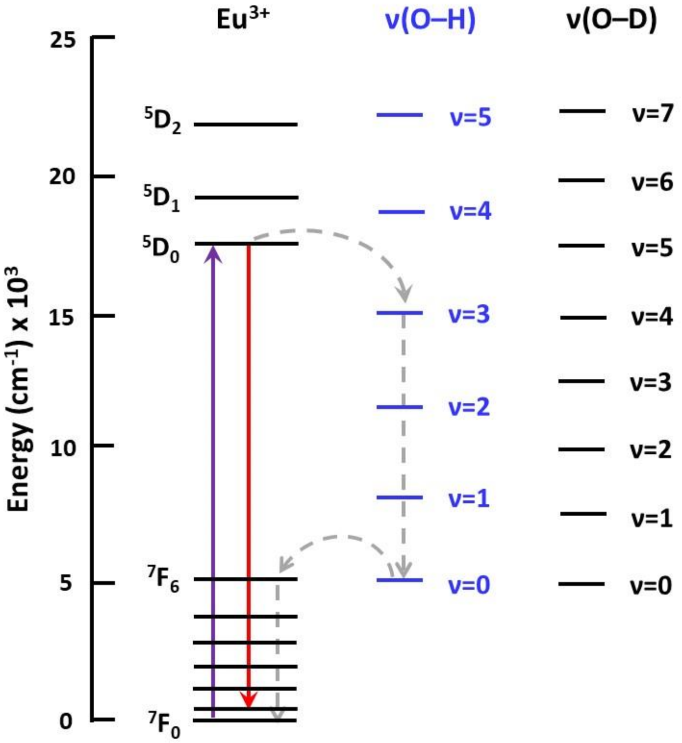

Figure 1.2. Electronic energy levels of Eu^{3+}. The red arrow from $^5D_0$ is an intense emissive transition. Non-radiative energy transfer competes with the radiative processes through coupling of the emissive states to the O-H vibrational overtones of surrounding H_2O molecules owing to their dipolar interactions with Eu^{3+}. The non-radiative energy transfer in case of D_2O is exceedingly inefficient because a higher overtone of O-D oscillator is involved. (adapted from ref. 52)

1.5 Colloidal Synthesis and Surface Modification of Nanoparticles

The controlled synthesis of monodispersed colloidal NPs, with a size dispersion of less than 5%, is essential for *in vivo* applications in bioimaging and therapeutics. Wet chemical (solution-based) synthetic methods have been explored to prepare various NPs by controlling the very many synthetic parameters such as reaction temperature, reaction time, pH, and concentration of precursors and surfactants. This has led to tuning of the crystal structure, size distribution, morphology, and even the facets of NPs.[53-55] Syntheses of sodium lanthanide fluoride and iron NPs have been specifically dealt with in the subsequent sections because these NPs have been synthesized, characterized, functionalized and applied as MRI contrast agents in the following chapters of this dissertation.

1.5.1 Synthesis of Sodium Lanthanide Fluoride ($NaLnF_4$) Nanoparticles

The synthetic methods dealing with $NaLnF_4$ (Ln^{3+} = Y^{3+}, Gd^{3+}, Dy^{3+}) in this dissertation are categorized into thermolysis and precipitation/co-precipitation.[54] Thermolysis refers to the decomposition of the organometallic precursors of Ln^{3+} such as acetates and trifluoroacetates of Ln^{3+} under an inert atmosphere in a high boiling solvent mixture of oleic acid and octadecene. Oleylamine is often added to this mixture which serves as the capping agent along with oleic acid to control the size and morphology of NPs. To obtain NPs with narrow size distribution, nucleation and growth processes can be altered by modulating temperature, heating rate, time, etc.

In a typical synthesis to produce cubic (α) phase $NaLnF_4$ NPs,[56] Ln^{3+}-acetate is formed by dissolving Ln^{3+}-oxides in deionized water and trifluoroacetic acid at 85 °C. After evaporating excess water, sodium trifluoroacetate, oleic acid, octadecene, and oleylamine are added to the Ln^{3+}-acetate and stirred under a continuous flow of argon at 285 °C for an hour. The reaction temperature and time depends on the intended size of the NPs. The resulting NPs are precipitated in ethanol, washed, collected by centrifugation, and dispersed in an organic solvent such as hexanes.

In precipitation/co-precipitation synthesis, simultaneous precipitation of several ions occurs leading to formation of NPs. Differences in the precipitation rates of the ions, coordinating surfactants and solvents in the reaction system play a major role in yielding monodisperse NPs. In organic media such as a solvent mixture of oleic acid and octadecene, Ln^{3+}-based oleates, acetates, chlorides, and nitrates are used to provide cations (Ln^{3+}), while NaF, NaOH, and NH_4F are used to provide anions. Methanol is used as a solvent to dissolve NaF, NaOH, NH_4F, which is then evaporated when the reaction temperature is raised high (280–310 °C) during NP synthesis.

In a typical synthesis to produce hexagonal (β) $NaLnF_4$ NPs,[56] Ln^{3+}-salts in the form of chlorides bearing waters of hydration are dissolved in an appropriate molar ratio of oleic acid and octadecene at a temperature of 120 °C under vacuum to form Ln^{3+}-oleates. The medium is cooled to room temperature at which NaOH and NH_4F (or NaF) dissolved in methanol are added to the reaction mixture and stirred for an hour. After evaporating methanol at 80 °C, the temperature of the reaction is raised to 280–310 °C as required for the intended size and shape of NPs. The resulting NPs after a certain reaction time are precipitated in ethanol, washed and dispersed in an organic solvent (e.g., hexanes). Reaction temperature, time, heating rate, molar ratios of solvents and salt precursors are modulated to obtain NPs of intended size, morphology and composition.

Although all the Ln^{3+} display similar chemical properties, the growth mechanism of $NaLnF_4$ in the solvent mixture of oleic acid and octadecene (and oleylamine) is still affected by the choice of Ln^{3+}. The light lanthanides (including Y^{3+}) favor the hexagonal (β) phase, while the cubic phase (α) is preferred in heavy lanthanides. Growth of $NaLnF_4$ NPs occurs via Ostwald ripening[57] in which larger NPs with smaller surface to volume ratios grow at the expense of the energetically less stable smaller NPs. This could often lead to a broad particle size distribution. But the ensemble of differently sized NPs "focuses" to one size. The "size focusing" of the β-phase (hexagonal phase) product particles occurs due to their growth in the presence of the α-phase (cubic phase) particles formed in the initial stages of synthesis.[58-60] The higher solubility of the α-phase relative to the β-phase provides a condition of supersaturation for β-phase particle growth, which leads to the size focusing as expected in the diffusion limited growth regime.

To synthesize core $NaLn^1F_4$ NPs with a shell of $NaLn^2F_4$ (two different Ln^{3+}: Ln^1 and Ln^2) around them, this effect can be exploited to produce size-focused, β-phase, core-shell NPs by ripening β-phase cores in the presence of sacrificial α-phase NPs which give rise to the shell material.[56] In a typical synthesis of the core-shell NPs,[61] the usual protocols of synthesizing the α- and β-phase NPs are followed. When the β-phase NPs reach the stage of intended size during their synthesis, a calculated amount of shell material (smaller α-phase NPs) is injected into the reaction medium containing the high boiling solvent mixture of oleic acid and octadecene keeping the reaction temperature constant. The sacrificial α-phase $NaLn^2F_4$ NPs dissolve while the more energetically favorable β-phase $NaLn^2F_4$ NPs grow over the core $NaLn^1F_4$ NPs owing to the matching lattice constants of Ln^1 and Ln^2. This approach requires the sacrificial NPs forming the shell to be smaller than the core NPs.

1.5.2 Synthesis of Iron Nanoparticles

Synthesis of monodisperse (particle size dispersion < 5%) magnetic NPs, specifically, SPIONs, has been achieved via wet-chemistry methods.[42] Despite the attractive magnetic properties of Fe metal, the synthesis of Fe NPs has been challenging due to their high tendency towards oxidation in air and moisture. For this reason, iron nanocubes with a passivated thin shell of iron oxide was synthesized by decomposing $Fe[N(SiMe_3)_2]_2$ in mesitylene in a H_2 atmosphere in a glove box[62] and also by decomposing iron oleate complex.[63] While Fe NPs have also been synthesized by thermal decomposition of $Fe(CO)_5$[64] and reduction of $Fe(acac)_3$[65] (acac = acetylacetonate), the resulting NPs either oxidize completely, are polydisperse, or the proof of NP stability in both organic and aqueous media is missing.

The organometallic compound, iron pentacarbonyl, $[Fe(CO)_5]$ has a standard enthalpy of formation of only -185 kcal mol^{-1} and the five carbon monoxide subunits each have an enthalpy of formation of -110.5 kcal mol^{-1} which account for its facile thermal decomposition.[66] Although the molecule is easy to decompose, the decomposition process occurs via multiple intermediate iron carbonyls and iron clusters which form and catalyze the decomposition. In a typical synthesis detailed in a subsequent chapter, hexadecylamine·hydrochloride in a solvent mixture of octadecene and oleylamine is deoxygenated under a continuous flow of argon. $Fe(CO)_5$ is injected at 180 ^{o}C which results in a burst of nucleation of Fe NPs. The growth and, hence, the resulting size of the NPs is controlled by maintain a constant temperature and appropriate reaction time. Oleic acid is injected into the reaction medium to cap the Fe NPs. The resulting NPs are precipitated in ethanol and dispersed in an organic solvent such as chloroform.

1.5.3 Aqueous Transfer of Nanoparticles (for bioconjugation)

For *in vivo* applications, the interface between a NP and its target has been the prime focus of research which determines the availability of the NP to its target. The main barriers to implementation of NPs for targeted-delivery is the surface chemistry that could lead to NPs' aggregation and deactivation. To render the hydrophobic NPs hydrophilic and biocompatible, several strategies have been used such as silanization or coating with amorphous silica,[67-68] coating with amphiphilic polymers [e.g., polyacrylic acid,[69] poly(L-lysine),[70] poly(maleic anhydride-*alt*-1-octadecene)[71], 6-aminohexanoic acid,[72] etc.], ligand exchange [e.g., with poly(ethylene glycol) (PEG)-phosphate,[73] mercaptopropionic acid,[74] hexanedioic acid,[75] etc.] and so on. Amphiphilic surfactants, such as phospholipids,[76] are used which adsorb to the surface of NPs with the hydrophilic portion of the surfactants exposed to aqueous media. The adsorption is driven by hydrophobic interactions between the surfactant and the NP surface. The work presented in the following chapters deals with coating NPs with phospholipids, thereby, mimicking the composition and functionality of the cells' external membrane.[77]

The as-synthesized oleate-capped ($NaLnF_4$ and Fe) NPs are dispersed in organic solvents. To transfer them to aqueous solvents – water or buffer – NPs can be coated with 1,2-distearoyl-*sn*-glycero-3-phosphoethanolamine-*N*-[methoxy(polyethylene glycol)-2000] (ammonium salt) [abbreviated as DSPE-mPEG] in which the PEGs impart hydrophilicity.[76] The aqueous transfer involves dispersing the oleate-capped NPs in chloroform containing a calculated amount of DSPE-mPEGs to coat all the NPs. Dimethyl sulfoxide (DMSO) is added to the dispersion which is miscible in both chloroform and water. The chloroform is selectively evaporated under vacuum due to its low boiling point which leaves behind the phospholipid coated NPs dispersed in DMSO. Water is further added to displace DMSO via centrifugal filtration.

The commercially available phospholipids (DSPE-PEGs) have functionalities, other than the methoxy groups (DSPE-mPEG) on them, such as amines (DSPE-PEG-NH_2), carboxylates (DSPE-PEG-COOH), biotin (DSPE-PEG-biotin), maleimides (DSPE-PEG-mal) and thiols (DSPE-PEG-SH). For target-specific bioapplications, these functional end groups of phospholipids coating NPs can be selectively attached to peptides or antibodies via bioconjugate chemistry, for instance, binding the primary amines from lysines of antibodies to carboxylates of phospholipids by amide bond formation, thiol-maleimide coupling (Michael addition) and noncovalent interaction (biotin-streptavidin).[78]

1.6 Outline of the Dissertation

The last section gave an overview of the two types of NPs – sodium lanthanide fluoride and iron – studied in this dissertation. Chapter 2 discusses the synthesis and characterization of paramagnetic Gd^{3+}-based NPs: small (3 nm sized) $NaGdF_4:Eu^{3+}$ and large (19 nm sized) $NaYF_4$-$NaGdF_4:Eu^{3+}$ core-shell NPs. These NPs are coated separately with polyvinylpyrrolidone and phospholipid-PEG to achieve hydrophilicity. T_1 and T_2 relaxation times were obtained on a 9.4 T MRI. The accessibility of water molecules to the surface paramagnetic Gd^{3+} in the NPs is probed by analyzing the excited state lifetime decays of Eu^{3+} which are highly sensitive to proximate water molecules. The T_1 and T_2 relaxation rate enhancement were found to be dominated by inner and second sphere relaxation in the small (3 nm sized) NPs while outer sphere relaxation exclusively dominated in the large (19 nm sized) NPs.

Chapter 3 details the synthesis and surface functionalization of paramagnetic $NaDyF_4$-$NaGdF_4$ core-shell NPs which show enhanced r_1 and r_2 relaxivities at both clinical field of 3 T and high field of 9.4 T compared to the current clinical CAs. These NPs are coated with phospholipids bearing functional end groups which are employed to conjugate with anti-PSMA antibodies to target the prostate specific membrane antigen (PSMA) rich cell membranes of human prostate adenocarcinoma (LNCaP) *in vitro* and *in vivo*. *In vitro* targeting was confirmed by confocal imaging while *in vivo* tracking of the paramagnetic NPs was accomplished on mice bearing LNCaP tumors in MRI at 9.4 T. PC3 cells, another type of prostate cancer cell line, was used as a negative control which do not express PSMA.

Chapter 4 demonstrates the bioconjugate chemistry between functionalized phospholipid-coated $NaDyF_4$-$NaGdF_4$ core shell NPs and anti-tau antibodies which are employed to target mild traumatic brain injury *in vitro*. Fluorescence imaging has been employed to track the NPs bound with a photostable dye called Alexa-488 in the neural-glial co-culture.

Chapter 5 discusses about the synthesis, characterization, surface modification, magnetic and relaxation times' measurements of three different batches of monodisperse Fe NPs possessing 8.8 nm, 12.0 nm and 15.2 nm diameters. Long term stability of these NP dispersions is assessed in organic (chloroform) and aqueous (water) media.

Chapter 6 demonstrates the concept of MRI correlation employing 20 nm sized $NaYF_4$-$NaGdF_4$ core-shell NPs as the 'T_1-only' NPs and 15 nm sized Fe NPs as the 'T_2-

only’ NPs. Relaxivity measurements are done for different volumetric combinations of either kinds of NPs to address the correlation of T_1 and T_2 relaxation times in generating image contrast.

Chapter 7 investigates the dynamics of phospholipids coating the NPs. The phospholipids adsorbed on to the NPs via hydrophobic interactions are shown to undergo exchange processes among NPs which is illustrated by Förster resonance energy transfer (FRET) experiments.

Chapter 8 concludes on the goals achieved in this dissertation and explores potential opportunities of the NP-based CAs.

Chapter 2. Validation of Inner, Second, and Outer Sphere Contributions to T_1 and T_2 Relaxation in Gd^{3+}-based Nanoparticles using Eu^{3+} Lifetime Decay as a Probe

2.1 Introduction

Magnetic resonance imaging (MRI) is a non-invasive diagnostic technique that produces tomographic information about whole tissue samples, animals and humans with high spatial resolution and excellent soft tissue contrast.[26] The radiofrequency (RF) pulses, external static magnetic field and time variable magnetic fields influence the nuclear spin of water protons allowing MR signal acquisition and image reconstruction. Following RF excitation longitudinal or spin-lattice (T_1) and transverse or spin-spin (T_2) relaxation processes at the tissue sites generate contrast in the MR image. Contrast agents (CAs) are often introduced to enhance the relaxation rates of water protons and, thus, improve diagnostic capabilities of MRI.[29,40,79-81] Such agents, in the form of chelates of paramagnetic lanthanide (Ln^{3+}) ions, for example, Gd^{3+} possessing half-filled *f*-orbitals with 7 unpaired electrons, have widely been studied and employed clinically due to their ability to effectively shorten the T_1 proton relaxation time.[41] Despite progress in their design and synthesis, Gd^{3+} chelates are limited by low specificity, short blood half-life, and fast renal clearance and very low relaxivity at high magnetic fields ($\geq$ 3 T).[29,34,40-41,79] To overcome these constraints, nanoparticle (NP)-based CAs, possessing high density of metal ions *per* NP probe, are being developed and can be used at low doses or detect low concentration targets, thereby, mitigating dosage toxicity issues.[39,82-84] Their physiochemical, surface and magnetic properties can be tuned so as to generate MR images with high signal-to-noise ratio at high magnetic fields. A high magnetic field, such as 9.4 T, is advantageous over low fields (< 3 T) because it yields images with high contrast to noise ratio, high spatial resolution and/or reduced acquisition times. These benefits have led to the need for human imaging at 7, 9.4 and 11.7 T.[85-88] To design and optimize potential NP-based CAs for MRI applications, it is essential to understand the mechanism of how the NPs influence the relaxation rates (relaxivities) of water protons to produce the image contrast.

An NP, containing paramagnetic Ln^{3+} ions (e.g., Gd^{3+}) and dispersed in water, can be viewed as having three consecutive solvation spheres: (i) the inner sphere (IS) where the ligands/water molecules coordinate directly to the surface Gd^{3+} ions and follow the NPs in its Brownian reorientation and exchange with the surrounding free water molecules, (ii) the second sphere (2S) where the water molecules significantly bind to the surface coating ligands of the NP and indirectly to the surface Gd^{3+} ions via dipolar interaction, develop an electrostatic interaction with the surface lanthanide and sodium cations of the NP, rotate with the NP and exchange with the surrounding free water molecules and the ones coordinated to the ligands, and (iii) the outer sphere (OS) where free water molecules translate, diffuse, and rotate with their Brownian motion with respect to the NP.[29,89-90] Relaxation rate of water protons induced by paramagnetic NPs is influenced by the proximity of water protons to the Gd^{3+} ions in the NPs. The penetration of water in any of the solvation spheres is entirely governed by the surface functionalization of the NP. Although several theoretical studies and nuclear magnetic relaxation dispersion profiling have been carried out to understand the parameters regulating the relaxation rates of Gd^{3+} ions when water diffuses into inner, second, or/and outer spheres of coordination,[29,41,91-92] there is no direct experimental evidence that elucidates the proportion of contribution of inner, second, or/and outer sphere relaxation mechanisms towards the relaxivities of Ln^{3+}-based NPs. Articles simply assume one or the other for the interpretation of the results.

In this work, the permeation of water into the solvation spheres of PVP (polyvinylpyrrolidone) and DSPE-mPEG [1,2-distearoyl-*sn*-glycero-3-phosphoethanolamine-*N*-{methoxy(polyethylene glycol)}] coated $NaGdF_4:Eu^{3+}$ NPs (3 nm core diameter) and $NaYF_4$-$NaGdF_4:Eu^{3+}$ core-shell NPs (18.3 nm core diameter with a shell thickness of 0.5 nm) has been investigated by analyzing the excited state lifetime decay of trivalent europium Eu^{3+} ions doped in these NPs to understand the contribution of inner, second, and/or outer sphere relaxation mechanisms towards the relaxivities of NPs at 9.4 T. Eu^{3+} is well known for its strong luminescence in the red spectral region due to its characteristic emission transitions from the $^5D_0$ to the ^7F_J manifolds ($J = 0$–6).[48,54] Eu^{3+} doped in a low phonon energy (~360 cm^{-1}) bearing fluoride host has widely been studied for optical and optoelectronic applications.[93] Also, Eu^{3+} ions at the ground state are not expected to influence the paramagnetic properties of the NPs because the total electronic angular momentum of Eu^{3+}, J, is zero (Eu^{3+}, $4f^6$, $L = S = 3$).[94] The surface features of particles of nano-size dimensions play a vital role in influencing the luminescence properties of Eu^{3+} due to the particle's large surface to volume ratio.[50] Furthermore, the photoluminescence intensity of Eu^{3+} is sensitive to O–H vibrations in proximate water molecules, thus, yielding an excellent tool to probe water accessibility to Eu^{3+} ions on the surface of the NPs. As such, the excited state decay times of Eu^{3+} were investigated in two differently sized Gd^{3+}-based NPs serving as potential T_1-CAs (which brighten an MR image as opposed to T_2-CAs that darken the image): (1) $NaGdF_4$ NPs doped with Eu^{3+} (3 nm core diameter) and (2) $NaYF_4$-$NaGdF_4$ core-shell NPs (18.3 nm $NaYF_4$ core diameter) which have a 0.5 nm thick $NaGdF_4$ shell doped with Eu^{3+}. Both types of NPs were synthesized in an organic medium containing oleic acid and octadecene. These NPs dispersed in hexanes are then coated with PVP or DSPE-mPEG, which are water soluble molecules that impart excellent biocompatibility and hydrophilicity to the NPs.[76,95] The smaller NPs have a mean curvature of about 6 times larger than the bigger core-shell NPs which may provide easy accessibility of water molecules to coordinate to the surface cations of smaller NPs. In case of PVP-coated NPs, the oleate ligands on the surface of the NPs are completely replaced by the PVP molecules,[95] this may allow water access to the surface cationic sites of NPs. On the other hand, in DSPE-mPEG coated NPs, the oleate ligands remain on the NP surface as their alkyl chains interlock with the distearoyl phosphoethanolamine moieties of DSPE-mPEGs via hydrophobic interactions and the PEGs interact with the aqueous environment, likely allowing no direct access of water molecules to the surface of the NPs (although there are insignificant number of water molecules attached to the Ln^{3+}-based NPs during and post NPs' synthesis but their contribution is negligible compared to that of the bulk water molecules). The surface coatings of PVP and DSPE-mPEG were assessed with the extent of water accessibility by analyzing the lifetime decay curves of Eu^{3+}. MR relaxivity measurements were performed for PVP and DSPE-mPEG coated $NaGdF_4$ NPs at 9.4 T to correlate the underlying relaxation mechanism with the lifetime curves.

The excited state lifetime decay of Eu^{3+} ions which are present on the surface of NPs and are in proximity of water molecules prove to be an ideal probe to investigate the contribution of inner, second, and outer sphere relaxivities in NPs, thus, providing an appropriate approach to design NP-based MRI CAs.

2.2 Results and Discussion

2.2.1 Synthesis and characterization

Oleate-stabilized $NaGdF_4$, $NaGdF_4:Eu^{3+}$ and $NaYF_4$-$NaGdF_4:Eu^{3+}$ core-shell NPs were all synthesized in a binary solvent mixture of oleic acid and 1-octadecene following a high temperature route.[56,83] $NaGdF_4$ (including $NaGdF_4:Eu^{3+}$) NPs are known to grow fast.[83] As such, to obtain monodisperse NPs, controlling the nucleation stage in the reaction medium is vital to enable enough nuclei formation to achieve consistent growth of NPs. To obtain $NaYF_4$-$NaGdF_4:Eu^{3+}$ core-shell NPs, β-$NaYF_4$ NPs were grown first which served as seeds for the growth of the (Eu^{3+}-doped) $NaGdF_4$ shell. The shell precursor are small sacrificial α-$NaGdF_4$ NPs which were ~6 nm in diameter possessing the cubic phase as revealed from transmission electron microscopy (TEM) image and X-ray diffraction (XRD) analysis in Figure A1.1 in the Supplementary Information (Appendix 1), respectively. These α-$NaGdF_4$ NPs were injected into the reaction medium with core β-$NaYF_4$ NPs. The growth process proceeds via Ostwald ripening in which larger core particles with smaller surface to volume ratios are favored energetically and grow at the expense of the smaller particles.[56] The NP dispersed in hexanes were then transferred to deionized water by coating them with DSPE-mPEG[76] or exchanging the oleate ligands with PVP[95] on their surface which imparted colloidal stability, as illustrated in Figure 2.1.

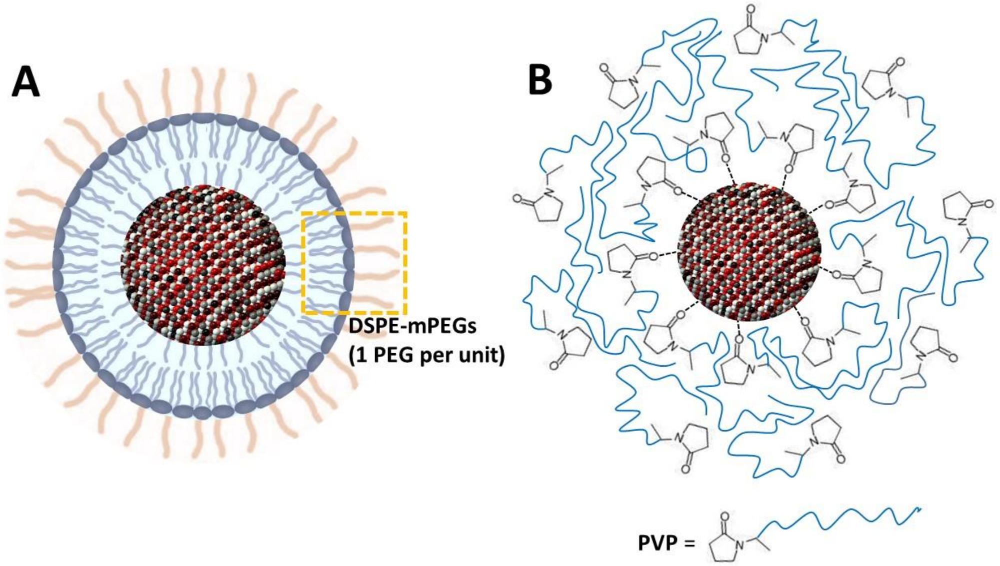

Figure 2.1. Schematic representation of NPs coated with (A) DSPE-mPEG and (B) PVP. A hydrophobic barrier is formed when the oleate chains on NPs interlock with the alkyl moieties of DSPE-mPEGs. In case of PVP-coated NPs, the C=O group of the pyrrolidone ring coordinates to metal cations on the surface of the NPs while the polyvinyl moieties organize in a densely compact structure due to hydrophobic interaction. The C=O groups of the PVP coating, which are not bonded to the metal cations, coordinate to water molecules via hydrogen bonding.

The as-synthesized NPs have hexagonal crystal phase, as confirmed by the XRD patterns of the NPs, which are well indexed with the standard patterns of their corresponding hexagonal phases, β-$NaGdF_4$ and β-$NaYF_4$ (see Figures 2.2 and A1.2A). The broad peaks in the XRD pattern of $NaGdF_4:Eu^{3+}$ NPs is indicative of the small size of the particles. The peaks for $NaYF_4$-$NaGdF_4:Eu^{3+}$ NPs are slightly shifted compared to the standard patterns due to the compressive strain induced by the $NaGdF_4$ shell on the core $NaYF_4$ NPs since ionic radius of Gd (0.938 Å)[96] is slightly larger than that of Y (0.900 Å).[61,96]

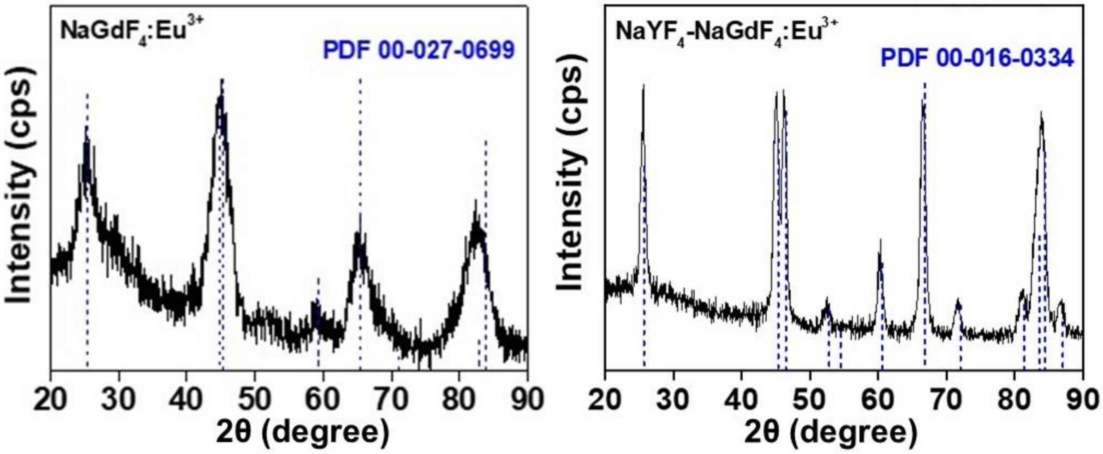

Figure 2.2. XRD patterns of $NaGdF_4:Eu^{3+}$ and $NaYF_4$-$NaGdF_4:Eu^{3+}$ core-shell NPs indexed with the corresponding standard patterns of the hexagonal phase of $NaGdF_4$ (PDF#00-027-0699) and $NaYF_4$ (PDF#00-016-0334).

Figures 2.3, 2.4A and A1.2B show TEM analyses of the three sets of NPs confirming a fairly uniform particle size distribution: β-$NaGdF_4:Eu^{3+}$, β-$NaYF_4$-$NaGdF_4:Eu^{3+}$ core-shell and β-$NaGdF_4$ NPs have diameters of 3.0 ± 0.8, 18.8 ± 1.8 and 3.2 ± 0.7 nm, respectively. These average sizes from the TEM images validate the sizes calculated from XRD peaks using the Scherrer equation (see Table A1.1). Furthermore, Figure A1.3 shows the TEM image of $NaYF_4$ core NPs before the injection of $NaGdF_4:Eu^{3+}$ NPs to form $NaYF_4$-$NaGdF_4:Eu^{3+}$ core-shell NPs. The difference in the diameters of the $NaYF_4$ core NPs (Figure A1.3) and $NaYF_4$-$NaGdF_4:Eu^{3+}$ core-shell NPs (Figure 2.4A) indicates the thickness of the $NaGdF_4:Eu^{3+}$ shell which is about 0.5 nm.

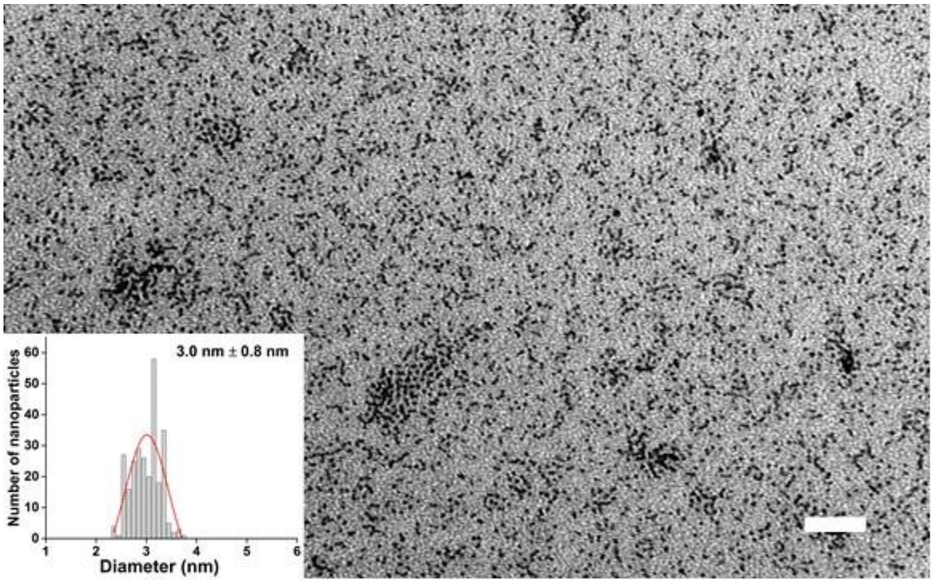

Figure 2.3. NaGdF$_4$:Eu^{3+} NPs: TEM image (white scale bar: 50 nm) and the corresponding histogram of particle size distribution.

Electron energy loss spectroscopy (EELS) line scans were acquired across a single β-NaYF$_4$-NaGdF$_4$:Eu^{3+} core-shell NP to provide evidence on the composition of core and shell. Figures A1.4 (A, B, C) show the high resolution scanning transmission electron microscopy (STEM) image of a single core-shell NP with the corresponding EELS spectrum of the Gd N$_{4,5}$ edge[97] at 140 eV. The signal intensity of Gd changes with position across the particle. The EELS signal intensity of Y in Figure A1.4B clearly indicates that Y is in the core of the NP while the Gd signal intensity confirms the presence of Gd in the shell. The signal intensity of Eu^{3+} was too low to be resolved. To complement with the EELS data on the structural analyses of the core-shell NP, elemental maps of Y, Gd and Eu acquired from energy dispersive X-ray (EDX) analyses were merged which confirm that Y is located at the core of the particle with Gd in the shell. It further substantiates the presence of Eu^{3+} ions in the shell (see Figures 2.4 B, C). Inductively coupled plasma mass spectrometry (ICP-MS) was done to obtain the lanthanide ion concentration after digesting the $NaYF_4$-$NaGdF_4$:Eu^{3+} core-shell NPs in concentrated nitric acid. The ionic concentration of Eu^{3+} was found to be 5 atomic % of the total lanthanide (Eu^{3+} and Gd^{3+}) composition in the shell of the NP.

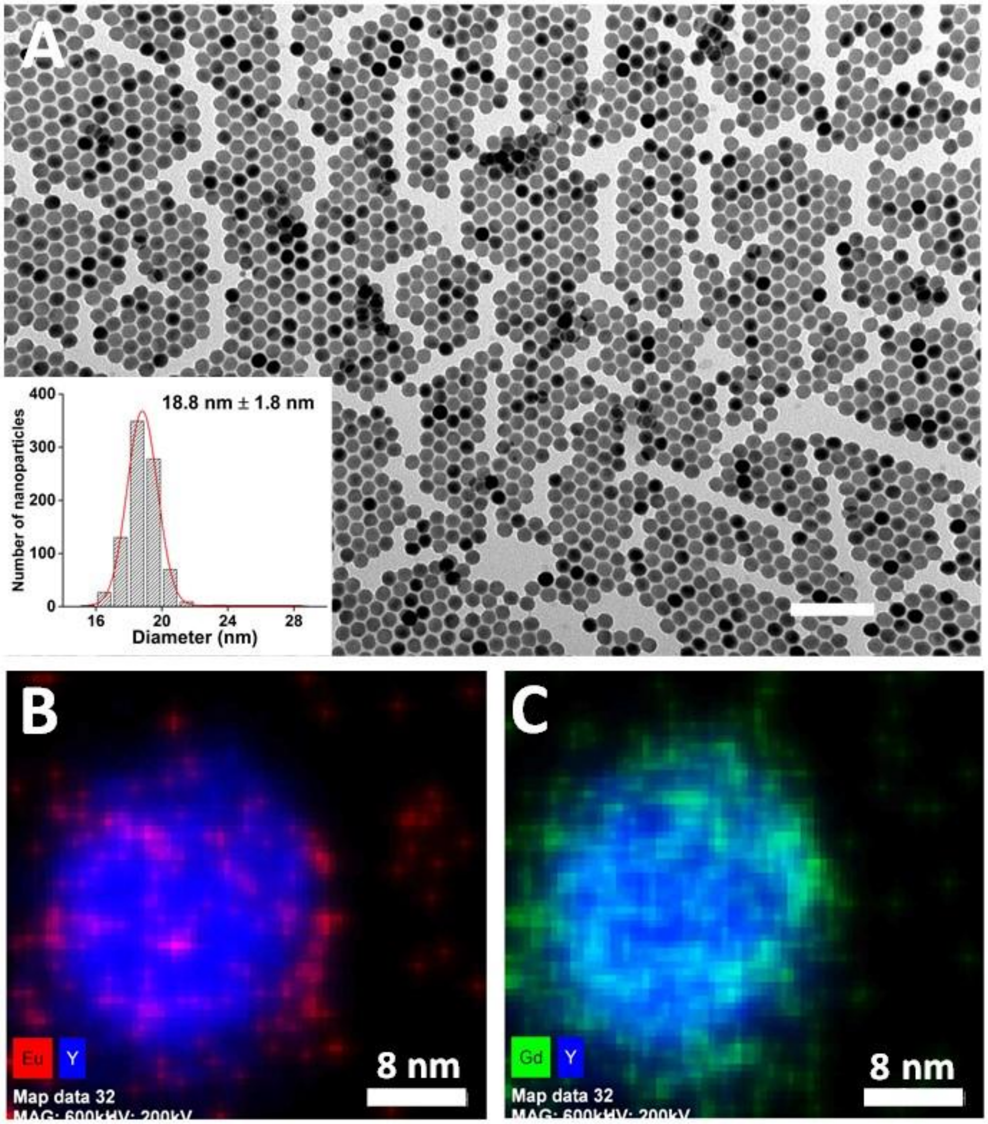

Figure 2.4. $NaYF_4$-$NaGdF_4$:Eu^{3+} core-shell NPs: (A) TEM image (white scale bar: 100 nm) and the corresponding histogram of particle size distribution. Single particle elemental maps from EDX analyses on STEHM in which (B) Y (blue) and Eu (red) maps are merged and (C) Y (blue) and Gd (green) maps are merged.

2.2.2 MR relaxivity results

$NaGdF_4$ NPs are characterized by their longitudinal and transverse relaxivity (r_1 and r_2, respectively), which is the change in relaxation rate ($1/T_1$ and $1/T_2$, respectively) of solvent water protons in presence of the NP, normalized to the concentration of Gd^{3+} ions, [Gd^{3+}], or NPs, as shown in the equation: $\boldsymbol{\frac{1}{T_i} = \frac{1}{T_i^0} + r_i[Gd^{3+}]; i = 1, 2}$. To determine Gd^{3+} ionic r_1 and r_2 relaxivities, the Gd^{3+} ion concentration in the dispersions of $NaGdF_4$ NPs coated with PVP and DSPE-mPEG was determined to be 1.15 mM and 1.12 mM in the colloidal dispersion, respectively, using ICP-MS. Gd^{3+} ionic relaxivities (r_1 and r_2) of $NaGdF_4$ and $NaYF_4$-$NaGdF_4$:Eu^{3+} core-shell NPs were obtained from the slope of the linear regression fit in the relaxivity plots obtained at 9.4 T shown in Figure 2.5 and A1.5, and the values are tabulated in Table 2.1. The y-intercept gives the value of $1/T_0$, i.e., the relaxation rate in absence of the NPs. PVP and DSPE-mPEG coated $NaGdF_4$ NPs have r_1 values of 1.77 ± 0.29 mM^{-1} s^{-1} and 1.84 ± 0.01 mM^{-1} s^{-1}, respectively, at 9.4 T. The corresponding r_1 relaxivity values calculated *per* NP[83] are 443 and 420 mM_{NP}^{-1} s^{-1}, respectively. Similarly, PVP and DSPE-mPEG coated $NaYF_4$-$NaGdF_4$:Eu^{3+} core-shell NPs show almost identical Gd^{3+} ionic r_1 relaxivities: 7.27 ± 0.72 mM^{-1} s^{-1} and 6.46 ± 0.35 mM^{-1} s^{-1}, respectively. The corresponding values *per* NP concentration are 15,800 and 17,500 mM_{NP}^{-1} s^{-1}. Furthermore, PVP and DSPE-mPEG coated $NaGdF_4$ NPs have r_2 values of 14.44 ± 0.59 mM^{-1} s^{-1} and 27.42 ± 0.73 mM^{-1} s^{-1}, respectively. The corresponding r_2 values for $NaYF_4$-$NaGdF_4$:Eu^{3+} core-shell NPs are 52.34 ± 2.53 mM^{-1} s^{-1} and 60.75 ± 2.38 mM^{-1} s^{-1}. It is acknowledged that the relaxivity values for the Eu^{3+}-doped core-shell NPs will be slightly lower than the undoped analogues because the number of Gd^{3+} ions *per* NP on an average is less when the same NP is doped with Eu^{3+}. However, they may serve nicely as bimodal CAs (i.e. for MRI and optical applications).

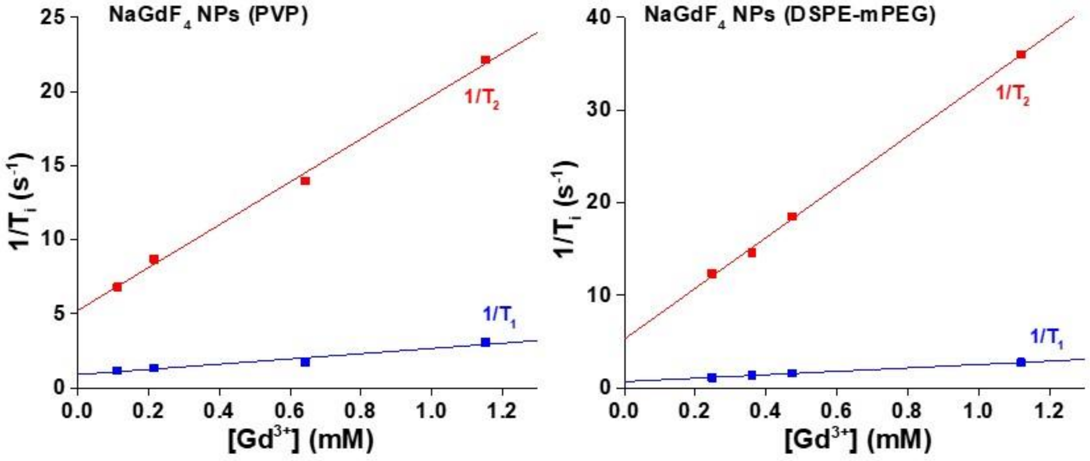

Figure 2.5. Longitudinal (r_1) and transverse (r_2) relaxivities obtained for PVP and DSPE-mPEG coated NaGdF$_4$ NPs at 9.4 T. Blue colored linear fits = $1/T_1$ and red colored linear fits = $1/T_2$. R-square (Coefficient of Determination) defining the goodness of a fit lie in the range of 0.94757–0.99987.

Table 2.1. r_1 and r_2 relaxivities for β-NaGdF$_4$ and NaYF$_4$-NaGdF$_4$:Eu^{3+} core-shell NPs with different surface coatings at 9.4 T.

NP type	**NP surface coating**	**Ionic relaxivity r_1/[Gd^{3+}] (mM^{-1} s^{-1})**	**Ionic relaxivity r_2/[Gd^{3+}] (mM^{-1} s^{-1})**	**Ionic relaxivity ratio r_2/r_1**	**NP relaxivity r_1/NP (mM$_{NP}^{-1}$ s^{-1})**	**NP relaxivity r_2/NP (mM$_{NP}^{-1}$ s^{-1})**
NaGdF$_4$	PVP	1.77 ± 0.29	14.44 ± 0.59	8.15	443	3,443
	DSPE-mPEG	1.84 ± 0.01	27.42 ± 0.73	14.90	420	6,263
NaYF$_4$-NaGdF$_4$:Eu^{3+}	PVP	7.27 ± 0.72	52.34 ± 2.53	7.20	15,800	115,200
	DSPE-mPEG	6.46 ± 0.35	60.75 ± 2.38	9.40	17,500	114,200

Dynamic light scattering (DLS) results, as shown in Figure A1.6 and summarized in Table A1.1, indicate similar hydrodynamic radii for PVP and DSPE-mPEG coated NaGdF$_4$ NPs: 8.9 nm ± 1.9 nm and 8.8 nm ± 1.8 nm, respectively. The hydrodynamic radii for larger sized NaYF$_4$-NaGdF$_4$:Eu^{3+} core-shell NPs coated with PVP and DSPE-mPEG are also close in values: 33.9 ± 1.2 nm and 34.3 nm ± 1.6 nm, respectively. Such close values of thicknesses of the surface coatings of NPs can be related to the similar r_1 (or r_2) relaxivities but these results do not explain the difference between T_1 and T_2 relaxation mechanisms and the role of inner, second, and/or outer spheres of coordination of water molecules, if any, to approach the Gd^{3+} ions on the surface of NPs. In addition, they do not explicitly say much about the characteristics of the surface coatings in terms of assisting with water accessibility to the surface Gd^{3+} ions on NPs. To understand these relaxation phenomena of Gd^{3+}-based NPs, $NaGdF_4$:Eu^{3+} and $NaYF_4$-$NaGdF_4$:Eu^{3+} core-shell NPs were subjected to steady-state and time-resolved measurements to assess the photoluminescence properties of Eu^{3+} ions which are sensitive to proximate water molecules. The photoluminescence lifetime decay of Eu^{3+} ions in NPs enabled to comprehend the relaxation mechanisms of Gd^{3+} ions in NPs since either of the events are susceptible to the proximity of water molecules to Eu^{3+} and Gd^{3+} ions, respectively.

2.2.3 Steady-state photoluminescence measurements

In Figure 2.6, $NaGdF_4$:Eu^{3+} and $NaYF_4$-$NaGdF_4$:Eu^{3+} core-shell NPs dispersed in hexanes show emission patterns characteristic of transitions of Eu^{3+} as reported in the past: $^5D_1$ – $^7F_0$ at 525 nm, $^5D_1$ – $^7F_1$ at 535 nm, $^5D_1$ – $^7F_2$ at 554 nm, $^5D_0$ – $^7F_0$ at 578 nm, $^5D_1$ – $^7F_3$ at 582 nm, $^5D_0$ – $^7F_1$ at 591 nm, $^5D_0$ – $^7F_2$ at 615 nm and $^5D_0$ – $^7F_4$ at 680–700 nm.[48,93,98] The excitation wavelength was chosen to be 394 nm because it corresponds to the most intense direct excitation of Eu^{3+} ions. The nature and symmetry of the Eu^{3+} ions are determined by analyzing the shape of non-degenerate $^5D_0$ – $^7F_0$ transition at 578 nm and the relative ratio of integrated areas under the peaks of the $^5D_0$ – $^7F_2$ (615 nm) to $^5D_0$ – $^7F_1$

(591 nm) transitions, known as the asymmetry ratio. The $^5D_0$ and $^7F_0$ states are non-degenerate implying that only a single Gaussian peak should appear for the $^5D_0$ – $^7F_0$ transition at 578 nm if all the Eu^{3+} ions are in the same crystal site. Deconvolution of the peak centered at 578 nm, obtained with the minimum measurable step size of 0.05 nm, is shown in Figure A1.7 which reveals three Gaussian peaks indicating the presence of Eu^{3+} ions in more than one symmetry site in the NPs such as the $1a$ and $1f$ sites with C_{3h} symmetry,[99] or the sites of lower symmetry, C_s, C_3, and/or C_1.[100] Furthermore, the asymmetry ratio was found out to be 1.83 for $NaGdF_4:Eu^{3+}$ NPs and 1.52 for $NaYF_4$-$NaGdF_4:Eu^{3+}$ core-shell NPs. Reduction of the centrosymmetric character of the crystal field around Eu^{3+} ions in $NaGdF_4$ NPs causes an enhancement in the relative intensity of the hypersensitive electric dipole transition $^5D_0$ – $^7F_2$ and, thus, a higher asymmetry ratio. Lowering of symmetry in crystal field around Eu^{3+} ions in $NaYF_4$-$NaGdF_4:Eu^{3+}$ core-shell NPs can be attributed to the Eu^{3+} ions bound to terminating oleate ligands which lead to increase in disorder in the crystal. For an NP of about 19 nm diameter, the number of oleate ligands on its surface is greater than that on an NP of 3 nm diameter, even though the surface density is different. In the former particle, a considerable number of Eu^{3+} ions on surface are exposed to the interaction with carboxylates of oleate ligands. The electric field from Eu^{3+} and Gd^{3+} ions, present on the NP surface and coordinated with oleates, causes polarization of the charge distribution in surface attached oleate ligands.[95] Hence, there may appear a perturbation of the electronic states of the lanthanide ion by the electric field of the oleate ligands. The electric dipole moment of *cis*-oleic acid is 0.7 D (1 $D = 3.328 \times 10^{-30}$ C m),[101] which can cause strong distortion in the local electric field on the NPs surface and affect the asymmetry ratio.

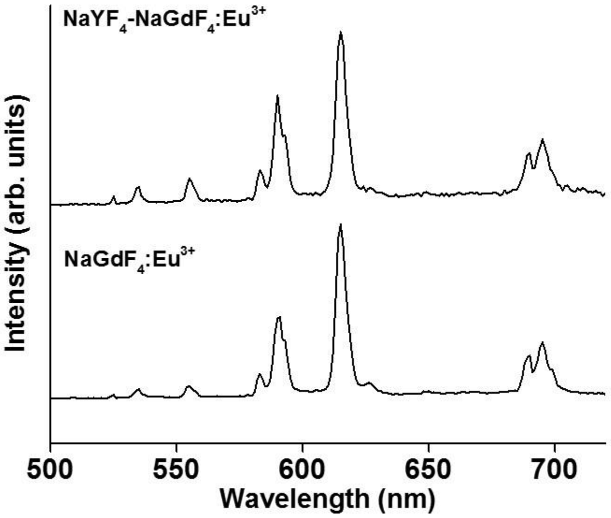

Figure 2.6. Emission spectra of $NaGdF_4:Eu^{3+}$ NPs and $NaYF_4$-$NaGdF_4:Eu^{3+}$ core-shell NPs dispersed in hexanes. The NPs were excited at 394 nm.

2.2.4 Time-resolved photoluminescence measurements

In the present study, the deconvolution of the $^5D_0 - {}^7F_0$ transition peak suggests the presence of Eu^{3+} ions in more than one crystal site in the $NaGdF_4:Eu^{3+}$ NP lattice. They are in the bulk of the particles away from the surface and on the surface of the particles. As depicted in the crystallographic representation of β-$NaGdF_4$ NP in Figure A1.8, Eu^{3+} ions (ionic radius = 0.947 Å)[96] can substitute for Gd^{3+} (ionic radius = 0.938 Å)[96] since Eu^{3+} has a slightly larger ionic radius and its occupation at 1*a* and 1*f* sites/Gd^{3+} is favorable energetically.[99] On the other hand, to occupy the position of larger Na^+ (ionic radius = 1.020 Å)[96] at the expense of more binding energy and charge compensation, e.g., cation vacancy, and/or interstitial defects, it is almost impossible for Eu^{3+} to substitute for Na^+. Thus, Eu^{3+} ions in the "bulk" of the NPs are surrounded by nine F^- ions while those on the surface by a lower number of F^- ions and O (from oleates) or O (from water) depending upon the coordinating ligand. Assuming spherical particles, the model describing the lifetime distribution of a $NaGdF_4:Eu^{3+}$ NP can be divided into shells of equal volume,[102] with Eu^{3+} ions present in the inner shell having a longer lifetime than the outer shell since the core Eu^{3+} ions are devoid of surface quenching effects, especially, in presence of aqueous medium. Similarly, a $NaYF_4$-$NaGdF_4:Eu^{3+}$ core-shell NP can be divided into shells in which the Eu^{3+} ions present on the surface have a shorter lifetime than those penetrating the undoped $NaYF_4$ core. The decay curves for $NaYF_4$-$NaGdF_4:Eu^{3+}$ core-shell NPs in hexanes and deuterated water are best fitted using the single exponential equation: $I_t = I_0 e^{-t/\tau_1} + B$. The decay curves of the $NaGdF_4:Eu^{3+}$ NPs dispersed in hexanes and deuterated water were fitted using the bi-exponential equation, $I_t = A_1 e^{-t/\tau_1} + A_2 e^{-t/\tau_2} + B$, while for the both types of NPs dispersed in deionized water or in a mixture of deionized and deuterated water, the tri-exponential equation, $I_t = A_1 e^{-t/\tau_1} + A_2 e^{-t/\tau_2} + A_3 e^{-t/\tau_3} + B$, was used. The effective lifetime in case of a biexponential decay is calculated using the equation, $\tau_{eff} = \frac{A_1\tau_1^2 + A_2\tau_2^2}{A_1\tau_1 + A_2\tau_2}$ and for a triexponential decay, $\tau_{eff} = \frac{A_1\tau_1^2 + A_2\tau_2^2 + A_3\tau_3^2}{A_1\tau_1 + A_2\tau_2 + A_3\tau_3}$.[103]

2.2.4.1 Lifetime decay of Eu^{3+}-doped in $NaGdF_4$ NPs (~3 nm diameter; TEM)

To address the decay curve of the excited state of Eu^{3+} ions in $NaGdF_4:Eu^{3+}$ NPs, these NPs when dispersed in hexanes yield lifetime values of 5.92 ms (τ_1) and 3.48 ms (τ_2) as shown in Figure A1.9. Following their surface modification with PVP and DSPE-mPEG and then transfer to deionized water, the NPs display three lifetime components: 3.15 ms (τ_1), 0.70 ms (τ_2) and 0.16 ms (τ_3) for the PVP-coated NPs and 4.03 ms (τ_1), 1.12 ms (τ_2)

and 0.27 ms (τ_3) for the DSPE-mPEG-coated NPs, after tri-exponential fitting of the decay curves as shown in Figures 2.7–2.8. Details of all the lifetimes and their corresponding contributions towards total lifetime are collated in Table 2.2.

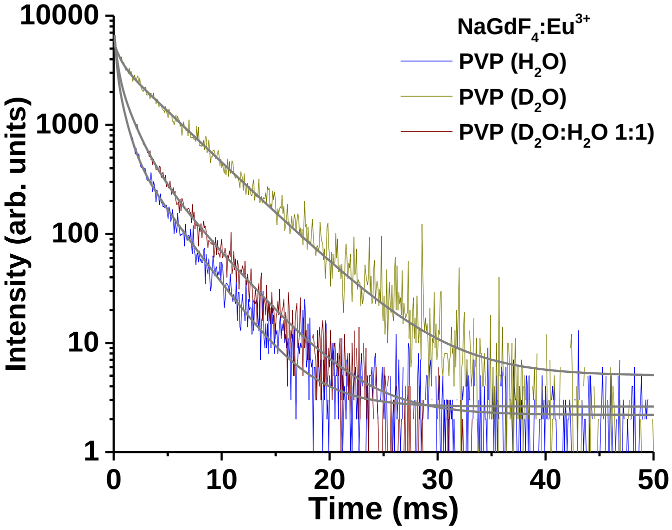

Figure 2.7. Decay curves monitored at 615 nm and fitted with corresponding exponential equations for $NaGdF_4:Eu^{3+}$ NPs coated with PVP and dispersed in D_2O and/or H_2O. The NPs were excited at 394 nm. R-squared (COD) for the curves is in the range of 0.99539–0.99937.

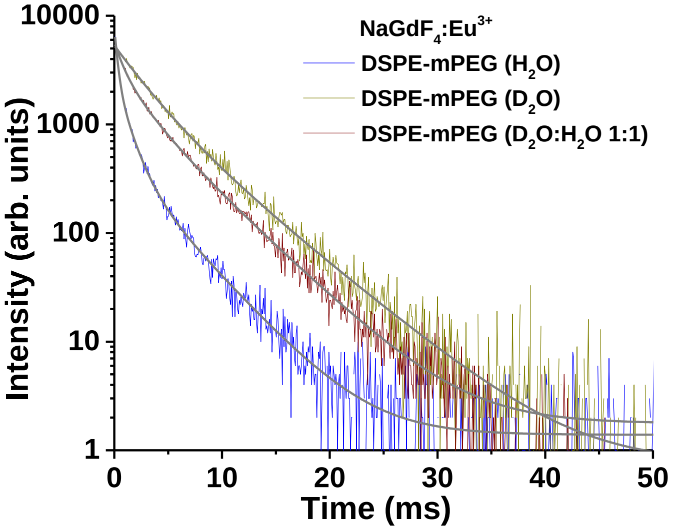

Figure 2.8. Decay curves monitored at 615 nm and fitted with corresponding exponential equations for $NaGdF_4:Eu^{3+}$ NPs coated with DSPE-mPEG and dispersed in D_2O and/or H_2O. The NPs were excited at 394 nm. R-squared (COD) for the curves is in the range of 0.99753–0.99904.

Table 2.2. Lifetime values (τ_1 and τ_2) obtained from the exponential decay curves monitored at 615 nm.

Sample	**Surface coating**	**Solvent**	τ_1 **(ms)**	τ_1 **%**	τ_2 **(ms)**	τ_2 **%**	τ_3 **(ms)**	τ_3 **%**	τ_{eff} **(ms)**	***q***
$NaGdF_4:Eu^{3+}$ NPs	Oleic acid	Hexanes	5.92	60	3.48	40	-	-	5.23	
	PVP	D_2O	4.62	68	0.57	32	-	-	4.40	
	PVP	Deionized water	3.15	09	0.70	33	0.16	58	1.74	4.65
	PVP	D_2O : Deionized water 1:1	3.88	12	1.24	34	0.20	54	2.36	3.26
		D_2O : Deionized water 1:1 (6 months after)	4.51	29	1.33	29	0.23	42	3.59	2.53
	DSPE-mPEG	D_2O	5.42	38	2.60	62	-	-	4.19	
	DSPE-mPEG	Deionized water	4.03	06	1.12	66	0.27	28	1.86	3.50
	DSPE-mPEG	D_2O : Deionized water 1:1	4.66	32	2.04	31	0.74	37	3.53	0.89
		D_2O : Deionized water 1:1 (6 months after)	4.45	15	1.47	45	0.57	40	2.61	1.34
$NaYF_4$-$NaGdF_4:Eu^{3+}$ core-shell NPs	Oleic acid	Hexanes	5.92	100	-	-	-	-		
	PVP	D_2O	6.14	100	-	-	-	-		
	PVP	Deionized water	5.08	16	0.98	44	0.24	40	3.44	4.10
	PVP	D_2O : Deionized water 1:1	5.18	27	1.36	43	0.28	30	3.93	3.44
		D_2O : Deionized water 1:1 (6 months after)	5.01	19	1.25	35	0.20	46	3.57	5.02
	DSPE-mPEG	D_2O	6.57	100	-	-	-	-		
	DSPE-mPEG	Deionized water	5.02	23	1.14	37	0.27	40	3.76	3.60
	DSPE-mPEG	D_2O : Deionized water 1:1	5.54	40	1.52	46	0.28	14	4.51	3.45
		D_2O : Deionized water 1:1 (6 months after)	5.46	44	1.49	44	0.23	12	4.58	4.31

$Eu(NO_3)_3\cdot 5H_2O$		D_2O	2.94	100	-	-	-	-		
		Deionized water	0.11	100	-	-	-	-		9.37
		D_2O : Deionized water 1:1	0.24	100	-	-	-	-		3.90

τ_1 %, τ_2 % and τ_3 % denote the amount of component lifetimes, τ_1, τ_2 and τ_3, respectively, contributing to the total lifetime. q is the (effective) hydration number. The values of τ_1, τ_2 and τ_3 obtained from the exponential fits had statistical uncertainties in the range of 0.001–0.010 ms. The experimental uncertainties were in the range of 0.010–0.100 ms as determined from the Edinburgh Instruments' software.

From the tri-exponential fitting of a curve, τ_1 and τ_2 are longer lifetime components which can be attributed to the Eu^{3+} ions in the core and away from the surface of the $NaGdF_4:Eu^{3+}$ NPs, respectively, that are protected from the direct effect of vibrational quenchers. The lifetime τ_3 is the shortest lifetime component which is assigned to the Eu^{3+} ions in proximity to or coordinated directly to water molecules that lead to quenching effects. The lifetime values, τ_1 and τ_2, are only slightly lower compared to the corresponding values in hexanes, which may be due to a combination of a different effective refractive index and some "indirect" quenching through energy migration to the (ground state) surface Eu^{3+} ions. Quenching clearly dominates on or near the surface of the NP. In the decay model, the outer shell (not to be confused with the outer sphere of relaxation) is in the vicinity of water molecules exhibiting lower lifetime values. The energy gap between the luminescent state and ground state manifold is approximately 12,000 cm^{-1} for Eu^{3+}. The energy gap between the emissive state and the highest lying sublevel of the ground state of Eu^{3+} are effectively spanned by the vibrational modes of O–H oscillators coordinated to Eu^{3+}. The coupling of the Eu^{3+} excited states to the high-frequency vibrational overtones of the O–H bond ($\tilde{\nu}_{O\text{–}H}$ = 3,600 cm^{-1}) provides an efficient mechanism for energy transfer, resulting in radiationless de-excitation of the Eu^{3+} ion excited state. The quenching efficiency is sharply decreased, as expected, in presence of the O–D bond as inferred from the lifetime values of PVP-coated [4.62 ms (τ_1) and 0.57 ms (τ_2)] and DSPE-mPEG coated [5.42 ms (τ_1) and 2.60 ms (τ_2)] $NaGdF_4:Eu^{3+}$ NPs dispersed in D_2O (Table 2.2, Figure 2.7–2.8). Coupling to a higher energy overtone, as required for the O–D oscillator ($\tilde{\nu}_{O–D}$ = 2,200 cm^{-1}), results in much less efficient quenching of the Eu^{3+} excited state and, thus, longer-lived Eu^{3+} luminescence. This phenomenon is aptly exhibited by free Eu^{3+} ions [from $Eu(NO_3)_3{\cdot}5H_2O$] when dispersed in D_2O, deionized water or a combination of two (Figure A1.10). The vibrational quenching of Eu^{3+} lifetime in deionized water can be used to determine the number of water molecules q interacting with Eu^{3+} ion in the inner-coordination sphere using Horrock's equation established for Eu^{3+}-complexes:[52,104-105]

$$q_{Eu}(H_2O) = 1.11 \times (\Delta k_{obs} - 0.31),\ \text{where}\ \ \Delta k_{obs} = k_{H_2O} - k_{D_2O} = 1/\tau_{H_2O} - 1/\tau_{D_2O}$$

(difference in reciprocals of lifetimes in H_2O and D_2O); Δk_{obs} is in ms^{-1}

When $Eu(NO_3)_3{\cdot}5H_2O$ is dispersed in deuterated water, deionized water or a mixture of the two (1:1 ratio), the free Eu^{3+} ion, which is a nine-coordinate species, is bound to 0, 9.37 (~ 9) or 3.90 (~ 4) water molecules, respectively (q values in Table 2.2). If the Horrock's equation is qualitatively applied to Eu^{3+} ions present on the surface of $NaGdF_4:Eu^{3+}$ NPs which are in proximity to water molecules, the smallest lifetime component τ_3 is taken into consideration for τ_{H2O}, while τ_2 of NPs dispersed in D_2O is considered for τ_{D2O} because of the latter's bi-exponential decay profile. For PVP and DSPE-mPEG coated $NaGdF_4:Eu^{3+}$ NPs dispersed in deionized water, effective q values are 4.65 and 3.50, respectively, with τ_3 values of 0.16 ms and 0.27 ms, as summarized in Table 2.2. When PVP and DSPE-mPEG coated $NaGdF_4:Eu^{3+}$ NPs are dispersed in a 1:1 v/v mixture of deuterated and deionized water, the corresponding values of q decrease to 3.26 and 0.89 because τ_3 values increase to 0.20 ms and 0.74 ms. Such differences in q and, specifically, τ_3 values, validate varying number of coordinated water molecules to surface Eu^{3+} ions of NPs dispersed in different media substantiating the exchange of the coordinated water molecules on the surface of NPs with the bulk water. This is illustrated by the three lifetime components which have higher values [3.88 ms (τ_1), 1.24 ms (τ_2) and 0.20 ms (τ_3) for PVP-coated and 4.66 ms (τ_1), 2.04 ms (τ_2) and 0.74 ms (τ_3) for DSPE-mPEG coated $NaGdF_4:Eu^{3+}$ NPs] in the 1:1 v/v mixture of deuterated and deionized water when compared to the values in deionized in water (Table 2.2). These lifetime measurements were repeated after six months using the same batch of NPs in the 1:1 v/v mixture of deuterated and deionized water yielding similar values as shown in Table 2.2 and Figure A1.11: 4.51 ms (τ_1), 1.33 ms (τ_2) and 0.23 ms (τ_3) for PVP-coated and 4.45 ms (τ_1), 1.47 ms (τ_2) and 0.57 ms (τ_3) for DSPE-mPEG coated $NaGdF_4:Eu^{3+}$ NPs. The τ_3 values are higher for the NPs dispersed in a 1:1 v/v mixture of deuterated and deionized water than that of the NPs dispersed in deionized water only, evincing water exchange at surface Eu^{3+} sites. The water exchange is also evident from the increase in τ_{eff} in the 1:1 v/v mixture of deuterated and deionized water compared to that in deionized water only. Such exchange of water in the inner coordination sphere of Eu^{3+}, despite having a hydrophobic barrier of PVP and DSPE-mPEG, can be ascribed to a “leaky” surface coatings owing to the very high curvature of the 3 nm core sized $NaGdF_4:Eu^{3+}$ NPs that creates loopholes for water accessibility.

2.2.4.2 Lifetime decay of Eu^{3+} in $NaYF_4$-$NaGdF_4:Eu^{3+}$ core-shell NPs (~19 nm diameter; TEM)

The single exponential decay curve of Eu^{3+} in $NaYF_4$-$NaGdF_4:Eu^{3+}$ core-shell NPs dispersed in hexanes is shown in Figure A1.9 which yields a lifetime value of 5.92 ms (τ_1) owing to minimal quenching effects. When dispersed in deionized water after coating them with PVP and DSPE-mPEG, the NPs display quenched lifetimes, 5.08 ms (τ_1), 0.98 ms (τ_2) and 0.24 ms (τ_3) for the former and 5.02 ms (τ_1), 1.14 ms (τ_2) and 0.27 ms (τ_3) for the latter, after tri-exponential fitting of the decay curves as shown in Figures A1.12–A1.13. These vibrational quenching phenomena in deionized water are similar to those observed in case of $NaGdF_4:Eu^{3+}$ NPs. When $NaYF_4$-$NaGdF_4:Eu^{3+}$ core-shell NPs are dispersed in 1:1 v/v mixture of deuterated and deionized water, the smallest lifetime component, τ_3 (0.28 ms for both PVP-coated and DSPE-mPEG coated NPs), arising due to the surface Eu^{3+} ions in proximity to water molecules, does not vary from its corresponding value (0.24 ms and 0.27 ms) in deionized water. This is contrary to the observations in case of $NaGdF_4:Eu^{3+}$ NPs. Such similar lifetime values in deionized water and in a 1:1 v/v mixture of deionized and deuterated water suggests hardly any exchange of water molecules coordinated to the surface Eu^{3+} ions with the bulk. The lower values of τ_3 of $NaYF_4$-$NaGdF_4:Eu^{3+}$ core-shell NPs dispersed in deionized water is suggestive of Eu^{3+}-bound water molecules formed in the course of NP synthesis which are completely isolated from the surrounding water molecules. The longer lifetime components [5.18 ms (τ_1), 1.36 ms (τ_2) for PVP-coated and 5.54 ms (τ_1), 1.52 ms (τ_2) for DSPE-mPEG coated NPs] do increase slightly from the corresponding values in deionized water (Table 2.2) due to decreased vibrational quenching in presence of D_2O. The value of q stays consistent for $NaYF_4$-$NaGdF_4:Eu^{3+}$

core-shell NPs in deionized water and in a 1:1 v/v mixture of deionized and deuterated water: 4.09 and 3.44 for PVP-coated, and 3.60 and 3.45 for DSPE-mPEG coated NPs, respectively. These lifetime and q values are suggestive of water molecules bound to surface Eu^{3+} ions of the 19 nm core sized $NaYF_4$-$NaGdF_4$:Eu^{3+} core-shell NPs but no, or very slow, exchange with the bulk in the outer sphere coordination environment. Moreover, the values of τ_{eff} in deionized water and 1:1 v/v mixture of deuterated and deionized water are too close in values (Table 2.2) indicating almost no water exchange. The lifetime measurements in the 1:1 v/v mixture of deuterated and deionized water were repeated after six months using the same NPs' dispersion yielding close values as shown in Table 2.2 and Figure A1.14: 5.01 ms (τ_1), 1.25 ms (τ_2) and 0.20 ms (τ_3) for PVP-coated and 5.46 ms (τ_1), 1.49 ms (τ_2) and 0.23 ms (τ_3) for DSPE-mPEG coated $NaYF_4$-$NaGdF_4$:Eu^{3+} core-shell NPs. Such exchange restraints can be attributed to the dense hydrophobic barrier of PVP and DSPE-mPEG on the surface of the bigger NPs which possess a lower curvature compared to the 3 nm core NP.

In DSPE-mPEG coated $NaYF_4$-$NaGdF_4$:Eu^{3+} core-shell NPs, the methoxy-terminated PEG chains act as the extended hydrophilic head groups for electrostatic interactions and hydrogen bonding with water. In case of PVP-coated $NaYF_4$-$NaGdF_4$:Eu^{3+} core-shell NPs, there is an extensive hydrogen bonding among free water molecules and the C–N and C=O group in the pyrrolidone moieties. As depicted in Figure 2,1, the distearoyl phosphoethanolamine moieties of DSPE-mPEGs interlock with the hydrophobic alkyl chains of oleates on the surface of NPs via hydrophobic interactions. When coated with PVP, oleate ligands on the NPs are completely exchanged by the PVP molecules.[83] As per DLS results, the hydrodynamic diameter of the DSPE-mPEG and PVP-coated

$NaYF_4$-$NaGdF_4$:Eu^{3+} core-shell NPs is similar (33.9 and 34.3 nm; Table A1.1 in Supplementary Information) indicating no marked difference in the thickness of the hydrophobic layer of the coatings of the NPs. The length of PEG2000 chain with a DSPE head, the PEG chain length can be about 2 nm[106] when in mushroom or brush confirmation or it can extend to a maximum length of 15 nm.[107] These values support the DLS results from which a thickness of about 7.5 nm of DSPE-mPEG coating interlocked with oleates around the ~19 nm sized NPs is implied. Previous reports on assessment of water permeability across Mn^{2+} entrapped dipalmitoyl phosphatidylcholine vesicles, employing ^{17}O and ^{1}H NMR, revealed that below 37 ^{o}C, these phospholipids acquire a gel phase.[108] In the gel phase, phospholipids are more or less locked in place and have limited mobility, as a result the water diffusion into the hydrophobic region is highly restricted, owing to the very high activation energy (15 kcal/mol) for water permeation. Hence, at the physiological (37 ^{o}C) and room (25 ^{o}C) temperatures, there is hardly any exchange of water with the bulk in the outer coordination sphere. This is evident from the lifetime value, τ_3, of $NaYF_4$-$NaGdF_4$:Eu^{3+} core-shell NPs dispersed in a mixture of deuterated and deionized water in a volumetric ratio of 1:1 being similar to that in deionized water (Table 2.2). In D_2O, phospholipids become more compact than in H_2O as D_2O raises the temperature of gel to liquid phase transition resulting in a dry hydrophobic interior. Molecular dynamics simulations have shown that there is a huge difference in the self-diffusion coefficient of H_2O and D_2O molecules hydrating the membrane.[109] Diffusion of D_2O molecules is 43% slower than that of H_2O molecules which leads to hydration of the polar head groups of DSPE-mPEGs including the PEG corona in H_2O in the 1:1 mixture of H_2O and D_2O. Studies have also shown that there is a strong preference for H_2O to hydrate the phospholipids even in a mixture composed of 98:2 D_2O:H_2O; such solvent isotope effect is more pronounced in hydration of a phospholipid than in bulk solvent mixture.[110] In case of PVP-coated NPs dispersed in water, although the glass to liquid transition temperature of PVP (M_w = 10,000 Da) is decreased (below 130 ^{o}C),[111] which imparts slight molecular mobility, the polyvinyl moieties entangle with each other creating a hydrophobic barrier excluding the water molecules to enter into the inner coordination sphere of Eu^{3+} ions. Because PVP-10 chain can extend to a length of 16 nm,[112] DLS data indicate that the NPs are coated with extended alkyl chains of PVP. In D_2O, the PVP coating is apparently completely dehydrated and forms a dense packed structure. To infer from the interpretation of the lifetime decays, DSPE-mPEG and PVP coatings around bigger $NaYF_4$-$NaGdF_4$:Eu^{3+} core-shell NPs exclude water molecules from directly exchanging with the ones coordinated with the Eu^{3+} ions on the surface of NPs in the inner coordination sphere. On the contrary, the smaller $NaGdF_4$:Eu^{3+} NPs have adequate exchange of water molecules with the coordinated ones at Eu^{3+} sites on the surface of the NPs.

2.2.5 Contribution of inner, second, and outer spheres of relaxation of water protons towards NP relaxivities.

High-field regime relaxation ($B_0 \geq 3$ T). Relaxivities r_i (i = 1, 2) of an NP are the sum of the inner sphere (IS), second sphere (2S) and outer sphere (OS) contributions from the water proton dynamics with respect to the NP, $r_i = r_i^{IS} + r_i^{2S} + r_i^{OS}$. A schematic representation of these contributions from the water protons with respect to an NP is depicted in Figure 2.9. The relaxivity equations discussed below for IS, 2S and OS of relaxation are from the Grenoble method.[113-114] In the high-field domain ($B_0 \geq 3$ T), the relaxivities are independent of the electronic spin relaxation.[29,89]

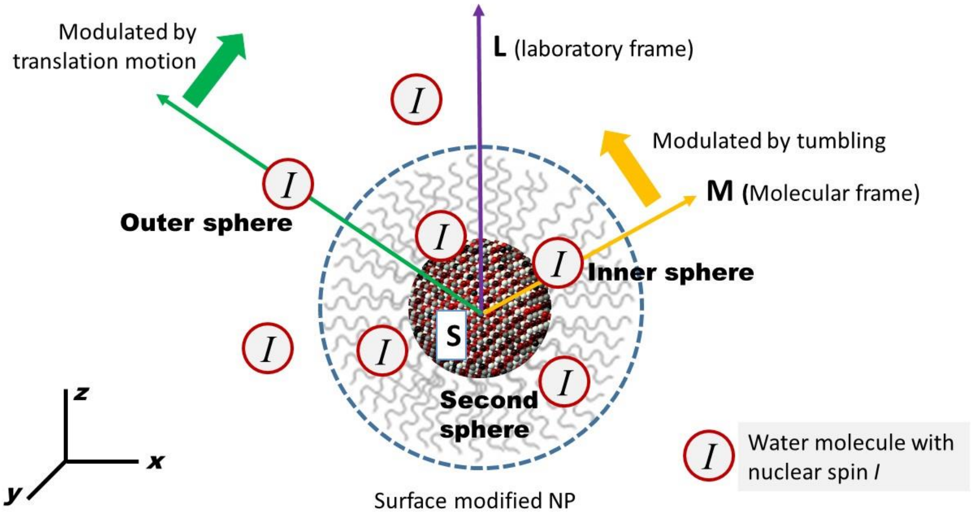

Figure 2.9. Schematic representation of contributions from inner, second, and outer spheres of relaxation of water protons towards relaxivities of an NP. Dipole-dipole interaction is between electron spin (S) of Gd^{3+} ion ensemble in NP and nuclear spin (I) of water molecule.

High-field inner and second sphere relaxation. The IS relaxivity is proportional to the number q of water molecules coordinated to the surface Gd^{3+} ions of NP and decreases rapidly with the mean distance r_H between NP (Gd^{3+}) and water proton distance as $1/r_H^6$. It is a function of the mean residence time of the coordinated water molecules τ_M and Brownian motion of the NP characterized by a tumbling time or a rotation correlation time of r_r. The IS relaxivity, $r_i^{IS} = Pq/(T_{iM} + \tau_M)$, where $i = 1, 2$; P is the ratio of the number of NPs to water molecules in a 1 mM solution, T_{iM} are the relaxation times of the protons of water molecules coordinated directly to the NP which are given by[113]

$$\frac{1}{T_{1M}} = A\frac{1}{4\pi r_H^6} + \frac{\tau_r}{1 + \omega_I^2 \tau_r^2}$$

$$\frac{1}{T_{2M}} = A\frac{\tau_r}{4\pi r_H^6}\left[\frac{2}{3} + \frac{1}{2}\frac{1}{1 + \omega_I^2\tau_r^2}\right]$$

where, $A = \left(\frac{\mu_0}{4\pi}\right)^2 (\frac{8\pi}{5})\gamma_I^2\mu_{eff}^2$ and $\mu_{eff} = g_S\mu_B[S(S+1)]^{1/2}$, g_S is the Landé factor of the electronic spin S, γ_I and γ_S $(= -g_S\mu_B/\hbar)$ are the gyromagnetic ratios of the interacting spins I and S through the dipolar coupling factor μ_0 is the permeability of vacuum, and ω_I and ω_S are the angular Larmor frequencies of the spins such that $\omega_I = 2\pi\nu_I = -\gamma_I B_0$ and $\omega_S = -\gamma_S B_0$.

The Eu^{3+} lifetime analyses of PVP and DSPE-mPEG coated $NaGdF_4:Eu^{3+}$ NPs manifested adequate exchange of water molecules with the coordinated ones at Eu^{3+} sites on the surface of these small NPs. This implies the direct access and coordination of water protons to the surface Gd^{3+} ions of the smaller NPs clearly showing the dominance of the inner sphere relaxation mechanism. Further, the contribution from the second sphere (2S) is obvious from the fact that a realistic model considers the 2S longitudinal and transverse relaxivities r_i^{2S} resulting from hydrogen bonding of the water molecules to the sites on the NP surface coating, for example, C=O and >N– sites in PVP and C=O, –NH– sites and PO_4 moiety in DSPE-mPEG, in which the water molecules are at different distances from the surface Gd^{3+} ions of the NP. The high field 2S relaxivity equations are simplified to follow the parameters similar to those in IS relaxivity equations because, ideally, there are many parameters involved in the 2S relaxivity description and their determination is beyond the scope of obtaining all experimental information from all possible available techniques. The 2S relaxivities, $r_i^{2S} = Pq'/(T'_{iM} + \tau'_{iM})$, where T'_{iM} are the relaxation times of the protons of 2S water molecules and the number of 2S water molecules is q', with effective residence time τ'_M and the effective distance between these water protons and NP is r'_H. The 2S relaxivities are given by[89]

$$\frac{1}{T'_{1M}} = A\frac{1}{4\pi {r'_H}^6} + \frac{\tau'_c}{1+\omega_I^2 {\tau'_c}^2}$$

$$\frac{1}{T'_{2M}} = A\frac{\tau'_c}{4\pi {r'_H}^6}\left[\frac{2}{3} + \frac{1}{2}\frac{1}{1+\omega_I^2 {\tau'_c}^2}\right]$$

where the 2S correlation time τ'_c is given by

$$\frac{1}{\tau'_c} = \frac{1}{\tau_r} + \frac{1}{\tau'_M}$$

High-field outer sphere relaxation. OS relaxivity theory is based on the OS dipolar time correlation function $g_2(t)$. Suppose **r** is the vector joining the nuclear spin I of a water molecule M_I to the electronic spin S of Gd^{3+} ions in the NP and (r, θ, ϕ) are spherical coordinates in the laboratory (L) frame, the z axis of which is parallel to $\mathbf{B}_0$. Let $Y_{2q}(\theta, \phi)$ ($-2 \leq q \leq 2$) be the spherical harmonics of order 2. The function $g_2(t)$ of the random functions $r^{-3}Y_{2q}(\theta, \phi)$ of the interspin vector **r**, independent of the index q, is defined as[29,115]

$$g_2(t) = N_S \iint \frac{Y_{2q}(\theta_0, \phi_0)}{r_0^3}\frac{Y_{2q}^*(\theta, \phi)}{r^3} g_{site\ I-site\ S}^{OS}(r_0)\rho(\mathbf{r}_0, \mathbf{r}, t)\mathrm{d}\mathbf{r}_0 d\mathbf{r}$$

where N_S is the number of electron spins S or Gd^{3+} ions per unit volume, $g_{site\ I-site\ S}^{OS}(r_0)$ is the radial distribution function of the interspin distance r_0 at equilibrium and $\rho(\mathbf{r}_0, \mathbf{r}, t)$ is the OS propagator describing the random evolution of the interspin vector **r** in the course of time. In other words, $\rho(\mathbf{r}_0, \mathbf{r}, t)$ is the conditional probability that the interspin position is $\mathbf{r} \equiv (r, \theta, \phi)$ at time t given that it was at $\mathbf{r}_0 \equiv (r_0, \theta_0, \phi_0)$ at initial time $t = 0$. It is governed by the anisotropic translational and rotational Brownian motions of water protons and NPs without binding to the water molecules. The translational correlation time τ_d characterizes the time decay of $g_2(t)$ and is defined as $\tau_d = a^2/D$, where a is the average of all the closest inter-center distance between NP and water proton for a given relative orientation of the two over all their possible orientations, and D is the relative diffusion coefficient which is the sum of the self-diffusion coefficients of water proton and NP, $D = D_{M_I}^t + D_{NP}^t$. In case of an NP, its hydrodynamic radius is the distance of closest approach a of the water proton to the surface Gd^{3+} ions since an NP on its whole impacts on the relaxation of water protons. The dipolar spectral density is the Fourier transform of $g_2(t)$ defined as $j_2(\omega) = \int_0^\infty g_2(t)\cos(\omega t)\,dt$ and given by

$$j_2(\omega) = \frac{N_S}{Da} Re\left[\frac{4+x}{3(9+9x+4x^2+x^3)}\right]$$

where $x = \sqrt{i\omega\tau_d}$. The OS relaxivities are linear combinations of spectral density $j_2(\omega)$ of $g_2(t)$, and given by $r_1^{OS} = Aj_2(\omega_I)$ and $r_2^{OS} = A\left[\frac{2}{3}j_2(0) + \frac{1}{2}j_2(\omega_I)\right]$

In case of PVP and DSPE-mPEG coated NaYF$_4$-NaGdF$_4$:Eu^{3+} core-shell NPs, the Eu^{3+} lifetime decay analyses of the doped Eu^{3+} ions conveyed about the hydrophobic barrier around the NP that debars the access and exchange of water molecules with the ones coordinated to the surface Eu^{3+} ions of NPs in the inner coordination sphere. This suggests no water coordination (although there are insignificant number of water molecules attached to Ln^{3+}-based NPs during and post NPs' synthesis, but their effect is negligible compared to that of bulk water molecules), exchange or accessibility to the surface Gd^{3+} ions of the NPs indicating the dominance of outer sphere relaxation mechanism. The difference in the hydrodynamic diameter obtained from DLS and diameter of NPs determined from histograms developed from the corresponding TEM images gives the thickness of the hydrophobic barrier between the surface Gd^{3+} sites of NPs and the water protons. From Table A1.1, the hydrophobic layer is ~15 nm thick in both PVP and DSPE-mPEG coated $NaYF_4$-$NaGdF_4$:Eu^{3+} core-shell NPs indicating almost equal contribution from the OS relaxation. This is in agreement with the corresponding close values of r_1 relaxivities 15,800 and 17,500 mM_{NP}^{-1} s^{-1} *per* NP concentration (Gd^{3+} ionic relaxivities are 7.27 and 6.46 mM^{-1} s^{-1}) and r_2 relaxivities 115,200 and 114,200 mM_{NP}^{-1} s^{-1} *per* NP concentration (Gd^{3+} ionic relaxivities are 52.34 and 60.75 mM^{-1} s^{-1}). The difference in the r_1 and r_2 relaxivities ($r_1 < r_2$) of an NP comes largely from the spectral density terms $j_2(0)$ and $j_2(\omega_I)$.

The contribution of Curie relaxivity in the inner and outer spheres of relaxation has been discussed in published works.[40,116] Curie relaxation arises from the interaction of the fluctuating local magnetic fields at the position of the studied nuclear spin *I* with the various average magnetic moments of the spins *S* of the Gd^{3+} ions. The Curie correction factor is given by[89]

$$\varepsilon_{Curie} \equiv \frac{1}{3} S(S+1) \left(\frac{g_S \mu_B B_0}{k_B T} \right)^2$$

At magnetic field $B_0 \leq 10$ T at room temperature, the Curie correction factor, ε_{Curie}, which varies with field as B_0^2, is smaller than 1 %. As such, the Curie relaxivities can be neglected. $r_i^{total} = r_i + \varepsilon_{Curie} r_i = (1 + \varepsilon_{Curie}) r_i \cong r_i$

From the comprehensive analyses of Eu^{3+} lifetime decays, it is conclusive that at an applied magnetic field ≥ 3 T, the smaller $NaGdF_4$:Eu^{3+} NPs have a dominant contribution from the inner and second spheres towards their relaxivities while the larger

$NaYF_4$-$NaGdF_4$:Eu^{3+} core-shell NPs have a predominant contribution from outer sphere relaxation of water protons with respect to the surface Gd^{3+} ions of the NPs.

2.3 Conclusions

In conclusion, to understand the qualitative contribution of inner, second, and outer spheres of T_1 and T_2 relaxation mechanisms of water protons with respect to water dispersed Gd^{3+}-based NPs at a magnetic field of 9.4 T, systematic investigation on europium decay curves of $NaGdF_4$:Eu^{3+} and $NaYF_4$-$NaGdF_4$:Eu^{3+} core-shell NPs have been carried out. Inner and second sphere contributions have been proved to be predominant towards r_1 and r_2 relaxivities of the smaller $NaGdF_4$ NPs (3 nm diameter) owing to the "leaky" coatings on the high curvature NP surface and easy accessibility and exchange of water protons with the ones coordinated directly to the surface Eu^{3+} or Gd^{3+} ions. On the other hand, outer sphere contribution governs the relaxivities in the larger $NaYF_4$-$NaGdF_4$:Eu^{3+} core-shell NPs (18.3 nm core diameter with 0.5 nm thick shell) since the hydrophobic barrier on the low curvature NP surface forbids water accessibility to the surface Eu^{3+} or Gd^{3+} ions. The r_1 values of $NaGdF_4$ NPs were found to be almost identical for either type of surface coatings of PVP and DSPE-mPEG at 9.4 T. Similar observations were made for the r_1 and r_2 relaxivities of $NaYF_4$-$NaGdF_4$:Eu^{3+} core-shell NPs. The very many parameters, such as the time periods of different exchange processes and residence of water protons at the surface of a NP, translational correlation time, and spectral density terms, governing the inner, second, and outer sphere relaxation mechanisms of a paramagnetic ion/Gd^{3+}-based NP need to be well understood to design NPs with optimal relaxivities to obtain MR image contrast with high signal to noise ratio for efficient medical diagnosis.

2.4 Experimental Section

Chemicals. Gadolinium(III) oxide (99.9%), gadolinium(III) chloride hexahydrate (99.9%), europium(III) oxide (99.9%), europium(III) chloride hexahydrate (99.9%), yttrium(III) acetate hydrate, sodium trifluoroacetate (98%), ammonium fluoride (≥ 99.99%), polyvinylpyrrolidone (PVP-10, MW 10,000 Da), oleic acid (tech grade, 90%), 1-octadecene (tech grade, 90%), deuterium oxide (99.9%) and hexanes were purchased from Sigma Aldrich. Oleylamine (97%) was purchased from Acros, dichloromethane (DCM) from EMD chemicals, sodium hydroxide, trifluoroacetic acid, dimethyl sulphoxide (99.9%), toluene, dimethylformamide (DMF), anhydrous ethanol and methanol from Caledon laboratories and 1,2-distearoyl-*sn*-glycero-3-phosphoethanolamine-*N*-[methoxy(polyethylene glycol)-2000] (ammonium salt) from Avanti Polar Lipids.

Synthesis of hexagonal (β) phase $NaGdF_4$ NPs.[83] $GdCl_3.6H_2O$ (1 mmol), oleic acid (4 mL) and 1-octadecene (15 mL) were stirred together in a 100 mL three-necked round bottom flask and heated at 140 °C under vacuum until a clear solution formed. It was cooled down to room temperature after which a solution of NaOH (2.5 mmol) and NH_4F (4 mmol) in methanol (10 mL) was added. The reaction mixture was stirred at room temperature for 1 h. It was heated to 80 °C to remove methanol under an argon flow. Subsequently, the solution was heated (15 °C/min) and maintained at 260 °C for 10 min under an argon flow.

It was cooled to room temperature under air and the NPs were precipitated using 60 mL of ethanol, centrifuged (7,000 *g*, 10 min, Beckman Coulter Spinchron 15-rotor F0830) and washed with 60 mL of ethanol thrice. The collected NPs were dispersed in 10 mL of hexanes. To synthesize 5% Eu^{3+}-doped β-$NaGdF_4$ NPs, $GdCl_3.6H_2O$ (0.95 mmol) and $EuCl_3.6H_2O$ (0.05 mmol) were used in this procedure.

Synthesis of 5% Eu^{3+}-doped cubic (α) phase $NaGdF_4$ NPs (denoted as $NaGdF_4$:Eu^{3+} NPs). Gd_2O_3 (0.95 mmol), Eu_2O_3 (0.05 mmol) and 50% trifluoroacetic acid (10 mL) were mixed together in a 100 mL three-necked round bottom flask and refluxed at 85 °C for 5 h. Excess water was evaporated at 65 °C overnight to yield gadolinium trifluoroacetate. Sodium trifluoroacetate (2 mmol), oleic acid (5 mL), oleylamine (5 mL) and 1-octadecene (10 mL) were added to it and heated at 130 °C for 45 min under vacuum to remove residual water and oxygen. Subsequently, the solution was heated to 285 °C under an argon atmosphere and stirred vigorously for 45 min. The solution was cooled down to room temperature in air. The NPs were precipitated and washed with 60 mL of ethanol thrice by centrifugation (7,000 *g*, 10 min, Beckman Coulter Spinchron 15-rotor F0830) and finally dispersed in 10 mL of hexanes.

Synthesis of hexagonal (β) phase $NaYF_4$-$NaGdF_4$ core-shell NPs with the shell doped with 5% Eu^{3+} (denoted as $NaYF_4$-$NaGdF_4$:Eu^{3+} core-shell NPs).[56] Yttrium(III) acetate hydrate (1 mmol), oleic acid (6 mL) and 1-octadecene (17 mL) were mixed in a 100 mL three-necked round bottom flask and stirred under vacuum at 130 °C for 45 min. The solution was cooled to room temperature, added with a solution of NaOH (2.5 mmol) and NH_4F (4 mmol) in methanol (10 mL) and stirred for 1 h. Methanol was removed thereafter at 80 °C. The temperature was raised to 300 °C (15 °C/min) under argon flow and the solution was stirred vigorously for 1 h. The cubic (α) $NaGdF_4$ (Eu^{3+}-doped) NPs in 1-octadecene (1 mL) was injected into the solution and stirred at 300 °C for 10 min to form a core-shell nanocrystal structure. The solution was cooled down to room temperature under air condition. The NPs were precipitated and washed with 60 mL of ethanol thrice by centrifugation (7,000 *g*, 10 min, Beckman Coulter Spinchron 15-rotor F0830) and finally dispersed in 10 mL of hexanes.

Phase transfer of NPs to water (and/or D_2O) using PVP-10.[83] Oleate capped NPs were exchanged with PVP-10 (molecular weight of 10,000 Da) in 1:1 DCM and DMF solvent mixture, refluxed at 85 ^{o}C for 18 h. NPs were precipitated in ethyl ether (100 mL) and dried under vacuum for 15 min. The amount of polymer for exchange was based on the NP size and calculated as such to accommodate ~60 PVP molecules per nm^2 of NP surface. After the exchange NPs were dispersed in appropriate solvents (deionized water and/or D_2O).

Phase transfer of NPs to water using phospholipids.[76] NPs were dispersed in 0.4 mL toluene at 7.0 mg/mL and added with DSPE-mPEG in 0.8 mL chloroform taking appropriate weight ratio of DSPE-mPEG to NP. 4 mL of DMSO was added slowly to the solution which was then incubated on a shaker for 30 minutes at room temperature. Chloroform and toluene were removed completely by vaporization under vacuum. Deionized water was added to the colloidal solution in DMSO to reach a total volume of 20 ml. DMSO was completely substituted with deionized water by three rounds of centrifugation in centrifugal filter tubes (Vivaspin Turbo 15, 100 kDa cutoff size) leaving a final volume of 1 mL of NP dispersion.

Phase transfer of NPs to D_2O using phospholipids. NPs were dispersed in 0.4 mL toluene at 7.0 mg/mL and added with DSPE-mPEG in 0.8 mL chloroform taking appropriate weight ratio of DSPE-mPEG to NP. Chloroform and toluene were completely removed with a rotary evaporator followed by storage under vacuum for 18 h. The NPs were dispersed in 10 mL D_2O.

Characterization. Transmission electron microscopy (TEM) images were acquired using a JEOL JEM-1400 microscope operating at 80 kV. The NP dispersion in hexane was drop-cast onto a formvar carbon film supported on a 300 mesh copper grid (3 mm in diameter) and allowed to dry in air at room temperature, before imaging. The size distribution was obtained from averaging a minimum of 300 NPs using ImageJ software (version 1.50i). Electron energy loss spectroscopy (EELS) and Energy-dispersive X-ray spectroscopy (EDX) measurements were done with an Hitachi HF-3300V Scanning Transmission Electron Holography Microscope (STEHM) operated at 200 kV and equipped with EELS (Gatan) and EDX (Bruker) detectors. The NP dispersion in hexane was drop-cast on a lacey carbon grid, dried in vacuum and cleaned in a UV chamber.

X-ray Diffraction (XRD) patterns were collected using a Rigaku Miniflex diffractometer with Cr Kα radiation ($\lambda = 0.2290$ nm, 30 kV, 15 mA) with a scan step size of 0.05 degrees (2θ). 15 drops of the NP dispersion in hexane were added onto an indented zero-background sample holder and dried to get the diffraction patterns. The standard powder diffraction files (PDFs) were retrieved from the International Center from Diffraction Data (ICDD 2015).

Dynamic light scattering (DLS) measurements were done using a Brookhaven Zeta PALS instrument with a 90Plus/BI-MAS Multi Angle Particle Sizing option, equipped with a 15 mW solid-state laser (658 nm). All data were obtained at a single scattering angle (90^o) and averaged over ten scans of the scattered intensity-weighted plots of the NPs dispersed in deionized water, filtered through glass microfiber filter of 0.45 μm pore size (Whatman, Sigma Aldrich) to get rid of dust.

Inductively coupled plasma mass spectroscopy (ICP-MS) analysis was carried out using a Thermo X-Series II (X7) quadrupole ICP-MS to determine the concentration of Eu^{3+}, Gd^{3+} and Y^{3+} ions in the NP stock solution. The aqueous dispersion of NPs was digested in concentrated nitric acid at 135 ^oC in sealed Teflon vials for 3 days and diluted with ultrapure water before analysis. Calibration was done by analyzing serial dilutions of a mixed element synthetic standard containing a known amount of europium, gadolinium and yttrium. Each sample, standard and blank, were spiked with indium (to a concentration of ∼7 ppb) as the internal standard to correct for signal drift and matrix effects.

Steady state excitation and emission and time resolved lifetime decay measurements were done using an Edinburgh Instruments’ FLS920 fluorimeter equipped with a tunable pulsed optical parametric oscillator (OPOTEK Radiant 355 HE 35 LD UVDM), pumped by the third harmonic (355 mm) of the Quantel Q-smart Nd:YAG pump laser. All the emission was collected using a Hamamatsu R928P PMT (200–700 nm) detector and the spectra were corrected for the instrument sensitivity. All NP dispersions were measured in a 1 cm path length quartz cuvette. Lifetime measurements were done by excitation of Eu^{3+} at 394 nm in the $^5L_6$ level and emission at 615 nm using the OPOTEK Radiant 355 high energy tunable UV-VIS-NIR laser system. A 420 nm short band-pass filter was used to block unwanted scattered wavelengths before the emitted light entered the detector. The data points for lifetime trace of the $^5D_0$ level of the Eu^{3+}-doped NPs were collected over a time range of 80 ms collected in bins of 16 µs. The data were analyzed using OriginPro 2015 (OriginLab, Northampton, MA, version b9.2.272) using relevant first-, second- and third-order exponential decay fittings: $I_t = I_0 e^{-t/\tau_1} + B$, $I_t = A_1 e^{-t/\tau_1} + A_2 e^{-t/\tau_2} + B$, and $I_t = A_1 e^{-t/\tau_1} + A_2 e^{-t/\tau_2} + A_3 e^{-t/\tau_3} + B$, where τ_1, τ_2 and τ_3 are the decay lifetime values, I_0 is the intensity at time $t = 0$, B is the background intensity and A_1, A_2 and A_3 denote the pre-exponential factors such that $A_1 + A_2 = I_0$ (at $t = 0$) for bi-exponential and $A_1 + A_2 + A_3 = I_0$ (at $t = 0$) for tri-exponential fittings. When nonlinear curve fitting was performed using OriginPro 2015, the reduced chi-square was obtained by dividing the residual sum of squares by the degrees of freedom. This quantity is typically not a good measure to determine the goodness of fit because if the y-axis data is multiplied by a scaling factor, the reduced chi-square is scaled as well. The r-square value, also known as coefficient of determination gives a good measure of the goodness of fit. If the fit is closer to the data points, the r-square value is closer to 1. Nevertheless, the adjusted r-square value, which accounts for the degrees of freedom, provides a better measure of the goodness of fit than r-square. The adjusted r-square value of all the Eu^{3+} decay curve fittings presented in this article lies in the range 0.99427–0.99939.

Relaxivity measurements. Aqueous dispersions of NPs were used to determine the relaxation times. The T_1 and T_2 measurements were carried out using a 9.4 T/21 cm bore magnet (Magnex, UK) and a Bruker console (Bruker, Germany) (by Dr. Barbara Blasiak and Dr. Boguslaw Tomanek, University of Calgary). A transmit/receive radio frequency volume birdcage coil was applied to excite protons and obtain resonant signal. For the T_2

measurements, a single slice multi-echo pulse sequence was used with the following pulse parameters: repetition time (TR) 5 s, matrix size 128 × 128, field of view (FOV) 3 cm × 3 cm, slice thickness 2 mm, 128 echoes 4 ms apart. T_2 relaxation times were calculated using a single exponential fitting of the echo train (Marevisi, Canada). For T_1 measurements, TRUE FISP method was used with the following pulse sequence parameters: TR 3 s, TE 1.5 s, matrix size 128 × 128, FOV 3 cm × 3 cm, slice thickness 3 mm, 60 frames × 4 segments, segment time 192 ms. The relaxation times were calculated using single exponential fitting of the data (MATLAB "1sqcurvefit") for different concentrations of NPs in deionized water.

The r_1 and r_2 relaxivities were obtained from the concentration dependent plots of the measured T_1 and T_2 relaxation times in OriginPro 2015 (OriginLab, Northampton, MA, version b9.2.272) using the equation, $\boldsymbol{\frac{1}{T_i} = \frac{1}{T_i^0} + r_i[Gd^{3+}]; i = 1, 2}$, where $[Gd^{3+}]$ is the concentration of Gd^{3+} ions in an NP solution obtained from ICP-MS, T_i^0 denote the relaxation times of the water protons in absence of the paramagnetic NPs.

Chapter 3. Target-Specific Magnetic Resonance Imaging of Human Prostate Adenocarcinoma using $NaDyF_4$-$NaGdF_4$ Core-Shell Nanoparticles

3.1 Introduction

Prostate cancer is the second most frequently diagnosed cancer in men with two-thirds of the cases reported in the Western world where only 17% of the world's male population resides.[117] The growth and spread of prostate tumor are often very slow and remain undetected at the early stages of the cancer. On the other hand, metastatic prostate cancer is not curable. If the prostate tumor is diagnosed early, there is a 98.9% chance of five year survival.[118] This necessitates the need for early diagnosis of prostate cancer which is crucial for devising effective strategies towards curative treatment and evaluating response to relapse.

Current diagnostic techniques for prostate cancer involve a combination of digital rectal examination, evaluation of prostate-specific antigen (PSA) serum concentrations and transrectal ultrasound (TRUS)-guided biopsy.[119-120] In spite of the fact that the PSA test significantly decreased the mortality rate, it has a low specificity, unable to provide information about tumor location and suffers from a high false positive rate.[121-122] Moreover, TRUS has inherent limitations as it cannot reliably delineate small cancer foci and differentiate among benign, inflammation, atrophy and malignant conditions of prostate tumor. Further, the invasive procedure of biopsy has a large sampling error, especially, for small tumor (< 11.9 mm)[123] and is associated with hemorrhaging, infections, and has the risk of spreading cancer cells.

To overcome the drawbacks of the current diagnostic techniques, a non-invasive target (prostate cancer) specific imaging is necessary. Prostate specific membrane antigen (PSMA), a transmembrane 750-amino-acid type II glycoprotein, is a promising biomarker of prostate cancer.[124] In a normal prostate, the expression level of PSMA is usually ten times higher than that in other types of organs, which is further increased ten folds in PSMA positive prostate tumors.[125] PSMA is markedly over-expressed (10^4 per cell) and localized on the cell membranes of the PSMA positive prostate tumors. The cytoplasmic domain of PSMA mediates internalization and endosomal recycling, which leads to high intracellular concentration of PSMA-targeting imaging probes.[126] PSMA is the single most well-established prostate epithelial cell membrane antigen, whereas PSA is a secretory protein.[127] These characteristics of PSMA have led to research on PSMA-targeting probes for early diagnosis of prostate cancer.

Magnetic resonance imaging (MRI), a non-invasive clinical technique, can be used for diagnosing prostate cancer because it provides three-dimensional information on the anatomical details of a human body with high spatial resolution and tissue contrast. The contrast to noise ratio in MR images depends on the proton density and on the longitudinal (T_1) and transverse (T_2) relaxation times of the water protons. As the differences in the relaxation times at the sites of tumor and normal tissues are often not sufficiently large to allow visible contrast, contrast agents (CAs) are administered that enhance the relaxation rates of the water protons at the tissue sites. Gd^{3+}-based CAs[34,83] produce positive (T_1) contrast in MR images while Dy^{3+}- and iron oxide-based CAs[39,128] produce negative (T_2) contrast.

The current work deals with synthesis, characterization and application of $NaDyF_4$-$NaGdF_4$ core-shell NPs in MRI of prostate cancer. $NaDyF_4$-$NaGdF_4$ core-shell NPs ($NaDyF_4$ core of 21.2 nm diameter with a 0.6 nm thick shell of $NaGdF_4$; sizes from transmission electron microscopy, TEM) were synthesized in a high boiling (306 ^oC) solvent mixture of oleic acid and 1-octadecene. The resultant oleate-capped $NaDyF_4$-$NaGdF_4$ core-shell NPs were transferred to deionized water by coating their surface with phospholipids bearing polyethylene glycol chains (1 PEG per unit) to impart hydrophilicity and biocompatibility. The core-shell NPs act as a dual modal CAs to produce enhancement of both T_1 and T_2 relaxation rates (= r_1 and r_2 relaxivities, respectively) from a single NP at both clinical field of 3 T and a high magnetic field of 9.4 T, where human imaging[85] has been made possible. The r_1 and r_2 relaxivities of the core-shell NPs at both 3 T and 9.4 T are higher than those of the current clinical CAs. Magnetic measurements were done using a superconducting quantum interference device (SQUID) to determine magnetization from their paramagnetic behavior. The magnetization was compared with a series of sodium lanthanide fluoride NPs [$NaDyF_4$, $NaYF_4$, $NaDyF_4$-$NaYF_4$ core-shell, $NaYF_4$-$NaDyF_4$ core-shell and $NaYF_4$-$NaGdF_4$ core-shell NPs] of approximately the same size to infer on the synergistic behavior of magnetization in $NaDyF_4$-$NaGdF_4$ core-shell NPs.

In vitro cell studies and *in vivo* MRI of prostate cancer were performed to assess the diagnostic capability of phospholipid coated $NaDyF_4$-$NaGdF_4$ core-shell NPs. The phospholipids coating $NaDyF_4$-$NaGdF_4$ core-shell NPs had functional end groups (such as –COOH) which were used to conjugate with amines of anti-PSMA antibody to specifically target PSMA rich cell membranes of LNCaP (lymph node carcinoma of the prostate) cells, a PSMA positive prostate cancer cell line. PC3 cells, a PSMA negative prostate cancer cell line was used as a negative control for the *in vitro* and *in vivo* studies. $NaDyF_4$-$NaGdF_4$ core-shell NPs tagged with anti-PSMA antibody act as potential non-invasive target-specific probes for MRI of PSMA positive prostate tumor.

3.2 Results and Discussion

3.2.1 Synthesis and Characterization of $NaDyF_4$-$NaGdF_4$ core-shell NPs

Prior to synthesis of $NaDyF_4$-$NaGdF_4$ core-shell NPs, cubic phase (α) $NaGdF_4$ NPs were synthesized which acted as the sacrificial NPs for the shell formation. XRD patterns of the NPs in Figure 3.1A are indexed with the standard patterns of the cubic phase of $NaGdF_4$ confirming the cubic phase of the $NaGdF_4$ NPs. A broad peak centered at ~30° (2θ) denotes the presence of oleates around NPs. TEM image in Figure 3.1B shows an average particle size of ~6 nm. To synthesize $NaDyF_4$-$NaGdF_4$ core-shell NPs, $NaDyF_4$ core NPs were prepared in a solvent mixture of oleic acid and 1-octadecene at a high temperature of 306 ^{o}C under a continuous flow of argon. A calculated amount of sacrificial α-$NaGdF_4$ core-shell NPs were injected to form the shell over the core $NaDyF_4$ NPs. Such epitaxial growth of the NPs proceeds via Ostwald ripening[57] in which the energetically more favorable larger NPs grow at the expense of smaller NPs[56] and the shell lattice adapts to the core lattice structure.

XRD patterns of as-synthesized $NaDyF_4$-$NaGdF_4$ core-shell NPs are shown in Figure 3.2 which are indexed with the standard patterns of the hexagonal phase (β) of $NaDyF_4$ (PDF#00-027-0687) that comprises the core. A broad peak at about 30° (2θ) indicates the presence of oleates around NPs. The XRD patterns of the core-shell NPs are slightly shifted compared to the standard patterns because of the compressive strain induced by the $NaGdF_4$ shell lattice comprising larger Gd^{3+} ions (ionic radius = 1.193 Å) on the core comprising Dy^{3+} ions (ionic radius = 1.167 Å).[61] TEM images of the core-shell NPs are shown in Figure 3.3. Particle size distribution analysis from the TEM images revealed a shell thickness of 0.6 nm as the core $NaDyF_4$ NP (prior to injection of $NaGdF_4$ NPs – shell precursors) showed a diameter of 21.2 ± 0.1 nm and the core-shell NPs showed a diameter of 21.8 ± 0.1 nm.

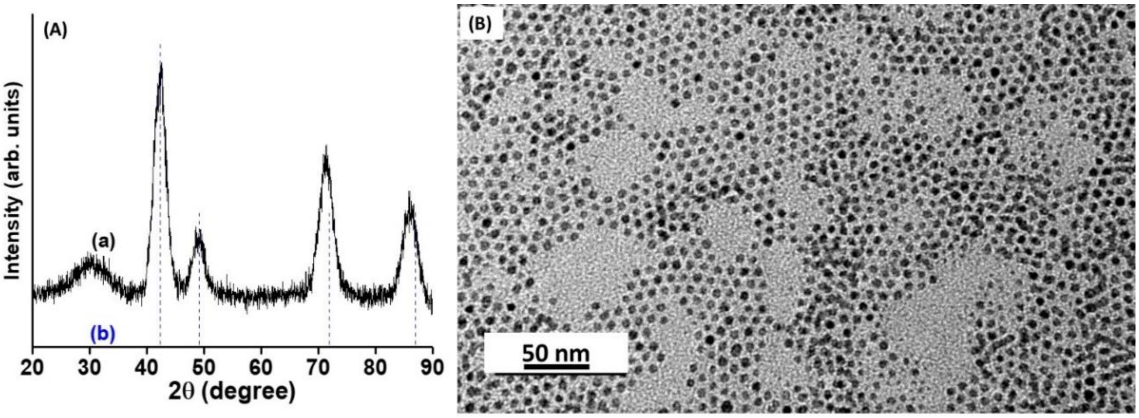

Figure 3.1. (A) XRD patterns of sacrificial α-$NaGdF_4$ NPs in (a) indexed with the standard patterns of the cubic phase of $NaGdF_4$ (PDF#00-027-0698; b). (B) TEM image of α-$NaGdF_4$ NPs.

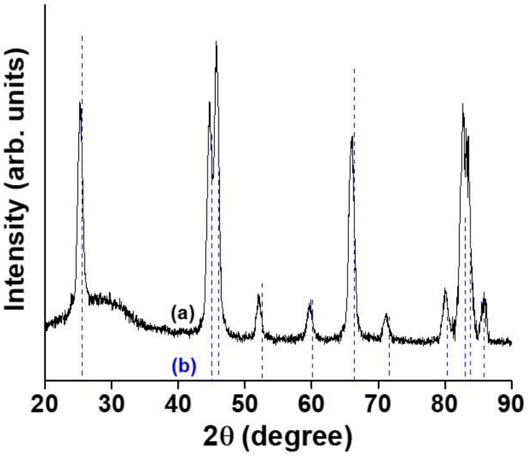

Figure 3.2. XRD patterns of (a) $NaDyF_4$-$NaGdF_4$ core-shell NPs indexed with (b) the standard patterns of the hexagonal phase of $NaDyF_4$ (PDF#00-027-0687).

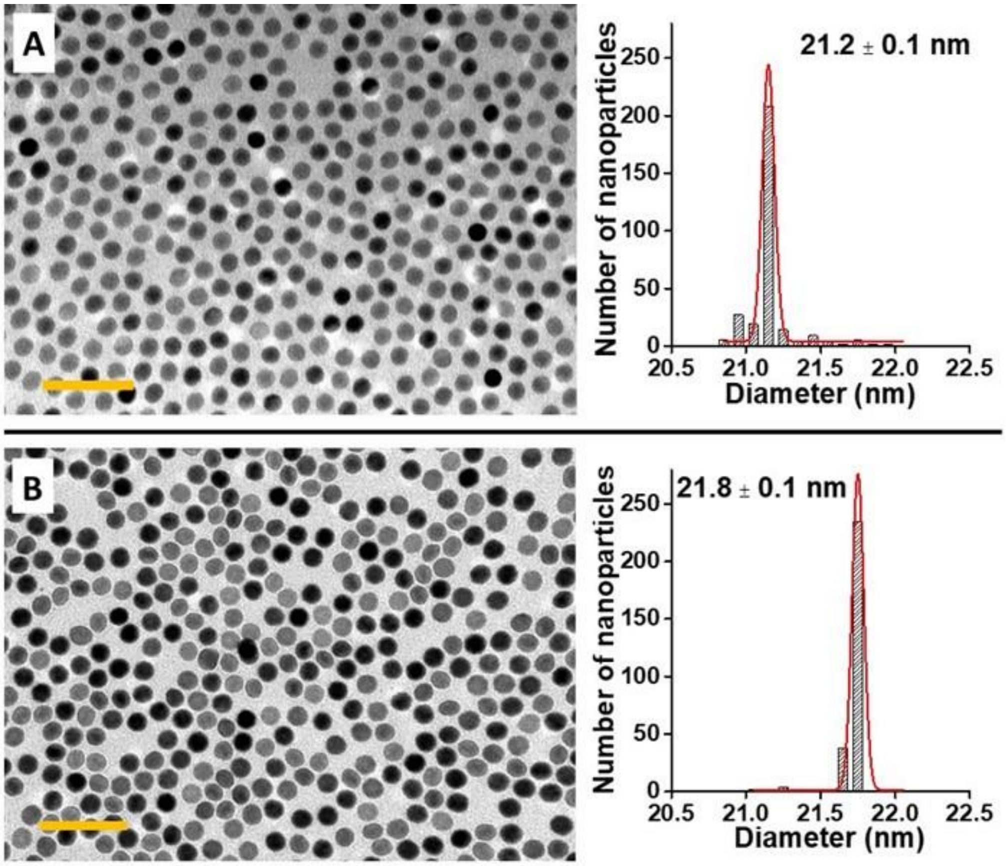

Figure 3.3. TEM images and the corresponding histograms of particle size distribution (A) $NaDyF_4$ NPs (prior to injection of sacrificial $NaGdF_4$ NPs) and (B) $NaDyF_4$-$NaGdF_4$ core-shell NPs. Yellow scale bar = 100 nm.

Energy-dispersive X-ray spectroscopy (EDX) was carried out on a scanning transmission electron holography microscope (STEHM) to yield information about the composition of NPs. In Figure 3.4, peaks corresponding to Gd and Dy are evident in the EDX spectrum. EDX scans across a NP were obtained for Gd and Dy (in Figure 3.5A–B). These two EDX (Gd and Dy) maps were merged (in Figure 3.5C) which revealed that the core of the NP comprises mostly of Dy while the shell has Gd. A thin irregular shell of Gd is visible in the merged image (in Figure 3.5C) because of the low signal to noise ratio while mapping a single particle at a high resolution. Another reason for an irregular shell could be ascribed to some facets of the core being more reactive than the others leading to non-uniform shell growth.

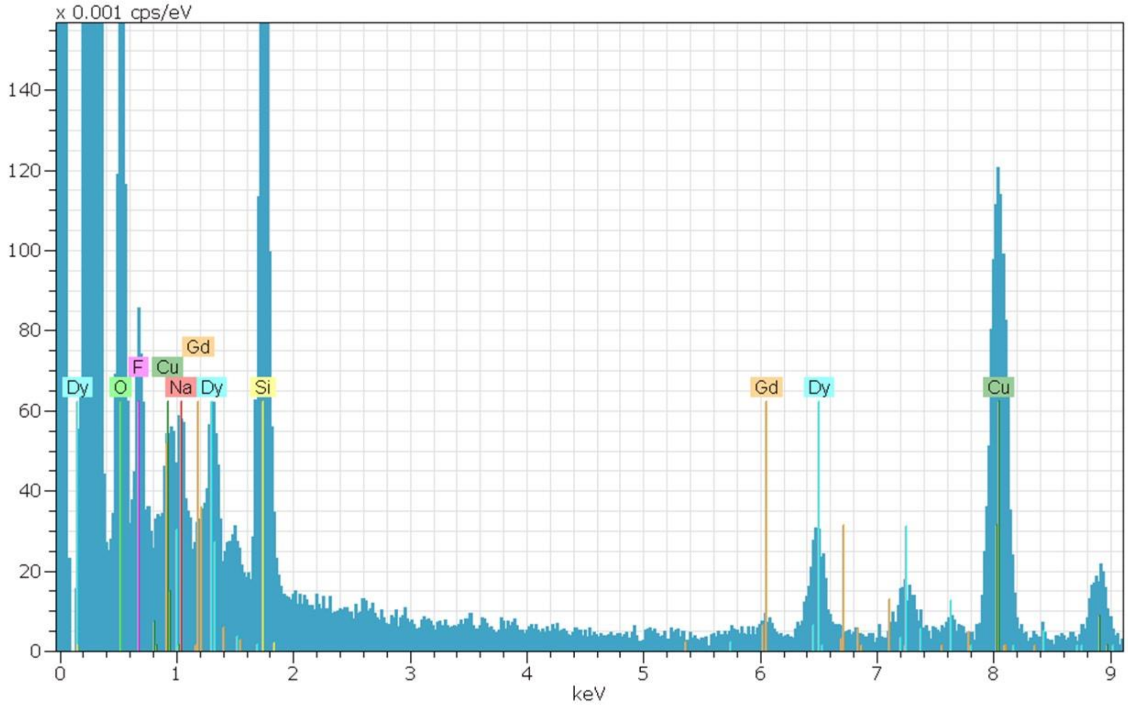

Figure 3.4. EDX analysis on STEHM showing the elemental composition in NaDyF$_4$-NaGdF$_4$ core-shell NPs.

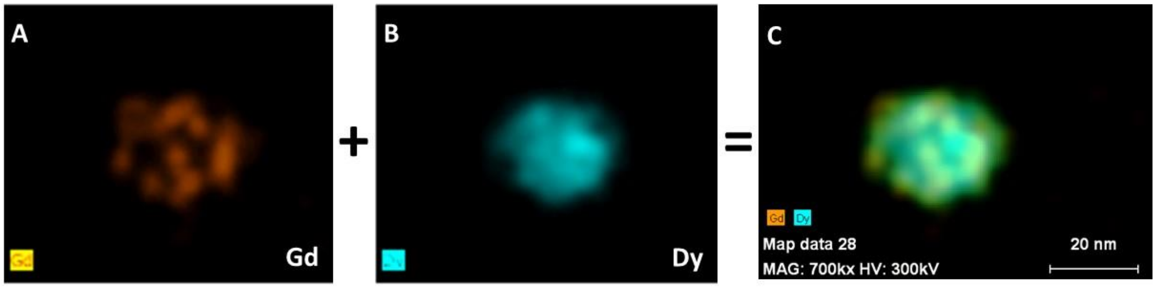

Figure 3.5. Single particle elemental mapping using EDX on STEHM: Elemental maps of (A) Gd (in the shell) and (B) Dy (in the core) merged in (C) showing the core-shell structure of NaDyF$_4$-NaGdF$_4$ core-shell NPs.

3.2.2 Relaxivities (r_1 and r_2) at 3 T and 9.4 T

The dispersions of $NaDyF_4$-$NaGdF_4$ core-shell NPs in hexanes were transferred to deionized water by coating them with functionalized phospholipids[76] as detailed in Section 3.2.3. For *ex vivo* measurements of the relaxation times (T_1 and T_2) at 3 T and 9.4 T, DSPE-mPEG coated $NaDyF_4$-$NaGdF_4$ core-shell NPs were employed. Inductively coupled plasma mass spectrometry (ICP-MS) of $NaDyF_4$-$NaGdF_4$ core-shell NPs revealed ionic concentration of Dy^{3+} and Gd^{3+} to be 1.07 mM and 0.10 mM, respectively. Figure 3.6 shows the linear fits of the rate of relaxation times ($1/T_1$ and $1/T_2$) at different ionic concentration. The *y*-intercepts denote the relaxation rate of water molecules in absence of the NPs. For simplicity and based on the inherent ability to produce T_1- and T_2-contrasts, T_1 contribution is solely attributed to Gd^{3+} while T_2 to Dy^{3+}. The ionic r_1 relaxivities of the core-shell NPs at a high magnetic field of 9.4 T and clinical field of 3 T were found to be 9.37 ± 0.18 mM^{-1} s^{-1} and 20.22 ± 0.42 mM^{-1} s^{-1}, respectively. The corresponding *per* NP r_1 relaxivities were determined to be $(9.01 \pm 0.17) \times 10^5$ mM_{NP}^{-1} s^{-1} and $(19.40 \pm 0.40) \times 10^5$ mM_{NP}^{-1} s^{-1}. The ionic r_1 relaxivity of these core-shell NPs at clinical field (3 T; 20.22 mM^{-1} s^{-1}) is more than four times higher than that of the currently used Gd^{3+}-based clinical CAs (e.g., 3.2 mM^{-1} s^{-1} for Gadovist, 3.1 mM^{-1} s^{-1} for Magnevist at 3 T) because of the higher concentration of Gd^{3+} ions *per* unit NP volume compared to a complex.[33] On the other hand, the ionic r_2 relaxivities of the core-shell NPs at 9.4 T and 3 T were found to be 157.96 ± 7.94 mM^{-1} s^{-1} and 35.26 ± 0.54 mM^{-1} s^{-1}, respectively. The corresponding NP r_2 relaxivities were determined to be $(161.50 \pm 8.10) \times 10^5$ mM_{NP}^{-1} s^{-1} and $(36.05 \pm 0.55) \times 10^5$ mM_{NP}^{-1} s^{-1}. The ionic r_1 relaxivity of $NaDyF_4$-$NaGdF_4$ core-shell NPs (20.22 mM^{-1} s^{-1} is two and half times higher than that of 20 nm sized $NaGdF_4$ NPs (8.78 mM^{-1} s^{-1})[129] at 3

T. The ionic r_2 relaxivity of NaDyF$_4$-NaGdF$_4$ core-shell NPs (157.96 mM^{-1} s^{-1}) is about 1.5 times higher than that of 20.3 nm sized NaDyF$_4$ NPs (101 mM^{-1} s^{-1})[39] at 9.4 T. The additional magnetic moment of Dy^{3+} increases the local magnetization of the NP, thus, affecting the magnetization of the Gd^{3+} ions in the shell and the overall synergistic effect causes the NaDyF$_4$-NaGdF$_4$ core-shell NPs to have enhanced r_1 and r_2 relaxivities compared to that of NaGdF$_4$ and NaDyF$_4$ NPs.

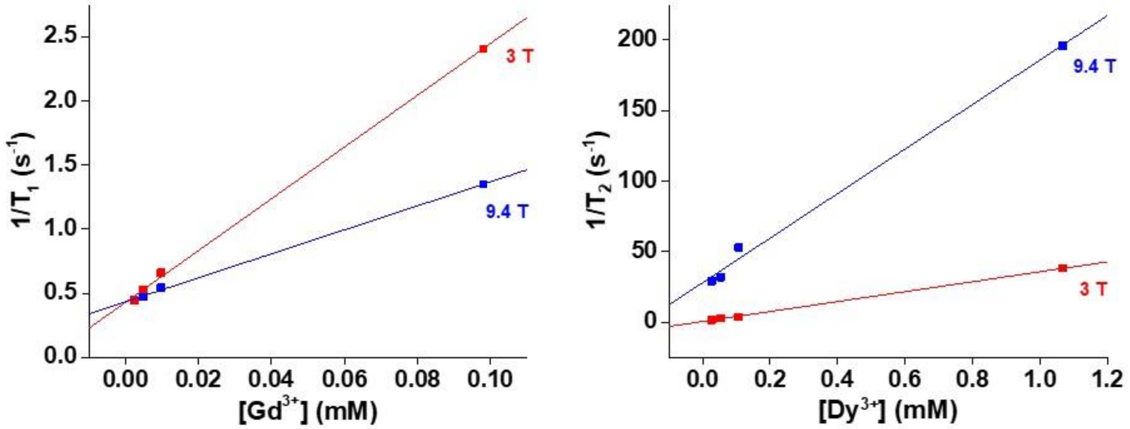

Figure 3.6. Longitudinal (r_1) and transverse (r_2) relaxivities of NaDyF$_4$-NaGdF$_4$ core-shell NPs. Blue colored linear fits are for 9.4 T, red colored linear fits for 3 T. R-square (Coefficient of Determination) defining the goodness of a fit lie in the range of 0.99497–0.99952.

Table 3.1. Ionic and NP relaxivities of NaDyF$_4$-NaGdF$_4$ core-shell NPs at 3 T and 9.4 T.

	9.4 T			**3 T**		
Relaxivities	r_1	r_2	r_2/r_1	r_1	r_2	r_2/r_1
Ionic (mM^{-1} s^{-1})	9.37 ± 0.18	157.96 ± 7.94	16.9	20.22 ± 0.42	35.26 ± 0.54	1.7
NP (mM$_{NP}^{-1}$ s^{-1})	(9.01 ± 0.17) × 10^5	(161.50 ± 8.10) × 10^5		(19.40 ± 0.40) × 10^5	(36.05 ± 0.55) × 10^5	

The r_1 relaxiviy of the $NaDyF_4$-$NaGdF_4$ core-shell NPs at 9.4 T is almost half of the value at 3 T while r_2 relaxivity is extremely high at 9.4 T, about 4.5 times of the value at 3 T. This is explained by the following relaxivity equations. As discussed in Chapter 2, large NPs (~20 nm inorganic diameter) with DSPE-mPEG coating exhibit outer sphere relaxation mechanism at an applied magnetic field of ≥ 3 T. This is also expected in case of the DSPE-mPEG coated $NaDyF_4$-$NaGdF_4$ core-shell NPs in which the r_1 and r_2 relaxivities are given by[89,130]

$$r_1 = A[\, j_2(\omega_I)]$$

$$r_2 = A\left[\frac{2}{3} j_2(0) + \frac{1}{2} j_2(\omega_I)\right]$$

where the spectral density function, $j_2(\omega) = \frac{N_S}{Da} Re\left[\frac{4+x}{3(9+9x+4x^2+x^3)}\right]$, $x = \sqrt{i\omega\tau_d}$ and translational correlation time, $\tau_d = a^2/D$, where a is the average of all the closest inter-center distance between NP and water proton for a given relative orientation of the two over all their possible orientations, D is the relative diffusion coefficient, and N_S is the number of paramagnetic Dy^{3+} or Gd^{3+} ions per unit volume.

$A = \left(\frac{\mu_0}{4\pi}\right)^2 \left(\frac{8\pi}{5}\right) \gamma_I^2 g_S^2 \mu_B^2 [S(S+1)]$, g_S is the Landé factor of the electronic spin S, γ_I and $\gamma_S\,(= -g_S\mu_B/\hbar)$ are the gyromagnetic ratios of the interacting nuclear (^1H from water) spin I and electronic (from Dy^{3+} and Gd^{3+}) spin S, μ_0 is the permeability of vacuum, μ_B is the dipole moment, and ω_I and ω_S are the angular Larmor frequencies of the spins. As observed in the equations of r_1 and r_2, the value of $A\, j_2(\omega_I)$ has to be comparatively smaller than $Aj_2(0)$ for a NP to exhibit very high r_2 relaxivity. This results in the dominating term $Aj_2(0)$ which is directly proportional to the magnetic moment of the ions in the NP. Since both Dy^{3+} and Gd^{3+} have high magnetic moment values (10.65 μ_B and 7.94 μ_B, respectively), the overall magnetic moment per unit volume (= magnetization, M) of the core-shell NP increases with increase in applied magnetic field (H) from the equation, $M = \chi_v H$, where χ_v is the volume magnetic susceptibility. This explains the r_2 relaxivity at 9.4 T which is about 4.5 times of that at 3 T due to the enhanced volume magnetization of the NP at higher field (9.4 T). This is further elaborated by the SQUID results in Section 3.2.3.

3.2.3 Magnetic measurements using SQUID

Magnetization versus field plots were obtained for six batches of NPs (18–20 nm sized; Table A2.1 in Appendix 2): $NaDyF_4$, $NaYF_4$, $NaDyF_4$-$NaYF_4$, $NaDyF_4$-$NaGdF_4$, $NaYF_4$-$NaDyF_4$, and $NaYF_4$-$NaGdF_4$ core-shell NPs. To compare the magnetization and relaxivities of $NaDyF_4$-$NaGdF_4$ core-shell NPs with other Ln^{3+}-based NPs, the Ln^{3+} composing the core and the shell was varied by employing diamagnetic Y^{3+}, and paramagnetic Gd^{3+} and Dy^{3+}. The detailed syntheses, characterization, magnetization and relaxivity plots of the six batches of NPs are mentioned in Appendix 2. As shown in Table A2.1, $NaYF_4$ NPs exhibit a negative value of magnetization, –1.518 emu cm^{-3}, due to the diamagnetic behavior of Y^{3+}. Magnetization increases when the shell has paramagnetic Gd^{3+} (magnetic moment of 7.94 μ_B) and Dy^{3+} (10.65 μ_B) in $NaYF_4$-$NaGdF_4$ (–0.437 emu cm^{-3}) and $NaYF_4$-$NaDyF_4$ (3.708 emu cm^{-3}) core-shell NPs, respectively. $NaDyF_4$ NPs show the highest value of magnetization (84.739 emu cm^{-1}) among the six batches owing to the high magnetic moment of Dy^{3+} (10.65 μ_B). The higher the number of magnetically susceptible ions in a NP, the higher the magnetization of the NP at an applied field. $NaDyF_4$-$NaYF_4$ core-shell NPs have a decreased magnetization (of 74.797 emu cm^{-3})

compared to $NaDyF_4$ NPs due to the shell composing diamagnetic Y^{3+}. $NaDyF_4$-$NaGdF_4$ core-shell NPs display a magnetization of 71.513 emu cm^{-3}. The paramagnetic NPs do not show saturation up to 7 T and beyond.

3.2.4 Bioconjugation for *in vitro* and *in vivo* studies

The dispersions of as-synthesized oleate-capped $NaDyF_4$-$NaGdF_4$ core-shell NPs in hexanes were transferred to deionized water (or phosphate buffer saline, pH = 7.4, for cell studies) after coating then with phospholipids (DSPE) bearing polyethylene glycol (PEG) chains, via dual solvent exchange method using dimethyl sulfoxide.[76] These phospholipids have functional end groups which were used to tag with targeting moieties (antibodies) for cell and animal studies. A phospholipid coating mimics the cell membrane structure and PEGs provide a neutral (no charge) surface over the NPs to have minimal non-specific binding and prolong *in vivo* circulation. For *in vitro* studies, $NaDyF_4$-$NaGdF_4$ core-shell NPs were tagged with anti-PSMA antibody (to target PSMA rich cell membranes of PSMA positive prostate cancer cell line) and Alexa-488 (as a fluorescent probe). As such, the NPs were coated with calculated amount of DSPE-mPEG, DSPE-PEG-COOH and DSPE-PEG-biotin. The amines on the lysin residues of the anti-PSMA antibodies were conjugated to the carboxylate end groups (of DSPE-PEG-COOH) via amide bond formation initiated by EDC/NHS [EDC = 1-{3-(dimethylamino)propyl}-3-ethylcarbodiimide and sulfo-NHS = *N*-hydroxysulfosuccinimide] coupling reaction. A schematic representation of the reaction between carboxylic acid and primary amine to form an amide via EDC/NHS coupling is shown in Figure 3.7.[78] Biotin end groups (from DSPE-PEG-biotin) on the NPs were tagged to streptavidin on the streptavidin-Alexa-488 conjugate via noncovalent bond interaction between biotin and streptavidin. The overall structure of the NP bearing anti-PSMA antibodies and Alexa-488 is illustrated in Figure 3.8. A negative control was used for *in vitro* studies in which NPs were tagged to Alexa-488 only (no antibody). Alexa-488 was used as a fluorescent probe in *in vitro* studies only. Figure 3.9 shows the dynamic light scattering results of the nanostructures used for *in vitro* studies. The hydrodynamic diameters of the phospholipid coated NPs, NPs tagged with anti-PSMA antibody and Alexa-488 and NPs, and NPs tagged with Alexa only were determined to be 33.9 ± 1.2 nm, 41.2 ± 1.9 nm and 35.7 ± 1.1 nm, respectively.

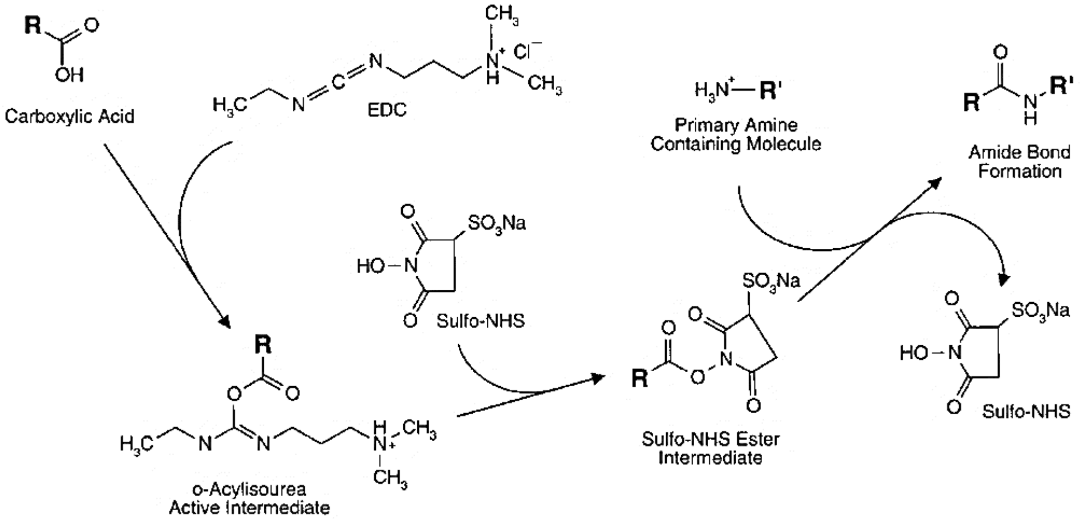

Figure 3.7. EDC/NHS coupling reaction between carboxylic acid and primary amine leading to amide bond formation (adapted from ref. 78).

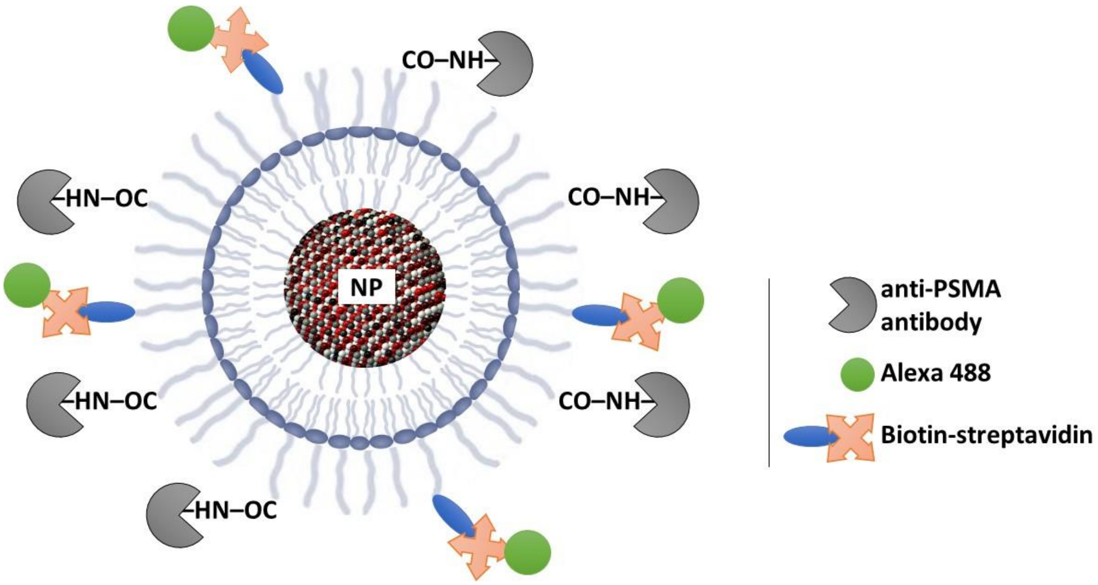

Figure 3.8. Schematic representation of the surface chemistry of phospholipids coated $NaDyF_4$-$NaGdF_4$ core-shell NPs after conjugation of (a) primary amines from anti-PSMA antibody to carboxylic acid groups on DSPE-PEG-COOH via amide bond formation, and (b) Alexa-488-streptavidin conjugate to the biotin end groups of DSPE-PEG-biotin via biotin-streptavidin interaction. The phospholipids not attached with an antibody or an Alexa-488 are DSPE-mPEGs.

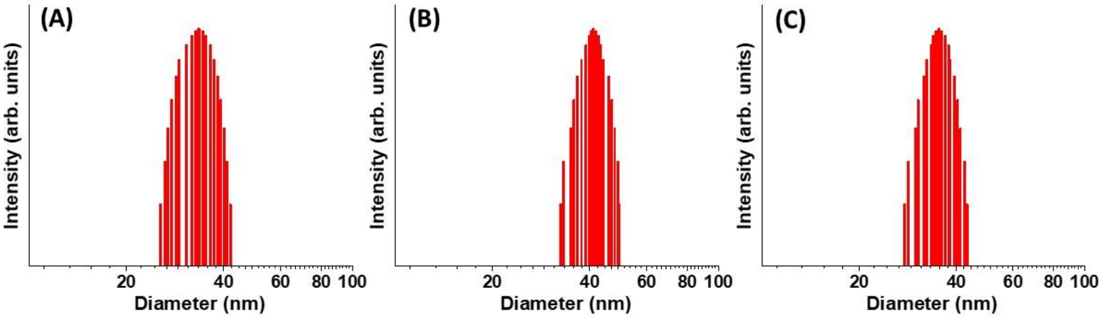

Figure 3.9. *In vitro* studies: DLS data of $NaDyF_4$-$NaGdF_4$ core-shell NPs (A) coated with functionalized phospholipids and tagged with (B) both anti-PSMA antibody and Alexa-488, and (C) Alexa-488 only (control).

For *in vivo* studies, $NaDyF_4$-$NaGdF_4$ core-shell NPs were coated with calculated amounts of DSPE-mPEG and DSPE-PEG-COOH (–COOH groups were used to tag with antibodies via EDC/NHS coupling). Three batches of NPs were prepared – (i) NPs tagged with anti-PSMA antibody, (ii) NPs tagged with a control (monoclonal kappa IgG) antibody, and (iii) NPs coated with DSPE-mPEG only (no antibody); the last two are control experiments. Their hydrodynamic diameters were found to be 34.6 ± 1.1 nm, 41.0 ± 1.7 nm and 40.4 ± 1.2 nm, respectively, from the DLS data shown in Figure 3.10.

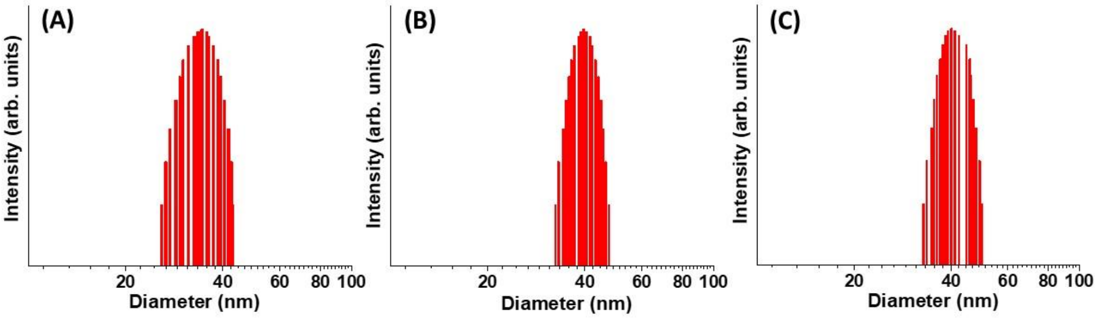

Figure 3.10. *In vivo* studies: DLS data of $NaDyF_4$-$NaGdF_4$ core-shell NPs (A) coated with functionalized phospholipids and tagged with (B) anti-PSMA antibody, and (C) monoclonal antibody (control).

The hydrodynamic sizes obtained for the phospholipid coated NPs and antibody tagged NPs prepared for *in vitro* and *in vivo* studies lie in the range of 30–45 nm which is well above the size allowance (≥ 5.5 nm)[15,131] for renal clearance and below the size constraint (≤ 100 nm)[97,131] established for rapid uptake by mononuclear phagocytic system (MPS) which consists of a network of organs, most notably, liver and spleen.

3.2.5 *In vitro* targeting studies in prostate cancer cells

LNCaP cells are human prostate adenocarcinoma cells which over-express prostate specific membrane antigen. The anti-PSMA antibody is known to detect specifically PSMA and was conjugated to the DSPE-PEG-COOH on the NPs via EDC/NHS coupling reaction. Streptavidin-Alexa-488 conjugate was further bound to DSPE-PEG-biotin on these NPs via noncovalent interaction of biotin and streptavidin. Alexa-488 acts as a fluorescent probe with excitation at 495 nm and emission at 519 nm. To validate the specificity of the anti-PSMA conjugated NPs to LNCaP cells, PSMA negative human prostate cancer PC3 cells were employed as negative control which do not over-express PSMA. LNCaP and PC3 cells were cultured and incubated in a 6-well culture plate with NPs tagged with anti-PSMA antibody and Alexa-488. In addition to PC3 cells as a negative control, another control experiment was carried out in which LNCaP cells were incubated with NPs bound to Alexa-488 only. After incubation at 4 °C for 1 h, cells were adhered to glass slides using poly-L-lysine. The nuclei of cells were stained blue with 4',6-diamidino-2-phenylindole (DAPI), cytoplasmic lipids were stained red with 1 % Nile blue and the cells were observed under Leica compound epifluorescence microscope. Images under channels of green emission from Alexa-488 (λ_{exc} = 495 nm, λ_{em} = 519 nm), blue from DAPI (λ_{exc} = 358 nm, λ_{em} = 460 nm) and red from Nile blue (λ_{exc} = 520 nm, λ_{em} = 568 nm) were collected and merged (Figures 3.11, A2.6). As shown in Figure 3.11(I), the anti-PSMA antibody tagged NPs preferentially bind to the PSMA rich LNCaP cell membranes as evident from the green emission from Alexa-488 localized around the cell membranes which confirms the presence of LNCaP cell bound NPs. While the control experiments with PSMA negative PC3 cells incubated with NPs-tagged with anti-PSMA antibody and

Alexa-488 [Figure 3.11(II)], and LNCaP cells incubated with NPs tagged with Alexa-488 only (no antibody) [Figure 3.11(III)] tested negative as the NPs did not show any specific binding to cells. There is hardly any non-specific binding observed.

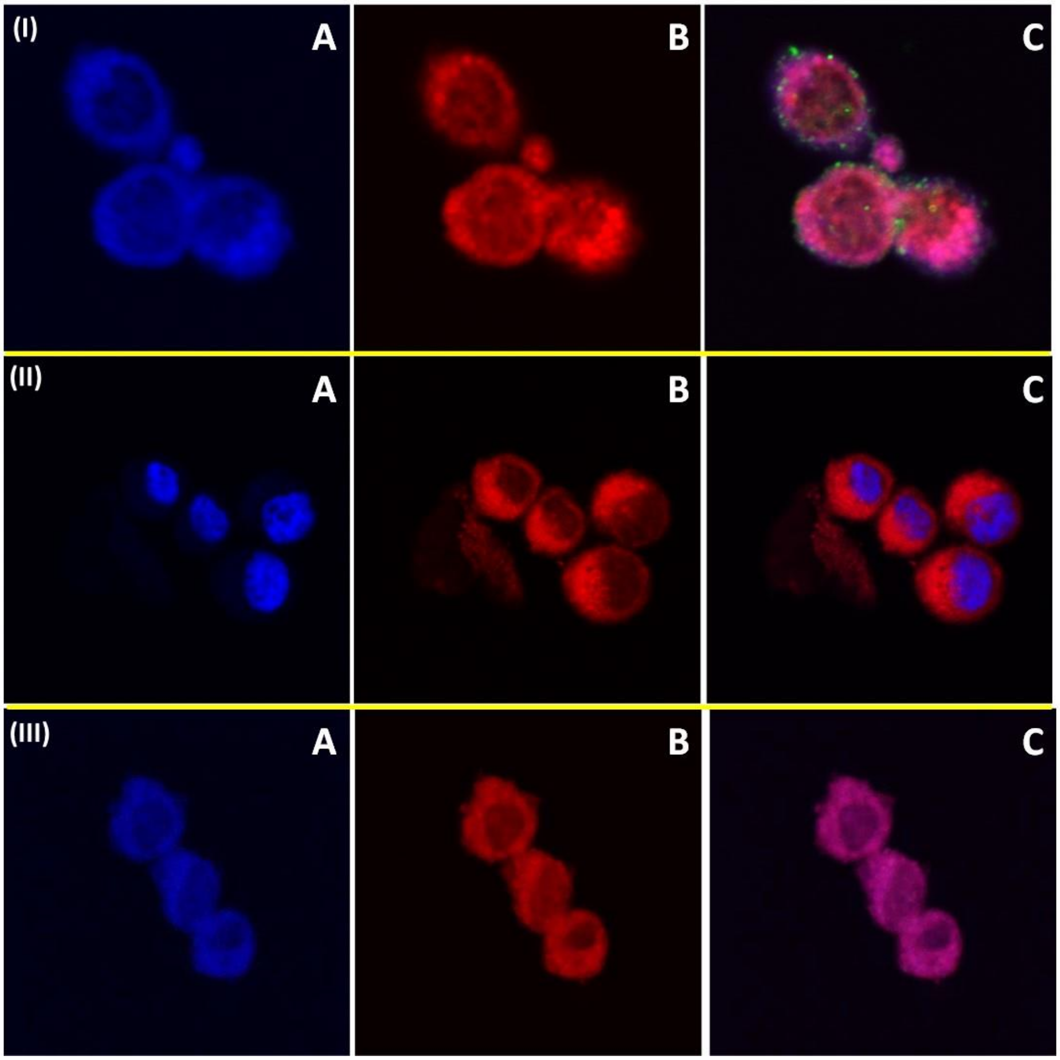

Figure 3.11. Confocal images of (I) LNCaP cells incubated with $NaDyF_4$-$NaGdF_4$ core-shell NPs tagged with anti-PSMA antibody and Alexa-488, (II) PC3 cells incubated with $NaDyF_4$-$NaGdF_4$ core-shell NPs tagged with anti-PSMA antibody and Alexa-488, and (III) LNCaP cells incubated with $NaDyF_4$-$NaGdF_4$ core-shell NPs tagged with Alexa-488 (control), taken under (A) blue channel, (B) red channel, and (C) blue, red and green channels merged. DAPI (blue channel): λ_{exc} = 358 nm, λ_{em} = 460 nm; Nile blue (red channel): λ_{exc} = 520 nm, λ_{em} = 568 nm; Alexa-488 (green channel): λ_{exc} = 495 nm, λ_{em} = 519 nm. (More images in Figure A2.6)

3.2.6 *In vivo* MRI studies in prostate cancer cells

$NaDyF_4$-$NaGdF_4$ core-shell NPs (no antibody tagged) were injected in PSMA negative PC3 tumors to visualize the enhanced permeation and retention (EPR) effect[132] in which NPs with long circulation times get trapped preferentially into tumor tissue through a leaky tumor vasculature and are then retained in the tumor bed due to reduced lymphatic drainage. Figure 3.12 shows T_2-weighted MR images of four mice (I, II, III, IV) developed with PSMA negative PC3 tumors and taken at different time points before and after injection of $NaDyF_4$-$NaGdF_4$ core-shell NPs (no antibody tagged). Mean pixel intensity was measured over the whole tumor area at different time points using ImageJ with standard pixel intensity scale lying in between 0 (= black) and 255 (= white). T_2 relaxation results in darkening of image. As observed qualitatively from the T_2-weighted images at different time points and quantitatively from the plots of change in mean pixel intensity at tumor site with time, gradual darkening at tumor site is achieved up to 2 h [Figure 3.12. I(C), III(C), IV(C)], after injection of the NPs. This is due to preferential accumulation of the NPs at the tumor sites due to EPR effect. At 24 h time point, the images brighten compared to that at 2 h. This is due to the NPs which leave the tumor site in 24 h and hence, T_2 relaxation effect is decreased dramatically. The image of mouse II in Figure 3.12 is an outlier in which the darkening effect at the tumor site is not significant after 2 h of injection. Three out of four mice show EPR effect taking place within 2 h of the injection of $NaDyF_4$-$NaGdF_4$ core-shell NPs.

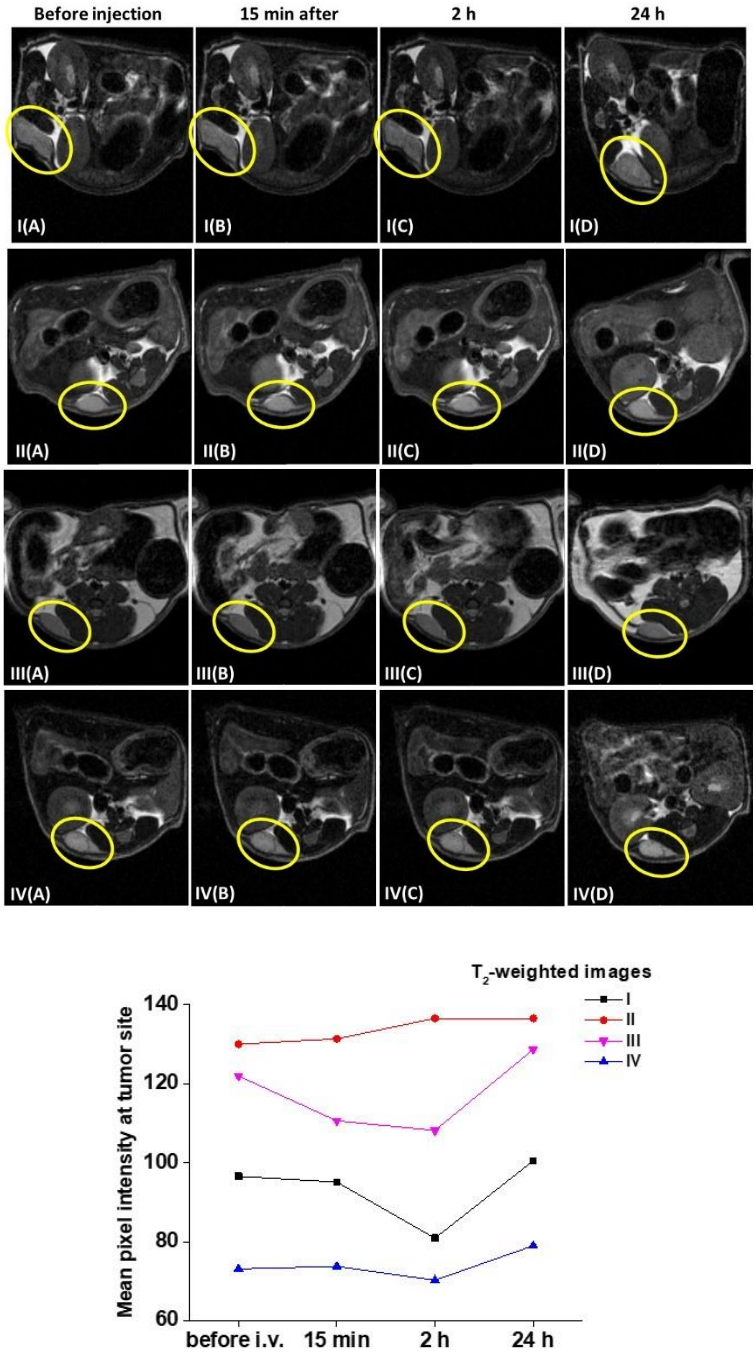

Figure 3.12. *In vivo* studies on four mice (I, II, III, IV) which developed PC3 tumors. T_2-weighted MR images were acquired (A) before (intravenous, i.v.) injection and after (B) 15 min, (C) 2 h and (D) 24 h of injection of DSPE-mPEG coated $NaDyF_4$-$NaGdF_4$ core-shell NPs (no antibody tagged) at 9.4 T. Yellow colored ellipse in MR images denotes PC3 tumor. Mean pixel intensity at tumor site at different time points are shown for respective T_1- and T_2-weighted MR images [Pixel intensity scale: 0 (black) – 255 (white)].

Active targeting studies were carried out with anti-PSMA antibody tagged $NaDyF_4$-$NaGdF_4$ core-shell NPs injected intravenously into four mice (V, VI, VII, VIII in Figure 3.13) developed with LNCaP tumors. The anti-PSMA antibody recognizes the extracellular domain of PSMA in LNCaP tumor cells. T_1- and T_2-weighted MR images were taken just before, and after 15 min and 24 h of injection of the anti-PSMA tagged NPs are shown in Figure 3.13. As evident from the plots of mean pixel intensity at tumor sites, T_2-contrast (i.e., darkening) increased in LNCaP tumor after intravenous injection of the NPs in the mice. The first 15 min after injection showed darkening compared to that before injection which is consistent with the accumulation and retention of anti-PSMA antibody tagged $NaDyF_4$-$NaGdF_4$ core-shell NPs ascribed to EPR effect. The darkening at tumor site was seen to be maximum after 24 h of injection. This is ascribed to the docking of the anti-PSMA antibody tagged NPs on the PSMA rich cell membranes of LNCaP tumors. Similarly, T_1-weighted images showed brightening at the tumor site after 24 h of injection. The image of mouse in VIII(C) is an outlier in which the brightening at tumor site is significant at 24 h time point in the T_1-weighted image while darkening is not seen in the T_2-weighted image. Passive targeting via EPR is a fast process which takes up to 2 h after injection of NPs while the active targeting is rather slow which takes about 24 h post NP injection. This provides a basis for potential targeted diagnosis of prostate cancer via MRI. It is essential to investigate the change in contrast beyond 24 h of injection to infer on the NP uptake by the reticuloendothelial system.

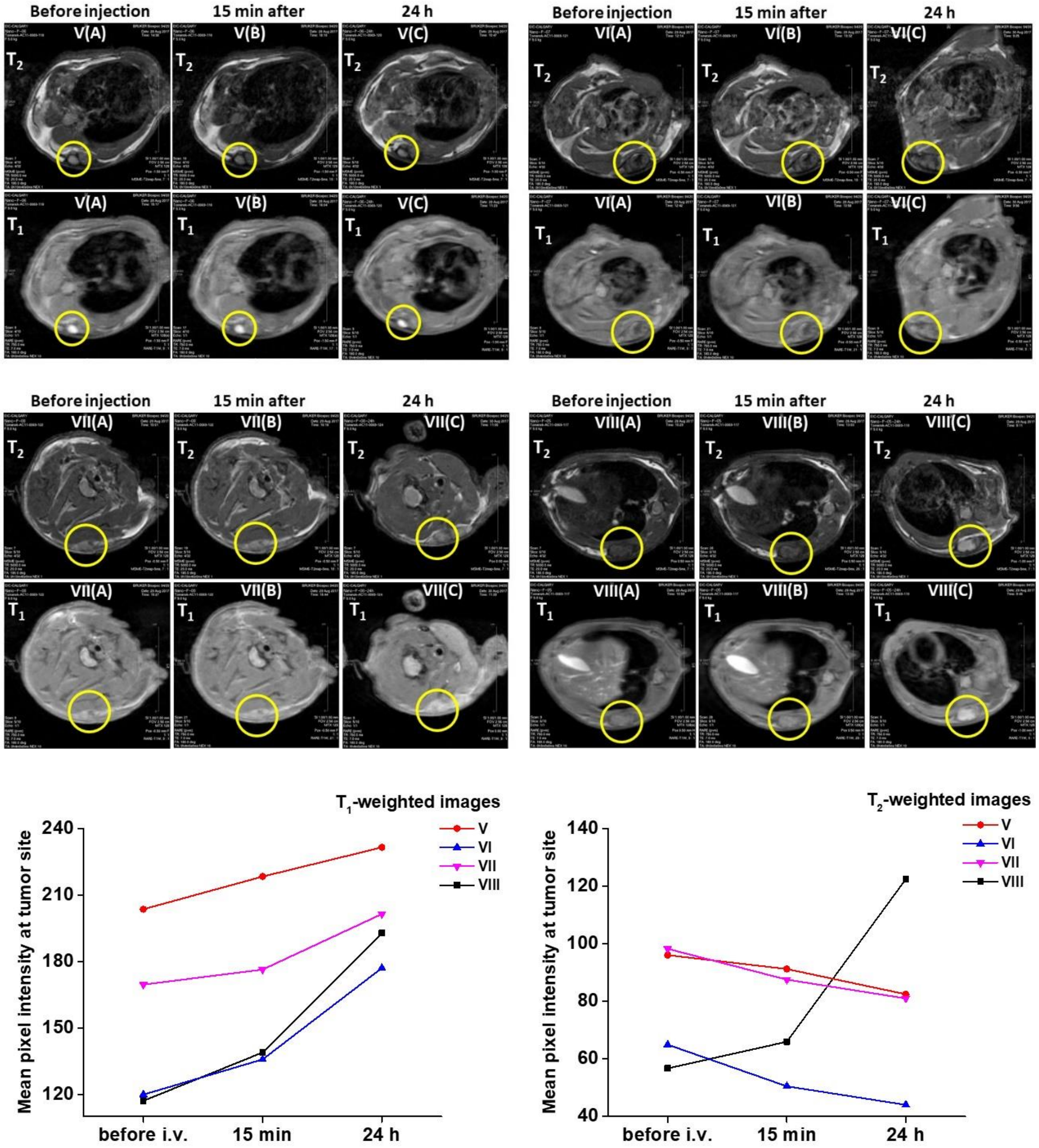

Figure 3.13. *In vivo* studies on four mice (V, VI, VII, VIII) which developed LNCaP tumors. T_1- and T_2-weighted MR images (at 9.4 T) were acquired (A) before (intravenous, i.v.) injection and after (B) 15 min, and (C) 24 h of injection of anti-PSMA antibody tagged $NaDyF_4$-$NaGdF_4$ core-shell NPs. Yellow circles denote LNCaP tumor sites. Mean pixel intensity at tumor site at different time points are shown for respective T_1- and T_2-weighted MR images [Pixel intensity scale: 0 (black) – 255 (white)].

Control experiments were carried out with control (IgG monoclonal) antibody tagged $NaDyF_4$-$NaGdF_4$ core-shell NPs injected into four mice (IX, X, XI, XII in Figure 3.14) developed with LNCaP tumors. Figure 3.14 shows T_1- and T_2-weighted images acquired before injection and after 15 min and 24 h of injection of control antibody tagged NPs. The mean pixel intensity at tumor site was measured at different time points. The tumor sites in the T_1-weighted images show brightening after 15 min of the injection of NPs. The brightening is decreased dramatically at 24 h time point indicating that the NPs accumulated in tumor after 15 min of injection consistent with the EPR effect induced by permeabilized tumor vasculature which traps the NPs in tumors. The lack of an effective lymphatic drainage in tumors also leads to NP accumulation. Similar trends in darkening at tumor sites is observed in the T_2-weighted MR images in Figure 3.14 except in mouse XII which is an outlier. At 24 h time point, the darkening is decreased compared to that at 15 min time point. Because the NPs are not tagged with anti-PSMA antibody, there is no active targeting, and the NPs are preferably taken up by liver and spleen in 24 h of injection.

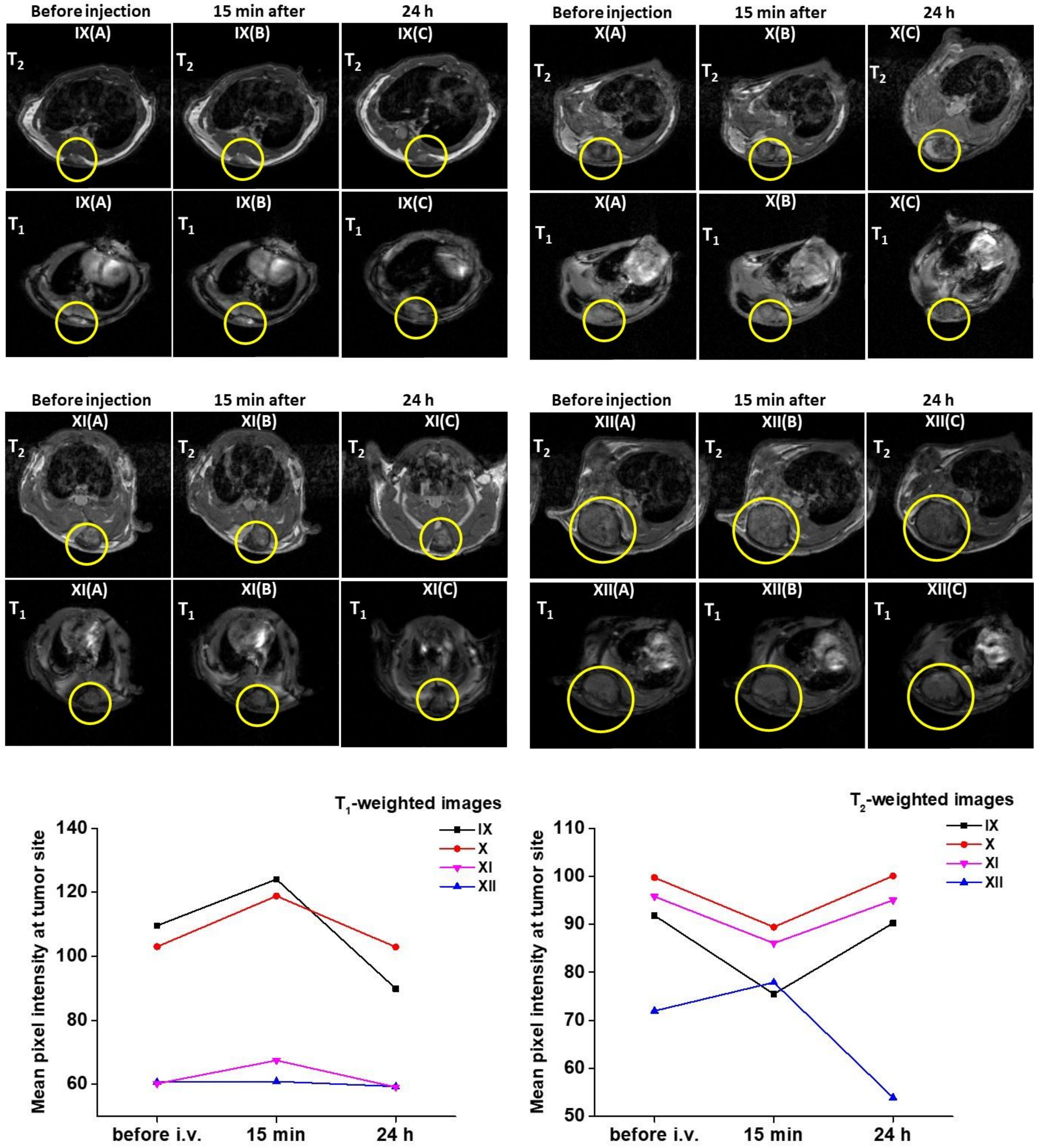

Figure 3.14. *In vivo* studies on four mice (IX, X, XI, XII) which developed LNCaP tumors. T$_1$- and T$_2$-weighted MR images (at 9.4 T) were acquired (A) before (intravenous, i.v.) injection and after (B) 15 min, and (C) 24 h of injection of monoclonal control antibody tagged NaDyF$_4$-NaGdF$_4$ core-shell NPs. Yellow circles denote LNCaP tumor sites. Mean pixel intensity at tumor site at different time points are shown for respective T$_1$- and T$_2$-weighted MR images [Pixel intensity scale: 0 (black) – 255 (white)].

3.3 Conclusions

$NaDyF_4$-$NaGdF_4$ core-shell NPs (21.8 nm, TEM) were synthesized for the first time which showed effective shortening of both T_1 and T_2 relaxation rates of water protons at clinical 3 T and a high field of 9.4 T. Comparison of the relaxivities of $NaDyF_4$-$NaGdF_4$ core-shell NPs with that of the similar sized (~20 nm) $NaDyF_4$ and $NaGdF_4$ NPs indicates a synergistic effect of relaxivity enhancement owing to the increased volume magnetization of the core-shell NP at an applied field. Phospholipid coating and further conjugation of anti-PSMA antibody with the core-shell NPs render these NPs as potential MRI-biomarkers for specific targeting of PSMA positive prostate carcinoma, as inferred from the *in vitro* studies. *In vivo* studies show consistent EPR effect of these NPs. Active targeting is slow (24 h) compared to passive targeting via EPR (2 h). It is essential to study active targeting versus passive targeting of these NPs in prostate cancer in order to design NPs for target-specific diagnosis in MRI.

3.4 Experimental Section

Chemicals. Dysprosium(III) chloride hexahydrate (99.9%), gadolinium(III) oxide (99.9%), sodium trifluoroacetate (98%), ammonium fluoride (≥ 99.99%), oleic acid (tech grade, 90%), 1-octadecene (tech grade, 90%), hexanes, 1-[3-(dimethylamino)propyl]-3-ethylcarbodiimide methiodide (EDC.MeI) and N-hydroxysulfosuccinimide sodium salt (sulfo-NHS, ≥ 98%) were purchased from Sigma Aldrich. Oleylamine (97%) was purchased from Acros, trifluoroacetic acid, dimethyl sulphoxide (99.9%), anhydrous ethanol and methanol from Caledon laboratories. 1,2-distearoyl-*sn*-glycero-3-

phosphoethanolamine-*N*-[methoxy(polyethylene glycol)-2000] (ammonium salt), 1,2-distearoyl-*sn*-glycero-3-phosphoethanolamine-*N*-[amino(polyethylene glycol)-2000] (ammonium salt), 1,2-distearoyl-*sn*-glycero-3-phosphoethanolamine-*N*-[carboxyl(polyethylene glycol)-2000] (ammonium salt) and 1,2-distearoyl-*sn*-glycero-3-phosphoethanolamine-*N*-[biotinyl(polyethylene glycol)-2000] (ammonium salt) were purchased from Avanti Polar Lipids. For simplicity, these last four compounds are referred to as DSPE-mPEG, DSPE-PEG-NH_2, DSPE-PEG-COOH and DSPE-PEG-Biotin, respectively. Anti-PSMA antibody and mouse IgG kappa monoclonal antibody (isotype control for anti-PSMA antibody) were purchased from Abcam. LNCaP and PC3 cell lines were obtained from ATCC. Streptavidin-Alexa-488 conjugate and NHS-Alexa-488 were purchased from Life Technologies.

Synthesis of sacrificial cubic (α) phase $NaGdF_4$ NPs. Gadolinium oxide (1.0 mmol) added to 10 mL of 50% trifluoroacetic acid in a three necked 100 mL round bottom flask was refluxed at 85 °C for 5 h. Excess water was evaporated at 65 °C overnight to yield gadolinium trifluoroacetate. 2 mmol sodium trifluoroacetate, 5 mL oleic acid, 5 mL oleylamine and 10 mL 1-octadecene were added to it and heated at 120 °C for 45 min under vacuum to remove residual water and oxygen. Subsequently, the solution was heated to 285 °C under argon and stirred vigorously for 45 min. The solution was cooled down to room temperature. The NPs were precipitated and washed by using 60 mL of ethanol with centrifugation at 7,000 *g* (Beckman Coulter Spinchron 15-rotor F0830) for 5 min and finally dispersed in 10 mL of hexanes.

Synthesis of hexagonal (β) phase $NaDyF_4$-$NaGdF_4$ core-shell NPs. Dysprosium(III) chloride hexahydrate (1 mmol) added to 1.5 mL oleic acid and 7.5 mL 1-octadecene in a three necked 50 mL round bottom flask was stirred under vacuum at 120 °C for 45 min. The solution was brought back to room temperature, added with 2.5 mmol sodium hydroxide and 4 mmol ammonium fluoride in 10 mL methanol and stirred for 1 h. Methanol was removed thereafter at 80 °C. The temperature was raised to 306 °C (~15 °C/min) under argon and the solution was stirred vigorously for 1 h 15 min.12 1 mL of the sacrificial cubic (α) $NaGdF_4$ NPs in 1-octadecene was injected into the solution and stirred for 15 min to form a core-shell nanostructure. The solution was cooled down to room temperature. The NPs were precipitated and washed by using 60 mL of ethanol with centrifugation at 7,000 g for 5 min and finally dispersed in 10 mL of hexanes.

Phase transfer of $NaDyF_4$-$NaGdF_4$ core-shell NPs via surface functionalization using phospholipids. $NaDyF_4$-$NaGdF_4$ core-shell NPs were dispersed in 0.4 mL toluene at 7.0 mg/mL and added with DSPE-PEGs in 0.8 mL chloroform taking appropriate weight ratio of DSPE-PEG to NP required for further steps of bioconjugation. 4 mL of DMSO was added slowly to the solution which was then incubated on a shaker for 30 minutes at room temperature. Chloroform and toluene were removed completely by vaporization under vacuum. Deionized water was added to the colloidal solution in DMSO to reach a total volume of 20 ml. DMSO was completely substituted with deionized water by three rounds of centrifugation in centrifugal filter tubes (Vivaspin Turbo 15, 100 kDa cutoff size) leaving a final volume of 1 mL of NP dispersion. The final solution was filtered through 0.45 µm glass microfiber filter.

Binding anti-PSMA antibody and streptavidin-Alexa-488 conjugate with NPs. $NaDyF_4$-$NaGdF_4$ core-shell NPs were coated with DSPE-PEG-biotin, DSPE-PEG-COOH and DSPE-mPEG and dispersed in deionized water. 350 µL of the NP solution was diluted to

1 mL in deionized water and added with 50 µL of 2 mg/mL EDC.MeI and 25 µL of 2 mg/mL sulfo-NHS. It was stirred for 30 min. 200 µL of 0.1 mg/mL anti-tau antibody (Tau-15 strain) in 10 mM phosphate buffered saline was added to the solution and stirred for 2 h at room temperature. The solution was dialyzed overnight. 100 µL of 0.1 mg/mL streptavidin-Alexa-488 conjugate was added and stirred for 0.5 h. The solution was centrifuged at 19,000 *g* for 30 min and resuspended in 1 mL of 10 mM phosphate buffered saline (pH 7.4).

Binding NHS-Alexa-488 with NPs as a basic control. $NaDyF_4$-$NaGdF_4$ core-shell NPs that were coated with DSPE-PEG-NH_2 and DSPE-mPEG were dispersed in deionized water. 10 µL of 1 mg/mL NHS-Alexa-488 in anhydrous DMF was added to 1 mL of the NP dispersion and stirred overnight in dark. The solution was centrifuged at 19,000 *g* for 30 min and the pellet was resuspended in 1 mL of 10 mM phosphate buffered saline.

Cell culture and immunolabeling of human prostate cancer cells with NPs. Human prostate cancer cells (LNCaP and PC3) were grown in tissue culture flask (T-25 cm^2) with RPMI-1640 growth medium supplemented with 10% fetal bovine serum (FBS) for 48 h. The cells were detached at 70% confluency using trypsin-EDTA and Dulbecco’s Phosphate Buffered Saline (DPBS) and subcultured in a T-25 cm^2. The cells were allowed to grow for 48 h and then washed multiple times with phosphate buffered saline (PBS). The cells were then incubated with anti-PSMA antibody conjugated with $NaDyF_4$-$NaGdF_4$ core-shell NPs at 4 °C for 1 h. After incubation the cells were washed with PBS. The cells were fixed on glass slides using poly-L-lysine. The nucleus of the cells was stained with 4',6-diamidino-2-pheylindole (DAPI) before confocal microscopy by using a Leica compound epifluorescence microscope.

In vivo mice MRI experiments (by Dr. Barbara Blasiak and Dr. Boguslaw Tomanek, Experimental Imaging Center, University of Calgary). Tumor Induction: (LNCaP and PC3) Cells were harvested using EDTA, counted and suspended ($5x10^6$ in 25 μL of PBS). These were prepared under sterile conditions at the laboratory and the syringes were inserted in autoclaved double bag. For cell injections, each mouse (female, NuNu BALB/cByJ, 6-8 weeks of age) was physically restrained and LNCaP cells (or, PC3 cells for negative control experiments) in a 0.1 mL suspension were subcutaneously injected into the left and right flanks.

Animals were monitored daily for any sign of distress and staples were removed one week after the injection. The weight and tumor size measurements were done three times per week. Once tumors reached approximately 5-10 mm in diameter (5 to 8 weeks following the injection), animals were selected for MRI.

250 μL of the contrast agent (batches of NPs tagged with anti-PSMA antibody, and monoclonal control antibody and NPs without any antibody) was injected into the tail vein (vehicle, 0.9 % saline). Anesthesia was induced using 4% isoflurane and was maintained with 2.7% isoflurane in 69% N_2O and 30% O_2. MR images were acquired 15 min, 30 min, 2 h, and 24 h after the administration of NPs. Post MRI examination, the animals were euthanized with 120 mg/kg (intravenous) pentobarbital. A 9.4 T pre-clinical MRI system (Biospec, Bruker, Germany) was used. The data acquisition was triggered with respiration to reduce possible motion artifacts. For axial multi-echo spin-echo (MESE) T_2-weighted tumor MRI and a transit/receive birdcage radiofrequency coil (3 cm diameter × 2.5 cm long) were used. The pulse parameters were: slice thickness 1 mm, field of view (FOV) = 3 × 3 cm, TR 5 s, 16 echoes, 10 ms apart, 128 frequency and 128 read encoding steps. The

data were fitted to the single exponent (Marevisi, NRC, Canada) to calculate T_2 values. For quantitative analysis, mean pixel intensities at the whole tumor area were measured in the MR images. The T_1 and T_2 relaxation times obtained at the tumor area in the T_1- and T_2-weighted MR images were all normalized with those of the muscle signals.

***Characterization*.** X-ray Diffraction (XRD) patterns were collected using a Rigaku Miniflex diffractometer with Cr Kα radiation (λ = 0.2290 nm, 30 kV, 15 mA) with a scan step size of 0.05 °C (2θ). About 10 drops of the NP dispersion in hexane were added onto an indented zero-background sample holder and dried to get the diffraction patterns.

Transmission electron microscopy (TEM) images were acquired using a JEOL JEM-1400 microscope operating at 80 kV. The NP dispersion in hexane was drop-cast onto a formvar carbon film supported on a 300 mesh copper grid (3 mm in diameter) and allowed to dry in air at room temperature, before imaging. The size distribution was obtained from averaging a minimum of 300 NPs. Energy-dispersive X-ray spectroscopy (EDX) measurements were done with an Hitachi HF-3300V Scanning Transmission Electron Holography Microscope (STEHM) operated at 200 kV and equipped with EDX (Bruker) detector. The NP dispersion in hexane was drop-cast on a lacey carbon grid, dried in vacuum and cleaned in a UV chamber.

Dynamic light scattering (DLS) measurements were done using Brookhaven Zeta PALS instrument with a 90Plus/BI-MAS Multi Angle Particle Sizing option, equipped with a 15 mW solid-state laser (658 nm). All data were obtained at a single scattering angle (90°) and averaged over ten scattered intensity weighted scans. Dust filter (30 μm) in the Zeta PALS software was ON. Zeta-potentials were determined using Zeta-PALS zeta-potential analyzer from Brookhaven Instruments Corp. equipped with a 15 mW solid-state laser (658 nm). Three runs of 30 cycles each were performed to determine the standard deviation of the measured zeta-potential values

Inductively coupled plasma mass spectroscopy (ICP-MS) analysis was carried out using a Thermo X-Series II (X7) quadrupole ICP-MS to determine the Dy^{3+} and Gd^{3+} ion concentration in the NP stock solution. The aqueous dispersion of NPs were digested in concentrated nitric acid at 135 ^{o}C in sealed Teflon vials for 3 days and diluted with ultrapure water before analysis. Calibration was done by analyzing serial dilutions of a mixed element synthetic standard containing a known amount of dysprosium and gadolinium. Each sample, standard and blank, were spiked with indium (to a concentration of ~7 ppb) as the internal standard to correct for signal drift and matrix effects. Accuracy was confirmed by analysis of a standard reference material.

The T_1 and T_2 relaxation measurements were performed at 9.4 T with a 21-cm magnet (Magnex, UK) and a Bruker console (Bruker, Germany) (by Dr. Barbara Blasiak and Dr. Boguslaw Tomanek, University of Calgary). A transmit/receive radio frequency (RF) volume birdcage coil was applied to excite protons and to obtain MR signal. A single-slice multi-echo pulse sequence was used for T_2 measurements with the following parameters: repetition time (TR) = 5 s, matrix size 128 × 128, field of view (FOV) 3 × 3 cm^2, slice thickness 2 mm, 128 echoes 4 ms apart. The T_2 relaxation time was calculated using a single exponential fitting of the echo train (Marevisi, NRC, Canada). For T_1 measurements the TRUE FISP method was used with the following parameters: slice thickness 3 mm, FOV 3 × 3 cm^2, matrix size 128 × 128, TR = 3 ms, TE = 1.5 ms, 60 frames × 4 segments, segment time 192 ms.

The T_1 and T_2 measurements at the clinically relevant magnetic field of 3 T were performed using the whole-body 3 T MRI system (Trio, Siemens, Germany) by Dr. Peter Latta, Central European Institute of Technology, Brno, Czech Republic. A standard head RF coil was used for all experiments. For T_1 measurements inversion recovery (IR) FLASH pulse sequence was used with TR = 10 sec, echo time (TE) = 2.9 s, inversion recovery (IR) times: 30, 60, 120, 240, 480, 960, 1920, 4,000 ms; FOV 10×10 cm^2; slice thickness 2 mm, matrix size 128×128. The T_2 measurements were performed using multi echo pulse sequence with TR = 5 sec, 32 echoes with 15 ms increments: TE = 15, 30, 45, to 480 ms. The relaxation times were calculated using single exponential fitting of the data (MATLAB "lsqcurvefit").

The rates of measured relaxation times were plotted as a function of the concentration of CA. The r_1 and r_2 relaxivities were obtained from the slope of the resulting graphs plotted in OriginPro 2015 (OriginLab, Northampton, MA, version b9.2.272) using the equation, $\boldsymbol{\frac{1}{T_i} = \frac{1}{T_i^0} + r_i[Ln^{3+}];\ i = 1, 2}$, where $[Ln^{3+}]$ is the concentration of paramagnetic lanthanide ions (Dy^{3+} or Gd^{3+}) in an NP solution obtained from ICP-MS, T_i^0 denote the relaxation times of the water protons in absence of the paramagnetic NPs.

Magnetic measurements were carried out in a Quantum Design MPMS XL-7S system (by Dr. Abhinandan Banerjee and Dr. Simon Trudel, University of Calgary). Weighed powdered samples were loaded into a gelatin capsule which was sealed with Kapton tape before being inserted into a clear diamagnetic plastic straw. Isothermal magnetization as a function of field strength measurements were carried out at 300 K by cycling the applied magnetic field between -7 T and +7 T.

Chapter 4. $NaDyF_4$-$NaGdF_4$ Core-Shell Nanoparticles for *in vitro* Targeting of Tau Following Mild Traumatic Brain Injury

4.1 Introduction

Traumatic brain injury (TBI) occurs when an external force transmitted to the head or the body results in impaired cognitive abilities and/or neurological dysfunction.[133] It is a major global health problem across all age groups, with most incidents reported in professions associated with frequent head injuries such as sports and military activities.[134] TBI patients suffer from neurological deficits, short and long term brain damage, cognitive, behavioral and emotional impairments, all of which depend on the severity of injury.[135] About 70% of the TBIs fall under the category of mild TBIs, often referred to as concussions, in which the loss of consciousness < 30 min and post-traumatic amnesia < 24 h, with transient changes in neurological function.[136] The diagnosis is complicated in case of mild TBIs because these TBIs do not appear in standard computed tomography (CT) scans and magnetic resonance imaging (MRI).[136] The current diagnostic practices involve studying the behavioral patterns of patients only. Although many patients recover fully from mild TBI, others go on to develop post-concussive syndrome such as physical symptoms (headache, dizziness, fatigue), cognitive disturbances (impaired concentration and memory), or emotional problems (depression and anxiety) and psychiatric illness.[137] Further, the risk of neurodegeneration and death increases with occurrence of consecutive concussions after the first. These facts mandate the need for a reliable diagnostic tool to identify mild TBI to avoid any post-concussion syndrome and recognize potential therapy.

Tau is a group of neuronal proteins in the central neural system that binds to microtubules and promotes their assembly and stabilization in order to form the cytoskeleton.[138] It plays a key role in the regulation of neurite extension and axonal transport. The proper functioning of tau is modulated by its site-specific phosphorylation.[139] Inappropriate phosphorylation of tau leads to tau dysfunction which is observed in pathological states resulting in to loss of cell viability. Such condition has been reported as accumulation of neurofibrillary tangles due to hyperphosphorylation of tau in patients suffering from mild TBI and neurodegeneration.[140-142]

The current chapter deals with optical visualization of intraneuronal tau following repetitive mild TBI, using $NaDyF_4$-$NaGdF_4$ core-shell NPs (which are potential MRI CAs as shown in Chapter 3) tagged with single domain anti-tau antibodies and Alexa-488 dye (fluorescent probe in cell studies). A single domain antibody (sdAb), derived from the variable domain of the heavy chain of camelid antibody, was chosen for the bioconjugation with NPs and *in vitro* experiments due to its small size, high antigen specificity and affinity (kinetic k_{on} and k_{off} are 10^5 to 10^6 M^{-1} s^{-1} and 10^{-2} to 10^{-4} s^{-1}, respectively), low immune response in humans, and remarkable stability at high temperature (several weeks at 37 ^{o}C and some sdAbs resist above 90 ^{o}C) and concentration (1–10 mg of sdAbs per mL of standard phosphate or tris buffers), compared to conventional antibodies.[143]

In this work, oleate-capped $NaDyF_4$-$NaGdF_4$ core-shell NPs were synthesized in a high boiling solvent mixture of oleic acid and octadecene. The as-synthesized NPs dispersed in hexanes were transferred to deionized water after coating them with phospholipids bearing PEGs and functional end groups for bioconjugation. Commercial tau was hyperphosphorylated using glycogen synthase kinase 3β (GSK-3β) to yield hyperphosphorylated tau. Two different anti-tau sdAbs, namely, Tau-15 and Tau-81 (same sizes, 138 amino acids, but slightly different isoelectric points, pI, 6.941 and 5.433, respectively) were obtained from NRC, Ottawa which were assessed for their affinities with commercial tau and the as-synthesized hyperphosphorylated tau. Based on the surface plasmon resonance studies on the affinities of the sdAbs, Tau-15 (anti-tau sdAb) was chosen to conjugate with the NPs for *in vitro* studies. The amine groups, from lysine residues, on the antibodies were conjugated to carboxylate end groups on the phospholipids that coat the core-shell NPs via amide bond formation initiated by the EDC/NHS coupling reaction. Alexa-488, which had a streptavidin group tagged to it, was bound to biotin groups on phospholipids around NPs via biotin-streptavidin interaction. *In vitro* studies revealed that the NP-sdAb-Alexa conjugates cross the neuronal membrane and bind to intracellular tau in the hippocampal neuronal cultures.

4.2 Results and Discussion

4.2.1 Synthesis of core-shell NPs and Characterization

To synthesize $NaDyF_4$-$NaGdF_4$ core-shell NPs, $NaDyF_4$ core NPs were prepared in a dual solvent mixture of oleic acid and 1-octadecene at a high temperature of 306 ^{o}C. As elaborated in Chapter 3, sacrificial $NaGdF_4$ NPs were injected to form a shell around the already formed $NaDyF_4$ NPs in the reaction mixture. The as-synthesized core-shell NPs were dispersed in hexane and transferred to water by coating them with functionalized phospholipids following the route of DMSO dual solvent exchange.[76] The phospholipid functional end group (DSPE-PEG-X where X = –COOH, biotin) was subsequently used for further bioconjugation, e.g., –COOH groups were employed to form amide bond with

–NH_2 groups on antibody via EDC-NHS coupling, and biotin was used to bind streptavidin-Alexa-488 conjugate.

X-ray diffraction (XRD) patterns shown in Figure 4.1 confirm the hexagonal phase of $NaDyF_4$-$NaGdF_4$ core-shell NPs as they are matched with the standard patterns of the hexagonal phase of $NaDyF_4$ (PDF#00-027-0687). The broad peak centered at about 28° (2θ) denotes the presence of oleic acid/oleates around the NPs. A slight shifting of the XRD peaks of the NPs is observed compared to the standard patterns due to the compressive strain arising due to the mismatch of ionic sizes of lanthanide ions in the core and the shell – larger sized Gd^{3+} ions (ionic radius of 1.193 Å) in $NaGdF_4$ forming a shell over the core $NaDyF_4$ containing smaller Dy^{3+} ions (ionic radius of 1.167 Å).[61]

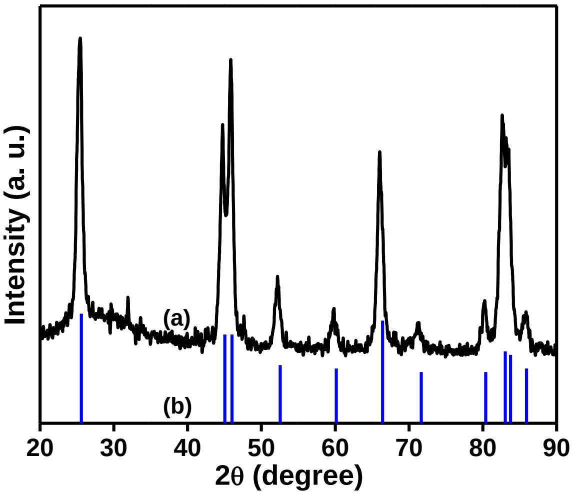

Figure 4.1. XRD patterns of (a) $NaDyF_4$-$NaGdF_4$ core-shell NPs indexed with (b) their corresponding standard patterns (PDF# 00-027-0687).

Transmission electron microscopy (TEM) images of the NPs depicted in Figure 4.2 show a fairly uniform and monodisperse size distribution before and after the formation of the $NaGdF_4$ shell around the core $NaDyF_4$ NPs. The particle diameters of the core $NaDyF_4$ and $NaDyF_4$-$NaGdF_4$ core-shell NPs in the TEM images were determined to be 11.8 ± 2.3 and 12.5 ± 1.9 nm.

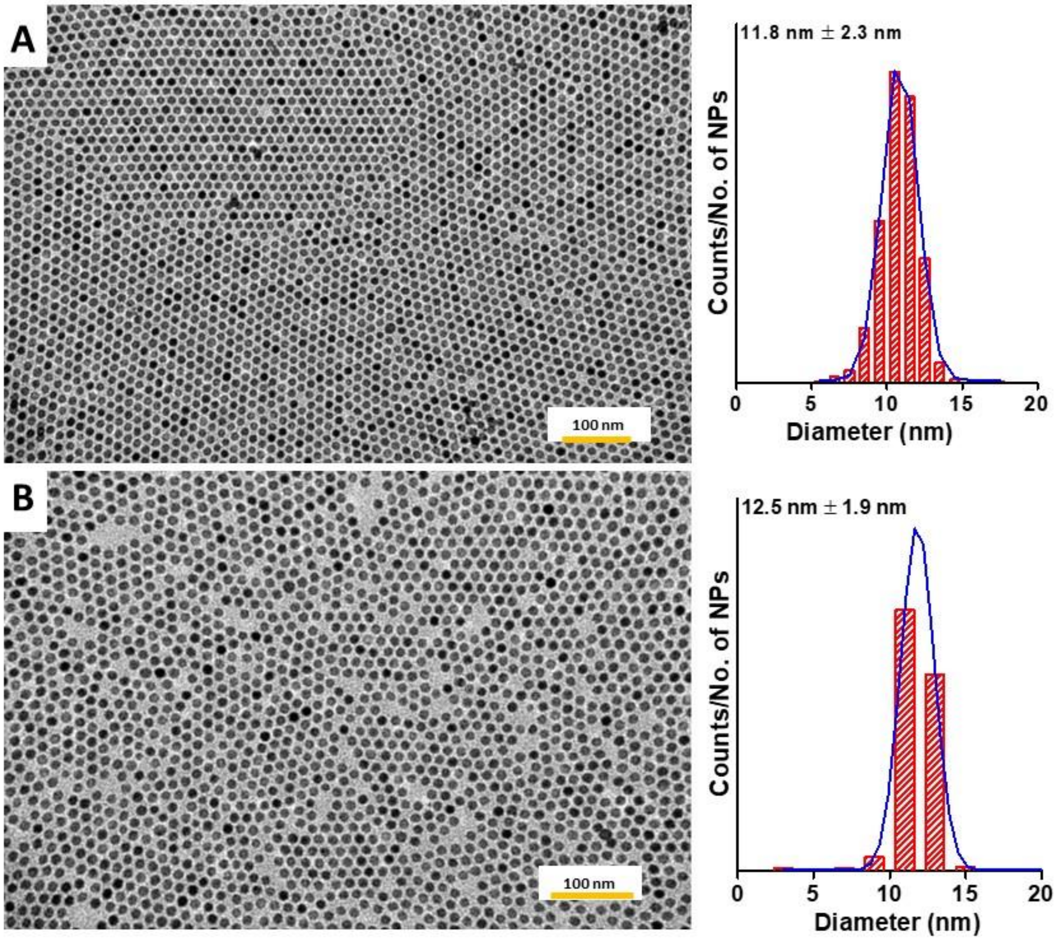

Figure 4.2. TEM images of the (A) core $NaDyF_4$ NPs prior to injection of sacrificial $NaGdF_4$ NPs and (B) $NaDyF_4$-$NaGdF_4$ core-shell NPs with the corresponding histograms showing particle size distribution. Yellow bar = 100 nm.

4.2.2 Synthesis of hyperphosphorylated tau and surface plasmon resonance studies

Commercially available tau protein (441 amino acids, 2N4R isoform, 45.8 kDa) was phosphorylated using glycogen synthase kinase 3β (GSK-3β) following the protocol by Rankin *et al*.[140] Figure 4.3 shows the 10% SDS-PAGE analysis in which phosphorylated tau protein band has its characteristic upward band shift in mobility (Lane C) when compared to the non-phosphorylated tau 441 (Lane B). The latter migrated approximately as a 70 kDa protein. As reported by Rankin *et al.*,[140] the band shift is attributed to the SDS-resistant conformational changes brought about by phosphorylation rather than a molecular weight increase due to added phosphates.

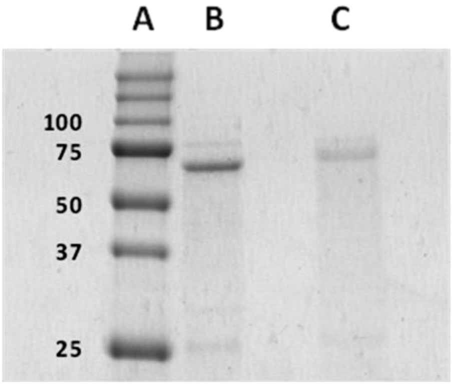

Figure 4.3. Coomassie stained 10% SDS-PAGE analysis. Lane A: Precision plus protein all blue standards (molecular weight markers), Lane B: non-phosphorylated tau 441 protein and Lane C: Phosphorylated tau.

Two different single domain anti-tau antibodies, namely, Tau-15 (136 amino acids, 15,235 Da, pI = 6.941) and Tau-81 (136 amino acids, 15,296 Da, pI = 5.433), were obtained from NRC, Ottawa. Both were tested for their affinities towards commercially available human tau and the as-synthesized hyperphosphorylated tau via surface plasmon resonance as shown in Figure 4.4A. The monomeric Tau-15 and Tau-81 sdAbs were injected over the tau surface at a concentration of 500 nM for the test run and concentrations ranging from 20–6,000 nM. Tau-15 sdAbs showed an affinity of 0.699 µM against tau and 0.622 µM towards hyperphosphorylated tau. Tau-81 sdAbs showed an affinity of 0.82µM to tau and 0.745 µM towards hyperphosphorylated tau. From the size exclusion chromatography profiles (Figure 4.4B), a minor population of aggregated Tau-81 sdAbs (less than 10%) exists. Based on the higher affinity towards tau and hyperphosphorylated tau and no definite aggregation, Tau-15 sdAb was chosen to conjugate with phospholipid functionalized NPs.

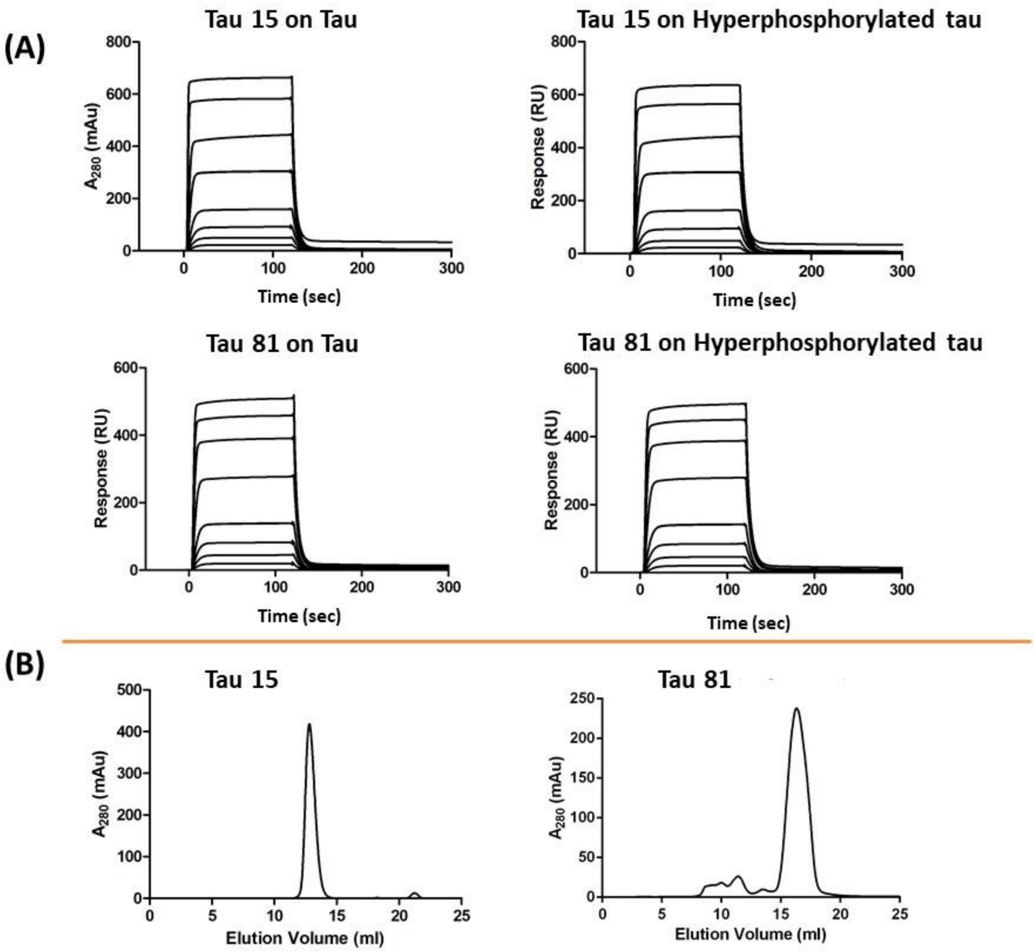

Figure 4.4. (A) Surface plasmon resonance analysis of sdAbs Tau-15 and Tau-81 binding to tau and hyperphosphorylated tau. (B) Superdex 75$^{\text{TM}}$ size exclusion chromatography profiles of sdAbs Tau-15 and Tau-81. The sdAbs were injected at concentrations of 20 µM.

4.2.3 *In vitro* studies on targeting tau

For *in vitro* targeting of tau, three batches of NP-sbAb-Alexa conjugates were tested which had an average of 4, 12 and 22 sdAbs bound *per* NP. To determine the concentration of antibodies and Ln^{3+} ions in a given NP-antibody conjugate sample, UV absorption spectroscopy and Inductively Coupled Plasma Mass Spectrometry (ICP-MS) were used, respectively, as detailed in the Experimental Section. Number of antibodies attached *per* NP was found out based on the Ln^{3+} concentration obtained from the ICP-MS analysis, assuming that all the antibodies in a given sample solution have attached to all the NPs present in that batch.

The NP-sdAb-Alexa conjugates in phosphate buffered saline were incubated in live hippocampal neuronal-glial co-cultures at the NeuroArm, University of Calgary. The conjugates with 4:1 ratio of sdAb to NP were only able to specifically bind to intracellular tau as demonstrated by specific neurite labelling shown in Figure 4.5A. Figure 4.5B reveals that NP-Alexa488 conjugate, used as a control, failed to label any distinct neuronal structure which validates the specificity of NP-sdAb-Alexa conjugate to bind to tau. The presence of the anti-tau sdAb on the NPs is essential for specific intracellular tau labeling because incubation of cell culture with the NP-Alexa488 conjugate (no antibody attached) alone resulted in a scattered non-specific background without any intracellular signal.

In Figure 4.6, dynamic light scattering results of the three batches of NP-sdAb conjugates with sdAbs:NP ratios of 4:1, 12:1, and 22:1 yielded similar hydrodynamic diameters, 35.5 ± 1.2 nm, 33.8 ± 1.4 nm and 34.6 ± 1.1 nm, respectively. No specific binding was observed with ratios 12:1 and 22:1 sdAb:NP which implies that crowding of sdAbs around NP would potentially obscure the (tau) receptor binding. Further, zeta potential of the conjugate with sdAb:NP ratio of 4:1 was -5 mV while 12:1 and 22:1 were -20 and -35 mV, respectively; the latter two values differing much from the isoelectric point ‘pI’ of the anti-tau sdAb. Highly negative zeta potential values on the NP-sdAb conjugates would eventually bind to available cationic sites on the macrophage surface and be recognized by scavenger receptors, thereby facilitating uptake and phagocytosis. The conjugate with 4:1 ratio proved to be favourable to transport the NP-sdAb conjugate across the membrane.

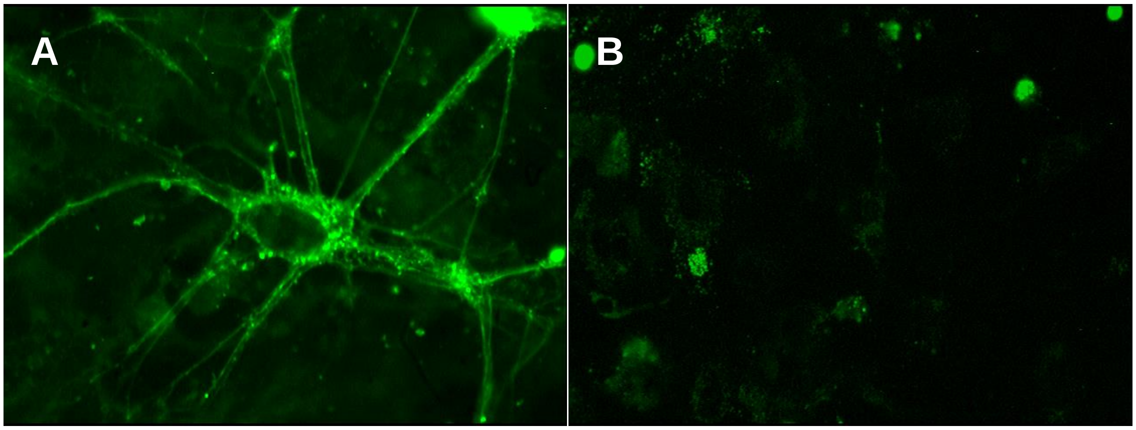

Figure 4.5. Live hippocampal neuron-glia co-cultures incubated with (A) anti-tau sdAb-NP-Alexa-488 which clearly labels neuronal tau protein (40X magnification), and (B) NP-Alexa-488 (control) which does not bind to tau (scattered green signal is due to non-specific binding; 20X magnification).

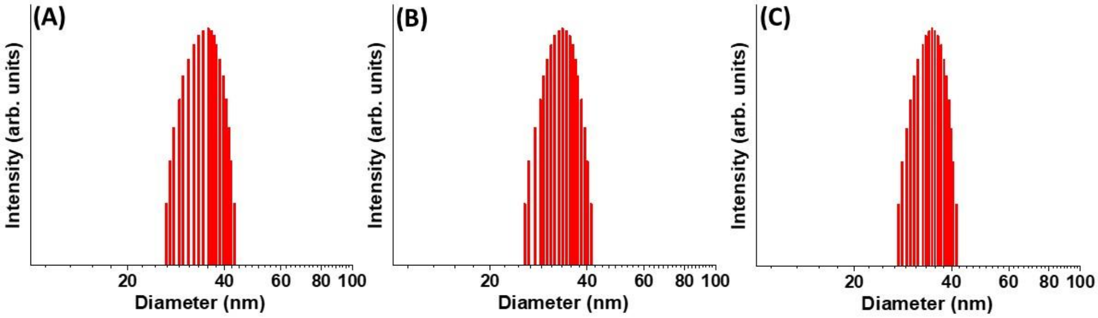

Figure 4.6. DLS results of NP-sdAb conjugates with different ratios of sdAbs:NP (A) 4:1, (B) 12:1, and (C) 22:1.

4.3 Conclusions

$NaDyF_4$-$NaGdF_4$ core-shell NPs tagged with anti-tau sdAb serve as potential MRI contrast agents and biomarkers to track intraneuronal tau in live hippocampal cell culture. Designing an antibody specifically against hyperphosphorylated tau is important to diagnose mild TBI as the current Tau-15 and Tau-81 anti-tau sdAbs are able to bind both commercial human tau and hyperphosphorylated tau. *In vivo* MRI could play a crucial role in detecting mild TBI by tracking the NP-sdAb conjugates targeting tau and hyperphosphorylated tau. It is essential to investigate the possible reasons behind the crossing of the NP-sbAb-Alexa-488 conjugates (4:1 ratio of sdAb:NP) through neuronal membrane (and possibly BBB) which was not observed with 12:1 or 22:1 ratio. The NP-sbAb conjugate ratios in optimal range would be accumulated in brain *in vivo* to bind their receptors while other ratios would not. A thorough study on elimination of these sdAb-NP conjugates from brain is also necessary because it can be speculated that these conjugates could be engulfed by microglia, the resident macrophages of brain, and undergo phagocytosis or could be taken up by the invading monocytes from blood stream to clear through organs like liver and spleen.

4.4 Experimental section

Chemicals. Dysprosium(III) chloride hexahydrate (99.9%), gadolinium(III) oxide (99.9%), sodium trifluoroacetate (98%), ammonium fluoride (≥ 99.99%), oleic acid (tech grade, 90%), 1-octadecene (tech grade, 90%), hexane, 1-[3-(dimethylamino)propyl]-3-ethylcarbodiimide methiodide (EDC.MeI) and *N*-hydroxysulfosuccinimide sodium salt (sulfo-NHS, ≥ 98%) were purchased from Sigma Aldrich. Oleylamine (97%) was purchased from Acros, trifluoroacetic acid, dimethyl sulphoxide (99.9%), anhydrous ethanol and methanol from Caledon laboratories. 1,2-distearoyl-*sn*-glycero-3-phosphoethanolamine-*N*-[methoxy(polyethylene glycol)-2000] (ammonium salt), 1,2-distearoyl-*sn*-glycero-3-phosphoethanolamine-*N*-[amino(polyethylene glycol)-2000] (ammonium salt), 1,2-distearoyl-*sn*-glycero-3-phosphoethanolamine-*N*-[carboxyl(polyethylene glycol)-2000] (ammonium salt) and 1,2-distearoyl-*sn*-glycero-3-phosphoethanolamine-*N*-[biotinyl(polyethylene glycol)-2000] (ammonium salt) were purchased from Avanti Polar Lipids. For simplicity, these last four compounds are referred to as DSPE-mPEG, DSPE-PEG-NH_2, DSPE-PEG-COOH and DSPE-PEG-Biotin, respectively. Anti-tau antibodies (Tau-15 and Tau-81) and A20.1 antibody were obtained from National Research Council (Human Health Therapeutics), Ottawa. Anti-PSMA antibody was purchased from Abcam. Streptavidin-Alexa-488 conjugate and NHS-Alexa-488 were purchased from Life Technologies. HEPES (≥ 99.5%), EGTA (≥ 97%), $MgCl_2$ (anhydrous, ≥ 98%), adenosine 5′-triphosphate disodium salt hydrate (ATP, 99%), recombinant glycogen synthase kinase (GSK-3β), recombinant human tau-441 (2N4R variant) were purchased from Sigma Aldrich. SDS-PAGE markers are Precision Plus Protein Standards from Bio-Rad. All chemicals were used as received.

Synthesis of cubic (α) phase $NaGdF_4$ NPs. Gadolinium oxide (1.0 mmol) added to 10 mL of 50% trifluoroacetic acid in a three necked 100 mL round bottom flask was refluxed at 85 °C for 5 h. Excess water was evaporated at 65 °C overnight to yield gadolinium trifluoroacetate. 5 mL of oleic acid, 5 mL of oleylamine and 10 mL of 1-octadecene were added to it and heated at 120 °C for 45 min under vacuum to remove residual water and oxygen. Subsequently, the solution was heated to 285 °C under argon and stirred vigorously for 45 min. The solution was cooled down to room temperature. The NPs were precipitated and washed by using 60 mL of ethanol with centrifugation at 7,000 *g* (Beckman Coulter Spinchron 15-rotor F0830) for 5 min and finally dispersed in 10 mL of hexane.

Synthesis of hexagonal (β) phase $NaDyF_4$-$NaGdF_4$ core-shell NPs. Dysprosium(III) chloride hexahydrate (1 mmol) added to 1.5 mL oleic acid and 7.5 mL 1-octadecene in a three necked 50 mL round bottom flask was stirred under vacuum at 120 °C for 45 min. The solution was brought back to room temperature, added with 2.5 mmol sodium hydroxide and 4 mmol ammonium fluoride in 10 mL methanol and stirred for 1 h. Methanol was removed thereafter at 80 °C. The temperature was raised to 306 °C (~15 °C/min) under argon and the solution was stirred vigorously for 1 h 15 min. 1 mL of the sacrificial cubic (α) $NaGdF_4$ NPs in 1-octadecene was injected into the solution and stirred for 15 min to form a core-shell nanostructure. The solution was cooled down to room temperature. The NPs were precipitated and washed by using 60 mL of ethanol with centrifugation at 7,000 *g* for 5 min and finally dispersed in 10 mL of hexane.

Phase transfer of $NaDyF_4$-$NaGdF_4$ core-shell NPs via surface functionalization using phospholipids.[76] $NaDyF_4$-$NaGdF_4$ core-shell NPs were dispersed in 0.4 mL toluene at 7.0 mg/mL and added with DSPE-PEGs in 0.8 mL chloroform taking appropriate weight ratio of DSPE-PEG to NP required for further steps of bioconjugation. 4 mL of DMSO was added slowly to the solution which was then incubated on a shaker for 30 minutes at room temperature. Chloroform and toluene were removed completely by vaporization under vacuum. Deionized water was added to the colloidal solution in DMSO to reach a total volume of 20 ml. DMSO was completely substituted with deionized water by three rounds of centrifugation in centrifugal filter tubes (Vivaspin Turbo 15, 100 kDa cutoff size) leaving a final volume of 1 mL of NP dispersion. The final solution was filtered through 0.45 µm glass microfiber filter.

Binding anti-tau antibody and streptavidin-Alexa-488 conjugate with NPs. $NaDyF_4$-$NaGdF_4$ core-shell NPs were coated with DSPE-PEG-biotin, DSPE-PEG-COOH and DSPE-mPEG and dispersed in deionized water. 350 µL of the NP solution was diluted to 1 mL in deionized water and added with 50 µL of 2 mg/mL EDC.MeI and 25 µL of 2 mg/mL sulfo-NHS. It was stirred for 30 min. 200 µL of 0.1 mg/mL anti-tau antibody (Tau-15 strain) in 10 mM phosphate buffered saline was added to the solution and stirred for 2 h at room temperature. The solution was dialyzed overnight. 100 µL of 0.1 mg/mL streptavidin-Alexa-488 conjugate was added and stirred for 0.5 h. The solution was centrifuged at 19,000 *g* for 30 min and resuspended in 10 mM phosphate buffered saline (pH 7.4). This procedure was also followed to bind the control antibodies, A20.1 for tau experiments and anti-PSMA antibody for immunolabelling of LNCaP cells.

Binding NHS-Alexa-488 with NPs as a basic control. $NaDyF_4$-$NaGdF_4$ core-shell NPs that were coated with DSPE-PEG-NH_2 and DSPE-mPEG were dispersed in deionized water. 10 µL of 1 mg/mL NHS-Alexa-488 in anhydrous DMF was added to 1 mL of the NP dispersion and stirred overnight in dark. The solution was centrifuged at 19,000 *g* for 30 min and the pellet was resuspended in 10 mM phosphate buffered saline.

Hyperphosphorylation of tau.[140] 20 µg of tau at a final concentration of 16 µM (20 µg tau/25 µL reaction) was incubated with 0.018 U GSK-3β/pmol of tau in phosphorylation buffer containing 40 mM HEPES, pH 7.64, 5 mM EGTA, 3 mM $MgCl_2$, and 2 mM ATP for 20 h at 30 °C. 1 unit of GSK-3β is defined as the amount of enzyme that will transfer 1 pmol phosphate from ATP to phosphatase inhibitor 2 per min at pH 7.5 at 30 °C. 1 µg of tau protein from the reaction mixture was analyzed by 10% SDS- polyacrylamide gel electrophoresis.

Surface Plasmon Resonance (by Dr. Sanju Llama, Dr. Garnette Sutherland and Dr. Michael Colicos, University of Calgary). Approximately 1,000 resonance units (RUs) of human tau-441 (Sigma-Aldrich Cat.#T0576-50UG; Lot#SLBH2359V) and as-synthesized hyperphosphorylated tau-441 were immobilized in 10 mM acetate buffer, pH 5.0 on a CM5 Series S sensor chip using an amine coupling kit (GE Healthcare Cat.#BR-1003-99 and BR-1000-50). Monomeric sdAbs were injected at a flow rate of 20 µL/min for 2 mins, with a dissociation time of 6 mins, over the immobilized tau surface at a concentration ranging from 20–6,000 nM for steady state analysis. The running buffer for all experiments was HBS-EP+ (10 mM HEPES, 150 mM NaCl, 3 mM EDTA, pH 7.4, 0.05% surfactant P20; GE Healthcare Ca.t# BR-1006-69). All binding assays were carried out at 25ºC on a Biacore™ T200 instrument (GE Healthcare). Data were analyzed using the Biacore™ T200 Evaluation Software Version 2.0.

Size Exclusion Chromatography (by Dr. Sanju Llama, Dr. Garnette Sutherland and Dr. Michael Colicos, University of Calgary). Tau-15 and Tau-81 sdAbs at concentrations of 0.5-1.0 mg/mL were applied to a Superdex™ 75 10/300 GL column (GE Healthcare) at a flow rate of 0.5 mL/min in a mobile phase which consisted of HBS-EP+ buffer (10 mM HEPES, pH 7.4, 150 mM NaCl, 3 mM EDTA, and 0.05% (v/v) P20 surfactant; GE Healthcare). The purified monomeric fractions, free of any possible aggregates, were used directly in the binding analyses.

Primary dissociated neuron-glia co-cultures (by Dr. Sanju Llama, Dr. Garnette Sutherland and Dr. Michael Colicos, University of Calgary). Primary dissociated co-cultures of hippocampal neurons and glia were prepared from newborn (P0) Sprague Dawley rat pups (Charles River, Wilmington, MA, USA).[144] Co-cultures were plated at a density of 105 cells/well in each well of a 24 well plate containing poly-D-lysine and laminin treated 12 mm round cover glass. Co-cultures were maintained in Basal Media Eagle supplemented with 4% fetal bovine serum (FBS), 2% B27, 10 mm HEPES, 1 mM sodium pyruvate, 100 U/ml penicillin, 100 ug/ml streptomycin and 2 mM l-glutamine. Two thirds of the growth medium was exchanged twice weekly.

Immunocytochemistry for live hippocampal co-cultures (by Dr. Sanju Llama, Dr. Garnette Sutherland and Dr. Michael Colicos, University of Calgary). Anti-tau sdAb and Alexa488 tagged with $NaDyF_4$-$NaGdF_4$ core-shell NPs, and Alexa488 tagged with $NaDyF_4$-$NaGdF_4$ core-shell NPs (no antibody), were directly added to the medium of hippocampal co-cultures at final concentrations of 1:5, 1:10, 1:20, or 1:50. Co-cultures were incubated with the NPs overnight at 37 °C, and images were taken under an Olympus BX61W1 microscope with 40×0.8NA water immersible lenses.

Characterization of NPs. Transmission electron microscopy (TEM) images were acquired using a JEOL JEM-1400 microscope operating at 80 kV. The NP dispersion in hexane was drop-cast onto a formvar carbon film supported on a 300 mesh copper grid (3 mm in diameter) and allowed to dry in air at room temperature, before imaging. The size distribution was obtained from averaging a minimum of 300 NPs.

X-ray Diffraction patterns were collected using a Rigaku Miniflex diffractometer with Cr Kα radiation (λ = 0.2290 nm, 30 kV, 15 mA) with a scan step size of 0.05 °C (2θ). 15 drops of the NP dispersion in hexane were added onto an indented zero-background sample holder and dried to get the diffraction patterns.

Inductively coupled plasma mass spectroscopy (ICP-MS) analysis was carried out using a Thermo X-Series II (X7) quadrupole ICP-MS to determine Dy^{3+} and Gd^{3+} ionic concentration in the NP-antibody stock solution. The aqueous dispersion of NPs was digested in concentrated nitric acid at 135 ^{o}C in sealed Teflon vials for 3 days and diluted with ultrapure water before analysis. Calibration was done by analyzing serial dilutions of a mixed element synthetic standard containing a known amount of dysprosium. Each sample, standard and blank, were spiked with indium (to a concentration of ~7 ppb) as the internal standard to correct for signal drift and matrix effects. Accuracy was confirmed by analysis of a standard reference material.

Determination of the number of antibodies per NP. To determine the concentration of antibodies and Ln^{3+} ions in a given NP-antibody conjugate sample, UV absorption spectroscopy and Inductively Coupled Plasma Mass Spectrometry (ICP-MS) were used, respectively. The concentration of Dy^{3+} determined by ICP-MS in the stock solution was used to calculate the mass of $NaDyF_4$ core employing the ratio: $\frac{M_{Dy}}{M_{NaDyF_4}} = 0.6215$. The $NaDyF_4$ core has a hexagonal closed pack crystal structure with a density of 5.1 g/cm^3. The mass of a NP was determined, considering the NP as a perfect sphere with radius *r* and volume, $V = (4/3)\pi r^3$. Comparing the mass of the single NP and the total mass determined from ICP-MS, the total number of NPs in the stock solution was determined.

The NP-antibody conjugates showed typical UV absorption peaks at 280 nm. The molar absorption coefficient of the antibody at 280 nm, ε_{280}, in M^{-1} cm^{-1}, is calculated using the following equation:[145-146] $\varepsilon_{280} = (5500 \times \eta_{Trp}) + (1490 \times \eta_{Tyr}) + (125 \times \eta_{S-S})$, where the numbers are the molar absorbance of tryptophan (Trp; 5500), tyrosine (Tyr; 1490) and cysteine (i.e., the disulphide bond, S-S; 125), η_{Trp}, η_{Tyr} and η_{S-S} are number of Trp, Tyr residues and disulphide bonds in the antibody, respectively. The concentration c of antibody was determined from the equation of Beer-Lambert law: Absorbance at 280 nm, $A = \varepsilon_{280}cl$, where l is the path length. Using the known molecular weights of antibodies, the average number of antibodies *per* NP in the stock solution was determined to be 4, 12 or 22.

Chapter 5. Colloidally Stable Monodisperse Fe Nanoparticles as T_2-Contrast Agents for Clinical and High Field Magnetic Resonance Imaging

5.1 Introduction

Magnetic resonance imaging (MRI) is unprecedented in its non-invasive functionality to generate images of anatomical details with high spatial resolution and soft tissue contrast.[22] Its low sensitivity, inherent in inductive detection of weakly polarized nuclear spins, often necessitates the introduction of contrast agents which impart localized changes in longitudinal (T_1) and transverse (T_2) relaxation times of water protons to enhance image contrast and, thus, improve diagnostic accuracy.[29] Magnetic nanoparticles (NPs) bearing appropriate surface chemistry and pharmacokinetics have been of particular interest as contrast agents in MRI,[147] in addition to their applications in hyperthermia,[148] bio-separation,[149] and drug delivery[150] owing to their size dependent magnetic properties[151] and biocompatibility.[152] For example, iron oxide nanoparticles (IONPs) which are intrinsically negative (T_2) contrast agents (CAs) have been extensively tailored and commercialized for imaging.[42,128] Despite the enormous efforts on optimizing the magnetic properties of IONPs, the oxidized state of iron limits their saturation magnetization (M_S = 80 emu/g for γ-Fe_2O_3 and 100 emu/g for Fe_3O_4 at 293 K, in bulk). This, in principle, could be overcome by NPs composed of elemental iron (M_S = 218 emu/g for Fe at 293 K, in bulk)[153] which have a higher saturation magnetization than IONPs of the same size, thus, allowing their increased interaction with applied magnetic fields at a lower dose. The higher M_S value of Fe further permits much stronger shortening of T_2 relaxation time than

IONPs, thus, making Fe NPs excellent candidates for MRI CAs. Furthermore, the transverse relaxation rate (or r_2 relaxivity) of current T_2 CAs, including the commercial ones, remains rather low, which could possibly lead to false positive diagnosis in the hypointense areas, such as blood pooling, calcification, and metal deposition.[30] This suffices the need for CAs with higher r_2 relaxivities to overcome such limitations of current clinical CAs.

Although a few synthetic procedures have been reported for Fe NPs, for instance, via decomposition of $Fe(CO)_5$,[64] $Fe[NSi(CH_3)_3]_2]_2$,[62] and $[Fe(C_5H_5)(C_6H_7)]$,[154] and reduction of $Fe(acac)_3$,[65] $FeCl_2$[148] and other iron salts like oleates,[155] there is hardly any citation in literature to prove the reproducibility of these syntheses. The development and reproducibility of Fe NPs has been challenging and, thus, limited compared to IONPs due to the very high tendency of zero-valent metallic Fe to oxidize in contact with air or water. The difficulty level of retaining Fe in its zero-valent state escalates when Fe NPs are dispersed in aqueous media for biological applications. Reproducibility of the synthetic procedures, surface modification for aqueous transfer, long-term stability of Fe NPs against oxidation over weeks and months have not been documented. Such issues on stability of Fe NPs can be overcome by maintaining inert synthetic conditions and passivating their surface with appropriate capping ligands.

Here, monodisperse (i.e., a batch of NPs with size dispersion < 5%) batches of cubic phase Fe NPs of three different sizes – 15.2 nm, 12.0 nm and 8.8 nm – have been synthesized using $Fe(CO)_5$ in a solvent mixture of 1-octadecene, oleylamine and oleic acid under a continuous stream of argon. The as-synthesized oleate-capped NPs were dispersed in chloroform. The stability of these NPs against oxidation in water have been assessed via transmission electron microscopy (TEM) over a period of three to six months. Magnetic analyses showed that these NPs are superparamagnetic at room temperature. To render these NPs water dispersible and biologically applicable, the oleate-capped Fe NPs were transferred to deionized water by coating them with polyethylene glycol modified phospholipids. 15.2 nm sized Fe NPs showed the highest stability against oxidation among the three batches of NPs dispersed in water. They exhibited a very high shortening of T_2 relaxation time over T_1 relaxation time compared to the IONPs synthesized till date at both clinical and high fields of 3 T and 9.4 T, respectively.

The long-term stability of Fe NPs against oxidation in deionized water combined with their ability to produce enhanced negative contrast compared to IONPs make these NPs potentially applicable as MRI CAs in diagnostics.

5.2 Results and Discussion

5.2.1 Synthesis and Characterization of Fe NPs

Monodisperse Fe NPs were synthesized via a facile thermal decomposition of $Fe(CO)_5$, an organometallic compound that has a high tendency of decomposition due to its standard enthalpy of formation of only -185 kcal mol^{-1}.[66] Prior to injection of $Fe(CO)_5$, the long chain primary alkyl-amines – hexadecylamine$\cdot$hydrochloride (HDA$\cdot$HCl) and oleylamine - were stirred in octadecene under a continuous stream of argon to get rid of any oxygen and/or moisture content. HDA$\cdot$HCl and oleylamine serve as surfactants. The injection of $Fe(CO)_5$ at a high temperature of 180 ^{o}C resulted in black coloration of the reaction medium within 30 s due to the decomposition pathway of $Fe(CO)_5$ leading to burst of nuclei of Fe. Kinetic modelling studies have revealed that $Fe(CO)_5$ decomposes to Fe NPs via a series of intermediate iron carbonyls and iron clusters which also catalyze the decomposition process (Figure A3.1, Appendix 3).[156] The decomposition of the intermediate iron carbonyls involves barrierless or low-barrier bond breaking reactions that lack rigid transition states, and because the entire surface of an iron cluster is essentially reactive (minimal steric hindrance), the decomposition runs rapidly to form a supersaturated concentration of Fe atoms. Once Fe nuclei of a critical size are formed, they grow rapidly by adsorbing the free Fe atoms in the reaction medium to form larger NPs. It could also be possible that oleylamine[157-158] and HDA·HCl form a complex with $Fe(CO)_5$, upon injection of the latter, and the complex undergoes thermal decomposition forming the zero-valent Fe NPs. The main advantage of this process is the absence of any byproduct (except CO which is easily degassed during the synthesis under argon flow). The reaction was quenched with the addition of oleic acid which capped the Fe NPs. The oleate-capped NPs were washed with ethanol and dispersed in chloroform. Syntheses of 15.2 nm, 12.0 nm and 8.8 nm sized Fe NPs had slight variations as detailed in Table 5.1. NPs sized 12.0 nm were obtained when the oleylamine volume was increased to 1 mL instead of 0.3 mL. The reason for the decrease of NP size from 15.2 nm to 12.0 nm could be the increased amount of $Fe(CO)_5$-oleylamine-HDA complexes which produce more nuclei for growth of NPs, and within the same time frame of 50 min at 180 °C, NP size could reach to a maximum of 12.0 nm. To synthesize 8.8 nm sized Fe NPs, slightly different route was followed in which $Fe(CO)_5$ was injected at 130 °C to provide the complexes with lower thermal energy. The reaction at 130 °C was carried out for 20 min which could form $Fe(CO)_5$-oleylamine-HDA complexes. The temperature was maintained at 180 °C for 50 min for NP growth. The volume of the capping agent, oleic acid, was increased to 2 mL which restrained further growth of the NPs.

Table 5.1. Reaction conditions followed to synthesize 15.2 nm, 12.0 nm and 8.8 nm sized Fe NPs.

Size of Fe NPs (nm)	**Volume of oleylamine (mL)**	**Injection temperature of $Fe(CO)_5$ (ºC)**	**Reaction time post injection of $Fe(CO)_5$ (min)**	**Volume of oleic acid injected at 165 ºC (mL)**
15.2	0.3	180	50	1.0
12.0	1.0	180	50	1.0
8.8	0.3	130	70	2.0

Figure 5.1 shows a fairly uniform particle size distribution of Fe NPs in the TEM images of the three batches of Fe NPs. Histograms of the particle size distribution built form the corresponding TEM images reveal particle diameters of 15.2 ± 1.8 nm, 12.0 ± 0.6 nm and 8.8 ± 0.8 nm. Figure 5.2 shows the X-ray diffraction (XRD) patterns of the as-synthesized Fe NPs which are well indexed with the standard patterns of the cubic phase of Fe, *Im-3m* space group. Broader peak for the 8.8 nm sized Fe NPs indicates their smaller diameter. Using the FWHM from the Gaussian fit of the peak at 2θ of 68.7° in the Scherrer formula,[159] crystallite size of NPs was found out to be 15.1 ± 0.7 nm, 12.2 ± 0.5 and 9.1 ± 0.9 nm which closely match with the values obtained from the histograms of the TEM images for the three batches of NPs.

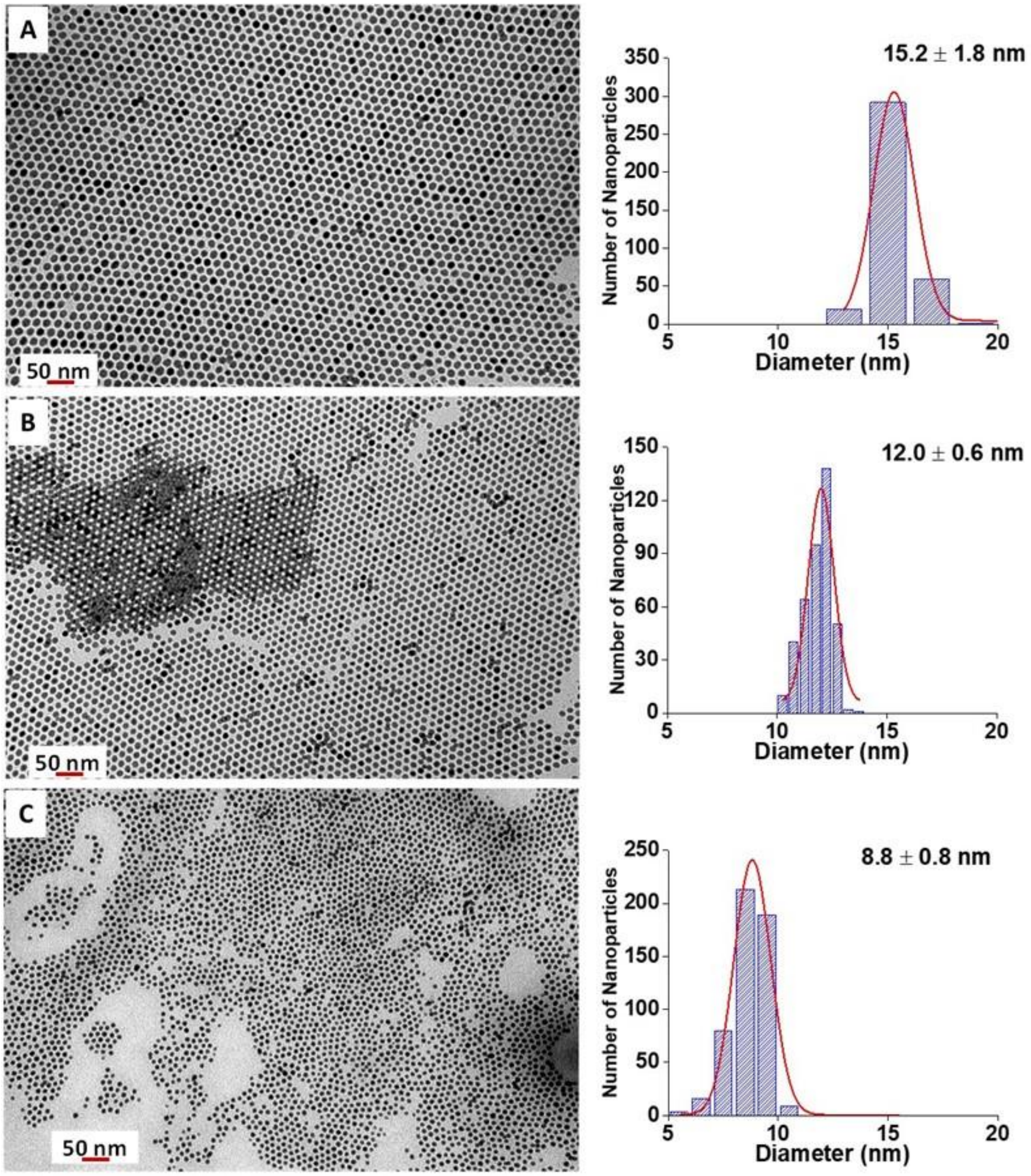

Figure 5.1. (A, B, C) TEM images of Fe NPs with corresponding histograms of particle size distribution for the three different batches of NPs.

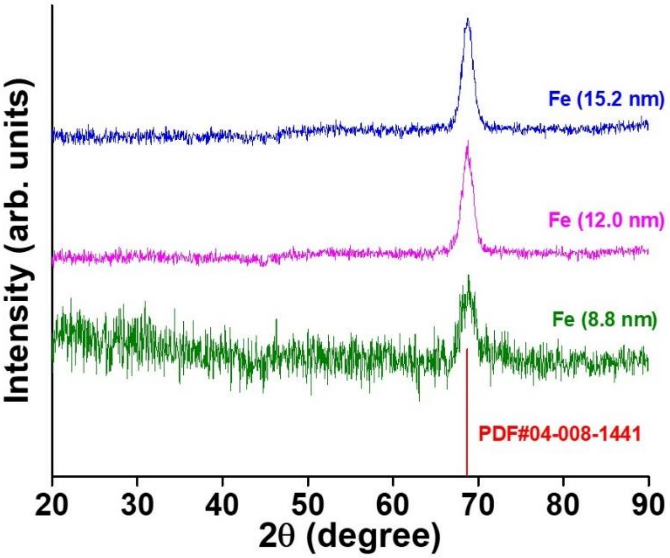

Figure 5.2. XRD patterns of Fe NPs indexed with the standard patterns of cubic phase of Fe (PDF#04-008-1441).

The stability of the NPs against oxidation was assessed by acquiring TEM images of the batches dispersed in chloroform at different time points, in terms of weeks and months. Figure 5.3 shows the TEM images of 15.2 nm sized Fe NPs dispersed in chloroform just after synthesis and a week, a month and 5 months post synthesis. Their corresponding high-resolution images are shown in Figure 5.4 which reveal a very thin layer of an amorphous layer of iron oxide (~0.4 nm in as-synthesized Fe NPs) which grows with time, thereby, shrinking the core diameter to < 10 nm in 5 months post synthesis. Amorphous iron oxide shell is inferred from two observations – (i) the contrast in the high-resolution images of the NPs showing darker core (Fe) with a comparatively brighter shell (iron oxide) and (ii) the XRD patterns of NPs (Figure 5.2) in which no crystalline peak of iron oxide is seen. The iron oxide layer is possibly formed during the work-up process when NPs are precipitated and washed with ethanol prior to their dispersion in chloroform.

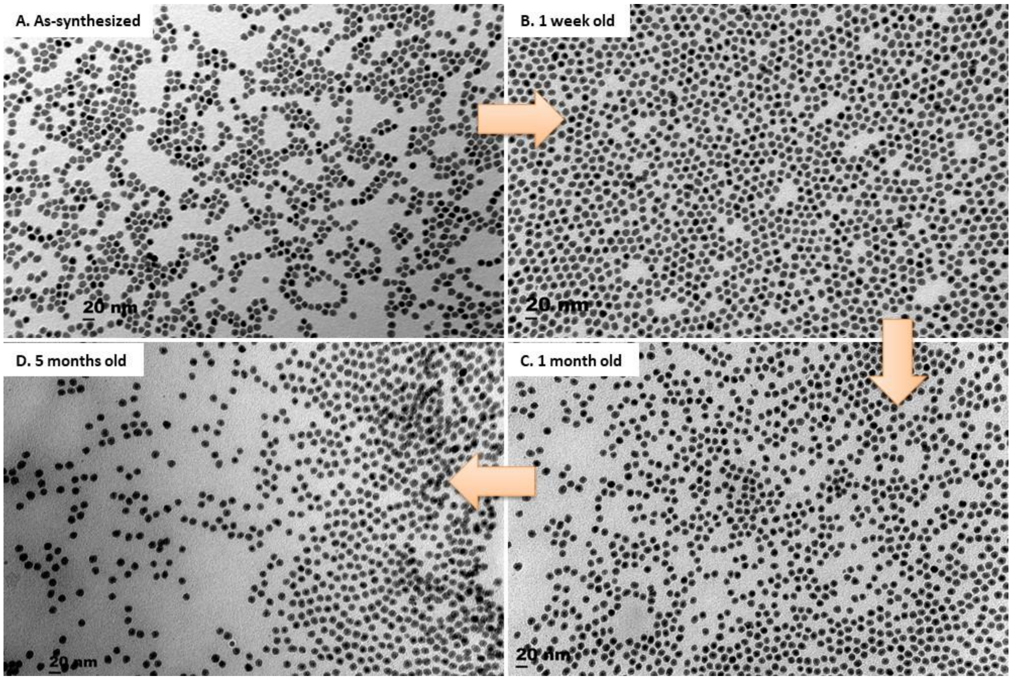

Figure 5.3. TEM images of 15.2 nm sized Fe NPs dispersed in chloroform at different time points post synthesis: (A) as-synthesized, (B) 1 week, (C) 1 month, and (D) 5 months. Their corresponding high-resolution images are shown in Figure 5.4.

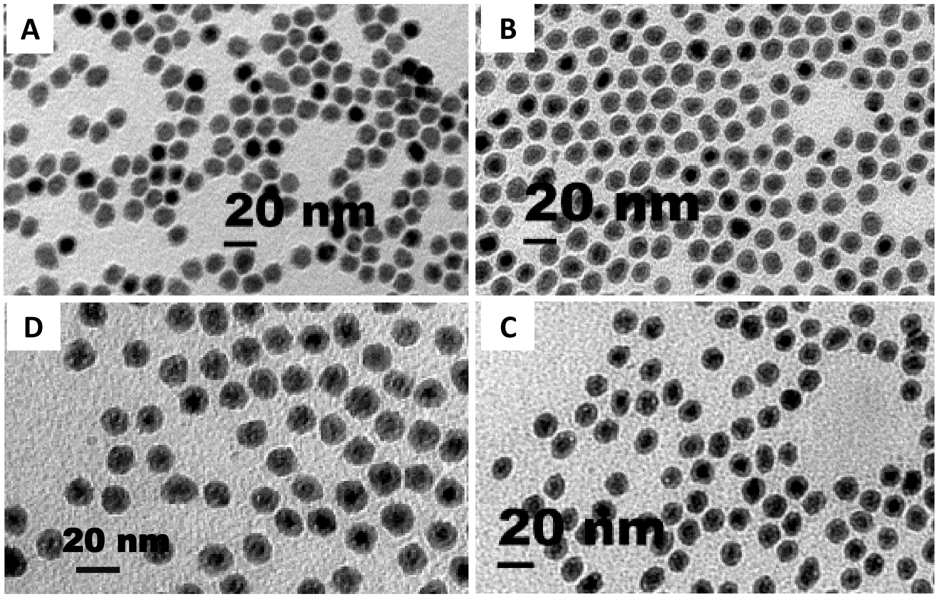

Figure 5.4. High-resolution TEM images of 15.2 nm sized Fe NPs dispersed in chloroform at different time points post synthesis: (A) as-synthesized, (B) 1 week, (C) 1 month, and (D) 5 months (see corresponding images in Figure 5.3).

TEM images (along with the high-resolution ones) of 12.0 nm and 8.8 nm sized Fe NPs dispersed in chloroform were obtained just after synthesis and 3 months post synthesis as shown in Figures A3.2–A3.3. Growth of amorphous iron oxide shell is clearly seen around the core Fe NPs in the high-resolution images. The images post 3 months of synthesis show a hollow core at the center of both 12.0 and 8.8 nm sized NPs as inferred from the contrast of the core and the shell of the particles. Similar to the oxidation phenomenon observed in 15.2 nm sized Fe NPs, gradual oxidation of Fe core with thickening of iron oxide shell with time could lead to completely oxidized NPs in case of 12.0 nm Fe NPs. Due to possible difference in atomic concentrations of oxygen and iron in the shell and the core of the NP, a steady state mass diffusion of oxygen from iron oxide shell to the core and Fe from the core to outer shell give rise to the hollow centers in NPs – the classical Kirkendall effect.[160-161] The hollow center of the NP, shown in high-resolution images of Figures A3.2(B)–A3.3(B), is the Kirkendall void.

Oleate-capped Fe NPs were transferred from chloroform to deionized water by coating them with DSPE-mPEG(2000). The alkyl chains of oleates and DSPE moieties of phospholipids interdigitate due to hydrophobic interaction, resulting in extension of the PEG chains of the phospholipids in the aqueous layer imparting hydrophilicity to the NP. Dynamic lights scattering (DLS) measurements were done to determine the hydrodynamic diameters of the DSPE-mPEG coated Fe NPs, which were 31.3 ± 1.1 nm, 28.1 ± 1.6 nm, and 19.4 ± 1.9 nm, respectively, for the 15.2 nm, 12.0 nm, and 8.8 nm (TEM) sized Fe NPs (Figure 5.5). The hydrodynamic diameters concur with the chain length of a PEG2000 with a DSPE head group, which can extend up to a maximum of 15 nm.[107]

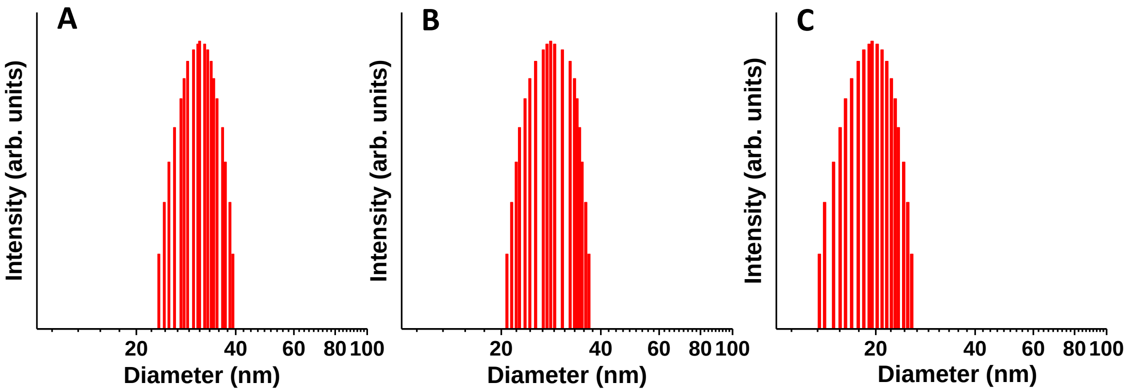

Figure 5.5. DLS results of Fe NPs of (TEM) sizes (A) 15.2 nm, (B) 12.0 nm, and (C) 8.8 nm.

Figure 5.6 shows a characteristic XPS survey spectrum of the 15.2 nm sized Fe NPs dried on a Si wafer. Signals from C, O, and Fe were detected. Carbon and oxygen signals can be attributed to oleic acid remaining on the NPs' surfaces. Oxygen peak is also ascribed to the thin shell of iron oxide formed over the NPs as seen in the TEM images in Figures A3.2 and A3.3 in Appendix 3. Similar patterns of peaks of Fe, O and C are observed in the XPS survey spectra of 12.0 nm and 8.8 nm sized Fe NPs which are shown in Figure A3.4. The peak positions of Fe 2$p_{1/2}$ and Fe 2$p_{3/2}$ depend on the formal charges of Fe. In the inset of Figure 5.7, Fe 2$p_{3/2}$ peak is narrower and stronger than Fe 2$p_{1/2}$ and the area of Fe 2$p_{3/2}$ peak is greater (~twice) than that of Fe 2$p_{1/2}$ because in spin–orbit (*j*–*j*) coupling Fe 2$p_{3/2}$ has degeneracy of four states while Fe 2$p_{1/2}$ has two. A deconvolution analysis of the Fe 2$p_{3/2}$ region (707–717 eV) in Figure 5.7 and Table 5.2 shows that the sample contains iron atoms exhibiting different formal charges: Fe^{3+} [could be from iron oleates, and iron oxides, Fe_3O_4 ($Fe^{2+}Fe_2^{3+}O_4$), Fe_2O_3] and Fe^{2+} [Fe_3O_4 ($Fe^{2+}Fe_2^{3+}O_4$), FeO] and Fe^0 (Fe NP). The peak for Fe^0 is prominent for the batch of 15.2 nm sized Fe NPs (Figure 5.5) while it is almost absent in case of 12.0 nm and 8.8 nm sized Fe NPs as per the deconvolution analyses in Figures A3.5–A3.6 and Tables A3.1–A3.2. Because dried, powdered samples of Fe NPs were used for XPS measurements, most of the zero-valent Fe is oxidized, more likely in case of 12.0 nm and 8.8 nm sized Fe NPs.

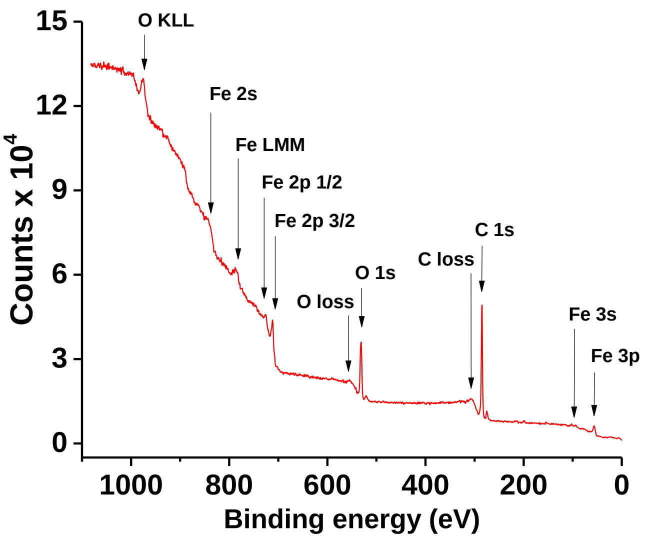

Figure 5.6. Survey XPS peaks of Fe NPs (15.2 nm sized) indexed with the corresponding elements.

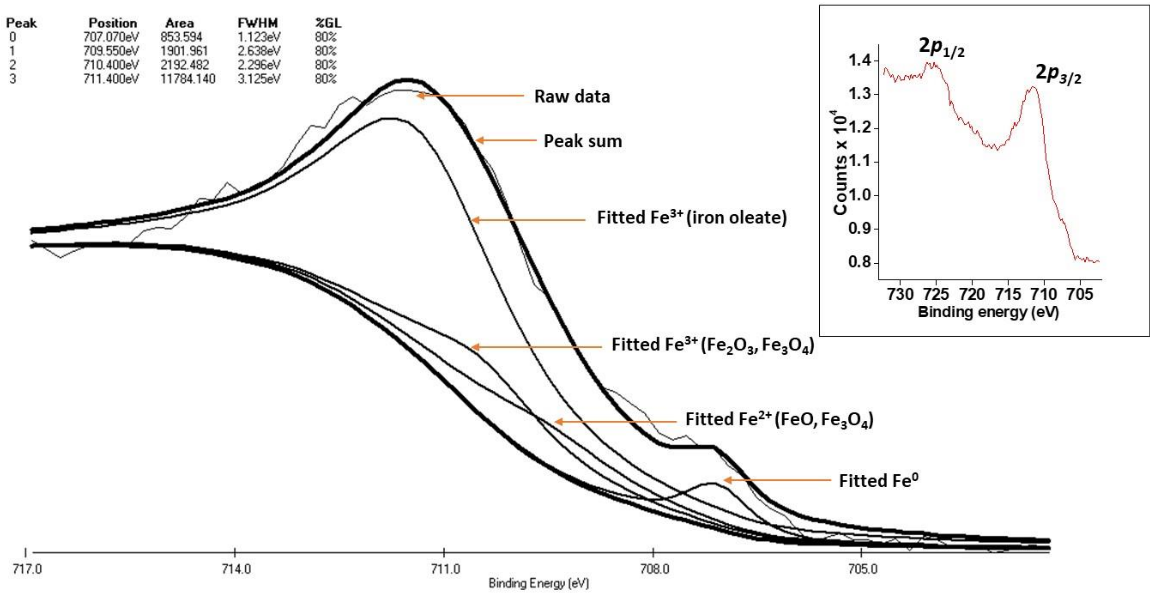

Peak	Position	Area	FWHM	%GL
0	707.070eV	853.594	1.123eV	80%
1	709.550eV	1901.961	2.638eV	80%
2	710.400eV	2192.482	2.296eV	80%
3	711.400eV	11784.140	3.125eV	80%

Figure 5.7. Deconvolution analysis of the Fe 2$p_{3/2}$ region for 15.2 nm sized Fe NPs. High resolution spectrum of the Fe 2p region (inset).

Table 5.2. Details of the deconvolution of the Fe 2$p_{3/2}$ peak shown in Figure 5.6.

Peak	Start BE (eV)	Peak BE (eV)	End BE (eV)	FWHM (eV)	Area
Fe^0	716.91	707.07	702.31	1.123	853.594
Fe^{2+} (FeO)	716.91	709.55	702.31	2.638	1901.961
Fe^{3+} (Fe_2O_3, Fe_3O_4)	716.91	710.40	702.31	2.296	2192.482
Fe^{3+} (iron oleate)	716.91	711.40	702.31	3.125	11784.140

5.2.2 Relaxivities (r_1 and r_2) of Fe NPs at 3 T and 9.4 T

The concentration of Fe in the three batches (15.2 nm, 12.0 nm and 8.8 nm sized) of Fe NPs was determined by inductively coupled plasma mass spectrometry (ICP-MS). The molar concentration of Fe was found out to be 6.9 mM, 9.5 mM, and 9.8 mM, respectively. These solutions were diluted further in deionized water to obtain relaxation times at different concentrations of Fe. The longitudinal (r_1) and transverse relaxivities (r_2) of the Fe NPs dispersed in deionized water NPs were determined from the slope of the linear fits of the rates of T_1 and T_2 relaxation times obtained for different concentrations of Fe, according to the empirical equation: $\boldsymbol{\frac{1}{T_i} = \frac{1}{T_i^0} + r_i[Fe]; i = 1, 2}$, where Fe concentration, [Fe], was obtained from ICP-MS analysis of the NPs; T_i^0 denote the relaxation times of the water protons in absence of the superparamagnetic NPs. Figure 5.8 shows the representative plots of $1/T_1$ and $1/T_2$ for different [Fe] at clinical 3 T and high 9.4 T. The relaxivities (r_1 and r_2) obtained from the slope of the linear fits of these plots are detailed in Table 5.3 which were used to calculate the NP relaxivities (r_1 and r_2 *per* NP) as listed in Table 5.4.

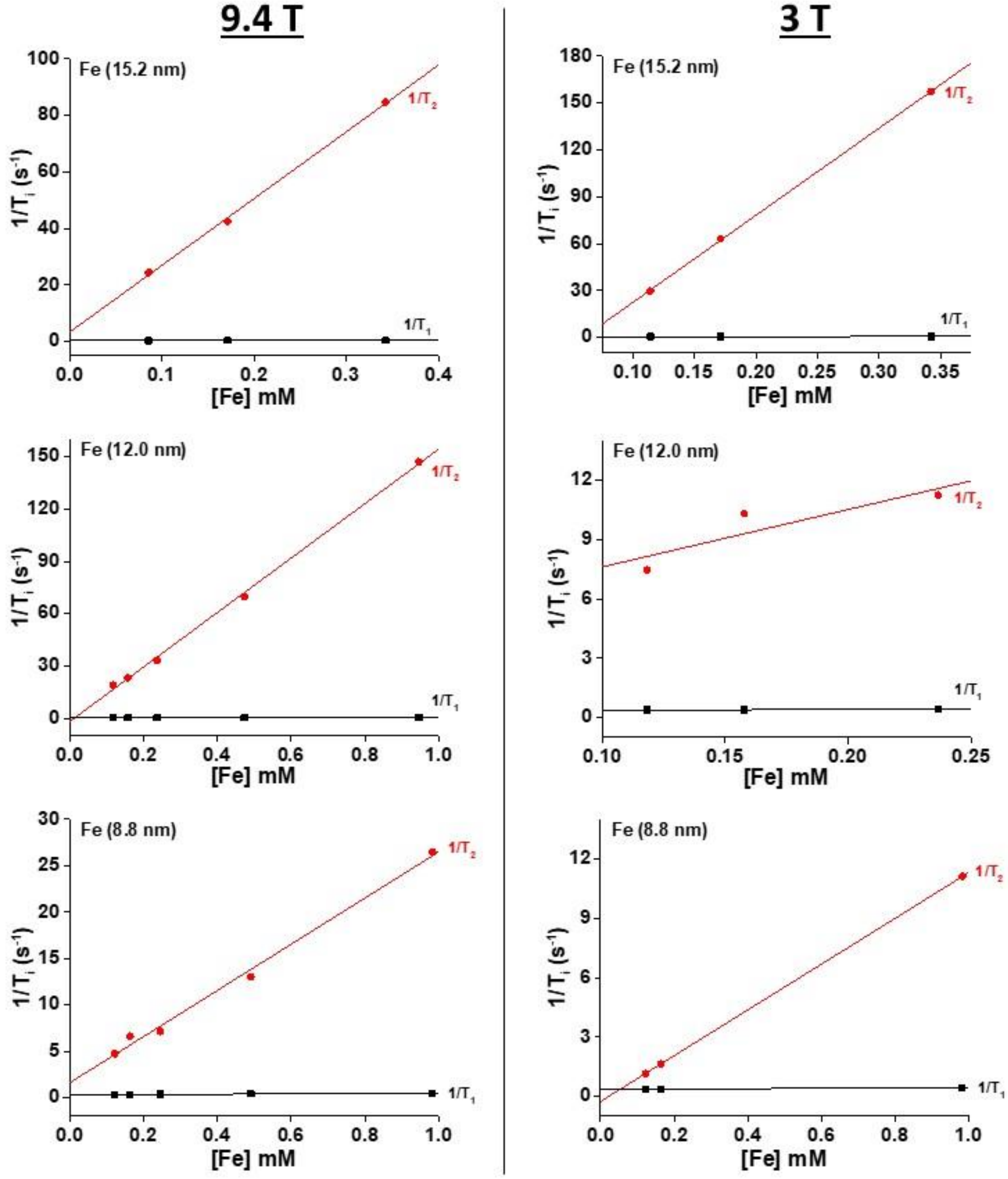

Figure 5.8. Longitudinal (r_1) and transverse (r_2) relaxivities obtained for 15.2 nm, 12.0 nm and 8.8 nm sized Fe NPs at 9.4 T (left column) and 3 T (right column). Black colored linear fits = $1/T_1$, red colored linear fits = $1/T_2$. R-square (Coefficient of Determination) defining the goodness of a fit lie in the range of 0.99101–0.99875, except the fits for the 12.0 nm sized NPs at 3 T (0.74317–0.79015).

Table 5.3. Relaxivities of Fe NPs (based on Fe concentration) at 3 T and 9.4 T.

Fe NPs	**9.4 T**			**3 T**		
Diameter (nm)	**r_1 (mM^{-1} s^{-1})**	**r_2 (mM^{-1} s^{-1})**	**r_2/r_1**	**r_1 (mM^{-1} s^{-1})**	**r_2 (mM^{-1} s^{-1})**	**r_2/r_1**
15.2	0.34 ± 0.02	236.40 ± 8.65	695	0.60 ± 0.02	557.33 ± 7.15	929
12.0	0.30 ± 0.01	156.06 ± 3.28	520	0.15 ± 0.09	29.02 ± 14.96	193
8.8	0.08 ± 0.02	24.90 ± 1.16	311	0.09 ± 0.01	11.57 ± 0.01	129

Table 5.4. Nanoparticle relaxivities of Fe NPs at 3 T and 9.4 T.

Fe NPs	**9.4 T**		**3 T**	
Diameter (nm)	**$r_1 \times 10^4$ (mM_{NP}^{-1} s^{-1})**	**$r_2 \times 10^6$ (mM_{NP}^{-1} s^{-1})**	**$r_1 \times 10^4$ (mM_{NP}^{-1} s^{-1})**	**$r_2 \times 10^6$ (mM_{NP}^{-1} s^{-1})**
15.2	743 ± 43	5,170 ± 189	1,310 ± 44	12,200 ± 156
12.0	243 ± 8	1,260 ± 26	122 ± 73	235 ± 121
8.8	26 ± 6	82 ± 4	30 ± 3	38 ± 0.03

The Fe NPs of 15.2 nm size show the highest r_2 value of 236.40 mM^{-1} s^{-1} at 9.4 T and 557.33 mM^{-1} s^{-1} at 3 T among the three batches (Table 5.3). The corresponding *per* NP r_2 relaxivities were determined to be 5,170 × 10^6 mM_{NP}^{-1} s^{-1} and 12,200 × 10^6 mM_{NP}^{-1} s^{-1}. The r_2/r_1 ratios, which give a qualitative idea on the darkening effect of NPs in MR images, were found to be 695 at 9.4 T and 929 at 3 T. The r_2 values and r_2/r_1 ratios are higher than that of the currently explored IONPs of the same size as of the Fe NPs (15 nm IONPs: 145 mM^{-1} s^{-1} at 9.4 T)[154] and clinical T_2 CAs (at clinical 3 T, Ferridex: r_2 = 93 mM^{-1} s^{-1}, r_2/r_1 = 23; Resovist: r_2 = 143 mM^{-1} s^{-1}, r_2/r_1 = 33).[33] Since r_1 values are often not mentioned in the literature for magnetic NPs (including IONPs), the comparison of r_2/r_1 ratios of the magnetic NPs with Fe NPs of the same sizes at a given magnetic field is not possible.

The Fe NPs of sizes 12.0 nm and 8.8 nm show r_2 of 156.06 mM^{-1} s^{-1} (r_2/r_1 = 520) and 24.90 mM^{-1} s^{-1} (r_2/r_1 = 311) at 9.4 T, respectively. With decrease in NP size from 15.2 nm to 12.0 nm and 8.8 nm, r_2 relaxivity decrease at a given magnetic field. This is consistent with the size dependent transverse relaxivity of magnetic NPs described in the outer sphere relaxation regime which follows as: $r_2 = \frac{\left(\frac{64\pi}{135{,}000}\right)\gamma^2 N_A M \mu_C^2}{rD}$, where N_A is Avogadro's number, M is the molarity, μ_C is the magnetic moment (called the Curie moment) of the NP, r is the effective radius of the NP, and D is the diffusion coefficient of water molecules. The r_2 relaxivity is directly proportional to the μ_C^2 of the NP and inversely proportional to its radius. Because the magnetic moment of a NP is proportional to its volume, the r_2 relaxivity increases with NP size. Such size effect on the increase in r_2 relaxivity is confined to the motional average regime in which the diffusion of water molecules between NPs occurs on a very fast time scale. This leads to averaging of the magnetic fields from NPs by fast diffusion resulting in their relaxivity proportional to the magnetization, and hence, size of NPs.[162-164] But such increase in r_2 relaxivity with increasing NP size does not follow when the NPs' size lie in the static dephasing regime in which a very strong magnetic field is generated by NPs such that diffusion has little influence on the T_2 relaxation process resulting in a plateau of the maximum r_2. Magnetic Fe NPs whose size lie in this static dephasing regime would be ferromagnetic.[162-165] When NP size exceeds the static dephasing regime, it enters in to the echo-limiting regime in which the nuclei spins are dephased so quickly that fewer spins are refocused by the echo sequence (echo time = time interval of the radiofrequency pulse that refocuses the nuclei spins), leading to decrease in the r_2 with increase in NP size.[162-164] When magnetic field is decreased from 9.4 T to 3 T, the r_2 value of 15.2 nm sized Fe NPs (hydrodynamic diameter of 31.3 nm) increases. This could be explained in terms of the higher volumetric magnetization of the 31.3 nm sized NPs at 9.4 T (than at 3 T) which renders them to align and assemble along the applied magnetic field. The congregation of NPs could lower the diffusion rates of water molecules which leads to a lower r_2 value at 9.4 T compared to that at 3 T.

The r_2 relaxivities of 12.0 nm and 8.8 nm sized Fe NPs at 3 T were determined to be 29.02 mM^{-1} s^{-1} (r_2/r_1 = 193) and 11.57 mM^{-1} s^{-1} (r_2/r_1 = 129), respectively, which are significantly lower compared to the r_2 value of 15.2 nm sized Fe NPs (557.33 mM^{-1} s^{-1}, r_2/r_1 = 929). This is due to lower magnetization of Fe NPs at 3 T compared to that at 9.4 T and the high tendency of 12.0 nm and 8.8 nm sized Fe NPs towards oxidation upon dispersion in deionized water. The latter is clearly shown in the TEM images in Figure 5.9 in which the Kirkendall effect apparently prevails in the 12.0 nm and 8.8 nm sized Fe NPs resulting in oxidized NPs with voids in their centers, while the dark core in 15.2 nm sized Fe NPs suggests that these NPs are stable against oxidation in deionized water.

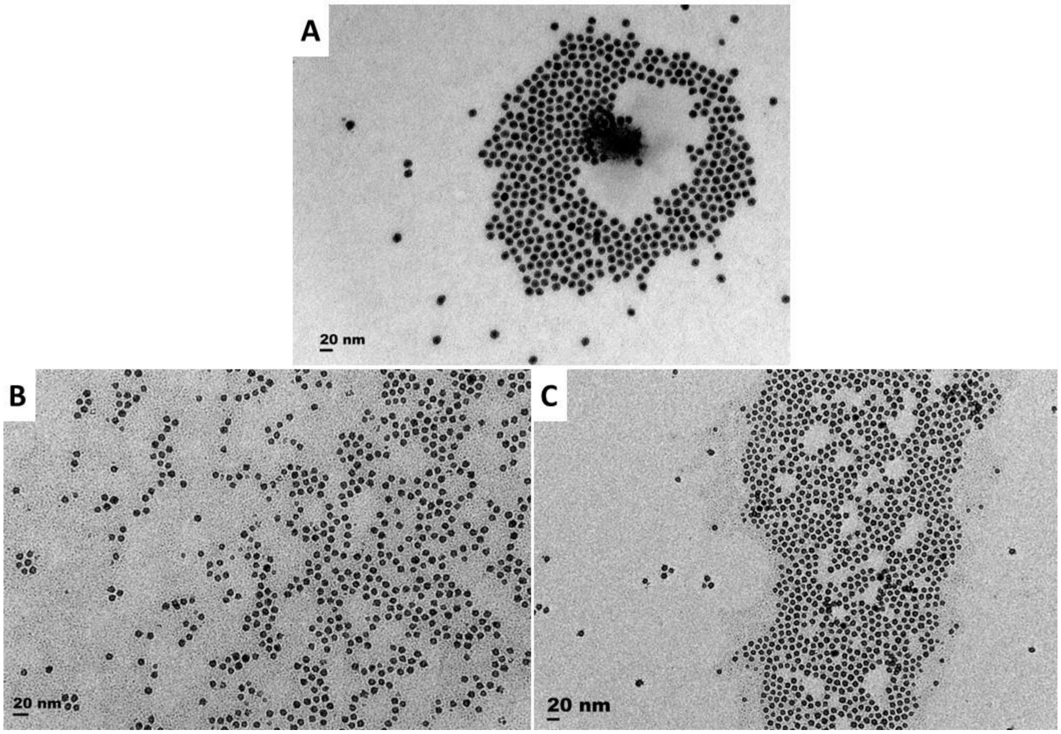

Figure 5.9. TEM images of (A) 15.2 nm, (B) 12.0 nm, and (C) 8.8 nm sized Fe NPs dispersed in deionized water.

Magnetic measurements were done on a superconducting quantum interference device (SQUID) at 1.9 K and 300 K. Magnetization curves, shown in Figure 5.10, reveal hysteresis loops of the three batches of NPs indicating their ferromagnetic behavior at 1.9 K. At 300 K, 15.2 nm, and 12.0 nm sized NPs show superparamagnetic behavior because of the absence of any hysteresis. The saturation magnetization of these NPs is less than 30 emu/g at 300 K as the NPs could easily oxidize in their powdered form as used in SQUID. The 8.8 nm sized Fe NPs show a straight line indicating paramagnetic behavior which is a characteristic of amorphous iron oxide. This suggests that the 8.8 nm sized NPs have completely oxidized to iron oxides in powdered form.

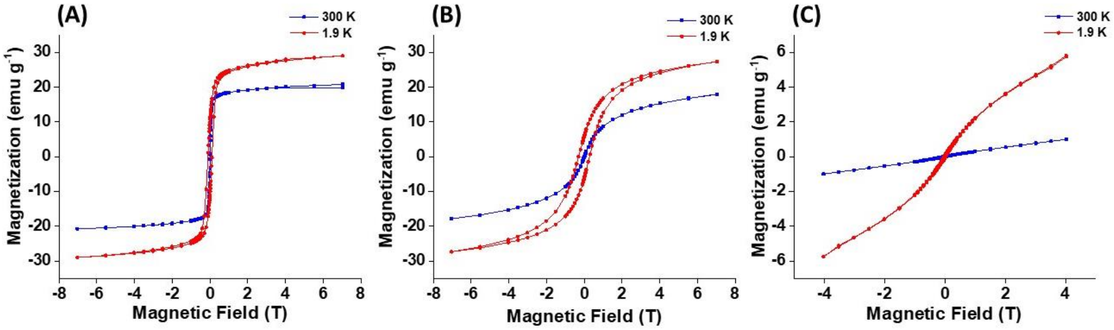

Figure 5.10. SQUID results: Magnetization vs. field plots for Fe NPs of sizes (A) 15.2 nm, (B) 12.0 nm, and (C) 8.8 nm.

5.3 Conclusions

Three different sizes of cubic phase oleate-capped Fe NPs were synthesized via facile thermal decomposition of $Fe(CO)_5$. The NPs were dispersed in chloroform which naturally got oxidized forming a thin shell of amorphous iron oxide layer around core Fe over time. The Fe NPs were transferred to deionized water by coating them with phospholipid molecules bearing polyethylene glycol chains. 15.2 nm sized NPs exhibited long-term stability against oxidation when dispersed in organic and aqueous phases. These NPs demonstrated high transverse relaxivities at both clinical 3 T and high 9.4 T compared to the 15 nm sized IONPs and currently used clinical T_2 CAs. Such T_2 contrast enhancement ability combined with long-term stability against oxidation make Fe NPs potentially applicable in diagnostic imaging and therapeutic applications like hyperthermia.

5.4 Experimental Section

Chemicals. Iron(0) pentacarbonyl [$Fe(CO)_5$, > 99.99%], hexadecylamine (HDA, 98%), oleic acid (tech grade, 90%), 1-octadecene (tech grade, 90%), diethylether (anhydrous, ≥ 99.0%), pentane (anhydrous, ≥ 99%), tetrahydrofuran (THF, ≥ 99.9%), chloroform, and hexanes were purchased from Sigma Aldrich. Oleylamine (97%) was purchased from Acros, hydrochloric acid (HCl, 37%), dimethyl sulphoxide (DMSO), anhydrous ethanol and toluene from Caledon laboratories, and 1,2-distearoyl-*sn*-glycero-3-phosphoethanolamine-*N*-[methoxy(polyethylene glycol)-2000] (ammonium salt) (DSPE-mPEG) from Avanti Polar Lipids.

Synthesis of HDA·HCl.[166] Prior to synthesis of Fe NPs, HDA·HCl was prepared by stirring a mixture of 1.5 mmol of HCl in 15 mL diethyl ether and 1 mmol of HDA in 50 mL of pentane for a minute. A white solid product immediately precipitated which was filtered off and washed with 15 mL of THF thrice by centrifugation (5,000 *g*, 5 min, Beckman Coulter Spinchron 15-rotor F0830). The white solid was vacuum dried overnight.

Synthesis of 15.2 nm and 12.0 nm sized Fe NPs. In a 100 mL three-necked round bottom flask, 0.2779 g of HDA·HCl was dissolved in 0.3 mL oleylamine and 20 mL 1-octadecene by stirring at 120 °C for 2 h under argon flow. The temperature was raised to 180 °C (15 °C/min) at which 5.2 mmol of $Fe(CO)_5$ was injected. The solution turned black in less than a minute after injection. It was stirred for 50 min at 180 °C. The temperature was decreased to 165 °C at which 1 mL of oleic acid was injected. The solution was stirred at 130 °C for 30 min. The reaction medium was cooled to room temperature. The black product was collected off magnet using hexanes, precipitated using 60 mL of ethanol, centrifuged (4,000 *g*, 10 min, Beckman Coulter Spinchron 15-rotor F0830) and washed with 60 mL of ethanol thrice. The resultant Fe NPs are 15.2 nm sized which were dispersed in 10 mL of chloroform. To synthesize 12.0 nm sized Fe NPs, the above procedure was followed exactly except that the volume of oleylamine was 1 mL.

Synthesis of 8.8 nm sized Fe NPs. To synthesize 8.8 nm sized Fe NPs, the procedure for 15.2 nm sized Fe NPs was followed except that the injection temperature of $Fe(CO)_5$ was 130 °C which was maintained for 20 min before heating at 180 °C and the volume of oleic acid injected was 2 mL. Briefly, 0.2779 g of HDA·HCl was added to a solvent mixture of 0.3 mL oleylamine and 20 mL 1-octadecene in a 100 mL three-necked round bottom flask and stirred at 120 °C for 2 h under argon flow. The temperature was raised to 130 °C at which 5.2 mmol of $Fe(CO)_5$ was injected. The solution turned brick orange. It was stirred at 130 °C for 20 min after which the temperature was ramped up to 180 °C (15 °C/min). The solution turned black when the temperature reached 150 °C during this ramp up. After stirring at 180 °C for 50 min, the temperature was decreased to 165 °C at which 2 mL of oleic acid was injected. The solution was stirred at 130 °C for 30 min. It was then cooled to room temperature. The black product was collected off magnet using hexanes. The NPs were precipitated using 60 mL of ethanol, centrifuged (4,000 *g*, 10 min, Beckman Coulter Spinchron 15-rotor F0830) and washed with 60 mL of ethanol thrice. The resultant 8.8 nm sized Fe NPs were dispersed in 10 mL of chloroform.

Aqueous transfer of NPs using phospholipids.[76] 0.4 mL of NPs dispersed in chloroform (at 5.0 mg/mL) was added to DSPE-mPEG in 0.8 mL chloroform considering appropriate weight ratio of DSPE-mPEG to NP. A volume of 4 mL of DMSO was added to the solution. This solvent mixture was held on a rotary shaker for 30 min at room temperature. Chloroform was removed completely under vacuum using a rotary evaporator. Deionized water was added to the black colloidal solution in DMSO to reach a total volume of 20 mL. After three rounds of centrifugation (4,000 *g*, 5 min, Beckman Coulter Spinchron 15-rotor F0830) using centrifugal filter tubes (Vivaspin Turbo 15, 100 kDa cutoff size), DMSO was completely substituted with deionized water leaving a final volume of 1 mL of NP dispersion.

Characterization. X-ray Diffraction (XRD) patterns were obtained with a scan step size of 0.05 degrees (2θ) using a Rigaku Miniflex diffractometer with Cr Kα radiation ($\lambda = 0.2290$ nm, 30 kV, 15 mA). 10 drops of the NP dispersion in chloroform were dried on an indented zero-background sample holder to acquire the XRD patterns.

Transmission electron microscopy (TEM) images were collected using a JEOL JEM-1400 microscope operating at 80 kV. A drop of the NP dispersion in chloroform was dried on a formvar carbon film supported on a 300-mesh copper grid (3 mm in diameter) for imaging. NP size distribution was obtained by averaging the size of a minimum of 300 NPs using ImageJ software (version 1.50i).

Dynamic light scattering (DLS) measurements were done using a Brookhaven Zeta PALS instrument with a 90Plus/BI-MAS Multi Angle Particle Sizing option, equipped with a 15 mW solid-state laser (658 nm). All data were obtained at a single scattering angle of 90^o and averaged over ten scans of scattered intensity weighted plots of NPs dispersed in deionized water.

X-ray photoelectron spectroscopy (XPS) was performed using a Omicron and Leybold MAX200 X-ray photoelectron spectrometer (10 kV, 20 mA) equipped with monochromatic Al Kα X-ray source. The survey spectra and high-resolution peaks of Fe 2p and 3p were analyzed using XPSPEAK 4.1 software.

Inductively coupled plasma mass spectroscopy (ICP-MS) analysis was carried out to determine the concentration of Fe ions concentration in the NP stock solution using a Thermo X-Series II (X7) quadrupole ICP-MS. The aqueous dispersion of NPs was digested in concentrated nitric acid at 135 ^oC in sealed Teflon vials for 3 days and diluted with ultrapure water before analysis. Calibration was done by analyzing serial dilutions of a mixed element synthetic standard containing a known amount of iron. Each sample, standard and blank, were spiked with indium (to a concentration of ∼7 ppb) as the internal standard to correct for signal drift and matrix effects.

Relaxivity measurements. Aqueous dispersions of NPs were used to determine the relaxation times. T_1 and T_2 measurements were done using a 9.4 T/21 cm bore magnet (Magnex, UK) and a Bruker console (Bruker, Germany) (by Dr. Barbara Blasiak and Dr.

Boguslaw Tomanek, University of Calgary). A transmit/receive radio frequency volume birdcage coil was applied to excite protons and obtain resonant signal. For T_2 measurements, a single slice multi-echo pulse sequence was used with the following pulse parameters: repetition time (TR) 5 s, matrix size 128 × 128, field of view (FOV) 3 cm × 3 cm, slice thickness 2 mm, 128 echoes 4 ms apart. T_2 relaxation times were calculated using a single exponential fitting of the echo train (Marevisi, Canada). For T_1 measurements, TRUE FISP method was used with the following pulse sequence parameters: TR 3 s, TE 1.5 s, matrix size 128 × 128, FOV 3 cm × 3 cm, slice thickness 3 mm, 60 frames × 4 segments, segment time 192 ms. T_1 and T_2 measurements at clinically relevant magnetic field were performed at 3 T using the whole body 3 T system (Trio, Siemens, Germany). A standard head RF coil was used for all experiments. For T_1 measurements inversion recovery (IR) FLASH pulse sequence was used with TR = 10 sec, echo time (TE) = 2.9 s, inversion recovery (IR) times: 30, 60, 120, 240, 480, 960, 1920, 4,000 ms; FOV 10 x 10 cm; slice thickness 2 mm, matrix size 128 x 128. T_2 measurements were performed using multi echo pulse sequence with TR = 5 sec, 32 echoes with 15 ms increments: TE=15, 30, 45, to 480 ms. The relaxation times were calculated using single exponential fitting of the data (MATLAB “1sqcurvefit”).

The T_1 and T_2 relaxation times obtained for different dilutions of NPs in deionized water were plotted against concentration of Fe ions in the NP solution, [Fe], to obtain the values of r_1 and r_2 relaxivities from the slope of the linear fit, using the empirical equation: $\boldsymbol{\frac{1}{T_i} = \frac{1}{T_i^0} + r_i[Fe]; i = 1, 2}$. The Fe concentration was obtained from ICP-MS analysis of the NPs; T_i^0 denote the relaxation times of the water protons in absence of the superparamagnetic NPs.

Superconducting quantum interference device (SQUID) magnetometry measurements were carried out in a Quantum Design MPMS XL-7S system (by Dr. Abhinandan Banerjee and Dr. Simon Trudel, University of Calgary). Weighed powdered samples were loaded into a gelatin capsule which was sealed with Kapton tape before being inserted into a clear diamagnetic plastic straw. Isothermal magnetization as a function of field strength measurements were carried out at 300 K by cycling the applied magnetic field between -7 T and +7 T.

Chapter 6. MRI Correlation

6.1 Introduction

In a general term, correlation is a statistical measure that indicates the extent to which two (or more) variable have a linear relationship with each other. A positive correlation indicates the extent to which the variables change (increase or decrease) in parallel, while a negative correlation implies that one variable changes opposite to that of the other. Image correlation has been employed in clinical sciences utilizing the complementary information in computed (body) tomography (high spatial resolution, low counting statistics), magnetic resonance imaging (high spatial resolution, low sensitivity) and positron emission tomography (low spatial resolution, high sensitivity).[167] Such correlation from the complementary details of various modalities allows accurate definition of target volume of tissue, thereby, better sparing of the normal tissues, and increasing the therapeutic window. Image correlation has also been studied in fluorescence imaging which measures the spatial and temporal correlation of individual molecules with themselves.[103] To elaborate on this, the example of optical/fluorescence correlation on cell membrane structure is appropriate in the sense that the membrane structure is heterogenous (because of the heterogenous distribution of proteins and lipids or membrane domains that serve as signalling platform). The heterogenous cell membrane has functional implications, and the organization of signaling receptors on the surface is driven by specific intermolecular interactions. Image correlation could permit the study of these interactions and their dynamics by providing quantitative measurements of receptor distribution, receptor interactions, and the movement of receptor clusters. Quantitative measurements of receptor distributions on the cell surface could characterize whether the receptors are present as monomers or in clusters, what the number of receptor clusters per area (receptor cluster density) is at any particular time, and how many receptors are present in each of the clusters.[168-169] Further, quantitative measurements of receptor interactions on cell surfaces permit the determination of which types of receptors interact with each other in a given signaling event, with which of the membrane domains the receptors associate, and what fraction of a particular receptor is associated with another protein of interest for targeted diagnostic and therapeutic studies. Image (fluorescence/optical) correlation spectroscopy has been used to analyze pairs of images (of two different proteins or of the same protein labeled with a different chromophore) collected from the same area of the same cell at the same time to establish these associations.[170]

Correlation between T_1- and T_2-weighted contrast imaging in MRI is a novel idea that has not been reported. The basic idea of MRI correlation is analogous to that of, for instance, the optical correlation spectroscopy, in which signals are measured as a function of two or more independent variables (such as times) allowing the spin system to evolve under different relaxation mechanisms. In an MRI correlation experiment, the two independent variables could be longitudinal relaxation time, T_1, and transverse relaxation time, T_2, which are the corresponding time periods for decay of spin magnetization along z-axis and decay of transverse magnetization due to loss of spin coherence along x-y plane in an applied magnetic field. Nevertheless, T_1 and T_2 are coupled with each other and not completely independent in practice, which in other words means that a contrast agent exhibits both T_1 and T_2 relaxation.

Tissue specific differences in both longitudinal (T_1) and transverse (T_2) components in proton magnetic resonance relaxation can be potential diagnostic elements in bioimaging. MRI correlation can for instance help differentiate between a benign cystic lesion and a cystic neoplasm or tumor based on this idea. Image correlation can provide an important tool for planning and assessment of therapy. A more precise understanding of the geometric relation between tumor and normal tissue on a wide spectrum can be developed. The technique is potentially important in active targeted imaging in which NPs tagged with targeting moieties (antibodies) are employed for diagnosis and therapeutics, where the localization of tumor can be correlated with T_1/T_2 imaging. Such correlation could yield a qualitative biodistribution of NP/antibody based on the contrast.

T_1-and T_2-weighted contrast images could detect a structural change in tissue feasibly. When independent T_1 and T_2 images of the same tissue site are mapped, accurate spatial coordinates could be obtained for further diagnosis and therapeutics. For T_1-T_2 MRI correlation, a 'T_1-only' NP [a NP having high T_1 signal or r_1 relaxivity (and negligible T_2) that yields T_1 contrast (high r_1/r_2 ratio)] and a 'T_2-only' NP [another NP having high T_2 signal or r_2 relaxivity (and negligible T_1) that imparts T_2 contrast (high r_2/r_1 ratio)] are employed. The corresponding NPs used in the current Chapter are $NaYF_4$-$NaGdF_4$ core-shell NPs ($r_2 = 6.46$ mM^{-1} s^{-1} and $r_1/r_2 = 0.11$) and Fe NPs ($r_2 = 236.40$ mM^{-1} s^{-1} and $r_2/r_1 = 695$) after comparing the relaxivities of all the NPs' batches discussed in Appendix 2 and Chapter 5, respectively. The T_1- and T_2-weighted phantom images obtained from corresponding T_1 and T_2 CAs could be correlated. The current Chapter illustrates the concept of T_1-T_2 correlation for volumetric combinations of T_1-only and T_2-only NPs.

Furthermore, T_1-T_2 has potential diagnostic application in patients suffering from traumatic brain injury (TBI, Chapter 4). T_1-only and T_2-only NPs bound to antibodies targeting tau and hyperphosphorylated tau, respectively, could be used for target-specific MR imaging in patients suffering from TBI (Figure 6.1). The correlation would differentiate the normal healthy condition of neural tissues (where tau is only expressed) from the pathological state (where tau is hyperphosphorylated). Pathological and healthy tissue sites could be well distinguished for proper diagnosis and future therapy.

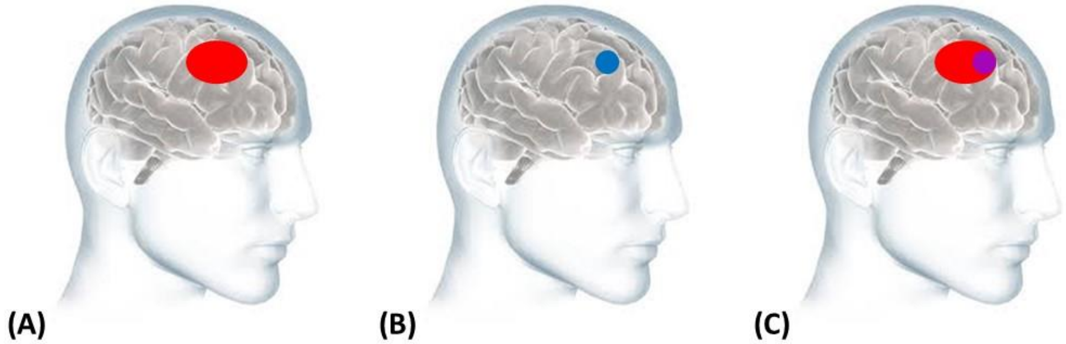

Figure 6.1. Schematic representation of T_1 and T_2 correlation in mild traumatic brain injury. (A) Normal tau in red, (B) hyperphosphorylated tau in blue, (C) correlation in magenta.

6.2 Results and Discussion

Among the very many batches of NPs discussed in this dissertation, $NaYF_4$-$NaGdF_4$ core-shell NPs (20.0 nm sized, Chapter 2) and Fe NPs (15.1 nm sized, Chapter 5) were selected to achieve T_1-only contrast and T_2-only-contrast. Figure 6.2 shows the XRD patterns and TEM images of both the NPs' batches. The XRD patterns of $NaYF_4$-$NaGdF_4$ core-shell NPs are well matched with the standard patterns of the hexagonal phase of

$NaYF_4$. The XRD pattern of Fe NPs is well indexed with that of the cubic phase of Fe. Both batches of NPs show a fairly uniform particle size distribution with diameters of 20.0 nm and 15.2 nm, respectively. The experimental and characterization details of $NaYF_4$-$NaGdF_4$ core-shell NPs and Fe NPs are in Appendix 2 and Chapter 5, respectively.

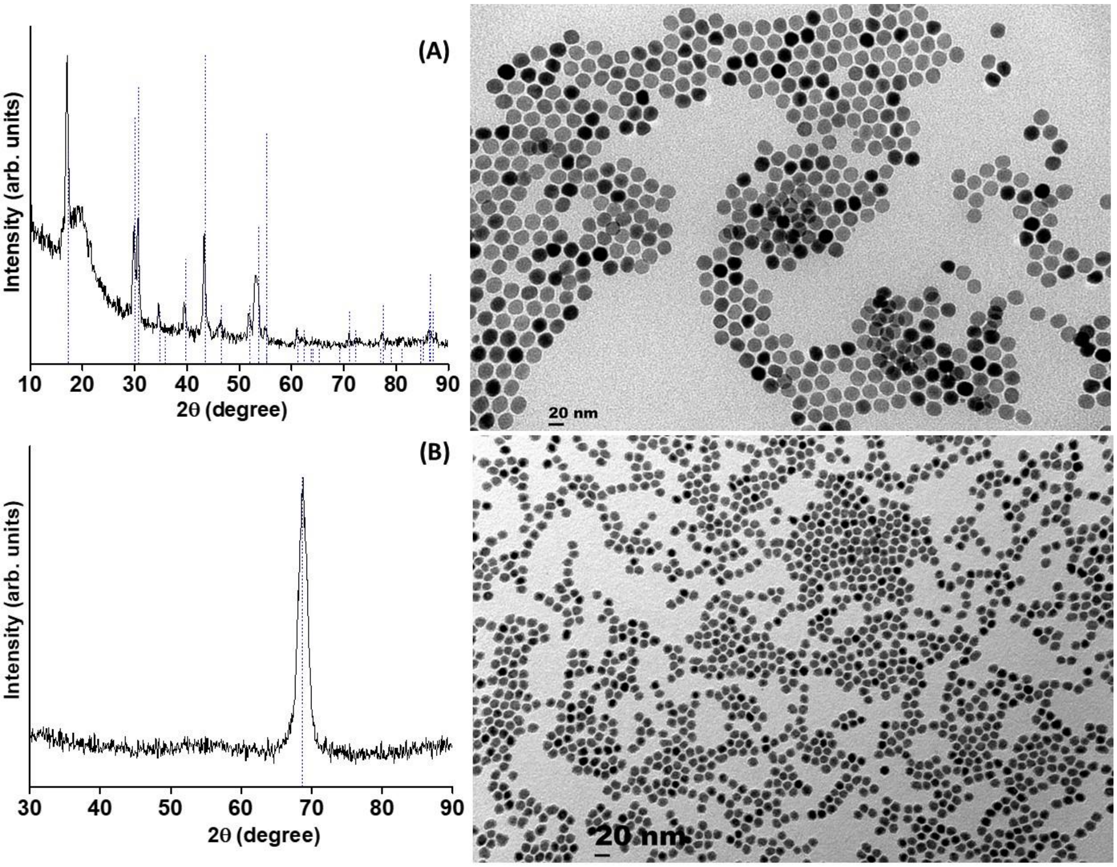

Figure 6.2. XRD patterns and TEM images of (A) $NaYF_4$-$NaGdF_4$ core-shell NPs (blue standard XRD lines from PDF#00-016-0334) and (B) Fe NPs (blue standard XRD lines from PDF#04-008-1441).

These NPs were chosen based on the fact that the T_1-only NPs have the highest r_1/r_2 ratio exhibiting a large shortening of T_1 relaxation compared to the T_2 relaxation, while the T_2-only NPs have the highest r_2/r_1 ratio producing a maximum shortening of T_2 relaxation among all the NPs' batches. The r_1 and r_2 relaxivities of both types of NPs were determined based on the following empirical equations.

$$\frac{1}{T_1} = \frac{1}{T_1^0} + r_1[Gd^{3+}],$$

$$\frac{1}{T_2} = \frac{1}{T_2^0} + r_2[Fe],$$

where [Gd^{3+}] and [Fe] are the concentration of Gd^{3+} ions and Fe in T_1-only and T_2-only NPs, respectively, obtained from ICP-MS, T_i^0 denote the relaxation times of the water protons in absence of the NPs.

T_1 and T_2 relaxation times were measured for mixed dispersions of T_1-only and T_2-only NPs in deionised water in different volumetric ratios. Assuming that the T_1 and the T_2 relaxation times are additive, the following equation was used for calculating the values of $1/T_1$ and $1/T_2$.

$$\frac{1}{T_i} = \frac{1}{T_i^0} + r_{i(Gd)}[Gd] + r_{i(Fe)}[Fe];\ i = 1, 2$$

The measured relaxation rates are $1/T_\mathrm{i}$ (left-hand side of the equation) while the calculated relaxation rates are from the right-hand sides of the equation. Table 6.1 details the measured and calculated relaxation rates for the different volumetric combinations of T_1-only and T_2-only NPs which are plotted in Figure 6.3. The measured and calculated relaxation rates when plotted against each other for the different NPs' combinations indicates that the relaxation rates are not additive. Both the plots of T_1 and T_2 relaxation rates show a systematic and steady pattern of increase of $1/T_\mathrm{i}$(calculated) vs. and $1/T_\mathrm{i}$(measured) for different volumetric combinations of T_1-only and T_2-only NPs as observed in Figure 6.3, starting with 4:1 to 3:1, 2:1, 1:1 and ending with 1:2, 1:3 and 1:4 of (T_1-only NPs):(T_2-only NPs). One data point is an outlier in the T_1 pattern because all these relaxation rates are just single point measurements which could yield random errors, unlike the ones obtained for different dilutions of the same batch of NPs (Chapters 2–5, 7). Because the T_1-only NPs also exhibit inherent r_2 relaxivity in addition to r_1 (unlike T_2-only NPs which have high r_2 relaxivity and negligible r_1), a potent T_1-only NP is essential to perfectly correlate the T_1-only and T_2-only signals. The two data points corresponding to 1:3 and 1:4 ratios can be discarded from T_2 pattern because the measured T_2 was below detection limit. Nevertheless, this initial experiment on the volumetric combinations of T_1-only and T_2-only NPs indicates that the relaxation rates are not additive (as assumed) because the patterns appear non-linear when the outliers are discarded. However, T_1-T_2 correlation could be proved in phantom images for future bio-applications.

Table 6.1. Measured and calculated relaxation rates (T_1 and T_2) for dispersions containing different volumetric ratios of T_1-only ($NaYF_4$-$NaGdF_4$ core-shell) and T_2-only (Fe) NPs.

Sample (ratio of NPs) T_1-only : T_2-only	**Raw data at 9.4 T**		**Measured values (Figures 1 and 2)**		**Calculated values (Figures 1 and 2)**	
	T_1 (ms)	**T_2 (ms)**	**$1/T_1$ (s^{-1})**	**$1/T_2$ (s^{-1})**	**$1/T_1$ (s^{-1})**	**$1/T_2$ (s^{-1})**
T_1 only	1902	231	0.53	4.33	24.21	197.81
T_2 only	513	1.5	1.95	666.67	0.62	126.85
1:1	1099	4	0.91	250.00	2.15	337.32
1:2	829	3.9	1.21	256.41	2.58	443.67
2:1	1286	4.7	0.78	212.77	1.68	224.23
1:3	711	1.5	1.41	666.67	4.96	503.56
3:1	1437	6.1	0.70	163.93	1.47	171.08
1:4	566	1.5	1.77	666.67	2.97	536.81
4:1	1506	7.8	0.66	128.21	1.33	137.83

Values in red were assumed to be 1.5 ms because they were below detection limit (< 2 ms) and could not be measured. If the T_2-only NPs are diluted in deionized water that gives a measurable T_2 value (above detection limit), this sample could be then added to T_1-only NPs in the same ratios as in Table 6.1 to obtain the T_1 and T_2 relaxation times.

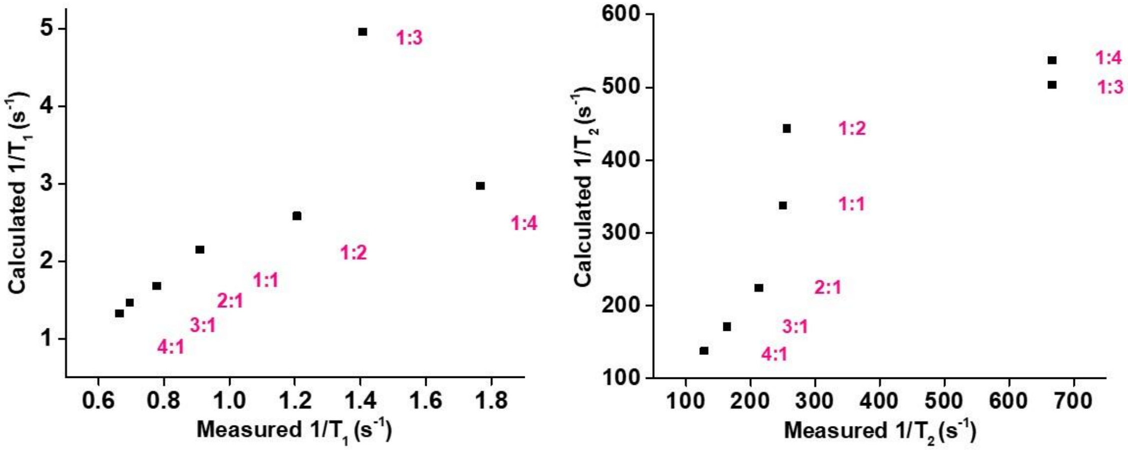

Figure 6.3. Calculated and measured relaxation rates of dispersions containing different volumetric ratios of T_1-only and T_2-only NPs.

6.3 Conclusion

A proof of concept of correlation of T_1 and T_2 relaxation rates was demonstrated employing $NaYF_4$-$NaGdF_4$ core-shell NPs as 'T_1-only' NPs [NPs that yield (only) T_1 contrast (high r_1/r_2 ratio) ideally] and Fe NPs as 'T_2-only' NPs [NPs that imparts (only) T_2 contrast (high r_2/r_1 ratio)]. The non-linear patterns of the plots of experimentally measured and theoretically calculated relaxation rates of different volumetric combinations of T_1-only and T_2-only NPs suggests that the relaxation rates are not additive. Contrasts from T_1- and T_2-weighted images could be correlated in MRI phantom imaging. MRI correlation has profound potential applications in differentiating normal/healthy tissues from pathological states in cancers and traumatic brain injury.

Chapter 7. Inter-particle Exchange Dynamics of Phospholipid-PEG coating on Nanoparticles

7.1 Introduction

The past two decades has witnessed extensive research on the biomedical applications of inorganic nanoparticles (NPs), especially, in the field of imaging and drug delivery.[171] In addition to their tunable optical and magnetic properties, the size, shape, surface chemistry and other physicochemical properties of the NPs are manipulated so as to facilitate their transport as target-specific diagnostic or therapeutic agents across biological barriers.[7-8] The surface coating properties of NPs play a significant role in their *in vivo* behavior by assessing their biocompatibility, cytotoxicity, pharmacokinetics and preventing aggregation in order to direct them to their intended target.[14,172] This has led to methodologies to study the design, stability, chemistry and dynamics of the surface coating of NPs for their potential clinical implementation.[172]

Nature's frequent use of phospholipid vesicles as carriers in biology has led to attention on encapsulating NPs with phospholipids to impart biocompatibility and mimic the composition and functionality of cell's external membrane.[76,173-175] Phospholipid coating strategies have been investigated in a wide variety of inorganic nanostructures such as quantum dots,[173] superparamagnetic iron oxide NPs,[76] silica NPs,[174] and lanthanide-based NPs[175] for potential medical applications. Phospholipids, not only render NPs water dispersible, but also provide a platform for conjugating targeting moieties due to their amphiphilic structural design which can bear functionalities for bioconjugation. Such features contribute to the interactions between NPs and their targets in the biological system.

Lanthanide-based NPs are of particular interest in bioimaging due to their unique optical and magnetic properties arising from the 4*f* electronic configuration of lanthanides.[54] For instance, $NaDyF_4$ NPs, with paramagnetic Dy^{3+} centers having high magnetic moment (10.65 μ_B), have proved to produce appreciable negative contrast in magnetic resonance imaging (MRI) at clinical field of 3 T and high field of 9.4 T, thereby, overcoming the limitations of presently used clinical complexes at high magnetic fields.[39] In spite of abundant literature on the development and promising applications of these types of NPs, lack of reliable methods to prevent adverse physiological consequences in a biological system owing to the surface chemistry of the NPs has restricted the use of NPs to the research labs. To address the challenges of clinical implementation of these NPs, surface coating dynamics need to be well investigated. To the best of our knowledge, there is no published experimental work, on the exchange dynamics of phospholipids coating (lanthanide-based) NPs. This is dealt with in the current chapter employing $NaDyF_4$-$NaYF_4$ core-shell NPs which are potential MRI contrast agents and are coated with phospholipids having amine end groups for bioconjugation and polyethylene glycol (PEG; one per phospholipid unit) moieties that prevent non-specific adsorption of proteins[17] on to the surface of NPs.

The present study investigates inter-particle exchange of phospholipids coating $NaDyF_4$-$NaYF_4$ core-shell NPs (~28 nm core diameter) employing fluorescence resonance energy transfer (FRET) between two Alexa dyes tagged on to the NPs. Alexa dyes are a class of highly fluorescent and photostable dyes compared to their conventional spectral analogues such as cyanine, rhodamine, fluorescein, etc.[176] The current work has used Alexa-488 and Alexa-594, which are the green fluorescent donor and the red fluorescent acceptor dyes, respectively, the *N*-hydroxysuccinimide (NHS) esters of which are conjugated to the amine end groups of phospholipids coating NPs via amide bond formation. Both the sets of Alexa-488 and Alexa-594 tagged NPs are mixed to allow for inter-particle exchange of phospholipids and then dialyzed for 24 hours to get rid of free, unbound molecules, if any, from the mixture. Excitation of the donor dye (Alexa-488) resulted in energy transfer to the acceptor dye (Alexa-594), as recorded in the fluorescence emission spectra, at several dilutions of the dialyzed mixture in deionized water and phosphate buffered saline (PBS). The mixtures were diluted to increase the average distance between NPs to such a large extent that it was theoretically impossible for a phospholipid bearing Alexa dye on a NP to traverse and transfer on to another NP in the time frame of ongoing experiments. At this point of high dilution, static quenching was confirmed because phospholipids bearing Alexa-488 and Alexa-594 were already on the same NP, as a result of the initial mixing before dialysis, yielding FRET, taking care of the fact that the Förster distance (i.e., the distance at which the energy transfer efficiency is 50%) between the dyes is 6 nm.[177] This was further justified from the fact that the donor to acceptor emission intensities decreased in the same ratio with dilution. Such a phenomenon of inter-particle exchange of phospholipids was estimated over different time points from a perspective of a practical bio-application. Although this exchange process is slow which can take up to several days or weeks, it can lower the efficiency of a target-specific diagnostic or therapeutic application of NPs because the NPs get diluted in blood after administration into a living system and the phospholipids bearing targeting moieties on the surface of NPs have a probability to strip off over time. The efficiency is estimated to decrease further if the injected dose is prepared and stored for several weeks at room temperature prior to administration. Nevertheless, the *in vitro* and *in vivo* experiments detailed in Chapters 3 and 4 are expected to be hardly affected with the phospholipid exchange because a high concentration (2 weight%) of NPs (tagged with or without antibodies) were employed in a short time frame (1 h of incubation of prostate cancer cells *in vitro*, 2 h of accumulation of NPs in prostate tumors and 24 h of active targeting *in vivo*). In addition, injection of NPs lead to dilution effect in

Inter-particle exchange of phospholipids has been shown via FRET between Alexa-488- and Alexa-594-tagged NPs in different media, deionized water and phosphate buffered saline, the latter being mimicked to the physiological environment. Such a phenomenon can decrease the efficiency of a target-specific bio-application.

7.2 Results and Discussion

7.2.1 Synthesis and Characterization of $NaDyF_4$-$NaYF_4$ core-shell NPs

$NaDyF_4$ NPs were synthesized in a high boiling solvent mixture of oleic acid and 1-octadecene at 306 ^{o}C in an inert atmosphere. Already synthesized cubic phase $NaYF_4$ NPs were injected into this reaction mixture to form a shell around the core $NaDyF_4$ NPs.[56] The NP growth process proceeds via Ostwald ripening where in larger NPs with lower surface area to volume ratio are energetically favorable over the smaller NPs with high surface area to volume ratio. The cubic phase $NaYF_4$ NPs dissolve in the high temperature reaction medium and grow as hexagonal phase over the $NaDyF_4$ core particles forming thermodynamically and colloidally stable oleate-capped core-shell NPs which are well dispersed in hexanes. To transfer them from the organic to aqueous media, the oleate capped NPs were coated with functionalized phospholipids (DSPE-mPEG and DSPE-PEG-NH_2), possessing one PEG per molecule, via dual solvent exchange route using DMSO.[76] Prior to the aqueous transfer, as-synthesized $NaDyF_4$-$NaYF_4$ core-shell NPs were characterized to determine their crystal phase, structure, dispersity and composition. In Figure 7.1(A), X-ray diffraction (XRD) patterns of the NPs are indexed with the standard patterns of hexagonal phase of $NaDyF_4$. The peaks are slightly shifted with respect to the corresponding standard pattern giving a sign of lattice mismatch. This arises due to the tensile strain induced between the core and the shell layer owing to the different ionic radii in the corresponding unit cells of Dy^{3+} (1.167 Å) and Y^{3+} (1.159 Å).[61] Figure 7.1(B) shows the transmission electron microscopy (TEM) image of the $NaDyF_4$-$NaYF_4$ core-shell NPs with a fairly uniform particle size distribution, 27.7 nm ± 0.8 nm, as depicted in the histogram. Inductively coupled plasma mass spectrometry (ICP-MS) was done to determine the concentration of Dy^{3+} (3.5 mM) and Y^{3+} (0.4 mM) ions composing the core and the shell, respectively. The concentration of Dy^{3+} in NPs was used to determine the longitudinal (r_1) and transverse (r_2) relaxivities of the NPs. $NaDyF_4$-$NaYF_4$ core-shell NPs are characterized by their r_1 and r_2 relaxivities, which are the corresponding change in relaxation rates ($1/T_1$ and $1/T_2$) of solvent water protons in presence of the NP, normalized to the concentration of Dy^{3+} ions, [Dy^{3+}], or NPs, as shown in the equation: $\boldsymbol{\frac{1}{T_i} = \frac{1}{T_i^0} + r_i[Dy^{3+}]; i = 1, 2}$. From Figure 7.1(C), their ionic r_1 and r_2 relaxivities were found to be 0.15 and 162.25 mM^{-1} s^{-1} while the corresponding NP relaxivities were 15,000 and 11,400,000 mM_{NP}^{-1} s^{-1}). Such a high value of r_2 relaxivity is due to the high magnetic moment of paramagnetic Dy^{3+} (10.65 μ_B) which results in high magnetization of the core $NaDyF_4$ at the applied field of 9.4 T.

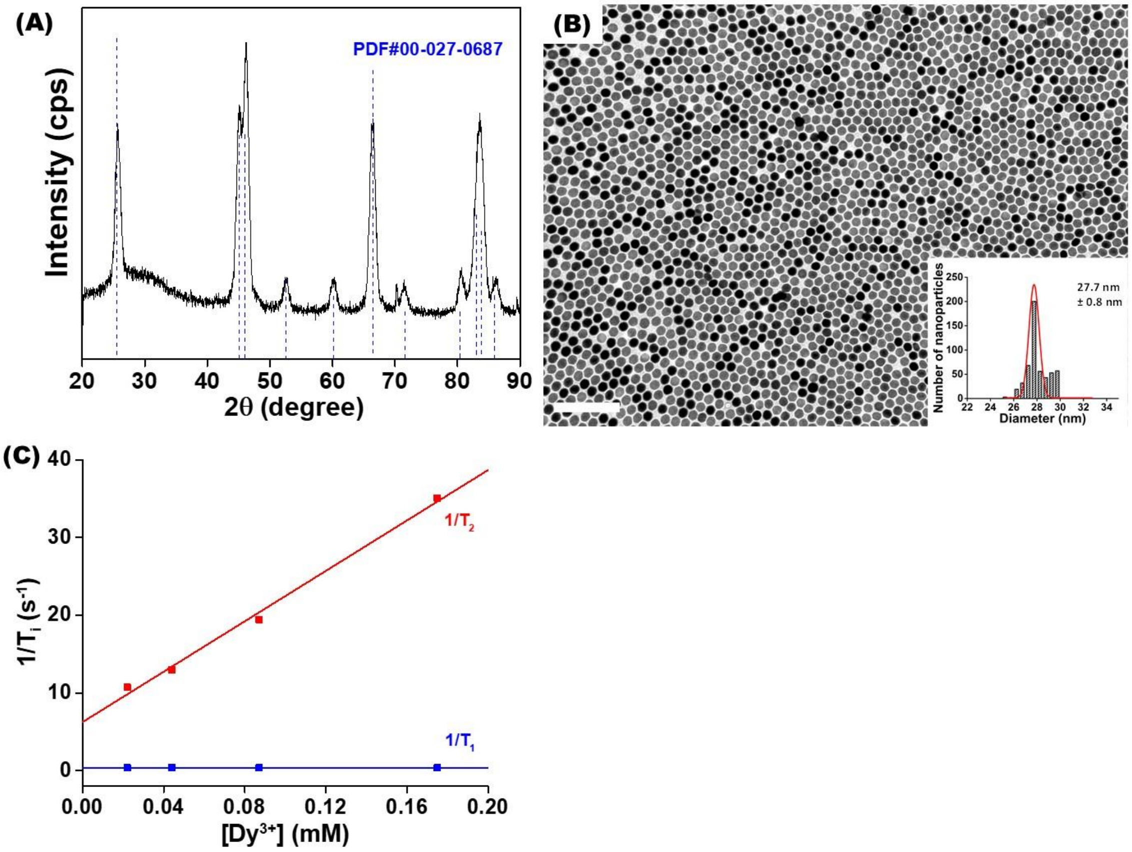

Figure 7.1. Characterization of $NaDyF_4$-$NaYF_4$ core-shell NPs: (A) XRD patterns of the NPs indexed with the standard patterns of the hexagonal phase of $NaDyF_4$ (PDF 00-027-0687). (B) TEM image of the NPs with the corresponding histogram showing particle size distribution. White scale bar = 100 nm. (C) Plots of T_1 and T_2 relaxation rates at 9.4 T in different dilutions of $NaDyF_4$-$NaYF_4$ core-shell NPs with the corresponding linear fits (blue = $1/T_1$, red = $1/T_2$). R-square (Coefficient of Determination) defining the goodness of a fit lie in the range of 0.98752–0.99429.

7.2.2 FRET studies for inter-particle exchange of phospholipids

The exchange processes of phospholipids coating NPs were studied based on the distance dependent energy transfer from the donor dye, Alexa-488, to the acceptor dye, Alexa-594, both being on the same NP after mixing and dialysis. Figure 7.2 depicts a schematic diagram of the inter-particle exchange process. As shown in step (A), two different batches of Alexa-488- and Alexa-594-tagged phospholipids coating NPs are mixed and dialyzed, resulting in (B) in which the phospholipids bearing dyes have exchanged among the NPs. These processes were investigated in deionized water and phosphate buffered saline whose pH (= 7.4) matches that of the physiological environment.

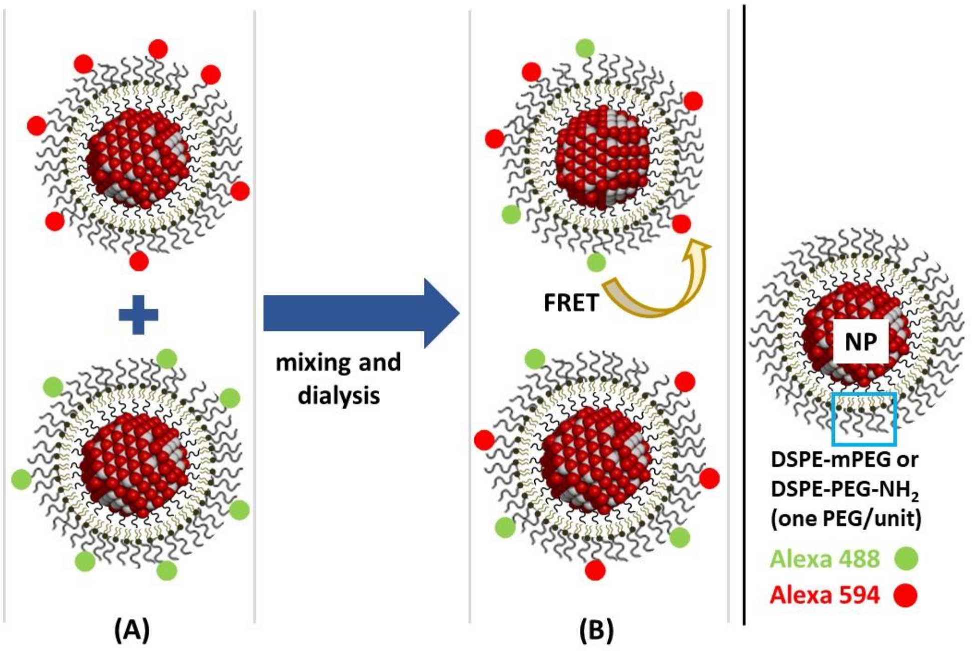

Figure 7.2. Schematic representation of inter-particle exchange of phospholipids. (A) Alexa-488- and Alexa-594-tagged phospholipids coating (oleate capped) NPs are dispersed in deionized water (or PBS) prior to mixing. (B) Alexa-488- and Alexa-594-tagged phospholipids have exchanged among NPs after mixing and dialysis. Because both the dyes are so close being on the same NP, excitation of Alexa-488 yields in emission of Alexa-594 via FRET.

7.2.2.1 Inter-particle exchange of phospholipids in deionized water

Alexa-488 was tagged on to phospholipids coating $NaDyF_4$-$NaYF_4$ core-shell NPs the emission spectrum of which is depicted in Figure 7.3 showing its characteristic peak[176] at 516 nm when excited at 495 nm. Similarly, Alexa-594 when tagged with the NPs shows its typical emission peak[176] at 614 nm when excited at 590 nm (Figure 7.3).

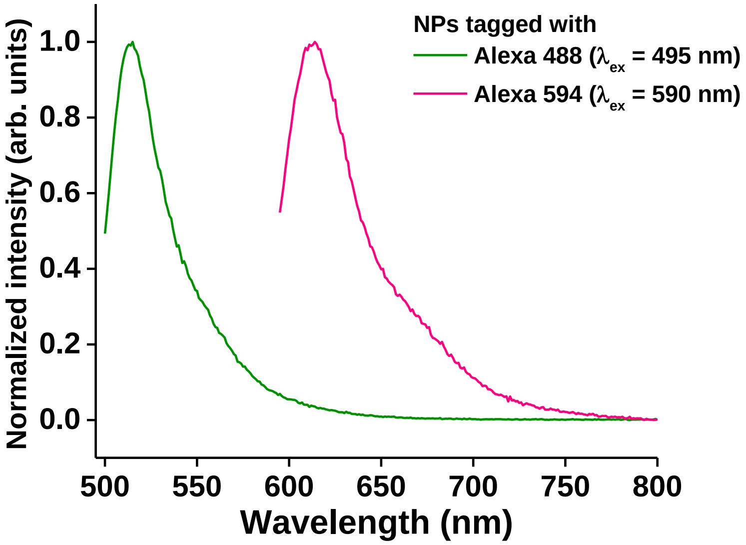

Figure 7.3. Emission spectra of Alexa-488 tagged NPs (green) and Alexa-594 tagged NPs (pink) before mixing. Excitation wavelengths are 495 nm and 590 nm, respectively.

After mixing of Alexa-488- and Alexa-594-tagged NPs on a rotary shaker for 3 h, dialysis was carried out for 24 h to get rid of any unbound, free dye or phospholipid molecules from the mixture in deionized water. The emission spectrum of this solution (0x) is shown in Figure 7.4 in which excitation of Alexa-488 at 495 nm results in emission peaks at 516 nm and 620 nm corresponding to Alexa-488 and Alexa-594. At this concentration, quenching of fluorescence emission can occur in terms of both dynamic and static quenching processes. Dynamic quenching[103] arises due to collisional electrostatic dipole-

dipole interaction between the donor and the acceptor dye-tagged phospholipids, within the lifetime of the excited donor. Such collisional quenching is evident in the emission peak shift of Alexa-594 to 620 nm from its typical 614 nm because multiple NPs collide resulting in non-radiative and radiative processes at different surface topographies. The emission peak of acceptor could shift to a few more nanometers of wavelength and/or broaden because the dye's polarity and polarizability is affected when multiple NPs come into contact with each other upon collision. On the other hand, static quenching arises when both Alexa-488- and Alexa-594-tagged phospholipids are on the same NP and close enough for FRET to occur. Since the Förster distance of Alexa-488 and Alexa-594 is 6 nm,[177] it is possible for the energy transfer to manifest when both the dyes are on the same NP.

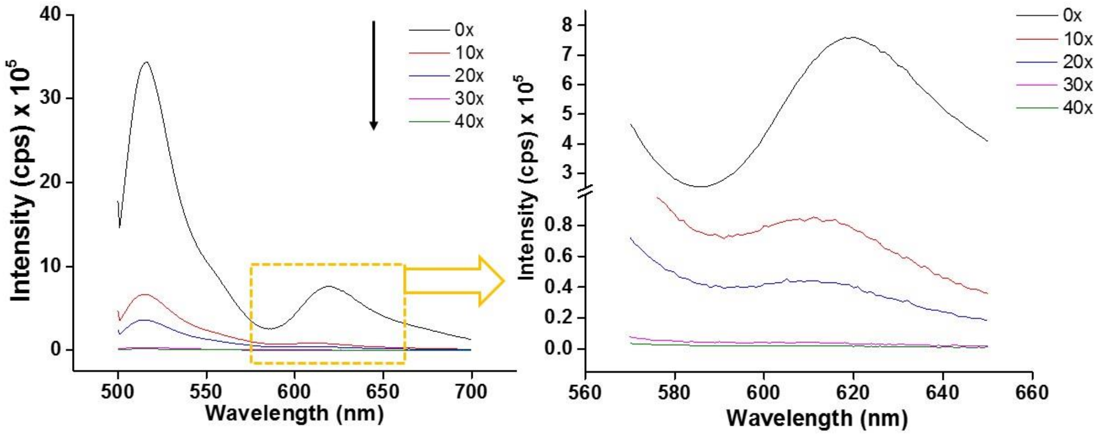

Figure 7.4. Emission spectra obtained for dialyzed NP solution in deionized water when excited at 495 nm.

For the 0x solution, ICP-MS yielded Dy^{3+} and Y^{3+} ionic concentrations from which molar concentration of NPs was determined to be 0.25 mmol/L of solution and 10^{13} NPs/mL used per reaction. From the probability density function of distance to the nearest neighbor particle in a 3D system with N particles in a volume V,[178] mean inter-particle distance, $r_s = 0.874 \times \left(\frac{3}{4\pi n}\right)^{1/3}$ where n = number density = N/V. Table 7.1 enlists r_s calculated for different dilutions of NPs. In the 0x solution, for 10^{13} NPs in 1 mL (1 cm^3) solution, $r_s = 0.252$ µm. This value of inter-particle distance is much higher than the Förster distance of Alexa-488 and Alexa-594. Since the NPs are in Brownian motion, there is a high probability of collisional energy transfer if the mean displacement of the NPs is higher than the inter-particle distance in a given period of time. From the Stokes-Einstein relation on Brownian motion, diffusion coefficient of the NPs, $D = \frac{k_B T}{6\pi\eta r}$, where k_B = Boltzmann's constant = 1.38×10^{-23} J K^{-1}, η = viscosity of the medium = 8.90×10^{-4} Pa.s at temperature, T = 298 K; hydrodynamic radius of NP = 20 nm. Introducing these values in the equation gives $D = 1.75 \times 10^{-7}$ cm^2 s^{-1}. For a particle diffusing over a distance, its mean displacement, $\langle x^2 \rangle = q_i D t$, where t = time, q_i = dimensionality (= 2, 4 or 6 for 1, 2 or 3-dimensional diffusion). Table 7.2 lists out the mean displacement values of NPs calculated for different periods of time. After 3 h of mixing and 24 h of dialysis, the mean displacement x of a NP is found out to be 0.267 cm. For the 0x solution, the mean displacement of NPs is higher than the inter-particle distance which suggests collision of NPs resulting in swapping of phospholipids.

Table 7.1. Inter-particle distance r_s between phospholipids coated $NaDyF_4$-$NaYF_4$ core-shell NPs dispersed in deionized water or PBS.

Dilution factor	**r_s (µm)**		**Dilution factor**	**r_s (µm)**		**Dilution factor**	**r_s (µm)**		**Dilution factor**	**r_s (µm)**
0	0.25		20	0.68		50	0.93		200	1.47
10	0.54		40	0.86		100	1.17		400	1.85

Table 7.2. Mean displacement ‘x’ of a $NaDyF_4$-$NaYF_4$ core-shell NP in deionized water in time ‘t’.

t	x (cm)		t	x (cm)		t	x (cm)
1 ns	2.71×10^{-8}		10 min	0.021		27 h	0.267
1 s	8.58×10^{-4}		3 h	0.089		30 days	1.381
1 min	0.006		24 h	0.252		3 months	2.392

The solution was diluted 10 times (10x) to decrease the possibility of collisional quenching because the inter-particle distance increases with dilution. The resulting emission peak intensities for donor and acceptor decreased with respect to that observed in 0x solution while Alexa-594 peak was at 614 nm showing very faint possibility of interaction with surrounding NPs bearing dyes. To observe static quenching in the phospholipid tagged dyes via FRET, the dialyzed solution was diluted further to 20, 30 and 40 times in deionized water. As depicted in Figure 7.3, an expected decrease in peak intensities is seen at 516 and 614 nm with subsequent NP dilutions. With dilutions from 10x–30x, all the peaks are shifted to 614 nm compared to the original 0x solution. This peak shift could be attributed to the change in polarity and polarizability of the fluorophore environment, for instance, Alexa-594 bearing phospholipid stripes off from one NP and adsorbs to another NP that has an Alexa-488 bearing phospholipid nearby resulting in FRET. Further, the ratio of donor to acceptor peak intensities is almost identical for 10x, 20x and 30x dilutions (in the range of 9.88–9.92) which is attributed to static quenching only – a scenario when both Alexa-488- and Alexa-594-tagged phospholipids are on the same NP after inter-particle exchange. At 40x dilution, the emission intensity of Alexa-594 is hardly observed. Figure 7.5 depicts the emission spectrum of the same batch of 40x dilution taken after 3 months which the shows Alexa-594 peak at 614 nm as a result of FRET indicating that the exchange process is slow because the acceptor emission intensity has only slightly increased over the months in the closed system/vial, while the ratio of donor and acceptor emission intensities is the same. The FRET studies were moved to phosphate buffered saline whose composition and pH match with that of the environment in blood.

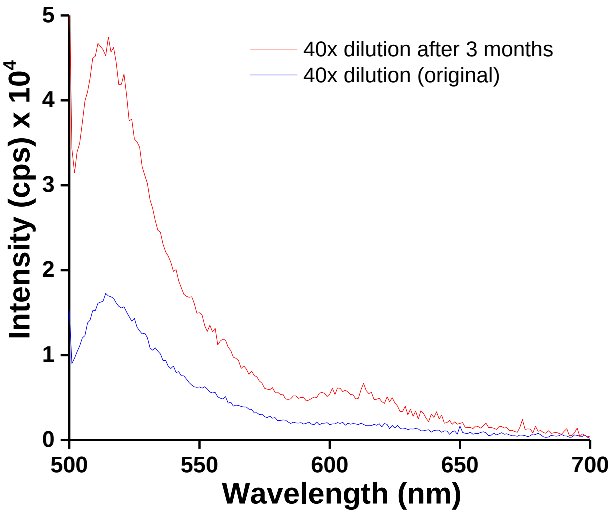

Figure 7.5. Emission spectra obtained for dialyzed NP solution (40x dilution) in deionized water after 3 months when excited at 495 nm.

7.2.2.2 Inter-particle exchange of phospholipids in phosphate buffered saline (pH 7.4)

The exchange dynamics was studies in phosphate buffered saline because it mimics the physiological environment including pH. Phospholipid-coated $NaDyF_4$-$NaYF_4$ core-shell NPs were tagged with Alexa-488 and Alexa-594 and dispersed in 10 mM of PBS. After mixing for 3 h and dialyzing for 24 h, emission spectra were obtained for different dilutions (10x–220x) of the mixture at Alexa-488 excitation (495 nm; donor). As shown in Figure 7.6, the broad peaks at 516 and 614 nm indicate the characteristic emission from Alexa-488 (donor) and Alexa-594 (acceptor), respectively. As anticipated, the peak intensities decreased at 516 and 614 nm with subsequent NP dilutions. Even after 220x dilution, the acceptor emission is clearly observed in the zoomed in image of Figure 7.6. The ratio of donor to acceptor peak intensities in 10x – 60x varied from 7.16–9.90. Such fluctuations could be ascribed to the prevalence of both dynamic and static quenching at these dilutions. The ratio became almost constant for the rest, 70x – 220x, dilutions (in the range 8.35–8.74). This indicates that both the peak intensities drop with the same intensity with dilution which can be ascribed to static quenching. These results suggest that the inter-particle exchange of phospholipids is more prominent in phosphate buffered saline than in deionized water since the emission peak intensity almost dropped completely at 40x dilution in deionized water, whereas in PBS, FRET is observed even at 220x dilution. The dilutions in either deionized water or PBS have the same concentration of NPs because both the media had identical initial concentration of the dye tagged NPs.

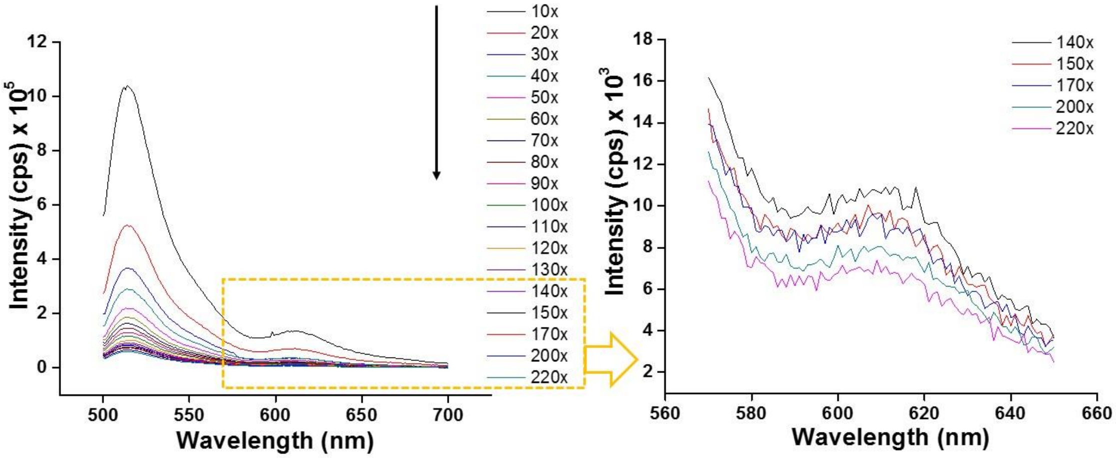

Figure 7.6. Emission spectra obtained for dialyzed NP solution in phosphate-buffered saline when excited at 495 nm.

To further confirm with the observation of FRET as a result of static quenching at higher dilutions of NPs, $NaDyF_4$-$NaYF_4$ core-shell NPs tagged with Alexa-488 and Alexa-

594 were mixed at a concentration same as in the 400x dilution in 10 mM PBS. 10 μL each of Alexa-488- and Alexa-594-tagged NPs were mixed in 4.4 mL of 10 mM PBS for 3 h and then centrifuged in Vivaspin centrifugal filters (MWCO 50,000 Da) at 500 *g* for 5 min. The filtrate collected should have the free phospholipids stripped off from NPs and/or the phospholipids undergoing exchange process. To validate static quenching of fluorescence, emission spectra, as shown in Figure 7.7, were obtained for (a) the donor in PBS before adding the acceptor, (b) the solution after 3 h of mixing and before centrifugal filtration, (c) the supernatant, and (d) the filtrate collected after centrifugal filtration. The donor in PBS shows a typical 516 nm emission peak of Alexa-488. As the NPs tagged with Alexa-594 (acceptor) are added and after 3 h of mixing, emission peak of Alexa-488 is drastically reduced, while Alexa-594 emission peak is observed prominently at 614 nm indicating FRET. After centrifugation through the 50,000 Da MWCO filters, the spectrum of the supernatant containing only the NPs tagged with dyes (no free phospholipids) still shows both the emission peaks of donor and acceptor confirming FRET because of inter-particle exchange of phospholipids even in a much diluted solution. The filtrate, as expected, shows the emission peaks of Alexa-488 and Alexa-594 indicating dynamic quenching because the ratio of donor to acceptor emission intensities is different from that of the supernatant.

At such a high dilution of 400x, the NP-tagged dyes are 1.85 μm apart (Table 7.2), it is unlikely to achieve FRET due to dynamic interaction of NPs at such a large dilution since Förster radius is 6 nm, for Alexa-488 and Alexa-594. Further, the excited state lifetime of Alexa-488 is 4.1 ns[177] and if FRET lifetime is 1 ns, the mean displacement of a NP in 1 ns is only 0.214 nm. This substantiates static quenching because in 1 ns a NP traverses much less than the inter-particle distance for collision to occur resulting in FRET.

This overrules the phenomenon of FRET as a result of collision of NPs undergoing Brownian motion. Considering the long time range of interparticle exchange of phospholipids in a much diluted environment in deionized water of PBS, it is unlikely that the experiments undertaken with antibody tagged NPs in Chapters 3 and 4 would be affected because a high concentration (micromolar) of antibody tagged NPs is used during incubation of cells (maximum of 1 h, *in vitro* prostate cancer studies; Chapter 3) or for *in vivo* studies (2 h accumulation in prostate tumors; Chapter 3) for a short time period.

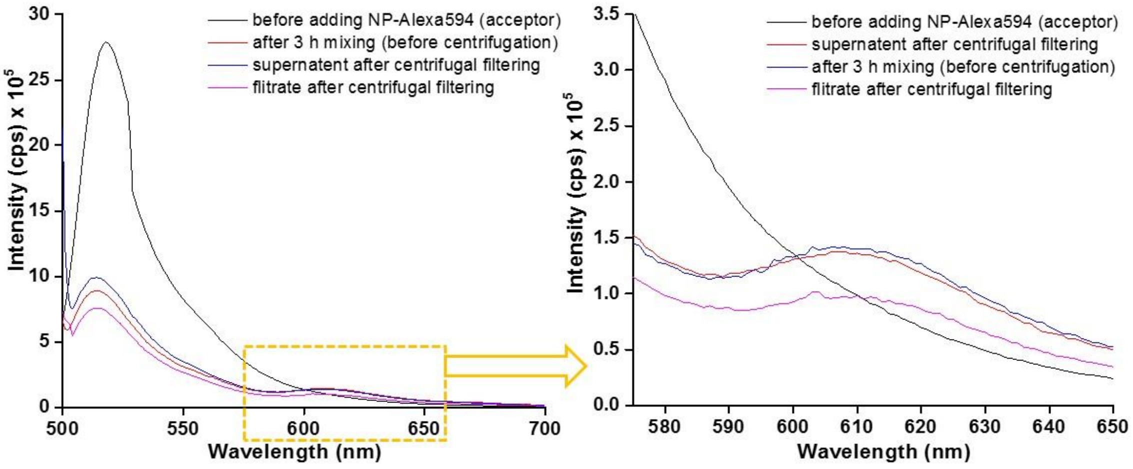

Figure 7.7. Emission spectra obtained for NP solution in phosphate-buffered saline at different stages of preparation. Excitation wavelength was chosen at 495 nm.

Inter-exchange of phospholipids has been observed as a natural phenomenon in the lipid bilayers of cell membranes.[179] Although this exchange process is slow in a biological system, it may prove unfavorable for NPs coated with phospholipids that are tagged with targeting moieties. The phospholipids bearing moieties can possibly strip off from the surface of NPs during the exchange process and undergo blood clearance hindering the target-specific application of NPs. Because less than 1% of injected NPs reach their target (tumor) *in vivo*,[131] it is essential to make stealth NPs that have stable surface chemistry to guide the NPs to their target.

7.3 Conclusions

$NaDyF_4$-$NaYF_4$ core-shell NPs, as potential NP-based MRI contrast agents, were synthesized, characterized and coated with phospholipids bearing PEGs to study the exchange dynamics of the lipids. Two highly photostable fluorophores, Alexa-488 and Alexa-594 were tagged on to the functionalized phospholipids coating NPs. Inter-particle exchange of phospholipids was observed via FRET when both Alexa-488 (donor) and Alexa-594 (acceptor) bearing phospholipids from different NPs swapped during mixing and dialysis and populated the same NP. The FRET studies yield useful information about the stability of phospholipid coated NPs which is vital for biomedical applications of NPs.

7.4 Experimental Section

Chemicals. Yttrium(III) oxide (99.9%), dysprosium(III) chloride hexahydrate (99.9%), sodium trifluoroacetate (98%), ammonium fluoride (≥ 99.99%), oleic acid (tech grade, 90%), 1-octadecene (tech grade, 90%), and hexanes were purchased from Sigma Aldrich. Oleylamine (97%) was purchased from Acros, sodium hydroxide, trifluoroacetic acid, dimethyl sulphoxide (99.9%), toluene, anhydrous ethanol and methanol from Caledon laboratories and 1,2-distearoyl-*sn*-glycero-3-phosphoethanolamine-*N*-[methoxy(polyethylene glycol)-2000] (ammonium salt) [abbreviated as DSPE-mPEG] and

1,2-distearoyl-*sn*-glycero-3-phosphoethanolamine-*N*-[amino(polyethylene glycol)-2000] (ammonium salt) [abbreviated as DSPE-PEG-NH_2] from Avanti Polar Lipids, and Alexa-488 NHS Ester (Succinimidyl Ester) and Alexa-594 NHS Ester (Succinimidyl Ester) (Figure 7.8) from Thermo Fisher Scientific. 10 mM (1X) sterile phosphate buffered saline (PBS, pH 7.4) was purchased from Bio-world.

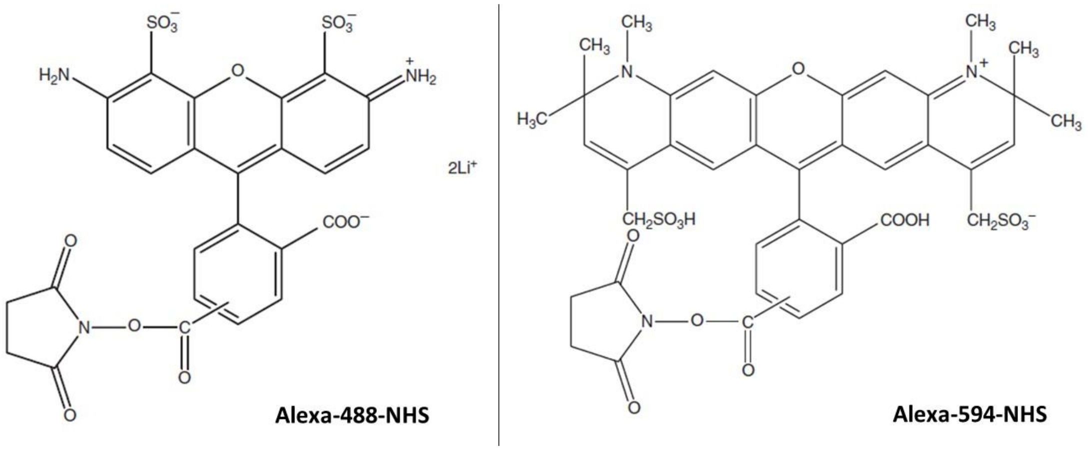

Figure 7.8. Structures of Alexa-488- and Alexa 594-carboxylic acid succinimidyl esters

Synthesis of cubic (α) phase $NaYF_4$ NPs (sacrificial NPs). In a 100 mL three necked round bottom flask, yttrium oxide (1 mmol) and 50% trifluoroacetic acid (10 mL) were mixed together and refluxed at 85 °C for 5 h. Yttrium trifluoroacetate was obtained after evaporating excess water at 65 °C overnight. After adding sodium trifluoroacetate (2 mmol), oleic acid (5 mL), oleylamine (5 mL) and 1-octadecene (10 mL) to it, the reaction medium was heated at 130 °C for 45 min under vacuum to remove residual water. Next, the solution was heated at 285 °C under argon, stirring vigorously for 45 min. The solution was cooled down to room temperature under air flow. The NPs were precipitated and washed with 60 mL of ethanol thrice by centrifugation (7,000 *g*, 10 min, Beckman Coulter Spinchron 15-rotor F0830) and finally dispersed in 10 mL of hexanes.

Synthesis of hexagonal (β) phase $NaDyF_4$-$NaYF_4$ core-shell NPs. Dysprosium(III) chloride hexahydrate (1 mmol), oleic acid (1.5 mL) and 1-octadecene (7.5 mL) were mixed and stirred under vacuum at 130 °C for 45 min. The solution was cooled to room temperature, added with a solution of NaOH (2.5 mmol) and NH_4F (4 mmol) in methanol (10 mL) and stirred for 1 h. Methanol was removed thereafter at 80 °C. The temperature was raised to 306 °C (~15 °C/min) under argon flow and the solution was stirred vigorously for 1 h 15 min. The cubic (α) $NaYF_4$ NPs in 1-octadecene (1 mL) was injected into the solution and stirred at 306 °C for 15 min to form a core-shell nanocrystal structure. The solution was cooled down to room temperature in air. The NPs were precipitated and washed with 60 mL of ethanol thrice by centrifugation (7,000 *g*, 10 min, Beckman Coulter Spinchron 15-rotor F0830) and finally dispersed in 10 mL of hexanes.

Phase transfer of NPs to water using phospholipids. NPs dispersed in hexanes were transferred to deionized water via dual solvent exchange using DMSO.[76] The NPs were dispersed in 0.4 mL toluene at 7.0 mg/mL and added with DSPE-mPEG and DSPE-PEG-NH_2 in 0.8 mL chloroform taking appropriate weight ratio of DSPE-mPEG and DSPE-PEG-NH_2 to NP. 4 mL of DMSO was added slowly to the solution which was then incubated on a shaker for 30 minutes at room temperature. Chloroform and toluene were removed completely by vaporization under vacuum. Deionized water was added to the colloidal solution in DMSO to reach a total volume of 20 ml. DMSO was completely substituted with deionized water by three rounds of centrifugation in centrifugal filter tubes

(Vivaspin Turbo 15, 100 kDa cutoff size) leaving a final volume of 1 mL of NP dispersion. The final solution was filtered through 0.45 µm glass microfiber filter.

***Conjugation of Alexa-488 and Alexa-594 with $NaDyF_4$-$NaYF_4$ core-shell NPs and inter-particle exchange of phospholipids*.** This reaction proceeds via amide bond formation between amines on the DSPE-PEG-NH_2 and *N*-hydroxysuccinimide (NHS) esters of the dyes. Appropriate amount of $NaDyF_4$-$NaYF_4$ core-shell NPs coated with DSPE-mPEG and DSPE-PEG-NH_2 was diluted to 2 mL in 10 mM phosphate buffer saline. The volume of NP solution and amount of the dye were used based on the number of amines from the phospholipid coating available to bind to the number of succinimidyl esters of Alexa-488 to form amide bond. 200 µL of 0.1 mg/mL Alexa-488 NHS was added to the NP solution and stirred for 1 h at room temperature. The resultant solution was dialyzed for 24 h using a 50,000 Da MWCO dialysis tubing (Spectra/Por from Spectrumlabs) in deionized water to get rid of any unreacted, unbound, free molecule. Similarly, Alexa-594 NHS was tagged with the NPs and dialyzed for 24 h. To allow for any inter-particle exchange of phospholipids, 500 µL of both batches of Alexa-488- and Alexa-594-tagged NPs were mixed on a shaker for 3 h and dialyzed for 24 h (50,000 Da MWCO dialysis tubing; Spectra/Por from Spectrumlabs) to get rid of any free molecules.

***Characterization*.** X-ray Diffraction (XRD) patterns were collected using a Rigaku Miniflex diffractometer with Cr Kα radiation (λ = 0.2290 nm, 30 kV, 15 mA) with a scan step size of 0.05 degrees (2θ). 15 drops of the NP dispersion in hexane were added onto an indented zero-background sample holder and dried to get the diffraction patterns.

Transmission electron microscopy (TEM) images were acquired using a JEOL JEM-1400 microscope operating at 80 kV. The NP dispersion in hexane was drop-cast onto a formvar carbon film supported on a 300-mesh copper grid (3 mm in diameter) and allowed to dry in air at room temperature, before imaging. The size distribution was obtained from averaging a minimum of 300 NPs.

Dynamic light scattering (DLS) measurements were done using Brookhaven Zeta PALS instrument with a 90Plus/BI-MAS Multi Angle Particle Sizing option, equipped with a 15 mW solid-state laser (658 nm). All data were obtained at a single scattering angle (90^o) and averaged over ten scans of scattered intensity weighted plots of NPs, dispersed in deionized water, filtered through 0.45 μm pore sized Whatman glass microfiber filter (Sigma Aldrich).

Inductively coupled plasma mass spectroscopy (ICP-MS) analysis was carried out using a Thermo X-Series II (X7) quadrupole ICP-MS to determine the concentration of Dy^{3+} and Y^{3+} ions concentration in the NP stock solution. The aqueous dispersion of NPs was digested in concentrated nitric acid at 135 ^oC in sealed Teflon vials for 3 days and diluted with ultrapure water before analysis. Calibration was done by analyzing serial dilutions of a mixed element synthetic standard containing a known amount of dysprosium and yttrium. Each sample, standard and blank, were spiked with indium (to a concentration of ~7 ppb) as the internal standard to correct for signal drift and matrix effects.

Steady state excitation and emission measurements were done using an Edinburgh Instruments' FLS920 fluorimeter equipped with 450 W arc Xe lamp. All the emission spectra were collected with a resolution of 1.00 nm using a Peltier-cooled Hamamatsu

R928P PMT (200–800 nm) detector. The emission patterns were corrected for the detector sensitivity. All dispersions were measured in a 1 cm path length quartz cuvette. The data were analyzed using Origin 2015 (OriginLab, Northampton, MA, version b9.2.272).

Relaxivity measurements. Aqueous dispersions of NPs were used to determine the relaxation times. T_1 and T_2 measurements were done using a 9.4 T/21 cm bore magnet (Magnex, UK) and a Bruker console (Bruker, Germany) (by Dr. Barbara Blasiak and Dr. Boguslaw Tomanek, University of Calgary). A transmit/receive radio frequency volume birdcage coil was applied to excite protons and obtain resonant signal. For T_2 measurements, a single slice multi-echo pulse sequence was used with the following pulse parameters: repetition time (TR) 5 s, matrix size 128 × 128, field of view (FOV) 3 cm × 3 cm, slice thickness 2 mm, 128 echoes 4 ms apart. T_2 relaxation times were calculated using a single exponential fitting of the echo train (Marevisi, Canada). For T_1 measurements, TRUE FISP method was used with the following pulse sequence parameters: TR 3 s, TE 1.5 s, matrix size 128 × 128, FOV 3 cm × 3 cm, slice thickness 3 mm, 60 frames × 4 segments, segment time 192 ms. The relaxation times were calculated using single exponential fitting of the data (MATLAB "1sqcurvefit").

The T_1 and T_2 relaxation times obtained for different dilutions of NPs in deionized water were plotted against concentration of Dy^{3+} ions in the NP solution, $[Dy^{3+}]$, to obtain the values of r_1 and r_2 relaxivities from the slope of the linear fit, using the empirical equation: $\boldsymbol{\frac{1}{T_i} = \frac{1}{T_i^0} + r_i[Dy^{3+}]; i = 1, 2}$. The Dy^{3+} concentration was obtained from ICP-MS analysis of the NPs; T_i^0 denote the relaxation times of the water protons in absence of the paramagnetic NPs.

Chapter 8. Conclusions and Possible Future Work

8.1 Conclusions

Synthesis, characterization and potential application of colloidal sodium lanthanide fluoride and iron NPs as MRI CAs have been investigated in this dissertation. The paramagnetic relaxation mechanism has been dealt with in Chapter 2 in details by unravelling the inner, second and outer sphere relaxation in two different sizes of NPs using Eu^{3+} as a probe to track the water exchange. Paramagnetic sodium lanthanide fluoride NPs with appropriate surface chemistry serve as potential MRI-biomarkers in specifically targeting prostate cancer and tracking intraneural tau protein following mild traumatic brain injury, as demonstrated in Chapters 3 and 4. Superparamagnetic iron NPs have been investigated for their colloidal stability in Chapter 5. Chapter 6 introduces the concept of MRI correlation. The phospholipid-PEG coating strategy used for NPs to mimic the cell membrane structure, to avoid a protein corona formation *in vivo*, actually undergoes some exchange dynamics which is demonstrated in Chapter 7.

Chapter 1 gives an overview of colloidal NPs with an emphasis on their surface chemistry for bioimaging. With the introduction of MRI, paramagnetic lanthanide and superparamagnetic iron based NPs have been discussed for their promising application as CAs in disease diagnosis.

Chapter 2 demonstrates the exchange phenomena of (un)coordinated water molecules with bulk in case of two different sized paramagnetic NPs by using europium lifetime decay as a probe which is highly sensitive to proximate O-H overtones. The water exchange phenomena have been deconvoluted to substantiate the inner, second and outer sphere relaxation of water protons surrounding a paramagnetic NP in an applied field. Bigger NPs (~20 nm sized) have contribution of outer sphere relaxation exclusively towards their relaxivities while the smaller NPs (~3 nm sized) have the contribution from inner, second, and outer spheres of relaxation.

Chapter 3 details on the synthesis and characterization of $NaDyF_4$-$NaGdF_4$ core-shell NPs which shorten both the longitudinal and transverse relaxation of water protons producing enhanced positive and negative contrast compared to clinical CAs. Surface modification of these NPs using phospholipid-PEGs renders them biocompatible and tagging them with anti-PSMA antibody make them potential MRI-biomarker in specific targeting of prostate cancer.

Chapter 4 extends the application of $NaDyF_4$-$NaGdF_4$ core-shell NPs in tracking the neuronal protein tau following mild traumatic brain injury. The conjugates of anti-tau antibody and NP, with a ratio of 4 antibodies *per* NP, could traverse through neuronal membrane to specifically bind to tau.

Chapter 5 unravels a facile synthesis of iron NPs of three different sizes out of which the 15.2 nm sized NPs were most stable against oxidation. They had remarkable colloidal stability when dispersed in water with the resistance to oxidation lasting for several months.

Chapter 6 illustrates the concept of MRI correlation for biological applications using T_1-only and T_2-only NPs based on their r_2/r_1 ratios.

Chapter 7 highlights on the exchange dynamics of phospholipids when coated on NPs. This interparticle exchange was observed via FRET between two highly photostable fluorophores, Alexa-488 and Alexa-594 tagged on to the functionalized phospholipids coating NPs. Useful information is gathered from FRET studies on this slow exchange process and stability of phospholipids coating NPs. Such phospholipid exchange is not expected to have influenced the targeting studies in Chapters 3 and 4 due to a short time frame (1 day) of the experiments.

8.2 Possible Future Work

Chapter 2, which deals with substantiating the inner, second and outer sphere relaxation in paramagnetic lanthanide based NPs, has many parameters which need to be understood. For instance, the water diffusion kinetics in different coordination spheres, translational correlation time, and more importantly, the spectral density terms bearing diffusion correlation time at different applied magnetic fields need to be investigated to design NPs to produce optimal contrast to noise ratio in MRI for efficient medical diagnosis.

Chapter 3 dealing with potential application of $NaDyF_4$-$NaGdF_4$ core-shell NPs as MRI CAs in prostate cancer could be elaborated in quantifying active targeting vs. passive targeting. Thorough investigation on specific uptake and retention, background or nonspecific uptake, EPR effect, blood clearance and organ distribution of NPs (tagged with and without antibodies) could be performed by studying the biodistribution of NPs in harvested organs and tumors using ICP-MS to quantify the NPs. This would quantify NP localization in tumors in a given time span.

Further potential application of $NaDyF_4$-$NaGdF_4$ core-shell NPs, extended in Chapter 4, in diagnosing mild TBI needs rigorous investigation on the reasons behind the

4:1 ratio of sdAb:NP in NP-sbAb-Alexa-488 conjugates crossing the neuronal membrane to target intracellular tau (and possibly cross the complicated BBB). *In vivo* MRI studies would confirm if this ratio is in the optimal range to bind to the receptors (tau and hyperphosphorylated tau) in brain. It is essential to design an antibody that specifically detects hyperphosphorylated tau following mild TBI in order to avoid a false positive result with an antibody that targets tau and hyperphosphorylated tau.

Based on the studies on Fe NPs in Chapter 5, the size of Fe NPs could be increased by altering the reaction conditions to obtain a high saturation magnetization matching to that of bulk Fe. Magnetic heating could be conducted on these NPs for their potential application in hyperthermia. The idea of using magnetic induction hyperthermia is based on the fact that when magnetic NPs are exposed to a varying magnetic field, heat is generated by the magnetic hysteresis loss, Néel relaxation, and Brown relaxation.[180] For biological application of these NPs, their colloidal stability and resistance to oxidation are essential.

Chapter 6 has a wide scope of biological applications. The concept of MRI correlation can be further demonstrated *in vivo* using two different antibodies attached to T_1-only and T_2-only NPs separately to specifically target two antigens on the same tumor/tissue site.

Chapter 7 could be extended to study temperature dependent FRET to observe the exchange dynamics of phospholipids coating NPs to mimic the physiological condition.

Appendix 1. Supplementary Information to Chapter 2

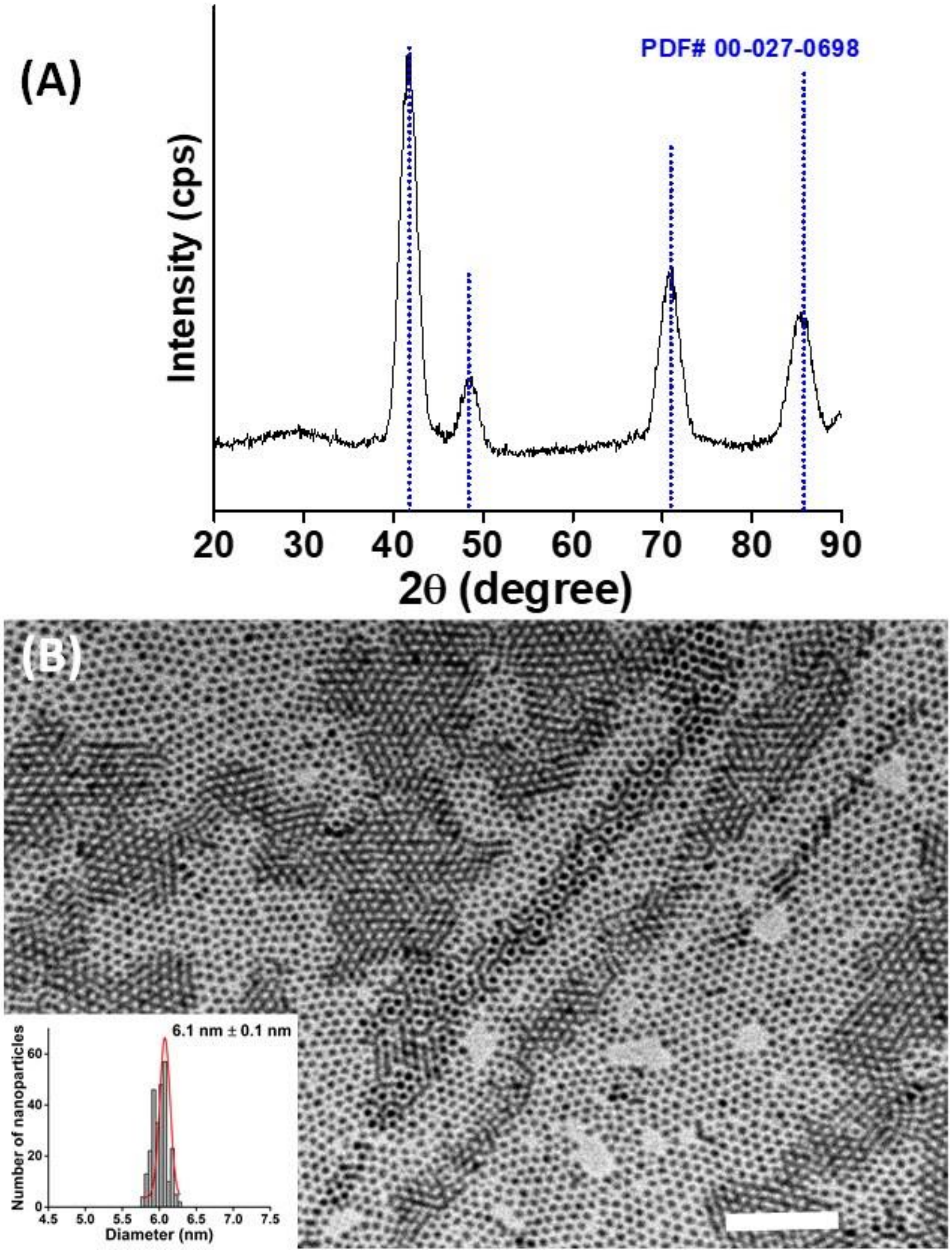

Figure A1.1. α-$NaGdF_4$ NPs: (A) XRD patterns indexed with the standard patterns of the cubic phase of $NaGdF_4$ (PDF 00-027-0698). (B) TEM image with the corresponding histogram of particle size distribution. White scale bar: 100 nm. These sacrificial NPs were injected to form the shell of $NaYF_4$-$NaGdF_4$:Eu^{3+} core-shell NPs.

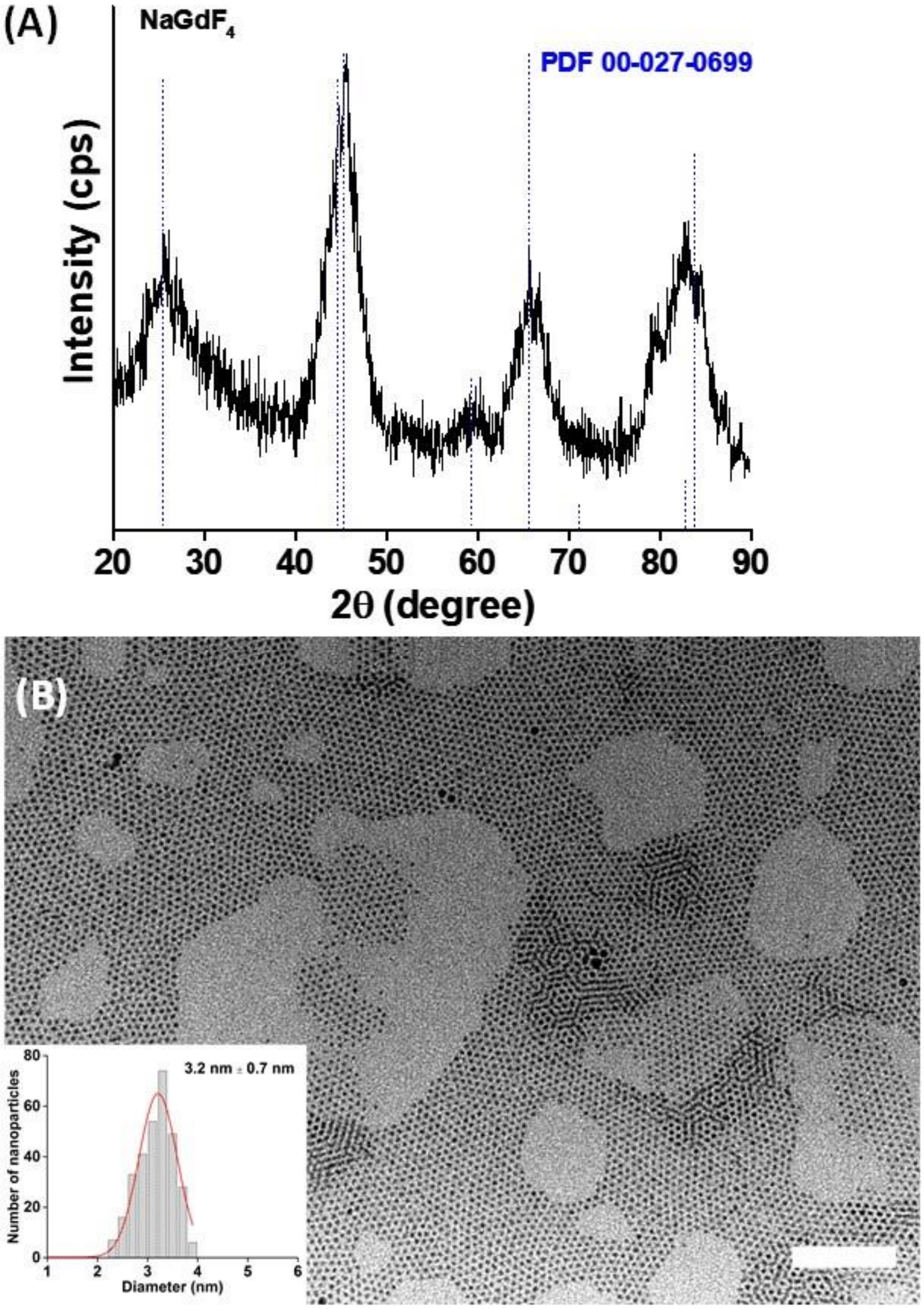

Figure A1.2. β-$NaGdF_4$ NPs: (A) XRD patterns indexed with the standard patterns of the hexagonal phase of $NaGdF_4$ (PDF 00-027-0699). (B) TEM image with the corresponding histogram of particle size distribution. White scale bar: 50 nm.

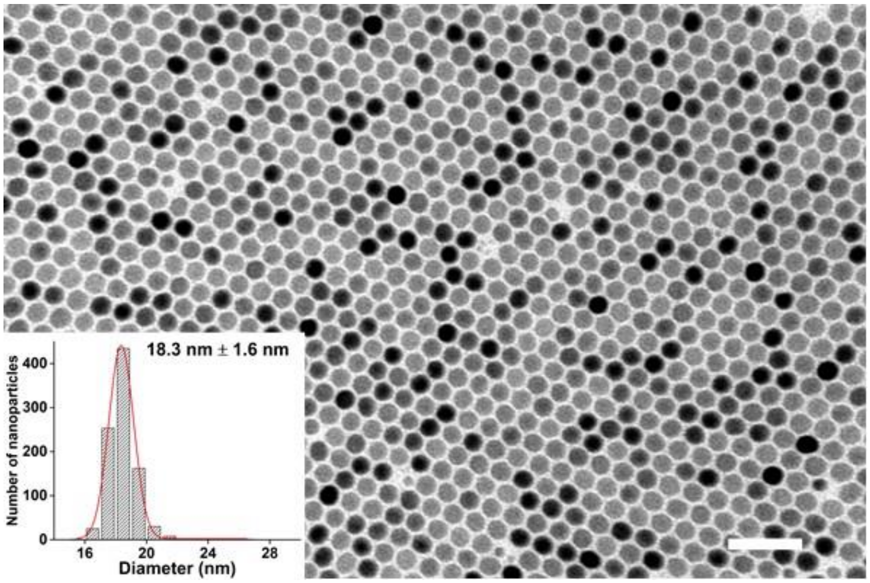

Figure A1.3. TEM image and the corresponding histogram of particle size distribution of $NaYF_4$ NPs before injection of $NaGdF_4:Eu^{3+}$ NPs to form $NaYF_4$-$NaGdF_4:Eu^{3+}$ core-shell NPs. (white scale bar: 100 nm)

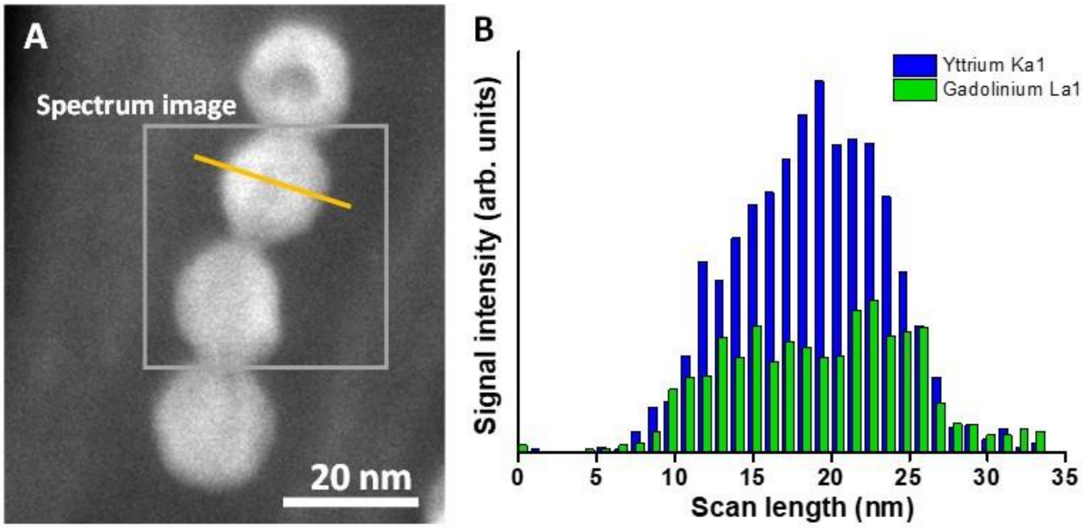

Figure A1.4. (A) STEM image of $NaYF_4$-$NaGdF_4:Eu^{3+}$ core-shell NPs and the corresponding EELS line scans showing (B) Gd residing predominantly in the shell and Y in the core from the plot of EELS signal intensity across scan length of the NP.

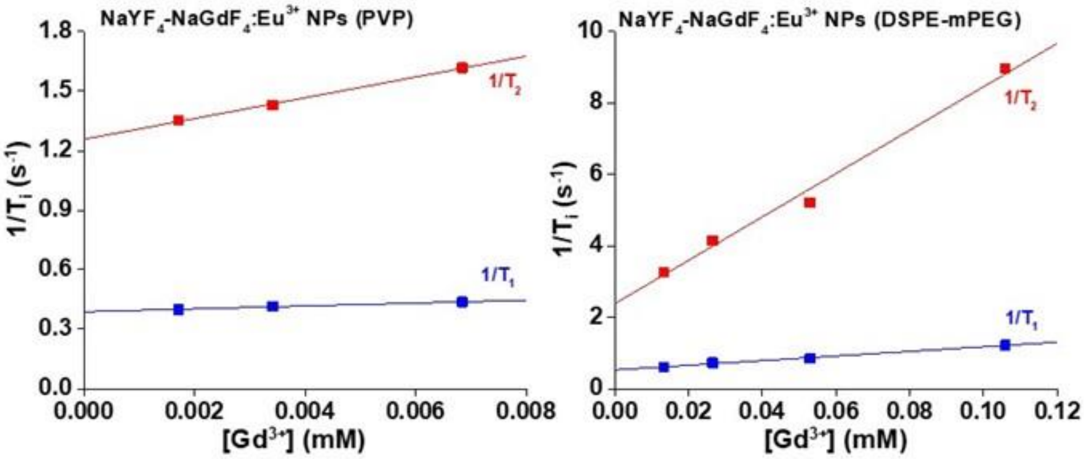

Figure A1.5. Longitudinal (r_1) and transverse (r_2) relaxivities obtained for PVP and DSPE-mPEG coated $NaYF_4$-$NaGdF_4$:Eu^{3+} core-shell NPs at 9.4 T. Blue colored linear fits = $1/T_1$ and red colored linear fits = $1/T_2$. R-square (Coefficient of Determination) defining the goodness of fit lie in the range of 0.98938–0.99766.

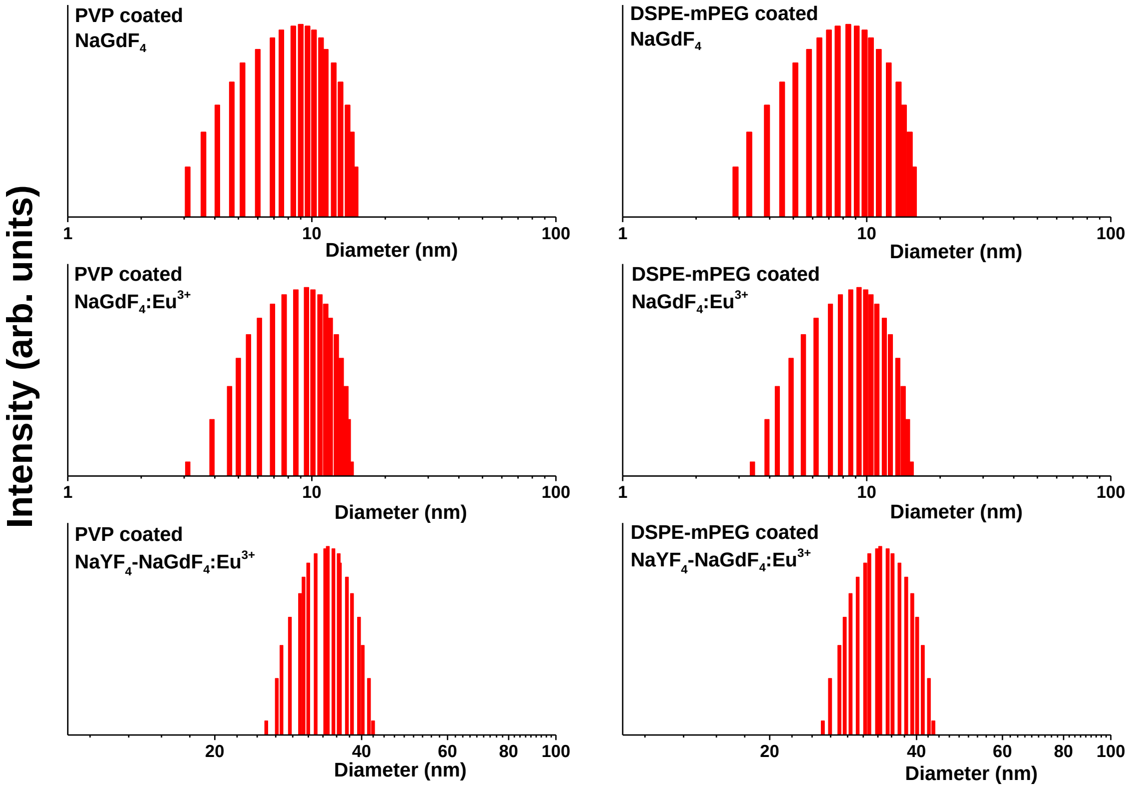

Figure A1.6. Dynamic light scattering (DLS) results showing the hydrodynamic diameter of the following NPs coated with PVP and DSPE-mPEG: $NaGdF_4$, $NaGdF_4$:Eu^{3+} and $NaYF_4$-$NaGdF_4$:Eu^{3+} core-shell NPs.

Table A1.1. Diameters of NPs obtained from XRD, TEM and DLS.

Type of NPs	XRD (nm)	TEM (nm)	DLS (nm): hydrodynamic diameter	
			PVP-coated	DSPE-mPEG coated
$NaGdF_4$	3.0	3.2 ± 0.7	8.9 ± 1.9	8.8 ± 1.8
$NaGdF_4:Eu^{3+}$	2.9	3.0 ± 0.8	9.4 ± 2.3	9.1 ± 1.8
$NaYF_4$-$NaGdF_4:Eu^{3+}$ core-shell	19.2	18.8 ± 1.8	33.9 ± 1.2	34.3 ± 1.6

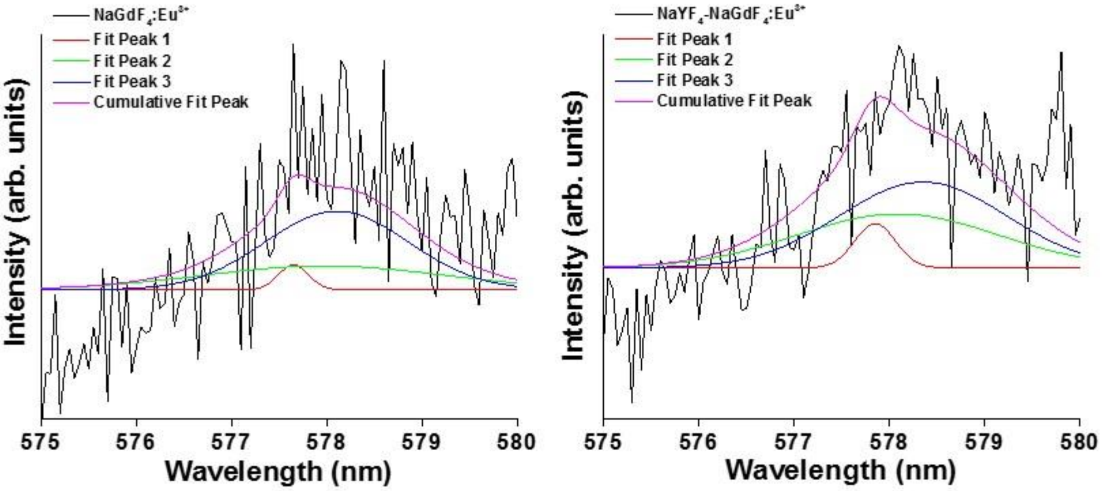

Figure A1.7. Deconvolution of the high resolution (0.05 nm) 578 nm peak from the emission spectra of $NaGdF_4:Eu^{3+}$ and $NaYF_4$-$NaGdF_4:Eu^{3+}$ core-shell NPs. The presence of three Gaussian peaks is seen along with the cumulative fit peak, indicating that Eu^{3+} ions are located in more than one crystal site within the NP. The fit is not smooth due to high signal to noise ratio.

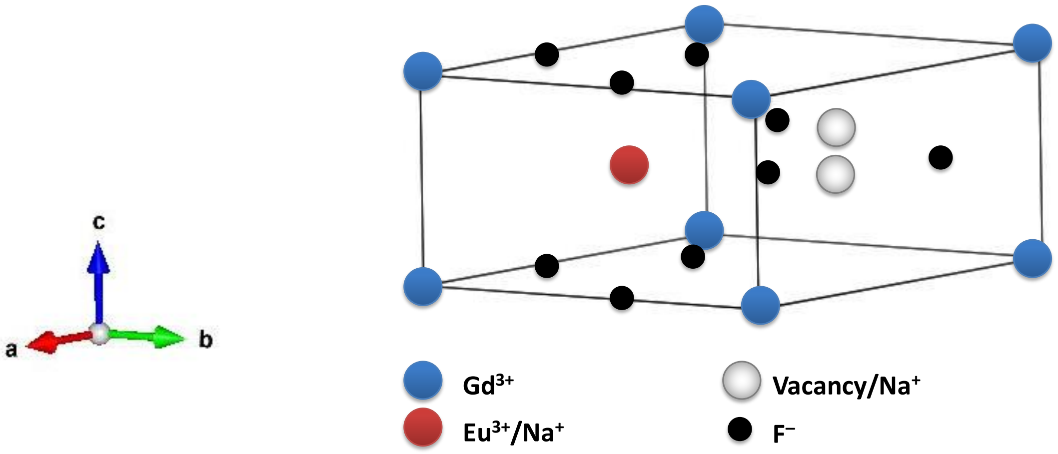

Figure A1.8. Crystallographic site symmetry of hexagonal phase $NaGdF_4$ NPs doped with Eu^{3+}.[99] Eu^{3+} can also occupy the 1*a* and 1*f* sites with C_{3h} symmetry substituting Gd^{3+} ions.

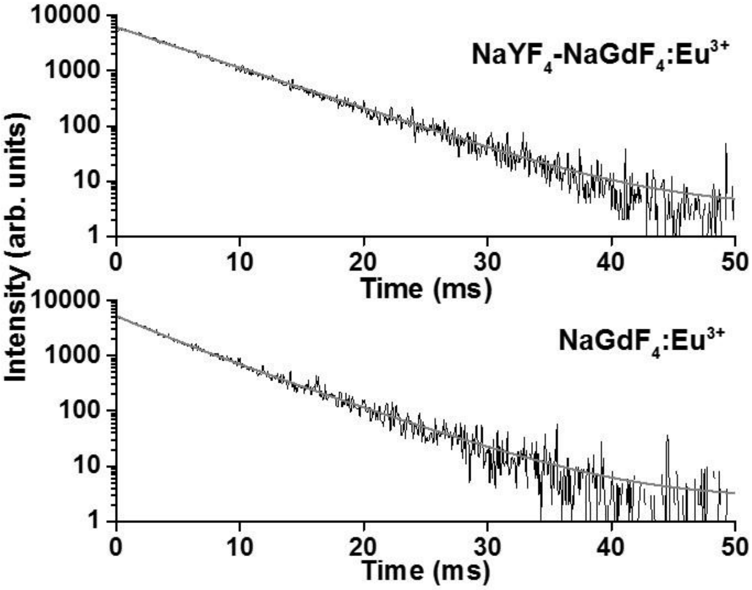

Figure A1.9. Decay curves monitored at 615 nm and fitted with corresponding exponential equations for oleate-capped NaGdF$_4$:Eu^{3+} and NaYF$_4$-NaGdF$_4$:Eu^{3+} core-shell NPs dispersed in hexanes. The NPs were excited at 394 nm. R-squared (Coefficient of determination, COD) for the curves is in the range of 0.99616–0.99689.

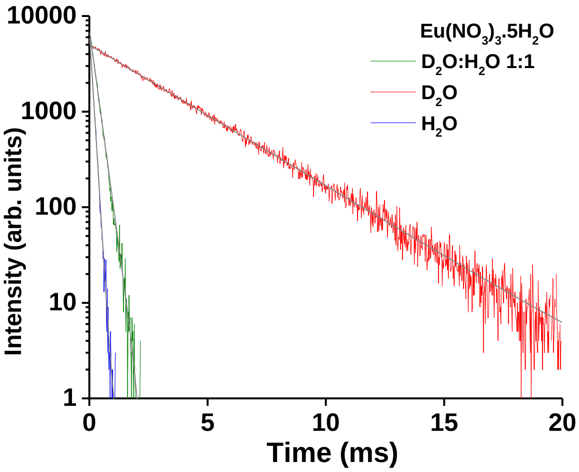

Figure A1.10. Decay curves monitored at 615 nm and fitted with corresponding exponential equations for Eu(NO$_3$)$_3$·5H$_2$O dispersed in D$_2$O, H$_2$O and their 1:1 mixture. The Eu^{3+} ions were excited at 394 nm. R-squared (COD) for the curves is in the range of 0.99797–0.99939.

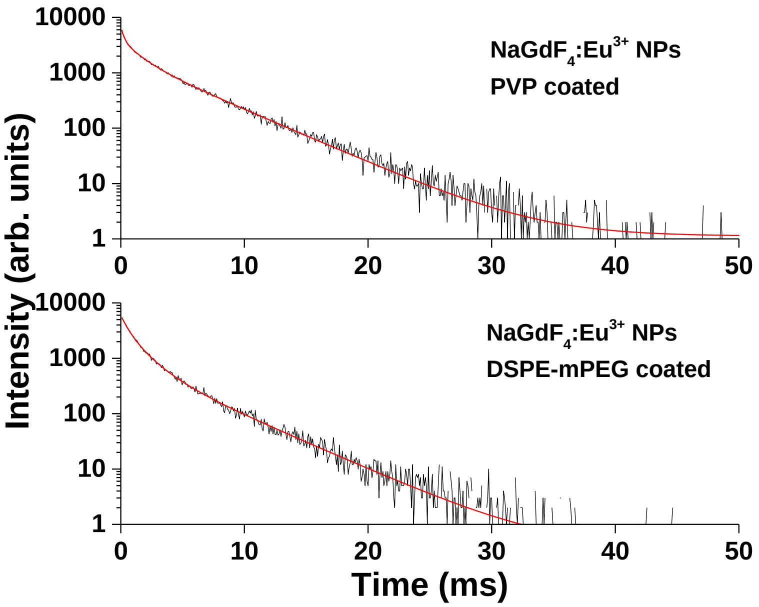

Figure A1.11. Decay curves monitored at 615 nm and fitted with corresponding exponential equations for NaGdF$_4$:Eu^{3+} NPs coated with PVP and DSPE-mPEG and dispersed in 1:1 mixture of D_2O and H_2O. The NPs were excited at 394 nm. These measurements were done 6 months after NP preparation in 1:1 mixture of D_2O and H_2O. R-squared (COD) for the curves is in the range of 0.99932–0.99933.

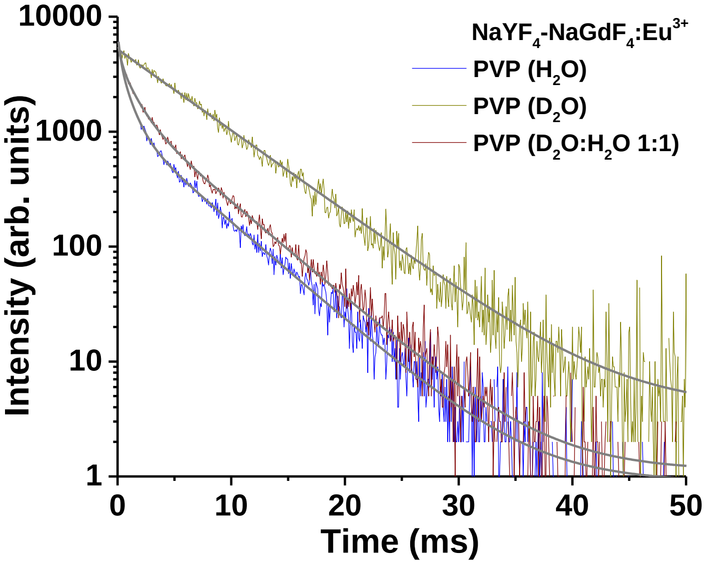

Figure A1.12. Decay curves monitored at 615 nm and fitted with corresponding exponential equations for NaYF$_4$-NaGdF$_4$:Eu^{3+} core-shell NPs coated with PVP and dispersed in D_2O and/or H_2O. The NPs were excited at 394 nm. R-squared (COD) for the curves is in the range of 0.99427–0.99908.

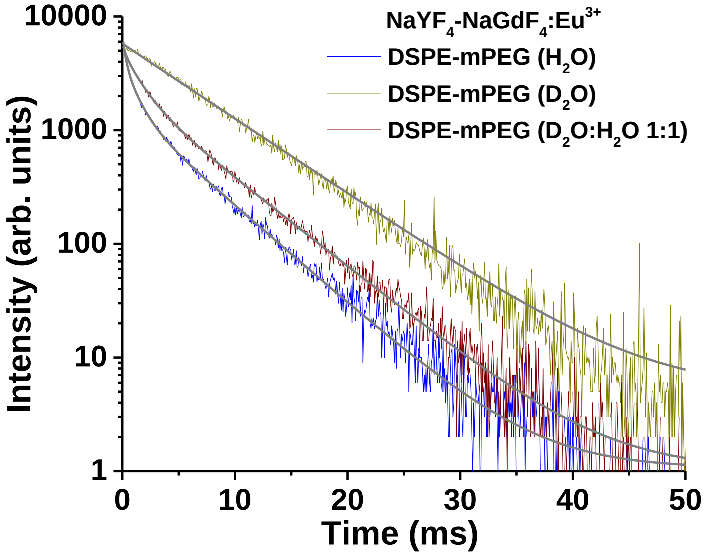

Figure A1.13. Decay curves monitored at 615 nm and fitted with corresponding exponential equations for $NaYF_4$-$NaGdF_4$:Eu^{3+} core-shell NPs coated with DSPE-mPEG and dispersed in D_2O and/or H_2O. The NPs were excited at 394 nm. R-squared (COD) for the curves is in the range of 0.99609–0.99918.

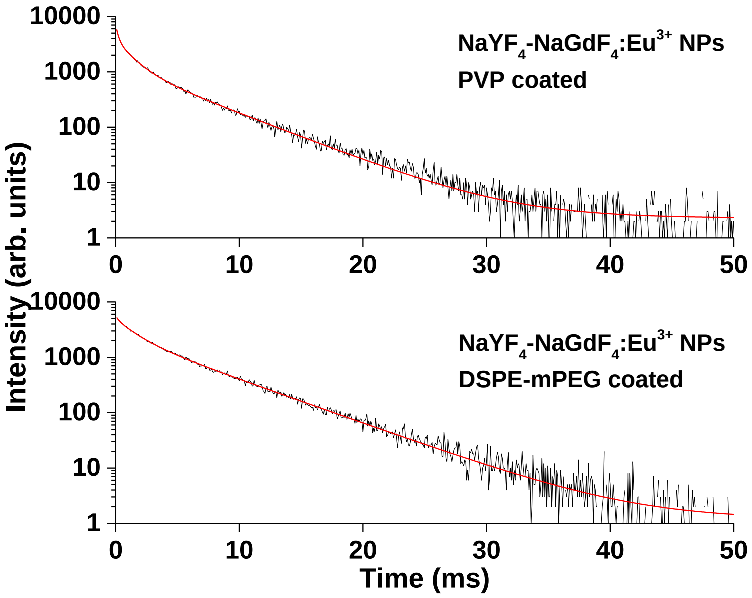

Figure A1.14. Decay curves monitored at 615 nm and fitted with corresponding exponential equations for $NaYF_4$-$NaGdF_4$:Eu^{3+} core-shell NPs coated with PVP and DSPE-mPEG and dispersed in 1:1 v/v mixture of D_2O and H_2O. The NPs were excited at 394 nm. These measurements were done 6 months after NP preparation in 1:1 v/v mixture of D_2O and H_2O. R-squared (COD) for the curves is in the range of 0.99919–0.99939.

Appendix 2. Supplementary Information to Chapter 3

Synthesis, Characterization, Magnetic (SQUID) Measurements and Relaxivities (r_1 and r_2 at 9.4 T) of $NaYF_4$, $NaDyF_4$, $NaDyF_4$-$NaYF_4$, $NaDyF_4$-$NaGdF_4$, $NaYF_4$-$NaDyF_4$, and $NaYF_4$-$NaGdF_4$ core-shell NPs.

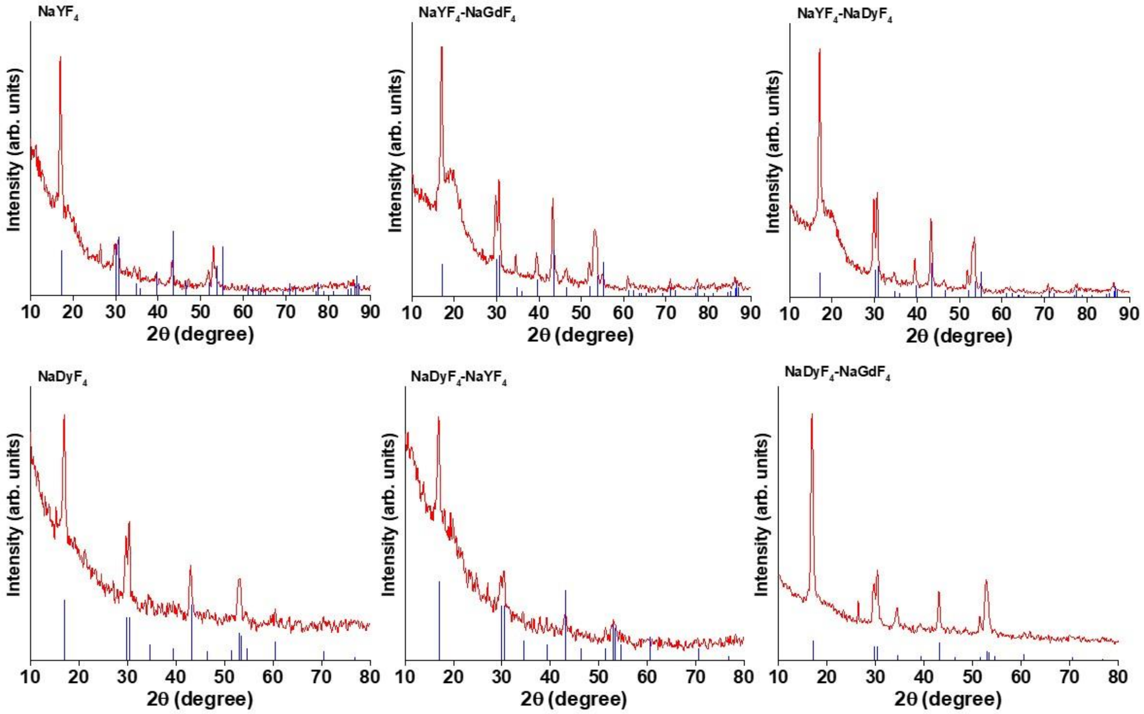

Figure A2.1. XRD patterns of $NaYF_4$, $NaYF_4$-$NaGdF_4$ core-shell and $NaYF_4$-$NaDyF_4$ core-shell NPs indexed with the standard patterns of the hexagonal phase of NaYF4 (PDF#00-016-0334). XRD patterns of $NaDyF_4$, $NaDyF_4$-$NaYF_4$ core-shell and $NaDyF_4$-$NaGdF_4$ core-shell NPs indexed with the standard patterns of the hexagonal phase of $NaDyF_4$ (PDF#00-027-0687).

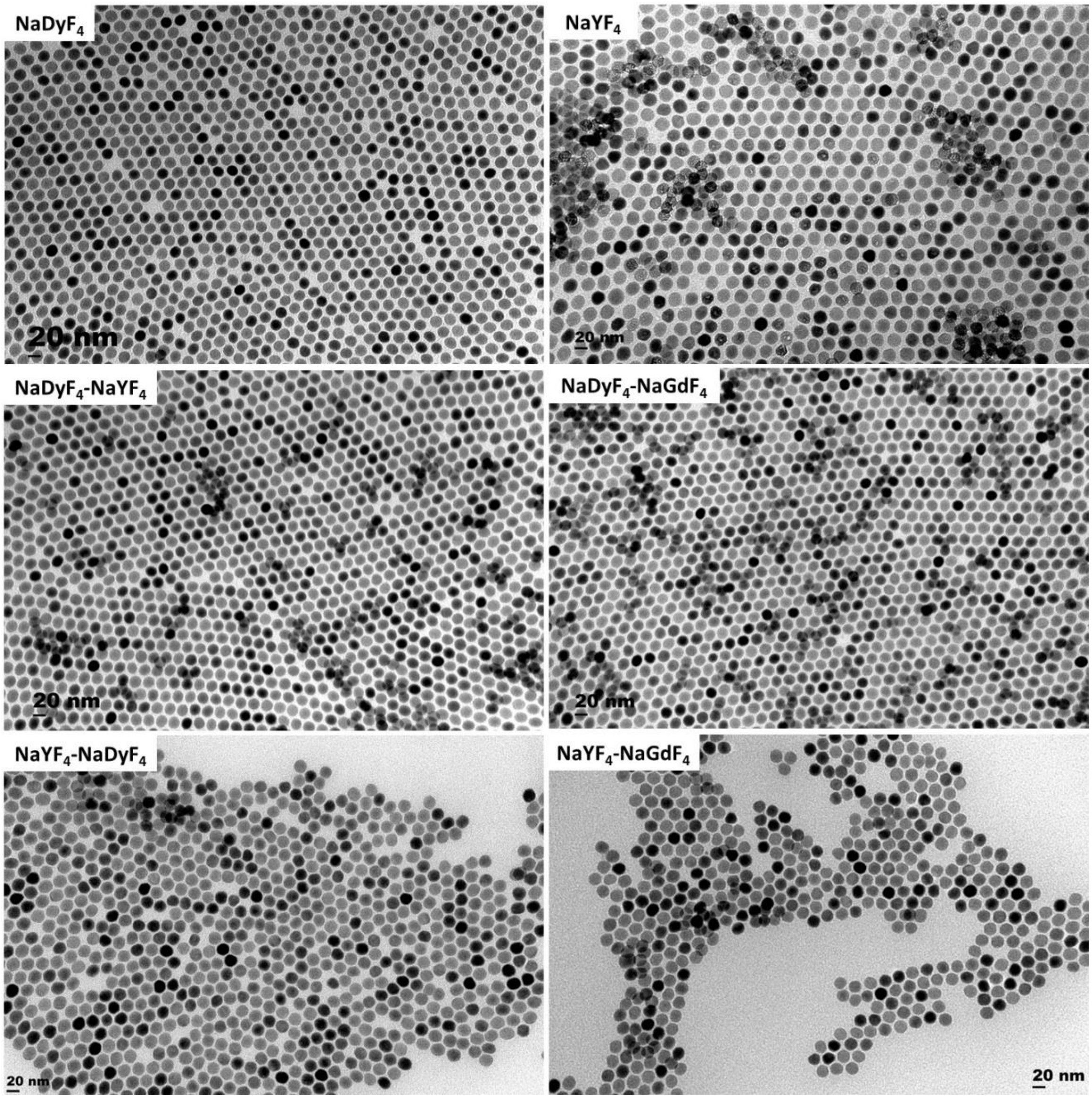

Figure A2.2. TEM images of $NaDyF_4$, $NaYF_4$, $NaDyF_4$-$NaYF_4$, $NaDyF_4$-$NaGdF_4$, $NaYF_4$-$NaDyF_4$, and $NaYF_4$-$NaGdF_4$ core-shell NPs.

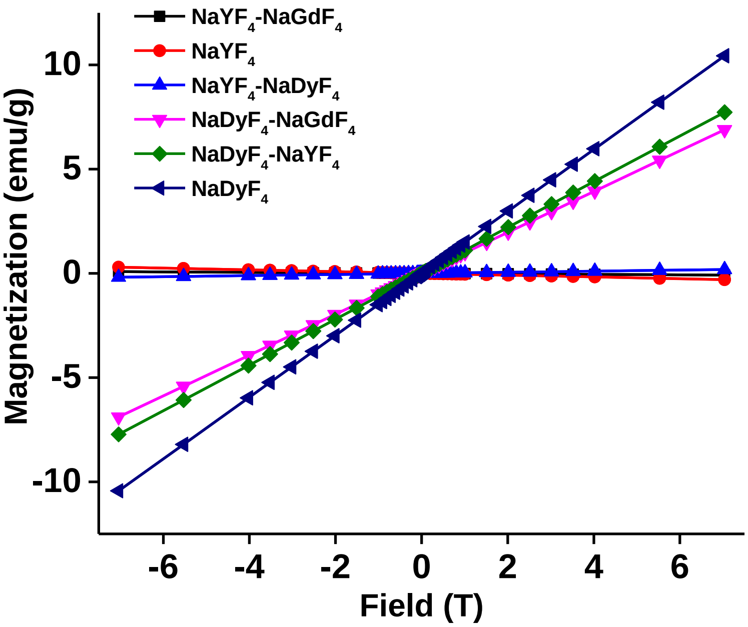

Figure A2.3. Magnetization versus field plots obtained for $NaDyF_4$, $NaYF_4$, $NaDyF_4$-$NaYF_4$, $NaDyF_4$-$NaGdF_4$, $NaYF_4$-$NaDyF_4$, and $NaYF_4$-$NaGdF_4$ core-shell NPs.

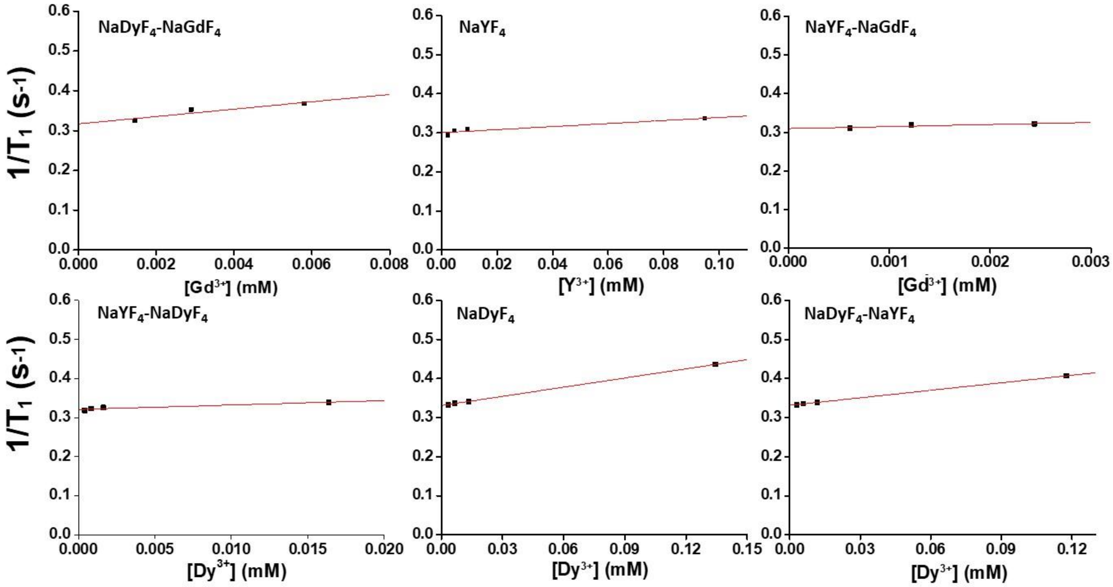

Figure A2.4. Longitudinal relaxivities (r_1) obtained from the linear fits of the longitudinal relaxation rates ($1/T_1$) plotted at different Ln^{3+} concentration of the following NPs' batches: $NaDyF_4$-$NaGdF_4$, $NaYF_4$, $NaYF_4$-$NaGdF_4$, $NaYF_4$-$NaDyF_4$, $NaDyF_4$, and $NaDyF_4$-$NaYF_4$ core-shell NPs.

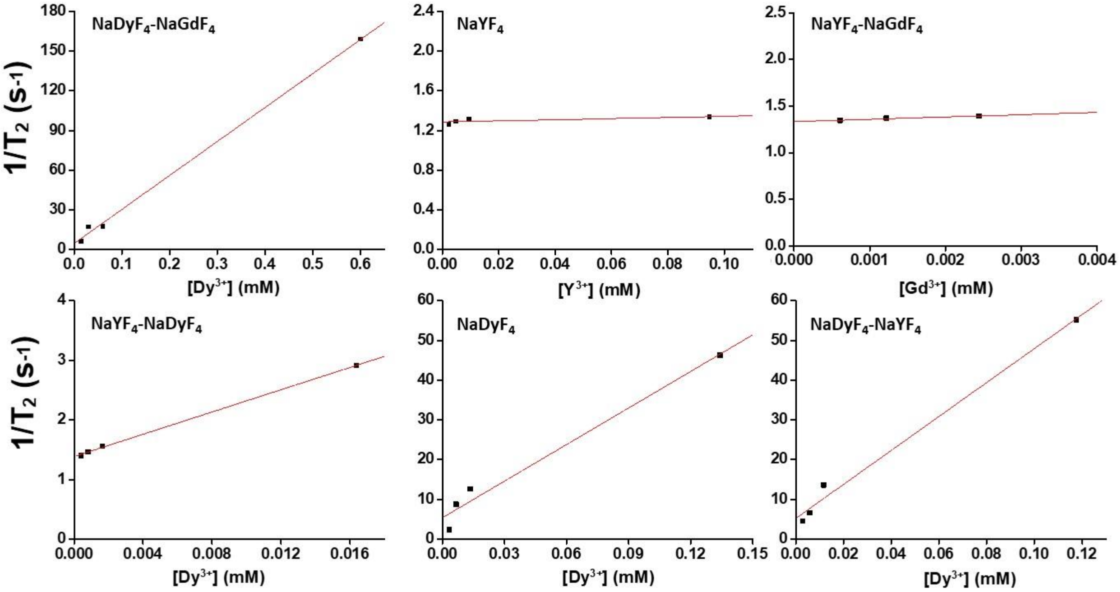

Figure A2.5. Transverse relaxivities (r_2) obtained from the linear fits of the transverse relaxation rates ($1/T_2$) plotted at different Ln^{3+} concentration of the following NPs' batches: $NaDyF_4$-$NaGdF_4$, $NaYF_4$, $NaYF_4$-$NaGdF_4$, $NaYF_4$-$NaDyF_4$, $NaDyF_4$, and $NaDyF_4$-$NaYF_4$ core-shell NPs.

Table A2.1. Magnetization (*per* unit volume, $M_{s,v}$, and *per* unit mass, $M_{s,m}$) from SQUID measurements (Figure A2.3) and ionic (r_1 and r_2) relaxivities determined from the plots (Figures A2.4, A2.5) of relaxation times at different concentrations of Ln^{3+} for a series of NPs at 9.4 T.

NPs	**Core diameter (nm)**	**Shell thickness (nm)**	**$M_{s,V}$ (emu cm^{-3})**	**$M_{s,m}$ (emu g^{-1})**	**r_1 (mM^{-1} s^{-1})**	**r_2 (mM^{-1} s^{-1})**	**r_2/r_1**
$NaDyF_4$-$NaGdF_4$ core-shell	18.5	0.6	71.513	12.197	9.25 ± 3.56	256.69 ± 8.65	27.75
$NaYF_4$	19.5		–1.518	–0.353	0.39 ± 0.09	0.57 ± 0.31	1.46
$NaYF_4$-$NaGdF_4$ core-shell	19.0	0.4	–0.437	–0.098	5.34 ± 2.59	24.61 ± 5.07	4.61
$NaYF_4$-$NaDyF_4$ core-shell	19.0	0.2	3.708	0.843	1.12 ± 0.22	93.39 ± 1.44	83.38
$NaDyF_4$	19.5		84.739	14.343	0.78 ± 0.003	306.83 ± 33.87	393.37
$NaDyF_4$-$NaYF_4$ core-shell	19.2	0.4	74.797	13.070	0.64 ± 0.01	427.55 ± 29.80	668.05

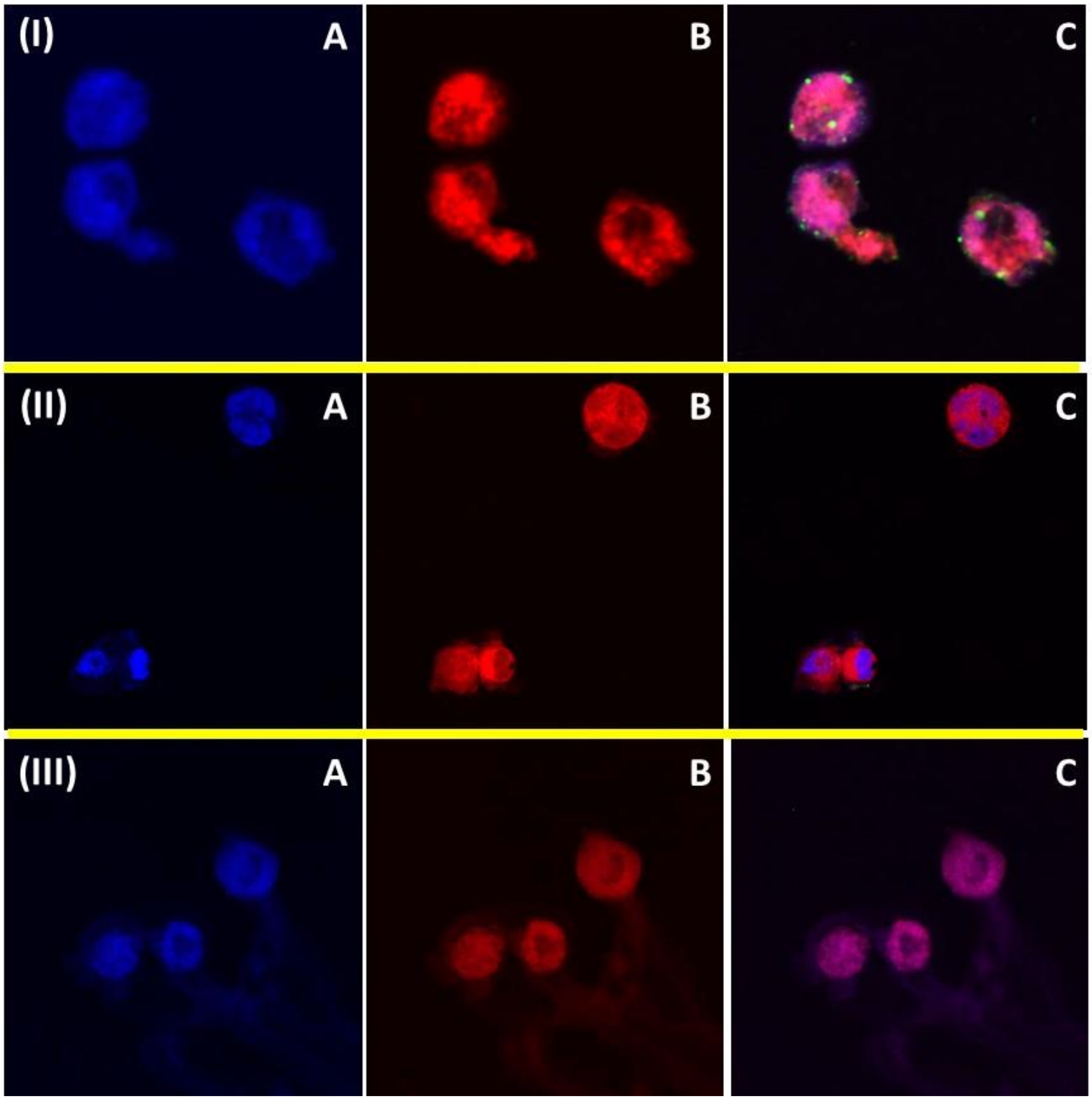

Figure A2.6. Confocal images of (I) LNCaP cells incubated with $NaDyF_4$-$NaGdF_4$ core-shell NPs tagged with anti-PSMA antibody and Alexa-488, (II) PC3 cells incubated with $NaDyF_4$-$NaGdF_4$ core-shell NPs tagged with anti-PSMA antibody and Alexa-488, and (III) LNCaP cells incubated with $NaDyF_4$-$NaGdF_4$ core-shell NPs tagged with Alexa-488 (control), taken under (A) blue channel, (B) red channel, and (C) blue, red and green channels merged. DAPI (blue channel): λ_{exc} = 358 nm, λ_{em} = 460 nm; Nile blue (red channel): λ_{exc} = 520 nm, λ_{em} = 568 nm; Alexa-488 (green channel): λ_{exc} = 495 nm, λ_{em} = 519 nm.

Experimental section for syntheses of $NaDyF_4$-$NaGdF_4$, $NaYF_4$, $NaYF_4$-$NaGdF_4$, $NaYF_4$-$NaDyF_4$, $NaDyF_4$, and $NaDyF_4$-$NaYF_4$ core-shell NPs.

Chemicals. Dysprosium(III) chloride hexahydrate (99.9%), dysprosium(III) oxide (99.9%), gadolinium(III) oxide (99.9%), yttrium(III) oxide (99.9%), yttrium(III) acetate hydrate (99.9%), sodium trifluoroacetate (98%), ammonium fluoride (≥ 99.99%), tech-grade oleic acid (90%), tech-grade 1-octadecene (90%), and hexanes were purchased from Sigma-Aldrich. Oleylamine (97%) from Acros, sodium hydroxide, trifluoroacetic acid, anhydrous ethanol and methanol from Caledon laboratories were used. All chemicals were used as received.

Synthesis of the cubic (α) phase (sacrificial) $NaLnF_4$ (Ln = Y, Gd and Dy) NPs. The synthesis of sacrificial $NaLnF_4$ NPs (which are used in forming the shell layer in core-shell NPs) is based on a reported method.[181] In a typical synthesis, 1 mmol of Ln_2O_3 was mixed with 10 mL of 50 % aqueous trifluoroacetic acid in a 100 mL three necked round bottom flask and refluxed at 85 °C overnight. Excess of water was then removed at 65 °C that produced $Ln(CF_3COO)_3$ as a white powder. An amount of 2 mmol of sodium trifluoroacetate, 5 mL of oleic acid, 5 mL of oleylamine, and 10 mL of 1-octadecene was added to the resultant $Ln(CF_3COO)_3$. The reaction mixture was stirred and heated to 120 °C (15 °C/min) under vacuum for 45 min to remove residual water and oxygen. This resulted in a transparent solution that was heated to 285 °C (~15 °C/min) with vigorous stirring under argon for 45 min. It was cooled down to room temperature and the NPs were precipitated by addition of 60 mL of ethanol, collected by centrifugation (at 7,000 *g* in

Beckman Coulter Spinchron 15-rotor F0830), washed thrice with 50 mL of ethanol and finally dispersed in 10 mL of hexanes.

Synthesis of the hexagonal (β) phase $NaYF_4$, $NaYF_4$-$NaGdF_4$ and $NaYF_4$-$NaDyF_4$ core-shell NPs. In a 100 mL round bottom three necked flask, 1 mmol of yttrium(III) acetate hydrate was stirred in a solvent mixture of 6 mL of oleic acid and 17 mL of 1-octadecene at 130 °C under vacuum for 30 min. The resultant solution of yttrium oleate was cooled down to room temperature, added with 2.5 mmol of sodium hydroxide and 4 mmol of ammonium fluoride dissolved in 10 mL of methanol, and stirred for 1 h. Methanol was evaporated by heating the reaction mixture at 80 ^{o}C for 20 min. Temperature was raised to 300 °C (~15 °C /min) and maintained for 1 h under an argon atmosphere, which produced the β-phase core $NaYF_4$ NPs. A calculated amount of sacrificial NPs (α-$NaLnF_4$, Ln = Gd and Dy) dispersed in 1-octadecene was injected into the reaction mixture and the reaction was continued for another 10 min to yield $NaYF_4$-$NaLnF_4$ core-shell (Ln = Gd and Dy) NPs. Subsequently, the reaction medium was cooled down to room temperature and the NPs were precipitated by the addition of 60 mL of ethanol, collected by centrifugation (at 7,000 *g* in Beckman Coulter Spinchron 15-rotor F0830), washed with 50 mL of ethanol thrice and dispersed in 10 mL of hexanes. The β-phase $NaYF_4$ NPs were synthesized using this protocol (except for the injection of the sacrificial NPs).

Synthesis of hexagonal (β) phase $NaDyF_4$, $NaDyF_4$-$NaGdF_4$ and $NaDyF_4$-$NaYF_4$ core-shell NPs. To synthesize $NaDyF_4$-$NaGdF_4$ core-shell NPs, 0.78 mmol of dysprosium(III) chloride hexahydrate was stirred with 1.5 mL of oleic acid and 7.5 mL of 1-octadecene in a 50 mL three necked round bottom flask at 140 °C under vacuum for 30 min. The resultant dysprosium oleate complex was cooled down to room temperature followed by the addition of 2.8 mmol of sodium hydroxide and 4 mmol of ammonium fluoride dissolve in 10 mL of methanol and stirring for 3 h at room temperature. The reaction mixture was heated at 80 °C to remove methanol. The temperature was raised to 306 °C (~15 °C /min) under an argon atmosphere for 1.5 h, which produced the β-phase core $NaDyF_4$ NPs. After 1.5 h of reaction time the calculated amount of sacrificial α-$NaGdF_4$ NPs dispersed in 1-octadecene was injected into the reaction mixture and the reaction was allowed to ripen for 10 min to yield the core/shell $NaDyF_4$/$NaGdF_4$ NPs. Subsequently, the reaction was cooled down to room temperature and the NPs were precipitated by the addition of 30 mL of ethanol, collected by centrifugation (at 7,000 *g* in Beckman Coulter Spinchron 15-rotor F0830), washed with 60 mL of ethanol thrice and dispersed in 10 mL of hexanes. To synthesize $NaDyF_4$-$NaYF_4$ core-shell NPs, *α*-$NaYF_4$ NPs were injected following this protocol. The *β*-phase $NaDyF_4$ NPs were synthesized using this protocol (except for the injection of the sacrificial NPs).

Characterization. X-ray Diffraction (XRD) patterns were collected using a Panalytical Empyrean X-ray diffractometer using Bragg-Brentano module and Cu Kα radiation (λ = 0.154 nm, 45 kV, 40 mA) with a scan step size of 0.10 degrees (2θ). A 10 mm fixed beam mask, a 0.04 rad Solar slit, a 1/2˚ Anti-scatter slit, and a 1/2˚ fixed Divergence slit were used for incident beam. A 0.04 rad large solar slit with the PIXcel 3D-Medipix3 1×1 detector with an active angle 2θ of 3.347˚ were used for diffracted beam. About 20 drops of NP dispersion in hexanes were dried on the sample holder to get the diffraction patterns.

Transmission electron microscopy (TEM) images were acquired using a JEOL JEM-1400 microscope operating at 80 kV. The NP dispersion in hexane was drop-cast onto a formvar carbon film supported on a 300 mesh copper grid (3 mm in diameter) and allowed to dry in air at room temperature, before imaging.

Superconducting quantum interference device (SQUID) magnetometry measurements were carried out in a Quantum Design MPMS XL-7S system (by Dr. Abhinandan Banerjee and Dr. Simon Trudel, University of Calgary). Weighed powdered samples were loaded into a gelatin capsule which was sealed with Kapton tape before being inserted into a clear diamagnetic plastic straw. Isothermal magnetization as a function of field strength measurements were carried out at 300 K by cycling the applied magnetic field between -7 T and +7 T.

Aqueous dispersions of NPs in different dilutions were used to determine the T_1 and T_2 relaxation times. T_1 and T_2 measurements were done using a 9.4 T/21 cm bore magnet (Magnex, UK) and a Bruker console (Bruker, Germany) (by Dr. Barbara Blasiak and Dr. Boguslaw Tomanek, University of Calgary). A transmit/receive radio frequency volume birdcage coil was applied to excite protons and obtain resonant signal. For T_2 measurements, a single slice multi-echo pulse sequence was used with the following pulse parameters: repetition time (TR) 5 s, matrix size 128 × 128, field of view (FOV) 3 cm × 3 cm, slice thickness 2 mm, 128 echoes 4 ms apart. T_2 relaxation times were calculated using a single exponential fitting of the echo train (Marevisi, Canada). For T_1 measurements, TRUE FISP method was used with the following pulse sequence parameters: TR 3 s, TE 1.5 s, matrix size 128 × 128, FOV 3 cm × 3 cm, slice thickness 3 mm, 60 frames × 4 segments, segment time 192 ms. The relaxation times were calculated using single exponential fitting of the data (MATLAB “1sqcurvefit”).

The T_1 and T_2 relaxation times obtained for different dilutions of NPs in deionized water were plotted against concentration of Ln^{3+} ions in the NP solution, $[Ln^{3+}]$, to obtain the values of r_1 and r_2 relaxivities from the slope of the linear fit, using the empirical equation: $\boldsymbol{\frac{1}{T_i} = \frac{1}{T_i^0} + r_i[Ln^{3+}]; i = 1, 2}$. The Ln^{3+} concentration was obtained from ICP-MS analysis of the NPs [using a Thermo X-Series II (X7) quadrupole ICP-MS]; T_i^0 denote the relaxation times of the water protons in absence of the NPs.

Appendix 3. Supplementary Information to Chapter 5

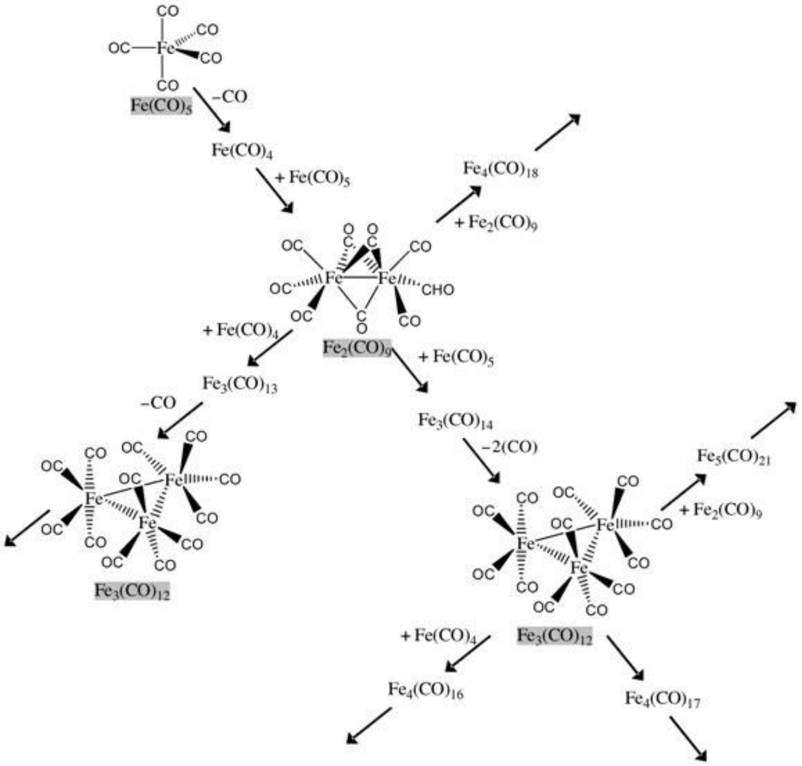

Figure A3.1. Schematic representation of decomposition of $Fe(CO)_5$ via a series of intermediates in a complicated pathway.[66]

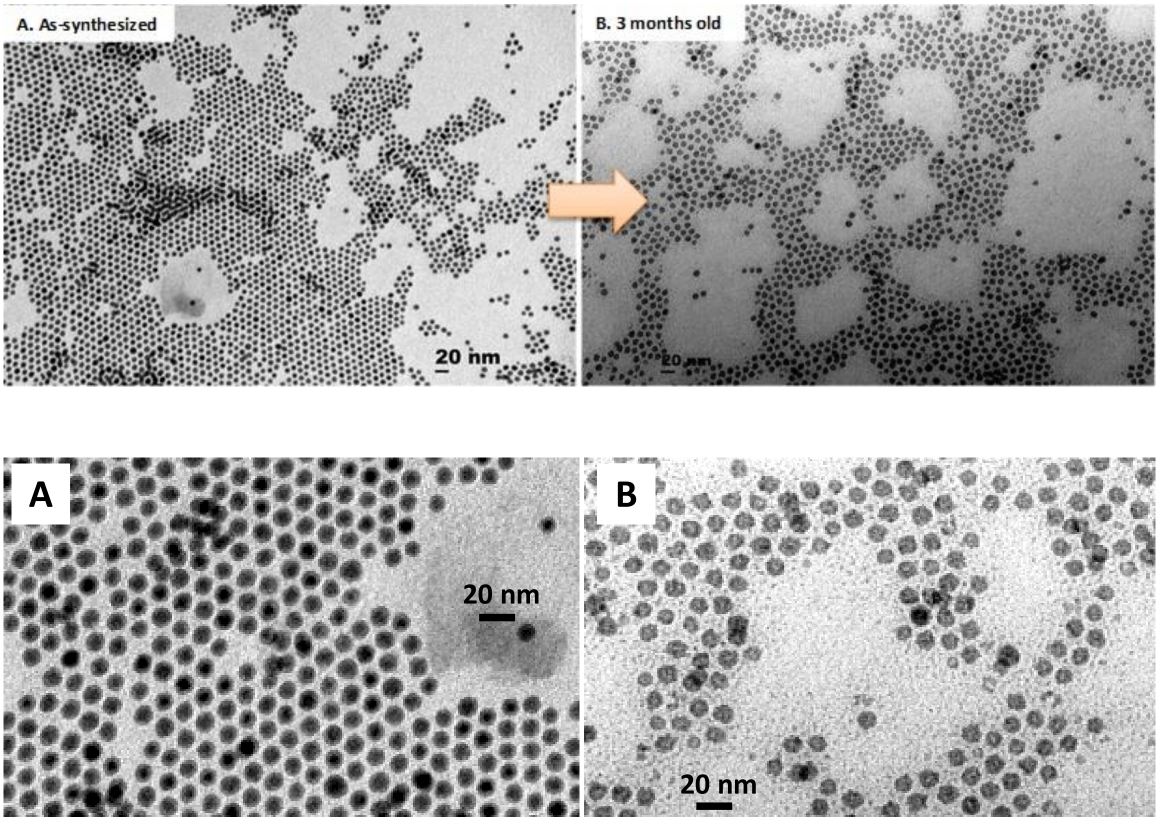

Figure A3.2. TEM images of (A) as-synthesized and (B) 3 months post synthesis of 12.0 nm sized Fe NPs dispersed in chloroform. Their corresponding high-resolution images are shown in the bottom row.

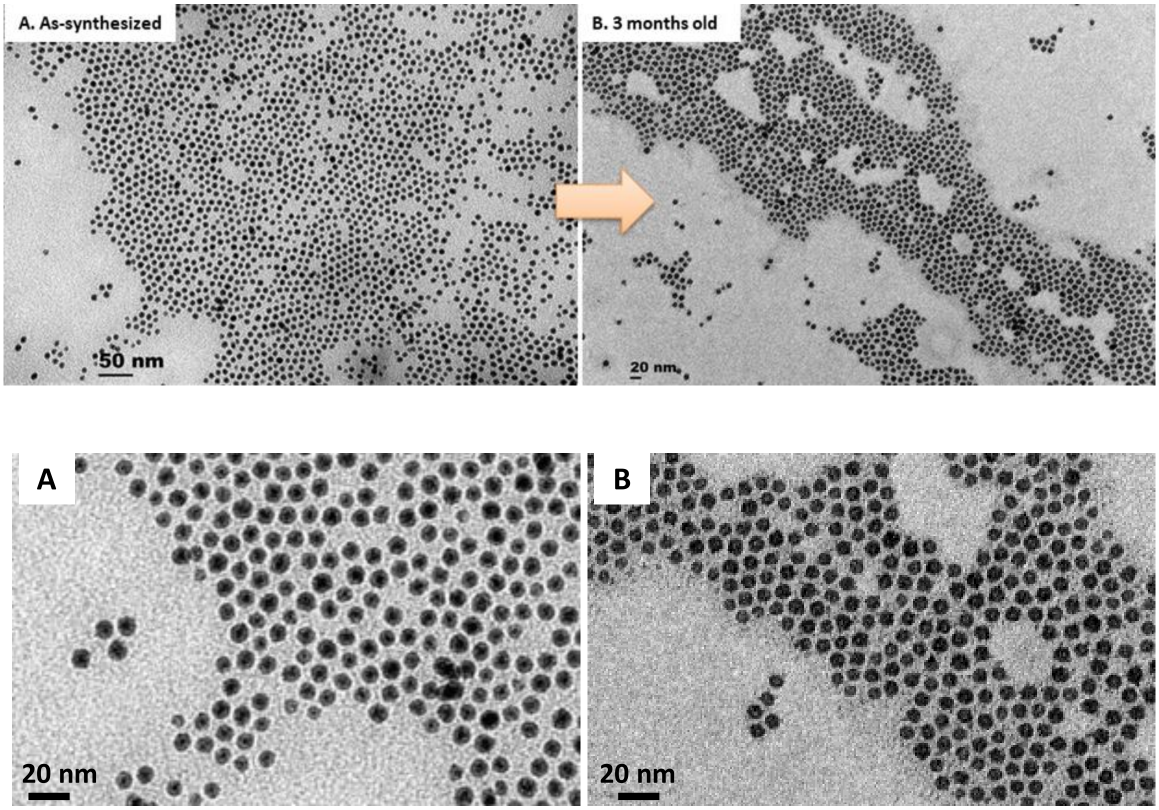

Figure A3.3. TEM images of (A) as-synthesized and (B) 3 months post synthesis of 8.8 nm sized Fe NPs dispersed in chloroform. Their corresponding high-resolution images are shown in the bottom row.

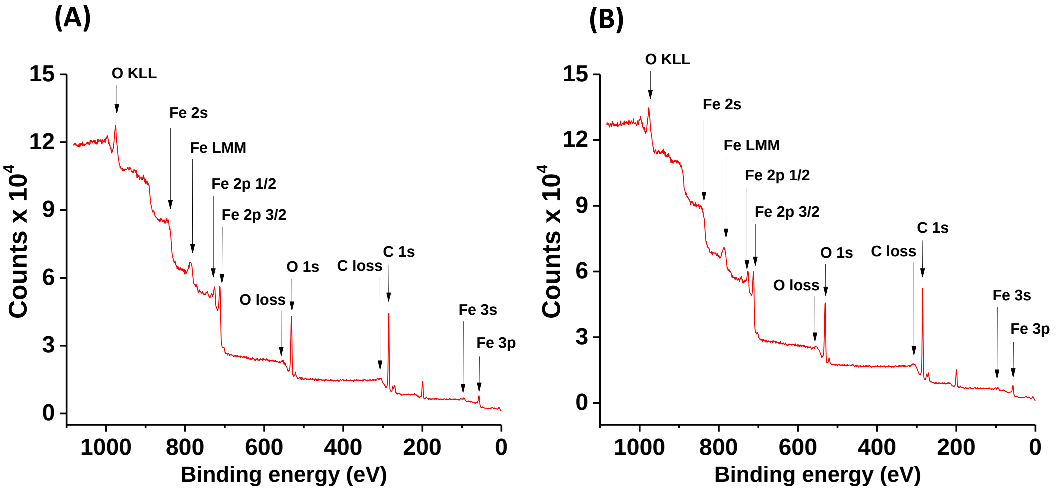

Figure A3.4. XPS survey spectral peaks indexed with their corresponding elements for (A) 12.0 nm and (B) 8.8 nm sized Fe NPs.

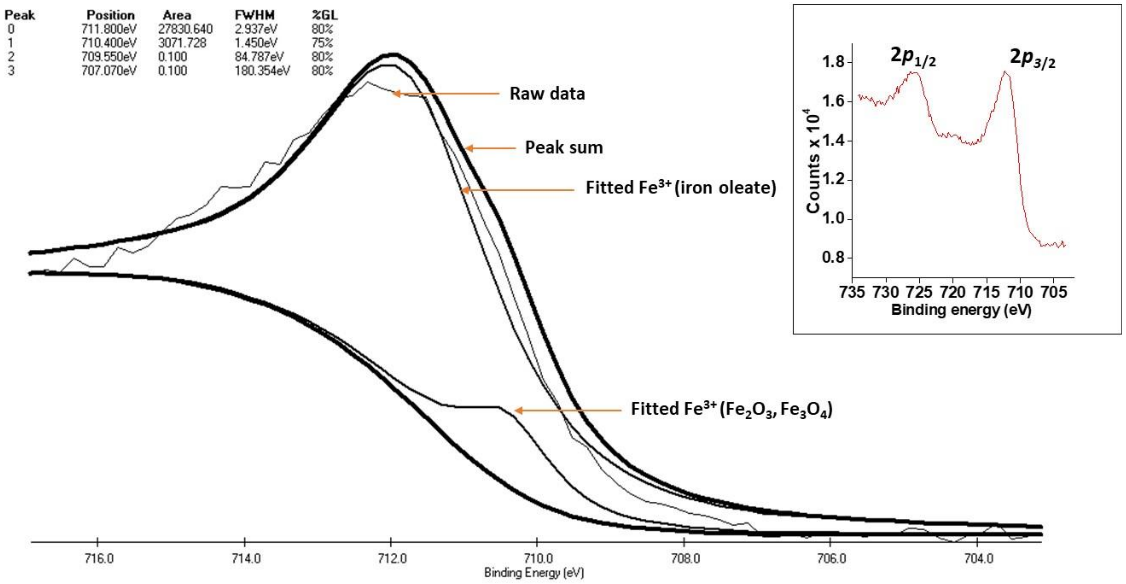

Peak	Position	Area	FWHM	%GL
0	711.800eV	27830.640	2.937eV	80%
1	710.400eV	3071.728	1.450eV	75%
2	709.550eV	0.100	84.787eV	80%
3	707.070eV	0.100	180.354eV	80%

Figure A3.5. Deconvolution analysis of the Fe $2p_{3/2}$ region for Fe NPs (12.0 nm sized). High resolution spectrum of the Fe $2p$ region (inset).

Table A3.1. Details of the deconvolution of the Fe $2p_{3/2}$ peak shown in Figure A3.5.

Peak	Start BE (eV)	Peak BE (eV)	End BE (eV)	FWHM (eV)	Area
Fe^0	716.92	707.07	703.12	180.354	0.101
Fe^{2+} (FeO)	716.92	709.55	703.12	84.787	0.100
Fe^{3+} (Fe_2O_3, Fe_3O_4)	716.92	710.40	703.12	1.450	3071.728
Fe^{3+} (iron oleate)	716.92	711.80	703.12	2.937	27830.640

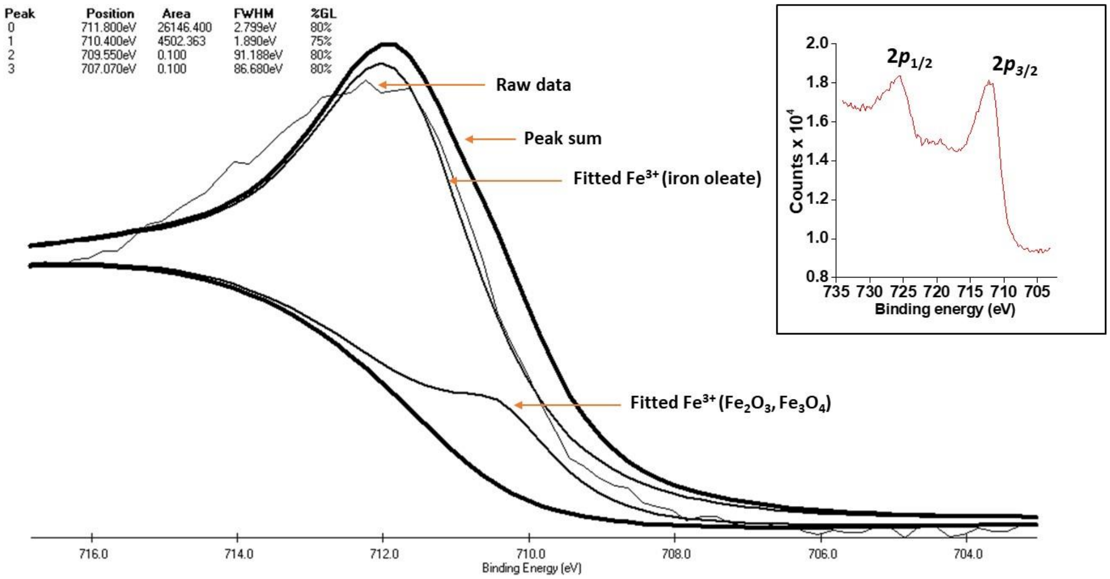

Figure A3.6. Deconvolution analysis of the Fe $2p_{3/2}$ region for Fe NPs (8.8 nm sized). High resolution spectrum of the Fe 2*p* region (inset).

Table A3.2. Details of the deconvolution of the Fe $2p_{3/2}$ peak shown in Figure A3.6.

Peak	Start BE (eV)	Peak BE (eV)	End BE (eV)	FWHM (eV)	Area
Fe^0	716.84	707.07	703.04	86.680	0.100
Fe^{2+} (FeO)	716.84	709.55	703.04	91.188	0.100
Fe^{3+} (Fe_2O_3, Fe_3O_4)	716.84	710.40	703.04	1.890	4502.363
Fe^{3+} (iron oleate)	716.84	711.80	703.04	2.799	26146.400

Bibliography

1. Donegá, C. d. M., *Nanoparticles: Workhorses of Nanoscience*. Springer: Berlin Heidelberg, 2014.

2. Schmid, G., *Nanoparticles: From Theory to Application*. WILEY: Weinheim, 2004.

3. Whitesides, G. M., Nanoscience, nanotechnology, and chemistry. *Small* **2005**, *1*, 172–179.

4. Prasad, P. N., *Introduction to Nanomedicine and Nanobioengineering*. Wiley-Interscience: Hoboken, NJ, 2012.

5. Wagner, V.; Dullaart, A.; Bock, A.-K.; Zweck, A., The emerging nanomedicine landscape. *Nat. Biotechnol. 24*, 1211–1218.

6. Pelaz, B.; Alexiou, C.; Alvarez-Puebla, R. A.; Alves, F.; Andrews, A. M.; Ashraf, S.; Balogh, L. P.; Ballerini, L.; Bestetti, A.; Brendel, C.; Bosi, S.; Carril, M.; Chan, W. C. W.; Chen, C.; Chen, X.; Chen, X.; Cheng, Z.; Cui, D.; Du, J.; Dullin, C.; Escudero, A.; Feliu, N.; Gao, M.; George, M.; Gogotsi, Y.; Grünweller, A.; Gu, Z.; Halas, N. J.; Hampp, N.; Hartmann, R. K.; Hersam, M. C.; Hunziker, P.; Jian, J.; Jiang, X.; Jungebluth, P.; Kadhiresan, P.; Kataoka, K.; Khademhosseini, A.; Kopeček, J. i.; Kotov, N. A.; Krug, H. F.; Lee, D. S.; Lehr, C.-M.; Leong, K. W.; Liang, X.-J.; Lim, M. L.; Liz-Marzán, L. M.; Ma, X.; Macchiarini, P.; Meng, H.; Möhwald, H.; Mulvaney, P.; Nel, A. E.; Nie, S.; Nordlander, P.; Okano, T.; Oliveira, J.; Park, T. H.; Penner, R. M.; Prato, M.; Puntes, V.; Rotello, V. M.; Samarakoon, A.; Schaak, R. E.; Shen, Y.; Sjöqvist, S.; Skirtach, A. G.; Soliman, M. G.; Stevens, M. M.; Sung, H.-W.; Tang, B. Z.; Tietze, R.; Udugama, B. N.; VanEpps, J. S.; Weil, T.; Weiss, P. S.; Willner, I.; Wu, Y.; Yang, L.; Yue, Z.; Zhang, Q.; Zhang, Q.; Zhang, X.-E.; Zhao, Y.; Zhou, X.; Parak, W. J., Diverse Applications of Nanomedicine. *ACS Nano* **2017**, *11*, 2313−2381.

7. Chan, W. C. W., Nanomedicine 2.0. *Acc. Chem. Res.* **2017**, *50*, 627−632.

8. Kim, B. Y. S.; Rutka, J. T.; Chan, W. C. W., Nanomedicine. *N. Engl. J. Med.* **2010**, *363*, 2434–2443.

9. Duan, X.; Li, Y., Physicochemical Characteristics of Nanoparticles Affect Circulation, Biodistribution, Cellular Internalization, and Trafficking. *Small* **2013**, *9*, 1521–1532.

10. Kang, T.; Li, F.; Baik, S.; Shao, W.; Ling, D.; Hyeon, T., Surface design of magnetic nanoparticles for stimuli-responsive cancer imaging and therapy. *Biomaterials* **2017**, *136*, 98-114.

11. Long, N.; Wong, W.-T., The Chemistry of Molecular Imaging. Long, N.; Wong, W.-T., Eds. John Wiley & Sons, Inc: Hoboken, New Jersey, 2015.

12. Bertrand, N.; Wu, J.; Xu, X.; Kamaly, N.; Farokhzadb, O. C., Cancer nanotechnology: The impact of passive and active targeting in the era of modern cancer biology. *Adv Drug Deliv Rev.* **2014**, *66*, 2–25.

13. Blanco, E.; Shen, H.; Ferrari, M., Principles of nanoparticle design for overcoming biological barriers to drug delivery. *Nat. Biotech.* **2015**, *33*, 941–951.

14. Ernsting, M. J.; Murakami, M.; Roya, A.; Li, S.-D., Factors controlling the pharmacokinetics, biodistribution and intratumoral penetration of nanoparticles. *J. Control. Release* **2013**, *172*, 782–794.

15. Yu, M.; Zheng, J., Clearance Pathways and Tumor Targeting of Imaging Nanoparticles. *ACS Nano* **2015**, *9*, 6655–6674.

16. Albanese, A.; Tang, P. S.; Chan, W. C. W., The Effect of Nanoparticle Size, Shape, and Surface Chemistry on Biological Systems. *Annu. Rev. Biomed. Eng.* **2012**, *14*, 1–16.

17. Liu, J.; Yu, M.; Ning, X.; Zhou, C.; Yang, S.; Zheng, J., PEGylation and Zwitterionization: Pros and Cons in the Renal Clearance and Tumor Targeting of Near-IR-Emitting Gold Nanoparticles. *Angew. Chem. Int. Ed.* **2013**, *52*, 12572–12576.

18. Anselmo, A. C.; Mitragotri, S., Nanoparticles in the clinic. *Bioeng. Transl. Med.* **2016**, *1*, 10–29.

19. Bobo, D.; Robinson, K. J.; Islam, J.; Thurecht, K. J.; Corrie, S. R., Nanoparticle-Based Medicines: A Review of FDA-Approved Materials and Clinical Trials to Date. *Pharma. Res.* **2016**, *33*, 2373-2387.

20. Yoo, D.; Lee, J.-H.; Shin, T.-H.; Cheon, J., Theranostic Magnetic Nanoparticles. *Acc. Chem. Res.* **2011**, *44*, 863–874.

21. Willmann, J. K.; Bruggen, N. v.; Dinkelborg, L. M.; Gambhir, S. S., Molecular imaging in drug development. *Nat. Rev. Drug Discovery* **2008**, *7*, 591–607.

22. Brown, M.; Semelka, R., *MRI: Basic Principles and Applications*. Wiley-Liss: Hoboken, New Jersey, 2003.

23. Bloch, F.; Hansen, W. W.; M. Packard, Nuclear Induction. *Phys. Rev.* **1946**, *69*, 127.

24. Purcell, E. M.; Torrey, H. C.; Pound, R. V., Resonance Absorption by Nuclear Magnetic Moments in a Solid. *Phys. Rev.* **1946**, *69*, 37–38.

25. Lauterbur, P. C., Image Formation by Induced Local Interactions: Examples Employing Nuclear Magnetic Resonance. *Nature* **1973**, *242*, 190–191.

26. Mansfield, P., Snapshot Magnetic Resonance Imaging (Nobel Lecture). *Angew. Chem. Int. Ed.* **2004**, *43*, 5456–5464.

27. Major, J. L.; Meade, T. J., Bioresponsive, cell-penetrating, and multimeric MR contrast agents. *Acc. Chem. Res.* **2009**, *42*, 893–903.

28. Laurent, S.; Henoumont, C.; Stanicki, D.; Boutry, S.; Lipani, E.; Belaid, S.; Muller, R. N.; Elst, L. V., MRI Contrast Agents: From Molecules to Particles. Springer Nature: Singapore, 2017.

29. Merbach, A. E.; Toth, E., The Chemistry of Contrast Agents in Medical Magnetic Resonance Imaging. John Wiley & Sons Ltd., Chichester (UK): 2001.

30. Terreno, E.; Castelli, D. D.; Viale, A.; Aime, S., Challenges for Molecular Magnetic Resonance Imaging. *Chem. Rev.* **2010**, *110*, 3019−3042.

31. Greenwood, N. N.; Earnshaw, A., *Chemistry of the Elements*. 2nd ed.; Elsevier, Butterworth-Heinemann: New York, 1997.

32. Cotton, S., Lanthanide and Actinide Chemistry. John Wiley & Sons Inc.: West Sussex, England, 2006.

33. Rohrer, M.; Bauer, H.; Mintorovitch, J.; Requardt, M.; Weinmann, H.-J., Comparison of Magnetic Properties of MRI Contrast Media Solutions at Different Magnetic Field Strengths. *Invest. Radiol.* **2005**, *40*, 715–724.

34. Caravan, P.; Ellison, J. J.; McMurry, T. J.; Lauffer, R. B., Gadolinium(III) Chelates as MRI Contrast Agents: Structure, Dynamics and Applications. *Chem. Rev.* **1999**, *99*, 2293–2352.

35. Reimer, P.; Balzer, T., Ferucarbotran (Resovist): a new clinically approved RES-specific contrast agent for contrast-enhanced MRI of the liver: properties, clinical development, and applications. *Eur. Radiol.* **2003**, *13*, 1266–1276.

36. Jung, C. W.; Jacobs, P., Physical and chemical properties of superparamagnetic iron oxide MR contrast agents: ferumoxides, ferumoxtran, ferumoxsil. *Magn. Reson. Imaging* **1995**, *13*, 661–674.

37. Xu, W.; Kattel, K.; Park, J. Y.; Chang, Y.; Kim, T. J.; Lee, G. H., Paramagnetic nanoparticle T_1 and T_2 MRI contrast agents. *Phys. Chem. Chem. Phys.* **2012**, *14*, 12687–12700.

38. Cotton, F. A.; Wilkinson, G., *Advanced Inorganic Chemistry*. 4th ed.; Wiley-Interscience: New York, 1980.

39. Das, G. K.; Johnson, N. J. J.; Cramen, J.; Blasiak, B.; Latta, P.; Tomanek, B.; van Veggel, F. C. J. M., $NaDyF_4$ Nanoparticles as T_2 Contrast Agents for Ultrahigh Field Magnetic Resonance Imaging *J. Phys. Chem. Lett.* **2012**, *3*, 524−529.

40. Norek, M.; Peters, J. A., MRI contrast agents based on dysprosium or holmium. *Nucl. Magn. Reson. Spec.* **2011**, *59*, 64–82.

41. Caravan, P.; Farrar, C. T.; Frullano, L.; Uppal, R., Influence of molecular parameters and increasing magnetic field strength on relaxivity of gadolinium- and manganese-based T_1 contrast agents. *Contrast Media Mol. Imaging* **2009**, *4*, 89–100.

42. Lee, N.; Hyeon, T., Designed synthesis of uniformly sized iron oxide nanoparticles for efficient magnetic resonance imaging contrast agents. *Chem. Soc. Rev.* **2012**, *41*, 2575–2589.

43. Laurent, S.; Forge, D.; Port, M.; Roch, A.; Robic, C.; Elst, L. V.; Muller, R. N., Magnetic Iron Oxide Nanoparticles: Synthesis, Stabilization, Vectorization, Physicochemical Characterizations, and Biological Applications. *Chem. Rev.* **2008**, *108*, 2064–2110.

44. Zhao, Z.; Zhou, Z.; Bao, J.; Wang, Z.; Hu, J.; Chi, X.; Ni, K.; Wang, R.; Chen, X.; Chen, Z.; Gao, J., Octapod iron oxide nanoparticles as high-performance T-2 contrast agents for magnetic resonance imaging. *Nat. Commun.* **2013**, *4*, 2266.

45. Jang, J.-t.; Nah, H.; Lee, J.-H.; Moon, S. H.; Kim, M. G.; Cheon, J., Critical Enhancements of MRI Contrast and Hyperthermic Effects by Dopant-Controlled Magnetic Nanoparticles. *Angew. Chem. Int. Ed.* **2009**, *48*, 1234−1238.

46. Vleck, J. H. V., The Puzzle of Rare-earth Spectra in Solids. *J. Phys. Chem.* **1937**, *41*, 67–80.

47. Hänninen, P.; Härma, H., *Lanthanide Luminescence: Photophysical, Analytical and Biological Aspects*. Springer: Berlin Heidelberg, 2011.

48. Bűnzli, J.-C. G., Lanthanide Luminescence for Biomedical Analyses and Imaging. *Chem. Rev.* **2010**, *110*, 2729–2755.

49. Bünzli, J.-c. G., The europium(III) ion as spectroscopic probe in bioinorganic chemistry. *Inorganica Chimica Acta* **1987**, *139*, 219-222.

50. Sudarsan, V.; van Veggel, F. C. J. M.; Herring, R. A.; Raudsepp, M., Surface Eu^{3+} ions are different than ‘‘bulk’’ Eu^{3+} ions in crystalline doped LaF_3 nanoparticles. *J. Mater. Chem.* **2005**, *15*, 1332–1342.

51. Binnemans, K., Interpretation of europium(III) spectra. *Coordin. Chem. Rev.* **2015**, *295*, 1–45.

52. Horrocks, W. D., Jr.; Sudnick, D. R., Lanthanide Ion Probes of Structure in Biology. Laser Induced Luminescence Decay Constants Provide a Direct Measure of the Number of Metal-Coordinated Water Molecules. *J. Am. Chem. Soc.* **1979**, *101*, 334-340.

53. Hühn, J.; Carrillo-Carrion, C.; Soliman, M. G.; Pfeiffer, C.; Valdeperez, D.; Masood, A.; Chakraborty, I.; Zhu, L.; Gallego, M.; Yue, Z.; Carril, M.; Feliu, N.; Escudero,

A.; Alkilany, A. M.; Pelaz, B.; Pino, P. d.; Parak, W. J., Selected Standard Protocols for the Synthesis, Phase Transfer, and Characterization of Inorganic Colloidal Nanoparticles. *Chem. Mater.* **2017**, *29*, 399−461.

54. Dong, H.; Du, S.-R.; Zheng, X.-Y.; Lyu, G.-M.; Sun, L.-D.; Li, L.-D.; Zhang, P.-Z.; Zhang, C.; Yan, C.-H., Lanthanide Nanoparticles: From Design toward Bioimaging and Therapy. *Chem. Rev.* **2015**, *115*, 10725−10815.

55. Kwon, S. G.; Hyeon, T., Colloidal Chemical Synthesis and Formation Kinetics of Uniformly Sized Nanocrystals of Metals, Oxides, and Chalcogenides. *Acc. Chem. Res.* **2008**, *41*, 1696-1709.

56. Johnson, N. J. J.; Korinek, A.; Dong, C.; van Veggel, F. C. J. M., Self-Focusing by Ostwald Ripening: A Strategy for Layer-by-Layer Epitaxial Growth on Upconverting Nanocrystals. *J. Am. Chem. Soc.* **2012**, *134*, 11068−11071.

57. Ostwald, W., *Analytische Chemie*. 3rd ed.; Engelman: Leipzig, 1901.

58. Voss, B.; Haase, M., Intrinsic Focusing of the Particle Size Distribution in Colloids Containing Two Different Crystal Phases. *ACS Nano* **2013**, *7*, 11242−11254.

59. Voss, B.; Nordmann, J.; Uhl, A.; Komban, R.; Haase, M., Effect of Crystal Structure of Small Precursor Particles on the Growth of β-NaREF$_4$ (RE = Sm, Eu, Gd, Tb) Nanocrystals. *Nanoscale* **2013**, *5*, 806−812.

60. May, P. B.; John D. Suter, I.; May, P. S.; Berry, M. T., The Dynamics of Nanoparticle Growth and Phase Change During Synthesis of β-NaYF4. *J. Phys. Chem. C* **2016**, *120*, 9482−9489.

61. Johnson, N. J. J.; van Veggel, F. C. J. M., Lanthanide-Based Heteroepitaxial Core–Shell Nanostructures: Compressive versus Tensile Strain Asymmetry. *ACS Nano* **2014**, *8*, 10517–10527.

62. Dumestre, F.; Chaudret, B.; Amiens, C.; Renaud, P.; Fejes, P., Superlattices of Iron Nanocubes Synthesized from Fe[N(SiMe$_3$)$_2$]$_2$. *Science* **2004**, *303*, 821–823.

63. Park, J.; An, K.; Hwang, Y.; Park, J. G.; Noh, H. J.; Kim, J. Y.; Park, J. H.; Hwang, N. M.; Hyeon, T., Ultra-large-scale syntheses of monodisperse nanocrystals. *Nat. Mater.* **2004**, *3*, 891-895.

64. Peng, S.; Wang, C.; Xie, J.; Sun, S., Synthesis and Stabilization of Monodisperse Fe Nanoparticles. *J. Am. Chem. Soc.* **2006**, *128*, 10676-10677.

65. Wilcoxon, J. P.; Provencio, P. P., Use of Surfactant Micelles to Control the Structural Phase of Nanosize Iron Clusters. *J. Phys. Chem. B* **1999**, *103*, 9809-9812.

66. Huber, D. L., Synthesis, Properties, and Applications of Iron Nanoparticles. *Small* **2005**, *1*, 482–501.

67. Graf, C.; Vossen, D. L. J.; Imhof, A.; van Blaaderen, A., A General Method To Coat Colloidal Particles with Silica. *Langmuir* **2003**, *19*, 6693–6700.

68. Jalil, R. A.; Zhang, Y., Biocompatibility of silica coated $NaYF_4$ upconversion fluorescent nanocrystals. *Biomaterials* **2008**, *29*, 4122–4128.

69. Yi, G. S.; Chow, G. M., Water-Soluble $NaYF_4$:Yb,Er(Tm)/$NaYF_4$/Polymer Core/Shell/Shell Nanoparticles with Significant Enhancement of Upconversion Fluorescence. *Chem. Mater* **2007**, *19*, 341–343.

70. Nichkova, M.; Dosev, D.; Gee, S. J.; Hammock, B. D.; Kennedy, I. M., Microarray Immunoassay for Phenoxybenzoic Acid Using Polymer Encapsulated Eu:Gd_2O_3 Nanoparticles as Fluorescent Labels. *Anal. Chem.* **2005**, *77*, 6864–6873.

71. Jiang, G. C.; Pichaandi, J.; Johnson, N. J. J.; Burke, R. D.; Veggel, F. C. J. M. v., An effective polymer cross-linking strategy to obtain stable dispersions of upconverting $NaYF_4$ nanoparticles in buffers and biological growth media for biolabeling applications. *Langmuir* **2012**, *28*, 3239–3247.

72. Cao, T. Y.; Yang, Y.; Gao, Y. A.; Zhou, J.; Li, Z. Q.; Li, F. Y., High-quality water-soluble and surface-functionalized upconversion nanocrystals as luminescent probes for bioimaging. *Biomaterials* **2011**, *32*, 2959–2968.

73. Wong, H. T.; Vetrone, F.; Naccache, R.; Chan, H. L. W.; Hao, J. H.; Capobianco, J. A., Water dispersible ultra-small multifunctional $KGdF_4$:Tm^{3+}, Yb^{3+} nanoparticles with near-infrared to near-infrared upconversion. *J. Mater. Chem.* **2011**, *21*, 16589–16596.

74. Kumar, R.; Nyk, M.; Ohulchanskyy, T. Y.; Flask, C. A.; Prasad, P. N., Combined optical and MR bioimaging using rare earth ion doped $NaYF_4$ nanocrystals. *Adv. Funct. Mater.* **2009**, *19*, 853–859.

75. Zhang, Q. B.; Song, K.; Zhao, J. W.; Kong, X. G.; Sun, Y. J.; Liu, X. M.; Zhang, Y. L.; Zeng, Q. H.; Zhang, H., Hexanedioic acid mediated surface-ligand-exchange process for transferring $NaYF_4$:Yb/Er (or Yb/Tm) up-converting nanoparticles from hydrophobic to hydrophilic. *J. Colloid Interface Sci.* **2009**, *336*, 171–175.

76. Tong, S.; Hou, S.; Ren, B.; Zheng, Z.; Bao, G., Self-Assembly of Phospholipid-PEG Coating on Nanoparticles through Dual Solvent Exchange. *Nano Lett.* **2011**, *11*, 3720–3726.

77. Alipour, E.; Halverson, D.; McWhirter, S.; Walker, G. C., Phospholipid Bilayers: Stability and Encapsulation of Nanoparticles. *Annu. Rev. Phys. Chem.* **2017**, *68*, 12.1–12.23.

78. Hermanson, G. T., *Bioconjugate Techniques*. 2nd ed.; Elsevier: Oxford, UK, 2008.

79. Caravan, P., Strategies for increasing the sensitivity of gadolinium based MRI contrast agents. *Chem. Soc. Rev.* **2006**, *35*, 512–523.

80. Blasiak, B.; Landry, J.; Tyson, R.; Sharp, J.; Iqbal, U.; Abulrob, A.; Rushforth, D.; Matyas, J.; Ponjevic, D.; Sutherland, G. R.; Wolfsberger, S., Molecular susceptibility weighted imaging of the glioma rim in a mouse model. *J. Neurosc. Meth.* **2014**, *226*, 132–138.

81. Blasiak, B.; Barnes, S.; Foniok, T.; Rushforth, D.; Matyas, J.; Ponjevic, D.; Weglarz, W. P.; Tyson, R.; Iqbal, U.; Abulrob, A.; Sutherland, G. R.; Obenaus, A.; Tomanek, B., Comparison of T2 and T2*-weighted MR molecular imaging of a mouse model of glioma. *BMC Med. Imaging* **2013**, *13*, 20–28.

82. Bridot, J. L.; Faure, A. C.; Laurent, S.; Riviere, C.; Billotey, C.; Hiba, B.; Janier, M.; Josserand, V.; Coll, J. L.; Vander Elst, L.; Muller, R.; Roux, S.; Perriat, P.; Tillement, O., Hybrid Gadolinium Oxide Nanoparticles: Multimodal Contrast Agents for In Vivo Imaging. *J. Am. Chem. Soc.* **2007**, *129*, 5076−5084.

83. Johnson, N. J. J.; Oakden, W.; Stanisz, G. J.; Prosser, R. S.; van Veggel, F. C. J. M., Size-Tunable, Ultra-Small $NaGdF_4$ Nanoparticles: Insights into their T_1 MRI Contrast Enhancement. *Chem. Mater.* **2011**, *23*, 3714–3722.

84. Zhang, X.; Blasiak, B.; Marenco, A. J.; Trudel, S.; Tomanek, B.; van Veggel, F. C. J. M., Design and Regulation of $NaHoF_4$ and $NaDyF_4$ Nanoparticles for High-Field Magnetic Resonance Imaging. *Chem. Mater.* **2016**, *28*, 3060−3072.

85. Vaughan, T.; DelaBarre, L.; Snyder, C.; Tian, J.; Akgun, C.; Shrivastava, D.; Liu, W.; Olson, C.; Adriany, G.; Strupp, J.; Andersen, P.; Gopinath, A.; Moortele, P.-F. v. d.; Garwood, M.; Ugurbil, K., 9.4T Human MRI: Preliminary Results. *Magn. Reson. Med.* **2006**, *56*, 1274–1282.

86. Kemper, V. G.; Martino, F. D.; Emmerling, T. C.; Yacoub, E.; Goebel, R., High resolution data analysis strategies for mesoscale human functional MRI at 7 and 9.4T. *NeuroImage* **2017**, pii: S1053-8119(17)30286-0.

87. Bihan, D. L.; Schild, T., Human brain MRI at 500MHz, scientific perspectives and technological challenges. *Supercond. Sci. Technol.* **2017**, *30*, 033003.

88. Vaughan, J. T.; Snyder, C. J.; DelaBarre, L. J.; Bolan, P. J.; Tian, J.; Bolinger, L.; Adriany, G.; Andersen, P.; Strupp, J.; Ugurbil, K., 7 T Whole Body Imaging: Preliminary Results. *Magn Reson Med.* **2009**, *61*, 244–248

89. Bonnet, C. S.; Fries, P. H.; Crouzy, S.; Delangle, P., Outer-Sphere Investigation of MRI Relaxation Contrast Agents. Example of a Cyclodecapeptide Gadolinium Complex with Second-Sphere Water. *J. Phys. Chem. B* **2010**, *114*, 8770-8781.

90. Bonnet, C. S.; Fries, P. H.; Crouzy, S.; Seneque, O.; Cisnetti, F.; Boturyn, D.; Dumy, P.; Delang, P., A Gadolinium-Binding Cyclodecapeptide with a Large High-Field Relaxivity Involving Second-Sphere Water. *Chem. Eur. J.* **2009**, *15*, 7083–7093.

91. Helm, L., Relaxivity in paramagnetic systems: Theory and mechanisms. *Prog. Nucl. Magn. Reson. Spec.* **2006**, *49*, 45–64.

92. Koenig, S. H.; Kellar, K. E., Theory of $1/T_1$ and $1/T_2$ NMRD Profiles of Solutions of Magnetic Nanoparticles. *Magn. Reson. Med.* **1995**, *34*, 227-233.

93. Bűnzli, J.-C. G.; Piguet, C., Taking advantage of luminescent lanthanide ions. *Chem. Soc. Rev.* **2005**, *34*, 1048–1077.

94. Kattel, K.; Park, J. Y.; Xu, W.; Kim, H. G.; Lee, E. J.; Bony, B. A.; Heo, W. C.; Lee, J. J.; Jin, S.; Baeck, J. S.; Chang, Y.; Kim, T. J.; Bae, J. E.; Chae, K. S.; Lee, G. H., A Facile Synthesis, In vitro and In vivo MR Studies of D-Glucuronic Acid-Coated Ultrasmall Ln_2O_3 (Ln = Eu, Gd, Dy, Ho, and Er) Nanoparticles as a New Potential MRI Contrast Agent. *ACS Appl. Mater. Interfaces* **2011**, *3*, 3325–3334.

95. Johnson, N. J. J.; Sangeetha, N. M.; Boyer, J.-C.; van Veggel, F. C. J. M., Facile ligand-exchange with polyvinylpyrrolidone and subsequent silica coating of hydrophobic upconverting β-$NaYF_4$:Yb^{3+}/Er^{3+} nanoparticles. *Nanoscale* **2010**, *2*, 771–777.

96. Shannon, R. D. J., Revised Effective Ionic Radii and Systematic Study of Inter Atomic Distances in Halides and Chalcogenides. *Acta Cryst.* **1976**, *A32*, 751–767.

97. Abel, K. A.; Boyer, J.-C.; Andrei, C. M.; van Veggel, F. C. J. M., Analysis of the Shell Thickness Distribution on $NaYF_4$/$NaGdF_4$ Core/Shell Nanocrystals by EELS and EDS. *J. Phys. Chem. Lett.* **2011**, *2*, 185–189.

98. Diamente, P. R.; van Veggel, F. C. J. M., Water-Soluble Ln^{3+}-Doped LaF_3 Nanoparticles: Retention of Strong Luminescence and Potential as Biolabels. *J. Fluoresc.* **2005**, *15*, 543−551.

99. Lao, A.; Yu, H.; Jin, J.; Zhang, X.; Guo, Y.; Shi, Y.; Fu, Y.; Gao, S.; Zhao, L., Direct evidence for transformation of multiple active crystallographic sites' symmetry in β-$NaGdF_4$:Eu^{3+} nanocrystals. *J. Alloys Comp.* **2016**, *67*, 113–119.

100. Tu, D.; Liu, Y.; Zhu, H.; Li, R.; Liu, L.; Chen, X., Breakdown of Crystallographic Site Symmetry in Lanthanide-Doped $NaYF_4$ Crystals. *Angew. Chem. Int. Ed.* **2013**, *125*, 1166 –1171.

101. Wawrzynczyk, D.; Bednarkiewicz, A.; Nyk, M.; Strek, W.; Samoc, M., Ligand-dependent luminescence of ultra-small Eu^{3+}-doped $NaYF_4$ nanoparticles. *J. Nanopart. Res.* **2013**, *15*, 15:1707.

102. Stouwdam, J. W.; Hebbink, G. A.; Huskens, J.; Veggel, F. C. J. M. v., Lanthanide-Doped Nanoparticles with Excellent Luminescent Properties in Organic Media. *Chem. Mater.* **2003**, *15*, 4604-4616.

103. Lakowicz, J. R., Principles of Fluorescence Spectroscopy. 3rd ed.; Springer Science+Business Media, LLC: 2006.

104. Supkowski, R. M.; Horrocks, W. D., Jr. , On the determination of the number of water molecules, *q*, coordinated to europium(III) ions in solution from luminescence decay lifetimes. *Inorganica Chimica Acta* **2002**, *340*, 44–48.

105. Supkowski, R. M.; Horrocks, W. D., Jr., Displacement of Inner-Sphere Water Molecules from Eu^{3+} Analogues of Gd^{3+} MRI Contrast Agents by Carbonate and Phosphate Anions: Dissociation Constants from Luminescence Data in the Rapid-Exchange Limit. *Inorg. Chem.* **1999**, *38*, 5616-5619.

106. Garbuzenko, O.; Barenholz, Y.; Priev, A., Effect of grafted PEG on liposome size and on compressibility and packing of lipid bilayer. *Chem. Phys. Lipids* **2005**, *135*, 117–129.

107. Wong, J. Y.; Kuhl, T. L.; Israelachvili, J. N.; Mullah, N.; Zalipsky, S., Direct Measurement of a Tethered Ligand-Receptor Interaction Potential. *Science* **1997**, *275*, 820–822.

108. Haran, N.; Shporer, M., Study of water permeability through phospholipid vesicle membranes by 17-O NMR. *Biochimica et Biophysica Acta* **1976**, *426*, 638–646.

109. Beranová, L.; Humpolíčková, J.; Sýkora, J.; Benda, A.; Cwiklik, L.; Jurkiewicz, P.; Gröbner, G.; Hof, M., Effect of heavy water on phospholipid membranes: experimental confirmation of molecular dynamics simulations. *Phys. Chem. Chem. Phys.* **2012**, *14*, 14516–14522.

110. Tokutake, N.; Jing, B.; Regen, S. L., Probing the Hydration of Lipid Bilayers Using a Solvent Isotope Effect on Phospholipid Mixing. *Langmuir* **2004**, *20*, 8958–8960.

111. Buera, M. d. P.; Levi, G.; Karel, M., Glass Transition in Poly(vinylpyrrolidone): Effect of Molecular Weight and Diluents. *Biotechnol. Prog.* **1992**, *8*, 144–148.

112. Zeng, X.; Zhou, B.; Gao, Y.; Wang, C.; Li, S.; Yeung, C. Y.; We, W., Structural dependence of silver nanowires on polyvinyl pyrrolidone (PVP) chain length. *Nanotechnology* **2014**, *25*, 495601.

113. Bonnet, C. S.; Fries, P. H.; Gadelle, A.; Gambarelli, S.; Delangle, P., A Rigorous Framework To Interpret Water Relaxivity. The Case Study of a Gd(III) Complex with an α-Cyclodextrin Derivative. *J. Am. Chem. Soc.* **2008**, *130*, 10401-10413.

114. Belorizky, E.; Fries, P. H.; Helm, L.; Kowalewski, J.; Kruk, D.; Sharp, R. R.; Westlund, P.-O., Comparison of different methods for calculating the paramagnetic relaxation enhancement of nuclear spins as a function of the magnetic field. *J. Chem. Phys.* **2008**, *128*, 052315.

115. Fries, P. H.; Gateau, C.; Mazzanti, M., Practical Route to Relative Diffusion Coefficients and Electronic Relaxation Rates of Paramagnetic Metal Complexes in

Solution by Model-Independent Outer-Sphere NMRD. Potentiality for MRI Contrast Agents. *J. Am. Chem. Soc.* **2005**, *127*, 15801-15814.

116. Kruk, D.; Korpała, A.; Taheri, S. M.; Kozłowski, A.; Förster, S.; Rössler, E. A., ^{1}H relaxation enhancement induced by nanoparticles in solutions: Influence of magnetic properties and diffusion. *J. Chem. Phys.* **2014**, *140*, 174504.

117. Global Cancer: Facts and Figures. 3rd ed.; American Cancer Society: Atlanta, 2015.

118. Dall'Era, M. A.; Albertsen, P. C.; Bangma, C.; Carroll, P. R.; Carter, H. B.; Cooperberg, M. R.; Freedland, S. J.; Klotz, L. H.; Parker, C.; Soloway, M. S., Active Surveillance for Prostate Cancer: A Systematic Review of the Literature. *Eur. Urol.* **2012**, *62*, 976–983.

119. Heidenreich, A.; Bastian, P. J.; Bellmunt, J.; Bolla, M.; Joniau, S.; van der Kwast, T.; Mason, M.; Matveev, V.; Wiegel, T.; Zattoni, F.; Mottet, N., EAU Guidelines on prostate cancer. Part 1: screening, diagnosis, and local treatment with curative intent. *Eur. Urol.* **2014**, *65*, 124–137.

120. Mottet, N.; Bellmunt, J.; Bolla, M.; Briers, E.; Cumberbatch, M. G.; Santis, M. D.; Fossati, N.; Gross, T.; Henry, A. M.; Joniau, S.; Lam, T. B.; Mason, M. D.; Matveev, V. B.; Moldovan, P. C.; Bergh, R. C. N. v. d.; Broeck, T. V. d.; Poel, H. G. v. d.; Kwast, T. H. v. d.; PhilipCornford, EAU-ESTRO-SIOG Guidelines on Prostate Cancer. Part 1: Screening, Diagnosis, and Local Treatment with Curative Intent. *Eur. Urol.* **2017**, *71*, 618-629.

121. Neal, D. E.; Leung, H. Y.; Powell, P. H.; Hamdy, F. C.; Donovan, J. L., Unanswered questions in screening for prostate cancer. *Eur. J. Can* **2000**, *36*, 1316-1321.

122. Selley, S.; Donovan, J.; Faulkner, A.; Coast, J.; Gillatt, D., Diagnosis, management and screening of early localised prostate cancer. *Health Technol. Assess.* **1997**, *1*, 1–96.

123. Obek, C.; Doganca, T.; Erdal, S.; Erdogan, S.; Durak, H., Core length in prostate biopsy: size matters. *J. Urol.* **2012**, *187*, 2051–2055.

124. Ghosh, A.; Heston, W. D., Tumor target prostate specific membrane antigen (PSMA) and its regulation in prostate cancer. *J. Cell. Biochem.* **2004**, *91*, 528–539.

125. Chang, S. S., Overview of prostate-specific membrane antigen. *Rev. Urol.* **2004**, *6(suppl 10)*, S13-S18.

126. Rajasekaran, S. A.; Anilkumar, G.; Oshima, E.; Bowie, J. U.; Liu, H.; Heston, W.; Bander, N. H.; Rajasekaran, A. K., A novel cytoplasmic tail MXXXL motif mediates the internalization of prostate-specific membrane antigen. *Mol. Biol. Cell* **2003**, *14*, 4835–4845.

127. Smith-Jones, P. M.; Vallabahajosula, S.; Goldsmith, S. J.; Navarro, V.; Hunter, C. J., In vitro characterization of radiolabeled monoclonal antibodies specific for the

extracellular domain of prostate-specific membrane antigen. *Cancer Res.* **2000**, *60*, 5237–5243.

128. Lee, N.; Yoo, D.; Ling, D.; Cho, M. H.; Hyeon, T.; Cheon, J., Iron Oxide Based Nanoparticles for Multimodal Imaging and Magnetoresponsive Therapy. *Chem. Rev.* **2015**, *115*, 10637−10689.

129. Hou, Y.; Qiao, R.; Fang, F.; Wang, X.; Dong, C.; Liu, K.; Liu, C.; Liu, Z.; Lei, H.; Wang, F.; Gao, M., $NaGdF_4$ Nanoparticle-BasedMolecular Probes for Magnetic Resonance Imaging of Intraperitoneal Tumor Xenografts *in Vivo*. *ACS Nano* **2013**, *7*, 330-338.

130. Fries, P. H., Computing Electronic Spin Relaxation for Gd^{3+}-Based Contrast Agents – Practical Implementation. *Eur. J. Inorg. Chem.* **2012**, 2156–2166.

131. Wilhelm, S.; Tavares, A. J.; Dai, Q.; Ohta, S.; Audet, J.; Dvorak, H. F.; Chan, W. C. W., Analysis of nanoparticle delivery to tumours. *Nat. Rev. Mater.* **2016**, *1*, 1–12.

132. Fang, J.; Nakamura, H.; Maeda, H., The EPR effect: Unique features of tumor blood vessels for drug delivery, factors involved, and limitations and augmentation of the effect. *Adv Drug Deliv Rev.* **2011**, *63*, 136-151.

133. Daneshvar, D. H.; McKee, A. C., Traumatic Brain Injury. In *Neurobiology of Brain Disorders: Biological Basis of Neurological and Psychiatric Disorders*, Elsevier: 2015; p 219−235.

134. DeKosky, S. T.; Ikonomovic, M. D.; Gandy, S., Traumatic Brain Injury - Football, Warfare, and Long-Term Effects. *New. Engl. J. Med.* **2010**, *363*, 1293−1296.

135. Blennow, K.; Hardy, J.; Zetterberg, H., The Neuropathology and Neurobiology of Traumatic Brain Injury. *Neuron* **2012**, *76*, 886−889.

136. Kulbe, J. R.; Geddes, J. W., Current status of fluid biomarkers in mild traumatic brain injury. *Exp. Neurol.* **2016**, *275*, 334–352.

137. Bales, J. W.; Wagner, A. K.; Kline, A. E.; Dixon, C. E., Persistent cognitive dysfunction after traumatic brain injury: a dopamine hypothesis *Neurosci. Biobehav Rev.* **2009**, *33*, 981–1003.

138. Buéea, L.; Bussiérec, T.; Buée-Scherrerb, V.; Delacourtea, A.; Hof, P. R., Tau protein isoforms, phosphorylation and role in neurodegenerative disorders. *Brain Res. Rev.* **2000**, *33*, 95–130.

139. Johnson, G. V. W.; Stoothoff, W. H., Tau phosphorylation in neuronal cell function and dysfunction. *J. Cell Sci.* **2004**, *117*, 5721–5729.

140. Rankin, C. A.; Sun, Q.; Gamblin, T. C., Pre-assembled tau filaments phosphorylated by GSK-3β form large tangle-like structures. *Neurobiol. Dis.* **2008**, *31*, 368–377.

141. Rankin, C. A.; Sun, Q.; Gamblin, T. C., Tau phosphorylation by GSK-3β promotes tangle-like filament morphology. *Mol. Neurodegener.* **2007**, *2*, 12.

142. Albayram, O.; Herbert, M. K.; Kondo, A.; Tsai, C. Y.; Baxley, S.; Lian, X.; Hansen, M.; Zhou, X. Z.; Lu, K. P., Function and regulation of tau conformations in the development and treatment of traumatic brain injury and neurodegeneration. *Cell Biosci.* **2016**, *6*, 59.

143. Muyldermans, S., Nanobodies: Natural Single-Domain Antibodies. *Annu. Rev. Biochem.* **2013**, *82*, 775–797.

144. Goda, Y.; Colicos, M. A., Photoconductive stimulation of neurons cultured on silicon wafers. *Nat. Protoc.* **2006**, *1*, 461−467.

145. Creighton, T. E., *Protein Structure: A Practical Approach*. IRL Press: Oxford, U. K., 1997.

146. Pace, C. N.; Vajdos, F.; Fee, L.; Grimsley, G.; Gray, T., How to measure and predict the molar absorption coefficient of a protein. *Protein Sci.* **1995**, *4*, 2411–2423.

147. Na, H. B.; Song, I. C.; Hyeon, T., Inorganic Nanoparticles for MRI Contrast Agents. *Adv. Mater.* **2009**, *21*, 2133–2148.

148. Hadjipanayis, C. G.; Bonder, M. J.; Balakrishnan, S.; Wang, X.; Mao, H.; Hadjipanayis, G. C., Metallic Iron Nanoparticles for MRI Contrast Enhancement and Local Hyperthermia. *Small* **2008**, *4*, 1925–1929.

149. Sen, T.; Sebastianelli, A.; Bruce, I. J., Mesoporous silica-magnetite nanocomposite: fabrication and applications in magnetic bioseparations. *J. Am. Chem. Soc.* **2006**, *128*, 7130–7131.

150. Sun, C.; Lee, J. S. H.; Zhang, M., Magnetic nanoparticles in MR imaging and drug delivery. *Adv. Drug Deliv. Rev.* **2008**, *60*, 1252–1265.

151. Lu, A.-H.; Salabas, E. L.; Schüth, F., Magnetic Nanoparticles: Synthesis, Protection, Functionalization, and Application. *Angew. Chem. Int. Ed.* **2007**, *46*, 1222–1244.

152. Jun, Y.-w.; Lee, J.-H.; Cheon, J., Chemical Design of Nanoparticle Probes for High-Performance Magnetic Resonance Imaging. *Angew. Chem. Int. Ed.* **2008**, *47*, 5122–5135.

153. Crangle, J.; Goodman, G. M., The magnetization of pure iron and nickel. *Proc. R. Soc. Lond. A, Math. Phys. Sci.* **1971**, *321*, 477–491.

154. Cheong, S.; Ferguson, P.; Feindel, K. W.; Hermans, I. F.; Callaghan, P. T.; Meyer, C.; Slocombe, A.; Su, C.-H.; Cheng, F.-Y.; Yeh, C.-S.; Ingham, B.; Toney, M. F.; Tilley, R. D., Simple Synthesis and Functionalization of Iron Nanoparticles for Magnetic Resonance Imaging. *Angew. Chem. Int. Ed.* **2011**, *50*, 4206 –4209.

155. Park, J.; Lee, E.; Hwang, N.-M.; Kang, M.; Kim, S. C.; Hwang, Y.; Park, J.-G.; Noh, H.-J.; Kim, J.-Y.; Park, J.-H.; Hyeon, T., One-Nanometer-Scale Size-Controlled Synthesis of Monodisperse Magnetic Iron Oxide Nanoparticles. *Angew. Chem.* **2005**, *117*, 2932–2937.

156. Wen, J. Z.; Goldsmith, C. F.; Ashcraft, R. W.; Green, W. H., Detailed Kinetic Modeling of Iron Nanoparticle Synthesis from the Decomposition of $Fe(CO)_5$. *J. Phys. Chem. C* **2007**, *111*, 5677–5688.

157. Mourdikoudis, S.; Liz-Marzán, L. M., Oleylamine in Nanoparticle Synthesis. *Chem. Mater* **2013**, *25*, 1465−1476.

158. Farrell, D.; Majetich, S. A.; Wilcoxon, J. P., Preparation and Characterization of Monodisperse Fe Nanoparticles. *J. Phys. Chem. B* **2003**, *107*, 11022-11030.

159. Scherrer, P., Bestimmung der Größe und der inneren Struktur von Kolloidteilchen mittels Röntgenstrahlen. *Göttinger Nachrichten Math. Phys.* **1918**, *2*, 98–100.

160. Wang, W.; Dahl, M.; Yin, Y., Hollow Nanocrystals through the Nanoscale Kirkendall Effect. *Chem. Mater* **2013**, *25*, 1179−1189.

161. Yang, Z.; Yang, N.; Pileni, M.-P., Nano Kirkendall Effect Related to Nanocrystallinity of Metal Nanocrystals: Influence of the Outward and Inward Atomic Diffusion on the Final Nanoparticle Structure. *J. Phys. Chem. C* **2016**, *119*, 22249−22260.

162. Brooks, R., T_2-Shortening by Strongly Magnetized Spheres: A Chemical Exchange Model. *Magn Reson Med.* **2002**, *47*, 388−391.

163. Brooks, R.; Moiny, F.; Gillis, P., On T_2-Shortening by Weakly Magnetized Particles: The Chemical Exchange Model *Magn. Reson. Med.* **2001**, *45*, 1014−1020.

164. Gillis, P.; Moiny, F.; Brooks, R. A., On T_2-Shortening by Strongly Magnetized Spheres: A Partial Refocusing Model. *Magn Reson Med.* **2002**, *47*, 257−263.

165. Lee, N.; Choi, Y.; Lee, Y.; Park, M.; Moon, W. K.; Choi, S. H.; Hyeon, T., Water-Dispersible Ferrimagnetic Iron Oxide Nanocubes with Extremely High r_2 Relaxivity for Highly Sensitive in Vivo MRI of Tumors. *Nano Lett.* **2012**, *12*, 3127−3131.

166. Meffre, A.; Lachaize, S.; Gatel, C.; Respaud, M.; Chaudret, B., Use of long chain amine as a reducing agent for the synthesis of high quality monodisperse iron(0) nanoparticles. *J. Mater. Chem.* **2011**, *21*, 13464–13469.

167. Pace, L.; Nicolai, E.; Luongo, A.; Aiello, M.; Catalano, O. A.; Soricelli, A.; Salvatore, M., Comparison of whole-body PET/CT and PET/MRI in breast cancer patients:

lesion detection and quantitation of 18F-deoxyglucose uptake in lesions and in normal organ tissues. *Eur. J. Radiol.* **2014**, *83*, 289-296.

168. Kolin, D. L.; Wiseman, P. W., Advances in Image Correlation Spectroscopy: Measuring Number Densities, Aggregation States, and Dynamics of Fluorescently labeled Macromolecules in Cells. *Cell Biochem. Biophys.* **2007**, *49*, 141–164.

169. Costantino, S.; Comeau, J. W. D.; Kolin, D. L.; Wiseman, P. W., Accuracy and Dynamic Range of Spatial Image Correlation and Cross-Correlation Spectroscopy. *Biophys. J.* **2005**, *89*, 1251–1260.

170. Petersen, N.; Höddelius, P. L.; Wiseman, P. W.; Seger, O.; Magnusson, K.-E., Quantitation of Membrane Receptor Distributions by Image Correlation Spectroscopy: Concept and Application. *Biophys. J.* **1993**, *65*, 1135-1146.

171. Doane, T. L.; Burda, C., The unique role of nanoparticles in nanomedicine: imaging, drug delivery and therapy. *Chem. Soc. Rev.* **2012**, *41*, 2885–2911.

172. Nam, J.; Won, N.; Bang, J.; Jin, H.; Park, J.; Jung, S.; Jung, S.; Park, Y.; Kim, S., Surface engineering of inorganic nanoparticles for imaging and therapy. *Adv. Drug Deliv. Rev.* **2013**, *65*, 622–648.

173. Dubertret, B.; Skourides, P.; Norris, D. J.; Noireaux, V.; Brivanlou, A. H.; Libchaber, A., In Vivo Imaging of Quantum Dots Encapsulated in Phospholipid Micelles. *Science* **2002**, *298*, 1759–1762.

174. Schooneveld, M. M. v.; Vucic, E.; Koole, R.; Zhou, Y.; Stocks, J.; Cormode, D. P.; Tang, C. Y.; Gordon, R. E.; Nicolay, K.; Meijerink, A.; Fayad, Z. A.; Mulder, W. J. M., Improved Biocompatibility and Pharmacokinetics of Silica Nanoparticles by Means of a Lipid Coating: A Multimodality Investigation. *Nano Lett.* **2008**, *8*, 2517–2525.

175. Li, L.-L.; Zhang, R.; Yin, L.; Zheng, K.; Qin, W.; Selvin, P. R.; Lu, Y., Biomimetic Surface Engineering of Lanthanide-Doped Upconversion Nanoparticles as Versatile Bioprobes. *Angew. Chem. Int. Ed.* **2012**, *51*, 6121 –6125.

176. Panchuk–Voloshina, N.; Haugland, R. P.; Bishop–Stewart, J.; Bhalgat, M. K.; Millard, P. J.; Mao, F.; Leung, W.-Y.; Haugland, R. P., Alexa Dyes, a Series of New Fluorescent Dyes that Yield Exceptionally Bright, Photostable Conjugates. *J. Histochem. Cytochem.* **1999**, *47*, 1179–1188.

177. Johnson, I. D., *The Molecular Probes Handbook: A Guide to Fluorescent Probes and Labeling Technologies*. 11th ed.; Life Technologies Corporation: 2010.

178. Chandrasekhar, S., Stochastic Problems in Physics and Astronomy. *Rev. Mod. Phys.* **1943**, *5*, 1.

179. Andreoli, T. E., Membrane Physiology. Springer US: 1980.

180. Mornet, S.; Vasseur, S.; Grasset, F.; Duguet, E., Magnetic nanoparticle design for medical diagnosis and therapy. *J. Mater. Chem.* **2004**, *14*, 2161–2175.

181. Mai, H.-X.; Zhang, Y.-W.; Sun, L.-D.; Yan, C.-H., Size- and Phase-Controlled Synthesis of Monodisperse $NaYF_4$:Yb,Er Nanocrystals from a Unique Delayed Nucleation Pathway Monitored with Upconversion Spectroscopy. *J. Phys. Chem. C* **2007**, *111*, 13730–13739.